Cork Open Research Archive
Cartlann Taighde Oscailte Chorcaí

UCC Library and UCC researchers have made this item openly available. Please let us know how this has helped you. Thanks!

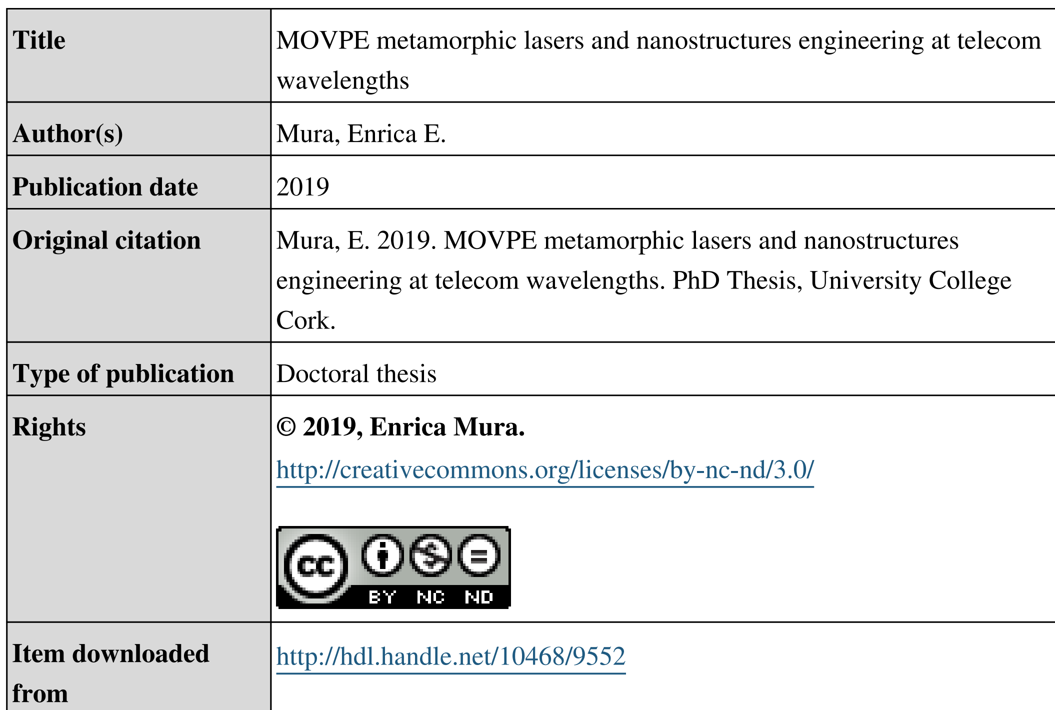

Title	MOVPE metamorphic lasers and nanostructures engineering at telecom wavelengths
Author(s)	Mura, Enrica E.
Publication date	2019
Original citation	Mura, E. 2019. MOVPE metamorphic lasers and nanostructures engineering at telecom wavelengths. PhD Thesis, University College Cork.
Type of publication	Doctoral thesis
Rights	**© 2019, Enrica Mura.** http://creativecommons.org/licenses/by-nc-nd/3.0/
Item downloaded from	http://hdl.handle.net/10468/9552

Downloaded on 2021-11-27T09:21:55Z

University College Cork, Ireland
Coláiste na hOllscoile Corcaigh

Ollscoil na hÉireann, Corcaigh

NATIONAL UNIVERSITY OF IRELAND, CORK

MOVPE metamorphic lasers and nanostructure engineering at telecom wavelengths

Thesis presented by

Enrica Mura

for the degree of

Doctor of Philosophy

Epitaxy and Physics of Nanostructures Group

Tyndall National Institute

Department of Physics

Research Supervisor: Dr. Emanuele Pelucchi

Head of the Department: Prof. John McInerney

December, 2019

Contents

Declaration of Authorship vii

List of Acronym xi

Abstract xv

Publication list xvii

1 Introduction 1
- 1.1 Context and motivation . . . 1
- 1.2 Semiconductor materials suitable for 1.3 μm applications . . . 4
- 1.3 Metamorphic telecom laser: state of art . . . 7
- 1.4 Structure of the thesis . . . 9

2 Material growth and characterization 15
- 2.1 MOVPE overview . . . 15
- 2.2 Our growth facility . . . 17
  - 2.2.1 High purity levels . . . 18
- 2.3 Characterization techniques . . . 20
  - 2.3.1 High resolution X-ray diffraction . . . 20
  - 2.3.2 Atomic Force Microscopy . . . 21
  - 2.3.3 Micro photoluminescence set-up . . . 23

3 The metamorphic buffer 27
- 3.1 Strained heterostructures . . . 27
- 3.2 $In_xGa_{1-x}As$ metamorphic substrate . . . 31
- 3.3 Characterization of the MBL for the 1.3 μm QWs laser . . . 35

4 Cladding: Superlattice approach 43
- 4.1 The choice of the cladding layer . . . 43
  - 4.1.1 Structure and growth condition of the cladding layer . . . 44
- 4.2 AlInGaAs . . . 45
  - 4.2.1 Effect of trimethylantimony . . . 45
  - 4.2.2 Effect of Strain Balancing Layer . . . 48

4.3 InGaP . . . 52
4.3.1 InGaP on MBL . . . 53
4.4 Roughness “inversion” study . . . 61
4.5 Superlattice approach . . . 67

5 Laser: active part (barriers and QWs) 77
5.1 Structure and growth condition of SCH structure . . . 77
5.2 Barriers . . . 78
5.3 Strained QWs . . . 79
5.4 Changes in the outer barrier . . . 81
5.5 QWs layer thickness . . . 83
5.6 Strain compensation: GaAs effect . . . 85
5.6.1 The digital alloy . . . 91
5.7 QWs vs Temperature . . . 93
5.7.1 Growth temperature 540°C . . . 93
5.7.2 Growth temperature 600°C . . . 98
5.7.3 Growth temperature 625 – 650°C . . . 100
5.8 Three strained QWs . . . 104
5.9 Summary . . . 107

6 Electro-optical characterization of the metamorphic laser 111
6.1 Laser characterization . . . 111
6.2 First full laser: cladding SL . . . 113
6.3 Second full laser: upper cladding SL ramp . . . 116
6.4 Third full laser: MBL substrate doping . . . 120
Three quantum wells (QWs) . . . 120
Lower cladding ramp . . . 121
metamorphic buffer layer (MBL) doping . . . 122
6.4.1 Third laser characterization . . . 125

7 InP(As) self-assembled nanostructures 131
7.1 Quantum size effect . . . 132
7.1.1 Self-organized standard growth of QDs . . . 133
7.2 Influence of the hydrides exposure . . . 134
7.2.1 Samples structure and growth parameters . . . 137
7.2.2 Zoology of the nanostructures . . . 139
7.3 Rings growth mechanism . . . 142
7.4 Nanostructures emission properties . . . 143
7.4.1 Capping studio and optical properties . . . 143

7.5 Summary 148

8 Conclusion and future work **153**

A Dislocations **159**

Acknowledgements **165**

Declaration of Authorship

I, **Enrica Mura**, declare that this thesis titled, "MOVPE metamorphic lasers and nanostructure engineering at telecom wavelengths" and the work presented in it are my own, and that it has not been submitted for another degree, either at University College Cork or elsewhere.

Enrica Mura
Tyndall National Institute,
University College Cork,
December, 2019

“*And as we wind on down the road*
Our shadows taller than our soul
There walks a lady we all know
Who shines white light and wants to show
How everything still turns to gold
And if you listen very hard
The tune will come to you at last
When all are one and one is all
To be a rock and not to roll
And she’s buying the stairway to heaven”

Led Zeppelin

List of Acronym

3D three-dimensional

$\boldsymbol{\alpha}_{\mathrm{i}}$ internall loss

AFM Atomic Force Microscopy

CAGR Compound Annual Growth Rate

CH cross-hatch

CIL interface controlling layer

CL cavity length

CW continuous wave

DOS density-of-states

EPN Epitaxy and Physics of Nanostructures

$\boldsymbol{\eta}_{\mathrm{i}}$ internal quantum efficiency

$\boldsymbol{\eta}_{\mathrm{d}}$ external differencial quantum efficiency

FWHM full width at half maximum

HAADF high angle annular dark field

$\mathbf{h_c}$ critical thickness

HRXRD High resolution X-ray diffraction

HVPE hydride vapor phase epitaxy

Hyds Hydrides

$\mathbf{I_{th}}$ threshold current

$\mathbf{J_{th}}$ density threshold current

LED light-emitting diode

L-I light-current

L-I-V Light-current-voltage

LM lattice matched

LPE liquid phase epitaxy

MBE molecular beam epitaxy

MBL metamorphic buffer layer

MD misfit dislocation

MFC mass flow controller

ML monolayer

MO metalorganic

MOCVD metalorganic chemical vapor deposition

MOVPE metal-organic vapour phase epitaxy

μPL micro photoluminescence set-up

MQW multi quantum well

N_2 nitrogen

NA numerical aperture

N-DIC (Nomarski) Differential Interference Contrast

NTT Nippon Telegraph and Telephone Corporation

PC pressure controller

PL photoluminescence

QD quantum dot

QR quantum ring

QW quantum well

RMS Root Mean Square

RPM revolution per minute

R_s series resistance

RSM Reciprocal Space Map

SAES Società Apparecchi Electrici e Scientifici

SBL Strain Balancing Layer

SCH separate confinement heterostructure

SL superlattice

STEM scanning transmission electron microscope

T_0 characteristic temperature

TD Threading dislocation

TDD Threading dislocation density

TEM transmission electron microscopy

TMAl trimethylaluminum

TMGa trimethylgallium

TMIn trimethylindium

TMSb trimethylantimony

T_{gr} growth temperature

TS tensile strained

V_0 turning voltage

VCSEL vertical-cavity surface-emitting laser

V-I voltage-current

Abstract

In recent years, considerable attention has been drawn to the design of heterostructures on GaAs substrates emitting in the 1.3-µm spectral range for replacing InP injection lasers in medium range fiber-optic communication links. Scaling considerations apart, the enhanced electronic confinement in GaAs-based devices can be expected to reduce carrier leakage at high temperatures, thereby overcoming one of the limiting factors associated with InP-based technologies. InGaAs metamorphic buffer heterostructures constitutes an alternative to the conventional routes relying on quantum dots or dilute nitride approaches, all with their own technical challenges and drawbacks. Metamorphic growth techniques provide compositionally graded buffer layers where the dislocations caused by strain relaxation are confined to the graded layers. However, when grown by metal-organic vapour phase epitaxy (MOVPE), it has been shown as extremely challenging to achieve $\sim 1.3\mu m$ emission in InGaAs metamorphic quantum well (QW) lasers (on GaAs substrate), due to a variety of strong, growth related issues, fundamentally linked to the overall epilayer thickness.

In this contribution we demonstrate a > 1.3 μm-band laser grown by MOVPE on an engineered metamorphic parabolic graded $In_xGa_{1-x}As$ buffer. A metamorphic multiple-quantum well structure containing cladding, active, and contact layers was grown. In the cladding, we exploit/control the correlation between epilayer thickness and defect generation and, importantly, demonstrate that the limiting factors introduced by surface instabilities during epitaxy can be managed by an innovative design. The bottom and the upper cladding are built as a combination of AlInGaAs and InGaP alloys in a superlattice (SL) structure. The improved quality of the material was confirmed, for example, by extensive Atomic Force Microscopy (AFM) analyses, showing low roughness (and no direct evidence of defect lines).

The heavily compressive strain in QWs and in the metamorphic buffer layer (in combination with the surface step bunched ordering) promoted three-dimensional (3D) features formation under certain growth temperatures and for certain percentage of indium in the QWs. To avoid and control the 3D nanostructuring we proposed as a possible solution the insertion of a GaAs layer deposited before the QW. Moreover, we individuated a range of growth temperature and indium content in the QWs 3D-nanostructures and defects free, verifying the emission of interest.

Building on these results, stripe waveguide lasers were fabricated, then characterized electro-optically. Best electro-optical result are reached with

modified lower and upper SL cladding structures, adding a graded composition layers at the interfaces following the aim to improve the carrier transport. A 500 μm long and 2.5 μm wide stripe waveguide exhibited a threshold current (I_{th}) of $\sim$ 152 mA, corresponding to a density threshold current (J_{th}) of $\sim$ 127 mA/cm^2 per QWs , operating at room temperature in pulse mode. The turning voltage was $\sim$ 0.8 V and the resistance series was 4.5 Ω. The emission wavelength was peaked at $\sim$ 1.34 μm, registered in pulse mode at low duty cycle. With shorter stripes laser, 10 μm and 20 μm wide, with different cavity lengths, we achieved the Light-current-voltage (L-I-V) curves in pulse and continuous wave (CW) mode. The threshold current varied from 130 mA to 170 mA in the operating temperature range of 30 °C-80 °C, and a characteristic temperature (T_0) of 95 K was calculated. The internall loss ($\boldsymbol{\alpha}_i$) and internal quantum efficiency ($\boldsymbol{\eta}_i$) extrapolated were $\sim$ 30 cm^{-1} and $\sim$ 57% respectively.

Those results prove that the epitaxial structure developed in this thesis work allow to fabricate one the few (specifically the second one, referring to that proposed by a Nippon Telegraph and Telephone Corporation (NTT) Japanese group in 2015 year) InGaAs metamorphic QW laser GaAs based, operating at $>$ 1.3 μm using the MOVPE technology.

Publication list

The following is a list of published work in which aspects of the research presented in this thesis have featured.

Publications

- E. E. Mura, A. Gocalinska, G. Juska, B. Corbett, and E. Pelucchi, "1.3 μm metamorphic laser", to be submitted.
- A. M. Gocalinska, E. E. Mura, M. Manganaro, G. Juska, V. Dimastrodonato, K. Thomas, A. Zangwill, D. D. Vvedensky, and E. Pelucchi, "Early stages of InP nanostructure aggregation on AlInAs", to be submitted.
- E. E. Mura, A. Gocalinska, G. Juska, and E. Pelucchi, "InP/InGaAs self-assembled nanostructures for broadband application", to be submitted.
- A. Pescaglini, A. Gocalinska, S. Bogusevschi, S. T. Moroni, G. Juska, E. E. Mura, J. Justice, B. Corbett, E. P. O'Reilly, and E. Pelucchi, "Three-Dimensional Self-Assembled Columnar Arrays of AlInP Quantum Wires for Polarized Micrometer-Sized Amber Light Emitting Diodes", ACS Photonics 5.4 (2018): 1318-1325.
- J. O'Callaghan, R. Loi, E. E. Mura, B. Roycroft, A. J. Trindade, K. Thomas, A. Gocalinska, E. Pelucchi, J. Zhang, G. Roelkens, C. A. Bower, and B. Corbett, "Comparison of InGaAs and InAlAs sacrificial layers for release of InP-based devices", Optical Materials Express 7.12 (2017): 4408-4414.
- E. E. Mura, A. Gocalinska, G. Juska, S. T. Moroni, A. Pescaglini, and E. Pelucchi, "Tuning InP self-assembled quantum structures to telecom wavelength: A versatile original InP (As) nanostructure workshop", Applied Physics Letters 110.11 (2017): 113101.

Conferences (poster/oral presentation)

- E. E. Mura, A. Gocalinska, G. Juska, S. T. Moroni, A. Pescaglini and E. Pelucchi, "The "metamorphosis" of InP nanostructures by MOVPE", EWMOVPE 2015, June 7-10 2015, Lund, Sweden.

- E. E. Mura (oral, presenting author), A. Gocalinska, G. Juska, S. T. Moroni, A. Pescaglini and E. Pelucchi, "Inp self-assembled nanostructures: morphological control, evolution and emission properties", Photonics Ireland, 2-4 September 2015, Cork, Ireland.

- E. E. Mura, A. Gocalinska, G. Juska, S. T. Moroni, A. Pescaglini and E. Pelucchi, "Influence of Hydrides on InP nanostructures grown by MOVPE", Summer school, Epitaxy updates and promise, 14-18 September 2015, Porquerolles, France.

- E. E. Mura, A. Gocalinska, G. Juska, S. T. Moroni, A. Pescaglini and E. Pelucchi, "InP nanostructures grown by MOVPE: hydrides influence", Intel Ireland Research Conference, 20 October 2015, Dublin, Ireland.

- E. E. Mura, A. Gocalinska, G. Juska, S. T. Moroni, A. Pescaglini, and E. Pelucchi, "Shape evolution and emission property of InP nanostructures under hydrides influence", Compound Semiconductor Week 2016, June 26-30, 2016, Toyama International Conference Center, Toyama, Japan.

- E. E. Mura (oral, presenting author), A. Gocalinska, G. Juska, S. T. Moroni, A. Pescaglini and E. Pelucchi, "InP(As) NanoRings and Quantum Dots on AlInAs: MOVPE controllable epitaxy for telecom wavelength nanostructures", 18th International Conference on Metal Organic Vapor Phase Epitaxy, July 10-15, 2016, Sheraton San Diego Hotel Marina, San Diego, California, US.

- E. E. Mura, A. Gocalinska, G. Juska, S. T. Moroni, and E. Pelucchi, "Development of 1.3 μm MOVPE metamorphic laser for optical interconnects", Intel Ireland Research Conference, 12 October 2016, Dublin, Ireland.

- E. E. Mura (oral, presenting author), A. Gocalinska, G. Juska, S. T. Moroni, J. O'Callagan, B. Corbet, and E. Pelucchi, "Controlling surface roughening instabilities as a viable paradigm for MOVPE-grown metamorphic lasers at 1.3 μm", Compound Semiconductor week, May 14-18, 2017 Berlin, Germany.

- E. E. Mura, A. Gocalinska, G. Juska, S. T. Moroni, J. O'Callagan, B. Corbet, and E. Pelucchi, "Surface Instability Management for MOVPE-Grown Metamorphic laser at 1.3 μm", 17th European Workshop on Metalorganic Vapour Phase Epitaxy, June 18-21, 2017, Grenoble, France.

- E. E. Mura(oral), A. Gocalinska, G. Juska, R. Loi, S. T. Moroni, B. Corbet, and E. Pelucchi,"MOVPE-Grown Metamorphic lasers at 1.3 μm: solving critical growth, material and design issues", 19th International Conference on Metalorganic Vapor Phase Epitaxy, June 3-8 2018, Nara Kasugano International Forum, Nara, Japan.

- E. E. Mura, A. Gocalinska, G. Juska, S. T. Moroni, R. Loi, B. Corbet, and E. Pelucchi, "Solving the elusive target of an MOVPE-Grown Metamorphic laser: managing strain and surface instabilities to enable reliable $>$1.3 μm emission", ICPS 2018, 34th International conference on the physics of semiconductors, July 29-3 August 2018 , Montpellier, France.

Contribution in conference talks

In addition, I have also contributed to, and have had aspects of my work presented in, the following conference talk, which was presented by my colleague and collaborator:

- E. Pelucchi (invited talk), G. Juska, V. Dimastrodonato, T. H. Chung, S. T. Moroni, A. Pescaglini, E. E. Mura and A. Gocalinska, "Site-controlled and self-assembled QDs: how to do it differently. . . (not to say better)", SemiconNano 2015 Lakeshore Hotel, Hsinchu, Taiwan, 2015

- A. Gocalinska (oral), E. E. Mura, G. Juska, S. Moroni, A. Pescaglini and E. Pelucchi, "InP(As) NanoRings and Telecom Band Quantum Dots on AlInAs: Strain- And Trick-Free Driven Epitaxy by MOVPE", Compound Semiconductor Week 2015, June 29-July 2nd 2015, Santa Barbara, California, USA.

- R. Loi (oral), J. O'Callaghan, B. Roycroft, A. Gocalinska, E. E. Mura, E. Pelucchi, A. J. Trindade, A. Fecioru, C. A. Bower, B. Corbett, "Heterogeneous integration of telecom lasers to Si substrates by micro transfer printing" Smart Systems Integration, International Conference and Exhibition on Integration Issues of Miniaturized Systems, Cork, Ireland, 8-9 March 2017.

- A. Gocalinska (oral), E. E. Mura, G. Juska, S. T. Moroni, A. Pescaglini, and E. Pelucchi, "Strain-free InP(As) quantum dots (QDs) - a versatile platform for optoelectronic applications", Photonics Ireland 2017, Radisson Blu Hotel, Galway, September 13-15th 2017, Ireland.

- R. Loi (oral), J. O'Callaghan, B. Roycroff, K. Thomas, E. E. Mura, A. Gocalinska, E. Pelucchi, A . Fecioru, A. J. Trindade , C. A. Bower and B. Corbett, "Transfer printable InP lasers for Si photonics", Photonics Ireland Conference 2018 Pairc ui Chaoimh, Cork, Ireland, 3-5 September 2018.
- A. Curran (oral), E. Secco, A. Pescaglini, A. Gocalinska, E. E. Mura, K. Thomas, I. M. Povey, E. Pelucchi, C. O'Dwyer, P. K. Hurley, and F. Gity, "Investigating Polycrystalline III-V Thin Films As Channel Materials for "Above IC" Logic and Memory Applications", AIMES 2018 meeting, ECS SMEQ meeting, Moon Palace Resort, Cancun, 30- September-4th October 2018.

Chapter 1

Introduction

In this initial chapter the credibility and the novelty level of this research work is described, painting in broad terms the scientific scenario where it is collocated. In the first part of the chapter are provided some considerations about economical trends of the global photonics market. Then, the attention is shifted towards the optical fibre as a transmission medium to provide the preferred large band communication channels not only for new and also "conventional" telecom applications (e.g. fibre to the home), but also in fields such as inter and infra data centres. A third section is devoted to the semiconductor materials suitable for telecom application in the 1.3 μm operation range, and a comparison between InP and GaAs based laser devices is provided. In conclusion the GaAs based (metamorphic) technological platform for the 1.3 μm telecom window is proposed as a valid alternative to the current InP based devices for accessing silicon photonics applications. Following this we provide an overview of the structure of this thesis.

1.1 Context and motivation

The photonics market has evolved in the last decades into a major new technology. According to recent trends and forecast data, the photonics market was valued at USD 636.63 billion in 2018 and is expected to reach a value of USD 1,001.3 billion by 2024, at a Compound Annual Growth Rate (CAGR) of 7.89% over the forecast period 2019 - 2024 (Figure 1.1).

This is a direct consequence of the demand for greater internet connectivity. For example CISCO [2] in the 2017–2022 white paper, is reporting that the demand for greater internet connectivity is growing at an average rate of 24 percent per year (Figure 1.2). All of this internet traffic flows through large data centres. A typical data centre consists of several hundred thousand servers interconnected by optical cables covering distances of several kilometres inside a building. The speed of connectivity within data centres is gradually

Figure 1.1: Photonics market, Source Mordor Intelligence [1]

increasing, as reflected by the connectivity standard evolution and particularly the ethernet standard.

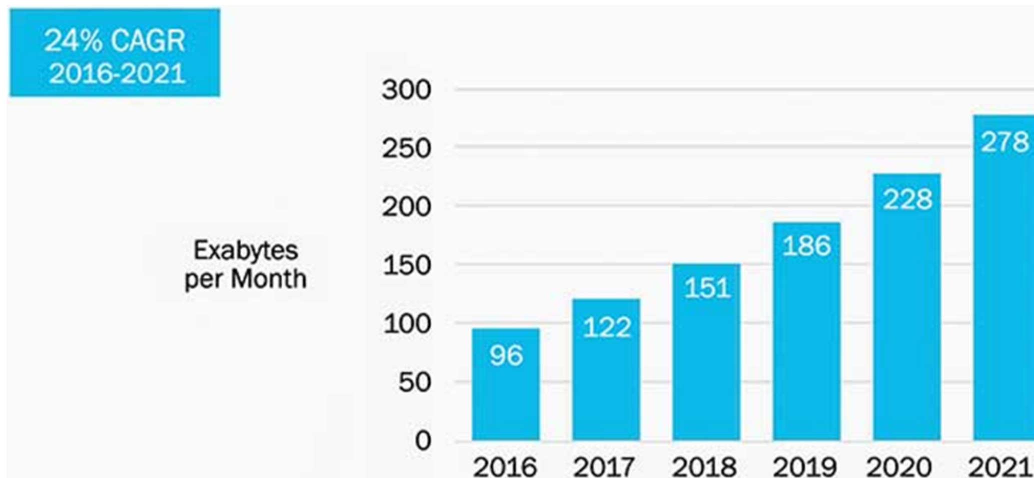

Figure 1.2: The demand for greater internet connectivity is increasing at an average rate of 24 percent per year. Source [2]

This connectivity was 40 Gbps in 2010 and 100 Gbps in 2015, and it is expected to reach 400 Gbps by 2022 [3]. The employment and the continuous development of optical communications, using optical fiber as a transmission medium, represent the key to achieving these levels of data rate transfer, and the main way of carrying information over long distances (> 100m). Optical fibers are replacing copper wires, offering three very big advantages:

- Less attenuation: (signal loss);
- No electromagnetic interference;
- Higher bandwidth.

On the other hand, fiber optics requires more and more optical components, such as lasers, modulators and multiplexers, to run in parallel, with several hybrid integration challenges to be surmounted, processing costs being a major one. An ever present issue is ensuring that a powerful technology is delivered in a cost effective manner while also being suitable for large scale production.

The optical signal attenuates during transmission over optical fiber as a function of the wavelength of the light beam, Figure 1.3.

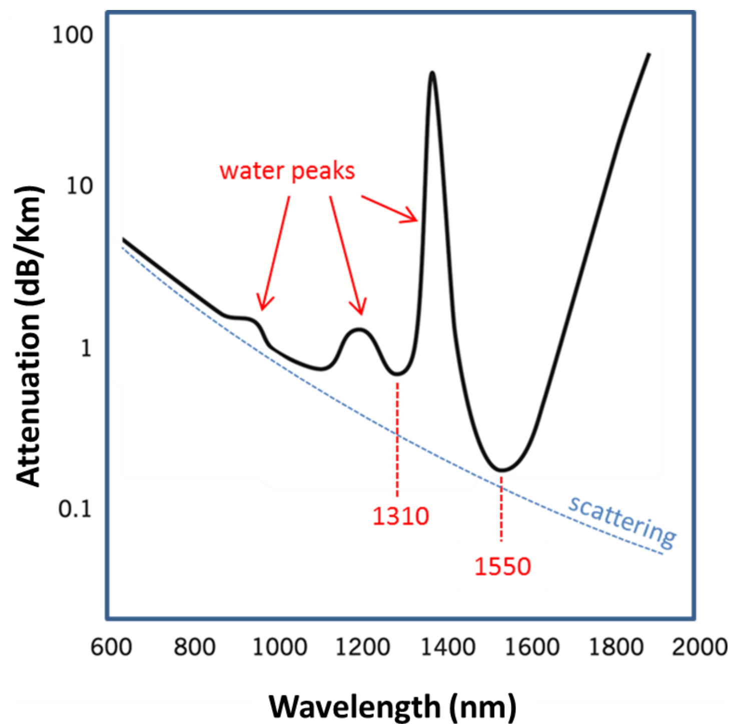

Figure 1.3: Representative attenuation and scattering vs wavelength graph

Partially for historic reasons, the transmission spectrum can be subdivided in three main bands or "windows": Short (window range 800-900 nm and operating wavelength 850 nm), Medium (window range 1260-1360 nm and operating wavelength 1310 nm) and Long Wavelength Band (window range 1500-1600 nm and operating wavelength 1550 nm). The first window was the first band used for optical fibre communication in the 1970s and early 1980s representing low cost optical sources and detectors in this band. However, the fibre losses are relatively high in this region, and fibre amplifiers are not well developed

for this spectral region. Therefore, the first telecom window is suitable only for short-distance transmission. The maxima of optical transparency of silica fibres occurs at 1310 nm and 1550 nm; in particular, the optical data transmission exploits minimal dispersion at 1310 nm and minimal attenuation at 1550 nm. The Medium Wavelength Band came into use in the mid 1980s. This band is attractive today because there is ∼zero fibre dispersion here (on single-mode fibre). While sources and detectors for this band are more costly than for the short wave band the fibre attenuation is only about 0.4 dB/km. The Long Wavelength Band (Third Window) has the lowest attenuation available on current optical fibre (about 0.26 dB/km).

Since operating at 1550 nm provides the best performance, it seems logical to choose 1550 nm for every link. However, a major part of the link cost is the laser. Lasers operating at 1550 nm are more difficult to manufacture than those at 1310 nm and consequently are more expensive. Therefore shorter links (up to 10km) would typically use a 1310 nm laser because it provides good performance at a lower cost. Also, as reported recently by FINISAR [4], one of the global leaders in optical communication, 1310 nm is preferable for higher operational temperatures, enabling uncooled operation at lower power and reducing cost. At 1550 nm the Auger recombination reduces the operational temperature.

In this context, an alternative for the expensive and relatively cumbersome InP based technology currently dominating the market, would represent a fundamental enabling breakthrough. The thesis work aims to develop (for the first time) an original, cheaper, and processing-friendly GaAs based metamorphic technological platform for the 1.3 μm telecom window - providing a valid alternative to the currently InP based devices for accessing silicon photonics applications and generally demonstrating its suitability for large scale technologies. This could fully replace the InP based platforms currently in existence and revolutionise the current compound semiconductor industry, significantly reducing costs and technological burdens, should it win the competition with other alternative efforts along similar lines.

1.2 Semiconductor materials suitable for 1.3 μm applications

Light sources are typically manufactured with direct-gap, III-V semiconductor materials (silicon and germanium are indirect bandgap semiconductor

and inefficient light emitter/absorber).

Figure 1.4 shows lattice parameter and bandgap energies of III-V binaries suitable for creating the active region of a 1.3 μm diode laser.

The GaAs and InP based materials and their compounds (InAs, InGaAs, InGaAsP, GaInNAs, etc.) are the most common materials used, covering the telecom wavelength range.

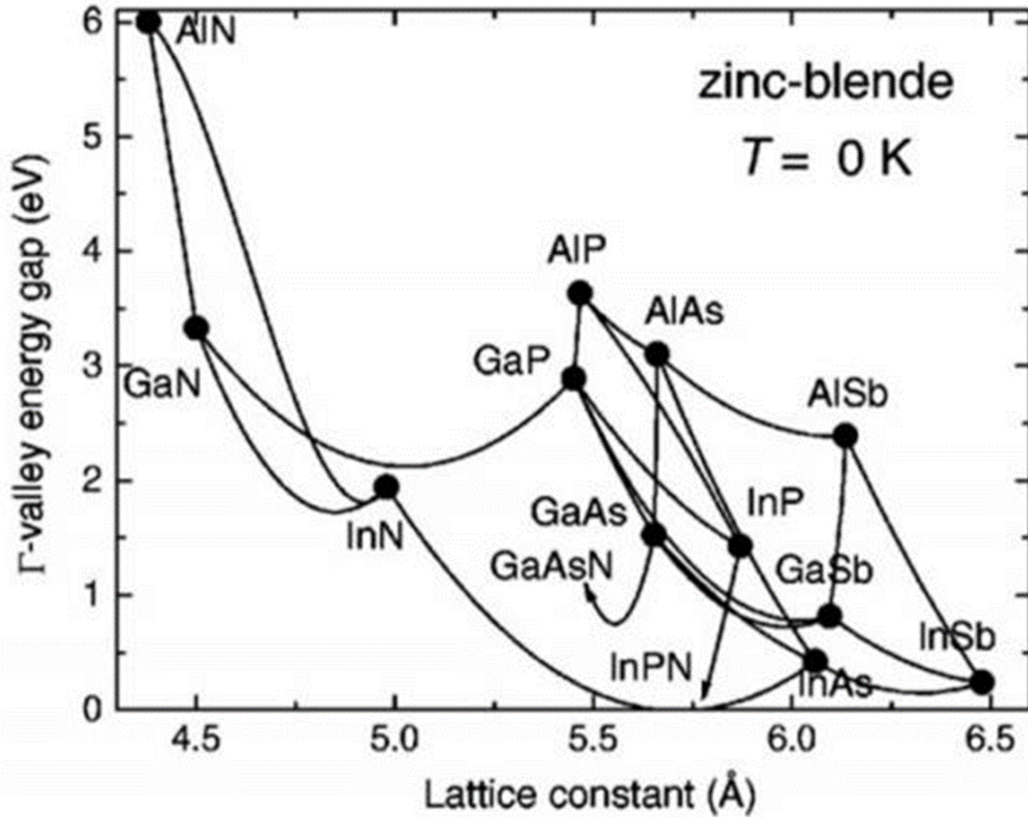

Figure 1.4: Energy gap versus lattice distance and corresponding emission wavelengths of the alloy.

Currently InGaAsP quaternaries grown on InP substrate is a relevant material system and historically the first used for fabricating 1.3 μm emitting devices for telecom applications. However, InP based devices present disadvantages due to the small bandgap offset, only 0.39 eV, between the 1.3 μm InGaAsP quantum well and InP barrier layers, which together with the small difference in refractive indexes of InGaAsP materials, make it difficult to find a reasonable compromise between the high optical confinement factor, Γ, which is usually defined as the fraction of the squared electric field confined to the active region [5–7], and the low thermal population of the waveguide region, i.e with the small conduction band offset several characteristics of devices are

degraded at high temperatures because of electron over- flow. This translates in poor characteristic temperature (T_0) of 1.3 μm InGaAsP lasers, with T_0 of about 60 K [8]. The exchange of InGaAsP with AlInGaAs in the quantum wells (QWs) region and InAlAs in the cladding barriers allows an increase in the bandgap offset and improves in the T_0, raising it to 90–110 K [9, 10]. However, even with this improved T_0 InP based diode lasers require thermoelectric cooling and uncooled operation has yet to be realised in practical applications and there remains a drive to improve the high-temperature and high-speed performance of 1.3 μm QW lasers.

From commercial and impacting scaling perspectives, InP based devices present at least others two main weak points:

1. The InP substrates come in limited size choice, currently up to 3 inch wafers for reliable operations and yield. Other electronic and photonics platforms based on Silicon or GaAs allow for 6 inch or more processing, with significantly reduced fabrication costs.

2. InP wafers present an intrinsic defectivity significantly larger than other technological platforms (i.e. lower yields).

One possible approach to overcome the limits imposed by the small band offset of the InP based devices is the use of ternary InGaAs substrates. It is theoretically predicated [11] that the use of a substrate with a lattice constant corresponding to $In_{0.3}Ga_{0.7}As$ would give maximum conduction band offset and thus a high T_0 value. Although an excellent 1.3 μm laser based on a InGaAs substrate has been demonstrated [12], one drawback for the ternary substrate remain that the heat dissipation can significantly influence the laser performance as the thermal conductivity becomes worse with an increase of the In content.

The others obvious candidates to overcome the InP disavantages and develop emitter emitting at 1.3 μm are GaAs based devices. First of all, GaAs substrates come in large diameters, their processing is cheaper and easier in many respects and their defect density is lower than InP. Furthermore, the GaAs based lasers can use for example lattice matched AlGaAs layers for better carrier (higher bandgap offset) and optical (higher refractive index mismatch) confinements, and compressively strained InGaAs QWs for the high gain possible, which lead to better performing devices at high temperatures.

Suitable materials that offer the possibility of long wavelength emission on GaAs substrates are, for example: In(Ga)As, GaAsSb and InGaAsN(Sb) (please refer to figure 1.4). Excellent results have been reached with both

InGaAsN(Sb) dilute nitride alloy QWs and In(Ga)As quantum dots (QDs) used as active materials on GaAs and 1.3 μm lasers have been demonstrated [13–17]. However lasers based on InGaAsN(Sb) QWs suffer from strong defect-related recombination [18], making the reliability and the repeatability the major issues for commercial applications. On the other hand, QD lasers have found a small niche market for short reach communications, emitting at slightly below 1.3 μm, despite large scale reproducibility issues and significant device sizes. The main issue is realizing QDs of both high density and good size- and shape-uniformity to reach an high gain and prevent inhomogeneous broadening of the gain profile [19].

Compared to the QD approach, InGaAs QW lasers in the wavelength range of 900–1200 nm have been industrial products for a long time, showing excellent laser performance and stability. However, the longest lasing wavelength is beyond ~ 1.26 μm [20], because the growth of highly strained InGaAs QWs on GaAs is limited by the accumulation of strain energy in the growing film resulting in dislocation and spontaneous three-dimensional island formation, due to the critical thickness and the increase of the indium content in the highly strained QWs.

This is where the work in this thesis comes in.

In this scenario of 1.3 μm InP and GaAs based laser devices, a different approach has been of increasing interest: the metamorphic growth technique. Metamorphic growth involves forming a buffer layer with a different lattice constant from that of the substrate by employing strain relaxation. In this way it is possible to grow a lattice mismatched metamorphic virtual substrate on traditional substrate. For example, by growing a relaxed $In_xGa_{1-x}As$ metamorphic buffer layer (MBL) on a GaAs substrate, heterostructures can then be grown with a lattice constant intermediate between that of GaAs and InP, maximising the advantage of GaAs substrate; in particular opening up the possibility to take advantage of the enhanced electronic and optical confinement offered, fo example, by (Al)GaAs-based heterostructures, reducing carrier spillover at high temperatures and tailoring the lattice constant to reach the desired telecom wavelength of interest.

1.3 Metamorphic telecom laser: state of art

The first metamorphic InGaAs/GaAs telecom laser on GaAs using a thin buffer was reported by Uchida *et al.* in 1994 [21]. Using metal-organic vapour phase epitaxy (MOVPE), they fabricated a strained $In_{0.40}Ga_{0.60}As$ quantum

well with an InGaP cladding layer on a GaAs substrate, incorporating a linear graded $In_xGa_{1-x}As$ MBL (up to x = 30%) 2.4 μm thick. With a stripe laser operating in pulse mode they reached 1.27 μm at room temperature with a density threshold current (J_{th}) of 500 A/cm^2 and a hight characteristic temperature (T_0) of 100 K. In 2003, the Ioffe's group fabricated a metamorphic laser structure, molecular beam epitaxy (MBE)-grown, using a 1 μm thick n+ $In_{0.40}Ga_{0.60}As$ uniform buffer. They reported a threshold current density and lasing wavelength of 5.2 kA/cm^2 and 1286 nm, respectively [22]. Later, Tångring *et al.* reported 1.27 μm metamorphic $In_{0.40}Ga_{0.60}As$ QW lasers on GaAs using a 0.8 μm Be-doped InGaAs buffer grown by MBE, obtaining not a very promising J_{th} of 1 kA/cm^2 with a ridge waveguide laser operating in pulsed mode [23]. Still using MBE, Wu *et al.* demonstrated a 1.34 μm metamorphic InGaAs quantum well (QW) lasers at 300 K under continuous wave (CW) operation. Employing a rapid thermal annealing of the sample reduced the threshold current density up to 205 A/cm^2 under CW operation [24]. The first remarkable achievement with MOVPE systems, comes with an NTT group in Japan. They demonstrated a 1.26 μm InGaAs QW laser on GaAs, using an abrupt 1600 nm thick n+ $In_{0.12}Ga_{0.88}As$ buffer layer to obtain a fully relaxed 100 nm thick $In_{0.1}Ga_{0.9}As$, reaching high characteristic temperature (T_0 = 220 K) and impressive high operating temperature (200 °C) [25]. Recently (year 2015), they went very close to 1.3 μm emission wavelength: photoluminescence measurement showed that the active layer emitted at 1.27 μm, whereas the lasing spectra range was between 1280-1310 nm at various injection currents from the fabricated multi-QWs laser diode [26]. They used the same metamorphic approach, but reducing the thickness of the $In_{0.12}Ga_{0.88}As$ buffer layer down to 240 nm followed by a 100 nm thick $In_{0.1}Ga_{0.9}As$ quasi-substrate. The results achieved by NTT highlighted two main important peculiarities of the metamorphic technique for telecom lasers: one more general, shared by every epitaxial growth technique, is that to obtain competitive laser performance and reach the 1.31 μm telecom wavelength, the key when growing metamorphic structures is not only to minimize the number of threading dislocations that penetrate through the active layer, but also to reduce the surface roughness caused by non-uniform growth on a strained surface. Second, more specific for the MOVPE technique, that the industry friendly MOVPE technology can actually achieve, based on a simple QW design on GaAs, low defect levels, providing emission close to the 1.3 μm window. Nevertheless the NTT approach is limited to a specific growth recipe, confining the in-plane lattice parameter of the virtual substrate to an equivalent 10% InGaAs substrate. This does

not allow for significant emission wavelength tunability that basically limits room temperature operation to just below 1.3 μm. To cover the full >1.3 μm telecom window and future broadband needs, and possibly extend to 1.55 μm, a different approach is required.

1.4 Structure of the thesis

This research work finds its main motivation in the development of a MOVPE grown >1.3μm-band laser on an engineered metamorphic graded InGaAs buffer. The intent is to show and explain in terms of morphology and surface organization each epitaxial step that is comprised in our "recipe" thanks to which a metamorphic laser emitting at wavelength >1.3 μm and possibly extendable to 1.55 μm has been demonstrated. The structure of this work is summarized in six additional chapters.

Chapter 2 is dedicated to the MOVPE growth mechanism and to the epitaxial characterization techniques used. A section is focused on the customized high purity level MOVPE system present in our facility.

The consecutive four chapters are organized following the order layer deposition of the epitaxial laser structure: buffer, claddings, barriers and active part, and full laser.

In particular, in **chapter 3** is provided an overview on the strained epitaxy, comparing pseudomorphic and metamorphic growths. The critical thickness concept is then introduced and how the limits imposed in pseudomorphic growth leads to the metamorphic approach. The chapter continues with the description of the general design beyond the $In_xGa_{1-x}As$ metamorphic substrate, focusing on the particular parabolic profile used to grow the substrate for the 1.3 μm laser structure, object of this thesis work. A morphological characterization of the surface is provided.

In **chapter 4** is presented a detailed description of the material choice as a cladding layer. The two different alloys selected, InGaP and AlInGaAs, are studied in terms of surface morphology and roughness control by Atomic Force Microscopy (AFM). The chapter ends presenting the characterization of a combination of the two alloys, which will be used in the final laser structure, as this particular "superlattice" cladding structure overcomes the roughness problems encountered during the deposition of a single alloy, be it InGaP or AlInGaAs.

In **chapter 5** the dissertation covers the growth related issue encountered during the deposition of the active part of the separate confinement

heterostructure (SCH) structure. The strain control and compensation using the appropriate growth parameters during the strained QWs deposition is debated. In particular, a section is dedicated to the role of the temperature and how this influences the 3D nanostructures formation during the QWs growth.

In **chapter 6** are presented the electro-optical characterization of three stripes waveguide laser resulting from all previous work.

The **7th last chapter** reviews a side work carried out during the doctoral period, concerning the unusual self-assembled InP(As) nanostructures, presented here as an alternative active material to the InGaAs multi quantum wells (MQWs) for telecom wavelengths.

Bibliography

[1] *Photonics-market*. URL: https://www.mordorintelligence.com/industry-reports/photonics-market-market.

[2] *CISCO 2017–2022 White Paper*. URL: https://www.cisco.com/c/en/us/solutions/collateral/service-provider/visual-networking-index-vni/white-paper-c11-738429.html.

[3] *Ethernet connectivity*. URL: https://www.photonics.com/Articles/Silicon-on-Insulator_Substrates_The_Basis_of/a63021.

[4] *FINISAR ECOC2017*. URL: https://www.finisar.com/sites/default/files/resources/1310nm_vs_1550nm_ecoc2017.pdf.

[5] W Anderson. "Mode confinement and gain in junction lasers". In: *IEEE Journal of Quantum Electronics* 1.6 (1965), pp. 228–236.

[6] Basil W Hakki and Thomas L Paoli. "Gain spectra in GaAs double- heterostructure injection lasers". In: *Journal of Applied Physics* 46.3 (1975), pp. 1299–1306.

[7] Dan Botez. "Analytical approximation of the radiation confinement factor for the TE 0 mode of a double heterojunction laser". In: *IEEE Journal of Quantum Electronics* 14.4 (1978), pp. 230–232.

[8] H Temkin et al. "High temperature characteristics of InGaAsP/InP laser structures". In: *Applied physics letters* 62.19 (1993), pp. 2402–2404.

[9] T Ishikawa et al. "Well-thickness dependence of high-temperature characteristics in 1.3-μm AlGaInAs-InP strained-multiple-quantum-well lasers". In: *IEEE Photonics Technology Letters* 10.12 (1998), pp. 1703–1705.

[10] K Takemasa et al. "High-temperature operation of 1.3 μm AlGaInAs strained multiple quantum well lasers". In: *Electronics Letters* 34.12 (1998), pp. 1231–1233.

[11] Hiroshi Ishikawa. "Theoretical gain of strained quantum well grown on an InGaAs ternary substrate". In: *Applied physics letters* 63.6 (1993), pp. 712–714.

[12] K Otsubo et al. “High T/sub 0/(140 K) and low-threshold long-wavelength strained quantum well lasers on InGaAs ternary substrates”. In: *Electronics Letters* 33.21 (1997), pp. 1795–1797.

[13] VM Ustinov and AE Zhukov. “GaAs-based long-wavelength lasers”. In: *Semiconductor science and technology* 15.8 (2000), R41.

[14] Nelson Tansu, Nicholas J Kirsch, and Luke J Mawst. “Low-threshold-current-density 1300-nm dilute-nitride quantum well lasers”. In: *Applied Physics Letters* 81.14 (2002), pp. 2523–2525.

[15] XD Wang et al. “High-quality 1.3/spl mu/m GaInNAs single quantum well lasers grown by MBE”. In: *Electronics Letters* 40.21 (2004), pp. 1338–1339.

[16] Kohki Mukai et al. “High characteristic temperature of near-1.3-μm InGaAs/GaAs quantum-dot lasers at room temperature”. In: *Applied Physics Letters* 76.23 (2000), pp. 3349–3351.

[17] OB Shchekin, J Ahn, and DG Deppe. “High temperature performance of self-organised quantum dot laser with stacked p-doped active region”. In: *Electronics Letters* 38.14 (2002), pp. 712–713.

[18] Robin Fehse et al. “A quantitative study of radiative, Auger, and defect related recombination processes in 1.3-/spl mu/m GaInNAs-based quantum-well lasers”. In: *IEEE Journal of selected topics in quantum electronics* 8.4 (2002), pp. 801–810.

[19] Kerry J Vahala. “Quantum box fabrication tolerance and size limits in semiconductors and their effect on optical gain”. In: *IEEE journal of quantum electronics* 24.3 (1988), pp. 523–530.

[20] LW Sung and HH Lin. “Highly strained 1.24-μm InGaAs/GaAs quantum-well lasers”. In: *Applied Physics Letters* 83.6 (2003), pp. 1107–1109.

[21] T Uchida et al. “1.3 mu m InGaAs/GaAs strained quantum well lasers with InGaP cladding layer”. In: *Electronics Letters* 30.7 (1994), pp. 563–565.

[22] AE Zhukov et al. “Metamorphic lasers for 1.3-μm spectral range grown on GaAs substrates by MBE”. In: *Semiconductors* 37.9 (2003), pp. 1119–1122.

[23] Ivar Tångring et al. “1.27 μm metamorphic InGaAs quantum well lasers on GaAs substrates”. In: *Electronics Letters* 42.12 (2006), pp. 691–693.

[24] Donghai Wu et al. "Low threshold current density 1.3 μm metamorphic InGaAs/GaAs quantum well laser diodes". In: *Electronics Letters* 44.7 (2008), pp. 474–475.

[25] Masakazu Arai, Wataru Kobayashi, and Masaki Kohtoku. "1.3-μm range metamorphic InGaAs laser with high characteristic temperature for low power consumption operation". In: *IEEE Journal of Selected Topics in Quantum Electronics* 19.4 (2013), pp. 1502207–1502207.

[26] Ryo Nakao et al. "1.3-μm InGaAs MQW Metamorphic Laser Diode Fabricated With Lattice Relaxation Control Based onIn SituCurvature Measurement". In: *IEEE Journal of Selected Topics in Quantum Electronics* 21.6 (2015), pp. 201–207.

Chapter 2

Material growth and characterization

2.1 MOVPE overview

Metal-organic vapor phase epitaxy (MOVPE), known also as metalorganic chemical vapor deposition (MOCVD) and by other permutations (OMVPE and OMCVD), is a chemical vapor deposition method for epitaxial growth of materials, especially III-V compound semiconductors. First pioneering work on the growth of III–V compounds from organometallic and hydride sources was reported in 1960 by Didchenko et al [1]. In their experiment, the trimethylindium (TMIn) was made to react with phosphine (PH_3) and InP was obtained in a closed-tube system: "*The compound decomposes sometimes explosively into indium phosphide and methane when heated to 270-300°C in inert atmospheres or in vacuo*". But it was only ten years later that Manasevit established the possibility of depositing many common compound semiconductors from organometallic materials and he coined the term MOCVD. First GaAs [2], GaAsP and GaAsSb [3], then AlGaAs [4], GaN, AlN [5] and In based compounds [6]. In 1975, a paper by Seki et al. [7] marked a turning point for MOVPE: growth of high purity GaAs layers, of a thickness $\geq 10\ \mu m$, with an electron mobility as high as $1.2 \times 10^5 cm^2/Vs$ and a carrier concentration of $7 \times 10^{13} cm^{-3}$ at low temperature was demonstrated. This led the scientific community to adopt several approaches for obtaining a reproducible growth mechanism for devices, until in 1978 growth of the first QW injection laser was demonstrated [8].

Compared to other conventional compound semiconductor epitaxy techniques, such as liquid phase epitaxy (LPE) and hydride vapor phase epitaxy (HVPE), MOVPE has advantages in the growth of complex optoelectronic structures (like vertical-cavity surface-emitting lasers (VCSELs)). Very high degree of control over thickness, composition and doping can be achieved

by MOVPE, the epitaxy of elemental materials can be layer-by-layer controlled and extremely sharp interfaces can be built up. Despite the sudden and enormous employment in semiconductor optoelectronics fabrication, the material quality issue still remains an open and disputed matter and represents one of the main differences between MOVPE and MBE. The interested reader can find a more detailed discussion about epitaxial techniques (summarized in table 2.1) in Stringfellow's book [9].

Table 2.1: Overview of epitaxy techniques

Techniques	Strengths	Weaknesses
LPE	Simple	scale economics
	High purity	inflexible
		nonuniformity
HVPE	Well developed	No Al alloys
	Large scale	Sb alloys difficult
		complex process/reactor
		Hazardous sources
MBE	simple process	As/P alloy difficult
	uniform	"oval" defects
	Abrupt interfaces	Expensive(capital)
	In situ monitoring	low throughput
MOVPE	Most flexible	expensive reactants
	Abrupt interfaces	most parameter
	Simple reactor	to control accurately
	High purity	hazardous precursors

In contrast to MBE the growth of crystals in MOVPE is by chemical reaction and not physical deposition. The simplest case involves a pyrolysis reaction of the vapours of a volatile metalorganic compound and a gaseous hydride which follows:

$$R_nA + DH_n \longrightarrow AD + nRH \tag{2.1}$$

R is an organic radical of some unspecified form but generally of lower order, such as methyl- or ethyl-radical, A and D are the constituent species for the deposited solid. This is a simplified form of the reaction and it ignores any intermediate steps that may occur.

The epitaxial growth of III-V semiconductor layers by MOVPE takes place by transporting different chemical sources by a purified carrier gas, either N_2 or H_2, to the heated reactor, under pressures varying between 20 and 1000 mbar. For the group III, the most used metalorganic (MO) sources are trimethylindium (TMIn), trimethylgallium (TMGa), and trimethylaluminum

(TMAl). Hydrides (Hyds), like arsine (AsH_3), phosphine (PH_3), can be employed as precursor for group V elements.

For example, gallium arsenide is formed by heating trimethylgallium ($Ga(CH_3)_3$) and arsine usually over a single crystal of GaAs or Si, at a temperature around 600°C, in this case the Eq. 2.1 can be write:

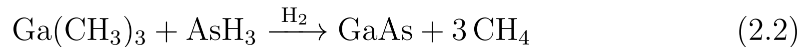

$$Ga(CH_3)_3 + AsH_3 \xrightarrow{H_2} GaAs + 3\,CH_4 \tag{2.2}$$

The reaction is actually much more complicated and comprises many successive steps and species in the chemistry of deposition [10] like, e.g., some steps of precursor decomposition.

2.2 Our growth facility

In this research activity all sample growths were carried out in a commercial horizontal MOVPE reactor at low pressure (80 millibars) with purified nitrogen (N_2) as the carrier gas. The choice of growth conditions, growth rate, V/III ratio and growth temperature, will be debated in a dedicated section, when relevant for the purpose of discussing the experimental results. The main parts and sequence of events occurring during an MOVPE process are represented in Figure 2.1. The carrier gas, after being purified (Purification A, see dedicated section) is bubbled through MOs and co-flows with the purified (Purification B, dedicated section) Hydrides (Hyds) toward the reactor. In no-run conditions, all flows are directed toward a vent system and sent either to the main (dry) pump or the by-pass line, without reaching the reactor. Both source gas and carrier gas flows are controlled by electronic mass flow controllers (MFCs) and pressure controllers (PCs), to assure that precise amounts of sources are delivered through the run lines to the reactor without significant fluctuation of their parameters. The precursor flows enter the reactor through an injector manifold flange in a horizontal reactor geometry and the sample is on a graphite satellite. A high flow of N_2 is introduced also into the reactor, via reactor purge and rotation lines, to assure a laminar flow necessary for a uniform and reproducible deposition of the epitaxial layers. The rotation speed of the satellite (∼70 revolution per minute (RPM)) establishes a uniform boundary layer over the substrate, through which the precursors diffuse. Once they reach the substrate surface, the thermal energy, provided by the heaters underneath the reactor, is enough to enable the chemical decomposition of the precursor molecules. A precise control of the temperature and its uniformity (depending on the rotation mechanism of satellite and the reactor geometry) is critical

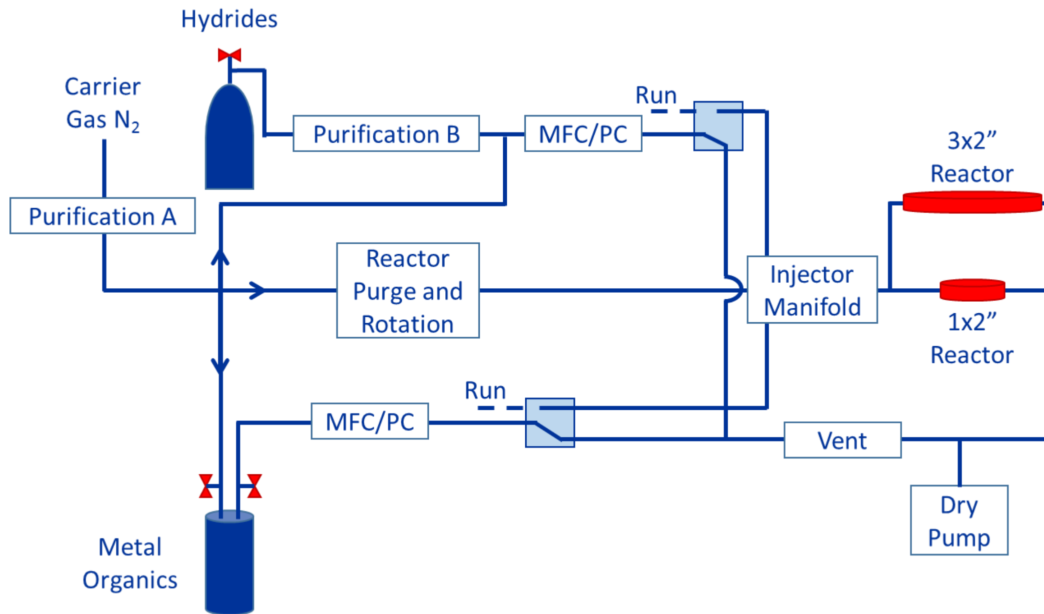

Figure 2.1: Schematic representation of the main components of an MOVPE system: source gases, both MOs and Hyds, with relative purification B panel, are transported by purified (Purification A) carrier gas (N_2) toward either the reactor (run line) or the vent system (selection occurs through pneumatic valves -cyan squares). The flows are controlled by MFCs and PCs. An injector manifold flange, comprising several pneumatic valves, injects the sources, purge and rotation fluxes into the reactor, whose working pressure is controlled by a (dry) pump.

for a controlled and reliable growth process. It should be added that many details about the epitaxial formation of the layers grown on the substrate are still not fully understood, due to the complexity of the process and the lack of monitoring through in-situ techniques of both chemical reactions and surface morphology reconstruction.

2.2.1 High purity levels

Our group boasts a MOVPE system customized to reach high purity levels [11]. Four main aspects lead to the delivery of carrier and source gases with extremely low contamination levels into a clean reactor environment:

A. Carrier gas purification system: using in the purification system of the carrier gas heated SAES Getters purifiers, which employ the metallic-alloy (zirconium based) technology [12]. This technique allows removal of all the major impurities in the gas in a single step[13], via irreversible chemical reactions, keeping the impurities level in the sub-ppb range [14]. In particular the getter removes gas contaminants such as O_2, H_2O, CO,

CO_2, H_2 and CH_4. The reactive getter surface decomposes the gaseous impurities and forms at room temperature stable chemical compounds, oxides and carbides, which passivate the surface. While the constant high T allows for the migration of the reacted compounds towards the bulk of the purifier, keeping a continuously clean reactive surface.

B. Hyds purification and line purging set-up: a main disadvantage of the group V hydrides is related to H_2O and O_2 contamination, especially during cylinder changes and its depletion. We notice that the most common and reliable practice for a thorough purging procedure consists in venting down the pressure (through a standard Venturi system) and perform then a combination of flow purging and pressure-vacuum cycles under N_2. For each Hyd source, two different purifiers are connected in series via a valve-line set-up which allows the use of either both of them or only a single one. The double purification system in a series configuration is sketch in Figure 2.2. Purging can be carried out periodically in our

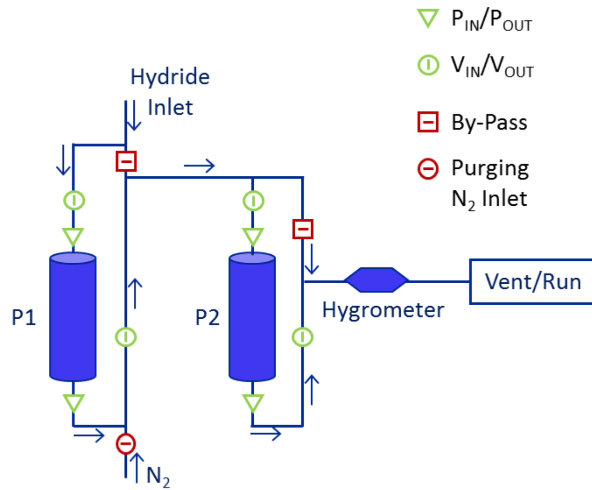

Figure 2.2: Sketch of a single Hyd panel designed to allow a double purification system and N2 purging of the lines. The valve configuration tracks the Hyd source direction through the two purifiers: the inlet P_{IN}, outlet P_{OUT} (green triangles) purifier valves and V_{IN}, V_{OUT} (green circles) valves are open such to allow for N_2 to flow first through P1 and then P2, the by-pass valves being closed (red squares). In order to switch to a purging configuration, P_{IN} and P_{OUT} need to be closed, while the N_2 inlet valve (red octagons) will be open, as well as each by-pass.

system to avoid long periods of static flow in the pipes. Moreover, since each Hyd panel is provided with its own N_2 inlet valve, it is possible to perform separate purging procedures and avoid cross-contamination.

C. General reactor handling: to reduce additional general contamination in the reactor (e.g, the substrate itself, especially after patterning process, might introduce organic contamination) at every growth is associated a deoxidation step at a (thermocouple) temperature as high as $\sim 700/800°C$, with high flow rate of AsH_3 in order to prevent surface depletion. In addition a periodic baking and coating of the inner walls of our reactor is performed. During the baking growth a very thick AlAs/GaAs multilayer structures is deposited in a dummy substrate, with high V/III ratios and at a temperature of 800°C. The Al is capable to incorporate C (and O_2) contaminations with a higher probability than Ga [15, 16], acting therefore as an in-situ getter for the following growth runs.

D. Dopant line isolation: to avoid any cross-contamination of dopant runvent lines from reactor 2 (R2, dedicated to the devices growth) to reactor 1 (R1, dedicate to hight purity process), the system is provided of a pneumatic valve, kept on a forced exclude R1 position, so as to divert any (memory bearing) dopant flow toward R2.

2.3 Characterization techniques

All samples grown in the MOVPE reactor were structurally characterized by Atomic Force Microscopy (AFM). High resolution X-ray diffraction (HRXRD) measurements were carried out for alloy concentration calibration and strain detection. Simple optical spectroscopy characterization was carried out to gather information about the energy states of the quaternary alloy and nanostructures (QWs and InP(As) three-dimensional (3D)-nanostructures, presented/studied in the last chapter). A brief introduction to these techniques now follows.

2.3.1 High resolution X-ray diffraction

High resolution X-ray diffraction techniques are indispensable for non-destructively characterize crystalline material in order to determine chemical composition, strain, defect densities and layer thickness with accuracies in the nanometer range. A typical high resolution X-ray diffractometer is illustrated in Fig. 2.3: the x-ray source produces a divergent beam with a broad spectrum which can be then conditioned by four-reflection (Bartels) monochromator (or other similar optics); the conditioned beam is then diffracted by the sample and measured by a detector. In the rocking curve mode, the specimen

is rotated about the ω axis perpendicular to the plane of the page and the diffracted intensity is measured as a function of the scanning angle ω. In general a full Bragg scan symmetrically varying incidence and detection angles is also necessary. Position, intensity and broadening of the intensity peaks in the diffraction profile are used to characterize the structural properties of the sample.

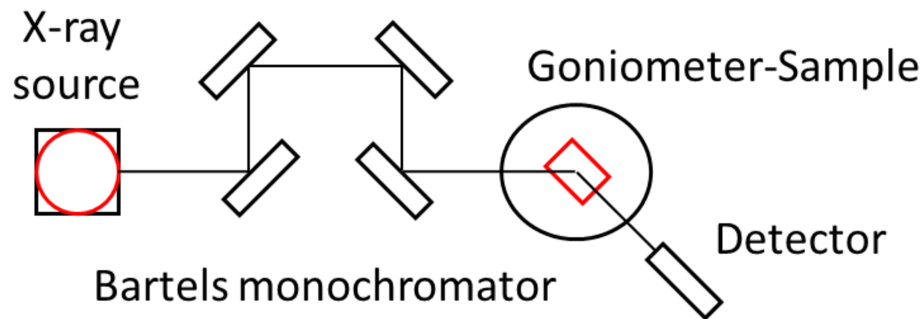

Figure 2.3: Sketch of X-ray diffraction principles. The X-ray beam is reflected by the Bartels monochromator and diffracted by the sample, mounted on the goniometer stage. The detector measured the diffracted intensity as a function of the scanning angle (rocking curve measurement).

2.3.2 Atomic Force Microscopy

Atomic force microscopy is a scanning probe technique giving information about the topography of the scanned samples by measuring the forces acting between them and a fine tip. This method was proposed to overcome the limitations of scanning tunnelling microscopy, which can be applied only to conducting samples [17]. In the AFM the tip is attached to the free end of a cantilever and is brought very close to a surface. Attractive or repulsive forces resulting from interactions between the tip and the surface can cause a positive or negative bending of the cantilever. The bending is detected by a position sensitive photodetector by means of a laser beam, which is reflected from the back side of the cantilever (Figure 2.4).

The AFM can operate in different modes; however we will focus on the $TappingMode^{TM}$ here, since, for our purposes, all measurements were performed in this dynamic fashion. During the tapping mode scan, the free air amplitude of the oscillations, obtained when the tip is far away from the sample, is damped as the tip approaches the surface, due to the interaction forces. Operation in air is done by maintaining this reduced amplitude constant, as

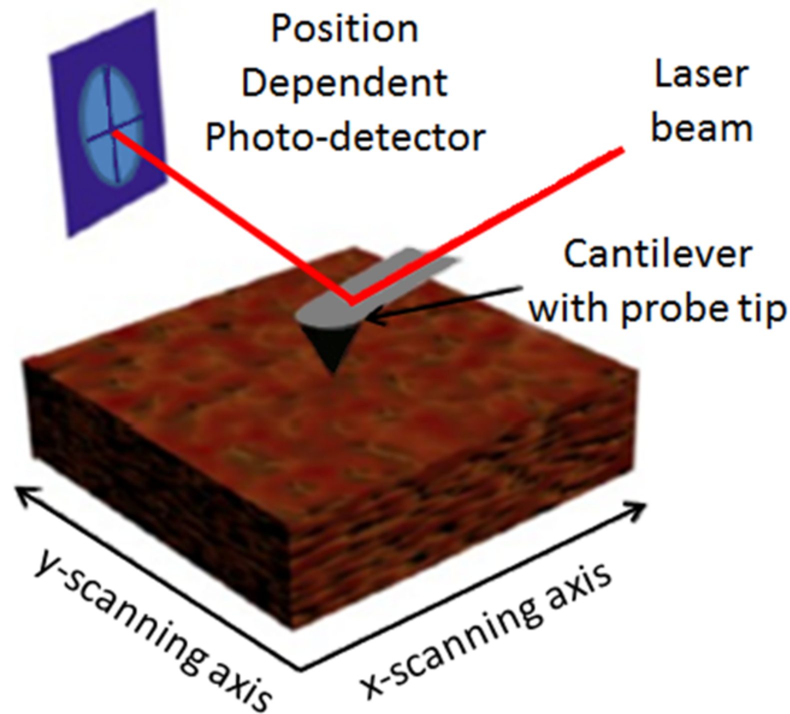

Figure 2.4: Schematic representation of the AFM working principles. The tip mounted at the free end of the cantilever scans the sample surface in Tapping Mode and its oscillations corresponding to the morphology of the sample are detected by the position dependent photo-detector through the laser beam.

the tip scans the surface, through a feedback loop that adjusts the tip-sample separation. Forces that act between the sample and the tip will cause not only a change in the oscillation amplitude, but also in the resonant frequency and phase of the cantilever. While, as above mentioned, the amplitude is used for the feedback, the vertical adjustments, achieved through piezoscanners, are recorded as a height image. Simultaneously the phase changes are presented in the phase image. All AFM scans reported in this thesis refer to the height signal, which, for our samples, delivers a better contrast. For our characterizations, we used a MultiMode AFM with a Veeco Nanoscope V control system. All scans were performed with a Si 3-sided tip (on an Al reflex coated cantilever) having a radius of 9 ± 2 nm, a nominal resonance frequency of ~ 70 KHz and a spring constant of 2 N/m. A noise as low as $\sim$0.3 Å Root Mean Square (RMS) was achieved in the vertical direction.

2.3.3 Micro photoluminescence set-up

The optical characterisation of the samples was performed in a standard micro photoluminescence set-up (μPL) (see Figure 2.5). The μPL consists of the following units: excitation source, beam splitter system and microscope, platform for fine movements, cryostat, detection and monitoring unit.

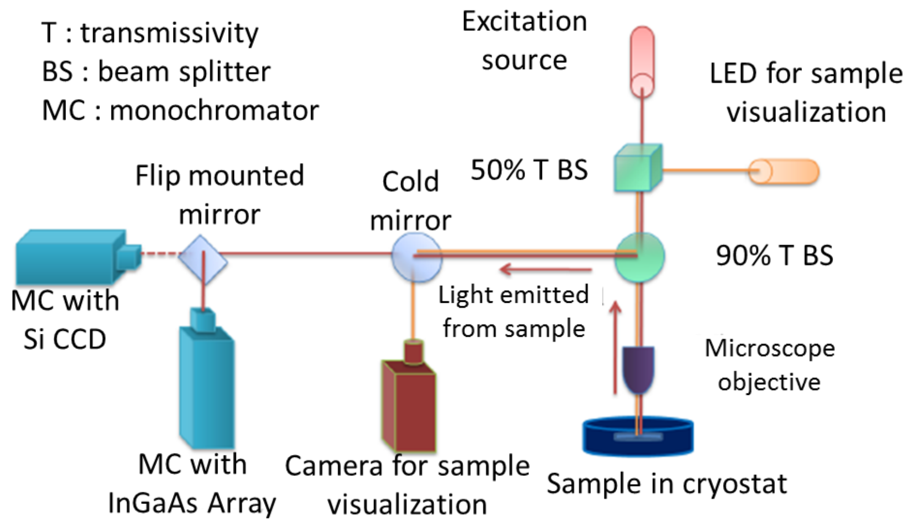

Figure 2.5: Simplified representation of the μPL set-up with its main units. The sample is kept in a cryostat at low temperature and can be excited with an optical source in different locations. Positioning of the excitation spot can be monitored via a camera. A microscope objective focuses and collects excitation and emitted photons respectively from the source and the sample. A beam splitter with 90% of transmissivity redirects the emitted beam toward the detection units, composed of two different monochromators.

Most of the time, a laser diode (PicoQuant LDH-D-C-635M) (λ=635nm) capable of operating in continuous-wave and pulsed modes (full width at half maximum of 100 ps) was used as excitation sources during this thesis work.

A series of two beam splitters, with a transmissivity of 50% and 90%, let through the source laser and light emitted from an LED used for sample visualization. The transmitted light is then collected in the microscope objective (Olympus, 100 $\times$, with numerical aperture (NA) = 0.8), used for both focussing the excitation light through an optical window in the cryostat onto the sample and for collecting the emitted luminescence. The objective used during the measurements gives a spatial resolution of $\sim 1\mu m$. The cryostat (ArsCryo Micro-Spectroscopy-closed cycle, low vibrations) can guarantee a temperature nominally as low as 7 K. The source light is then focussed onto different areas of the sample by moving a micrometer stage holding the entire beam splitter

and the microscope system. The emitted luminescence is directed through the 90% transmissivity beam splitter to the entrance slit of a spectrometer (Jobin Yvon, 1 m long, having a resolution of 18 μ eV at a wavelength equal to 870 nm with a 1800 lines grating), equipped with a liquid nitrogen Si-CCD camera. For detecting longer wavelengths a second monochromator is placed at an angle of 90° from the first one and it is combined with an InGaAs array detector, cooled with liquid nitrogen as well. Selection between the two different detection units is achieved through a flip mounted mirror positioned along the emitted light path. A cold mirror positioned before the detectors allows for the separation of visible and infrared wavelengths.

Bibliography

[1] R Didchenko, JE Alix, and RH Toeniskoetter. "Reactions of phosphine with trimethylindium". In: *Journal of Inorganic and Nuclear Chemistry* 14.1-2 (1960), pp. 35–37.

[2] Harold M Manasevit. "Single-crystal gallium arsenide on insulating substrates". In: *Applied Physics Letters* 12.4 (1968), pp. 156–159.

[3] HM Manasevit and W It Simpson. "The Use of Metal-Organics in the Preparation of Semiconductor Materials I. Epitaxial Gallium-V Compounds". In: *Journal of The Electrochemical Society* 116.12 (1969), pp. 1725–1732.

[4] HM Manasevit. "The Use of Metal-Organics in the Preparation of Semiconductor Materials III. Studies of Epitaxial III-V Aluminum Compound Formation Using Trimethylaluminum". In: *Journal of The Electrochemical Society* 118.4 (1971), pp. 647–650.

[5] HM Manasevit, FM Erdmann, and WI Simpson. "The use of metalorganics in the preparation of semiconductor materials IV. The nitrides of aluminum and gallium". In: *Journal of the Electrochemical Society* 118.11 (1971), pp. 1864–1868.

[6] HM Manasevit and WI Simpson. "The Use of Metalorganics in the Preparation of Semiconductor Materials V. The Formation of In-Group V Compounds and Alloys". In: *Journal of The Electrochemical Society* 120.1 (1973), pp. 135–137.

[7] Yasuo Seki et al. "Properties of epitaxial GaAs layers from a triethyl gallium and arsine system". In: *Journal of The Electrochemical Society* 122.8 (1975), pp. 1108–1112.

[8] RD Dupuis and PD Dapkus. "Continuous room-temperature operation of Ga (1- x) Al x As-GaAs double-heterostructure lasers grown by metalorganic chemical vapor deposition". In: *Applied Physics Letters* 32.7 (1978), pp. 406–407.

[9] Gerald B Stringfellow. *Organometallic vapor-phase epitaxy: theory and practice*. Elsevier, 1999.

[10] Triantafillos J Mountziaris and Klavs F Jensen. "Gas-Phase and Surface Reaction Mechanisms in MOCVD of GaAs with Trimethyl-Gallium and Arsine". In: *Journal of The Electrochemical Society* 138.8 (1991), pp. 2426–2439.

[11] Valeria Dimastrodonato et al. "Relevance of the purity level in a MetalOrganic Vapour Phase Epitaxy reactor environment for the growth of high quality pyramidal site-controlled Quantum Dots". In: *Journal of Crystal Growth* 315.1 (2011), pp. 119–122.

[12] *MonoTorr Heated Getter Purifiers*. URL: https://products4engineers.nl/images/default/FtSn5C-pdf.pdf.

[13] A Dobi et al. "Study of a zirconium getter for purification of xenon gas". In: *Nuclear Instruments and Methods in Physics Research Section A: Accelerators, Spectrometers, Detectors and Associated Equipment* 620.2-3 (2010), pp. 594–598.

[14] V Dimastrodonato et al. "AlGaAs/GaAs/AlGaAs quantum wells as a sensitive tool for the MOVPE reactor environment". In: *Journal of Crystal Growth* 312.21 (2010), pp. 3057–3062.

[15] Katsushi Fujii et al. "Dependence of carbon incorporation on growth conditions for unintentionally doped AlGaAs during metalorganic vaporphase epitaxy". In: *Journal of crystal growth* 204.1-2 (1999), pp. 10–18.

[16] Katsushi Fujii, Kazushige Kawamura, and Hideki Gotoh. "Impurity incorporation of unintentionally doped AlxGa1- xAs during MOVPE". In: *Journal of crystal growth* 221.1-4 (2000), pp. 41–46.

[17] CF Binnig. "Quate, and Ch. Gerber". In: *Phys. Rev. Lett* 56.9 (1986), pp. 930–933.

Chapter 3

The metamorphic buffer

This chapter present the process that brings to the parabolic graded MBL used in this thesis work to built the metamorphic laser diode at >1.3 μm wavelength telecom emission.

3.1 Strained heterostructures

In an unsophisticated manner the epitaxial growth can be subdivided in three classes: the homomorphic (or homoepitaxy), the pseudomorphic and the metamorphic growth. In the homomorphic epitaxy, the film and substrate are composed of the same material, they are perfectly lattice matched with zero misfit strain.

Pseudomorphic growth involves layers of different materials, but with fully coherent atomic bonds. The formation process of pseudomorphic growth can be sketched as in Figure 3.1. First consider two generic layers having the same cubic crystal structure, but different unstrained lattice constants a (Figure 3.1(a)).

If the layers are of similar thickness and the difference in the lattice constant is not to large (let us say below 1%), the layers may form an interface without structural defects and adopt a common in-plane lattice parameter $a_{\|}$ parallel to the interface, with an intermediate value $a_1 > a_{\|} > a_2$. The layer with the bigger lattice parameter is compressively strained in the lateral direction and experiences a vertical distortion. Therefore, the layer with the smaller lattice constant is tensile strained. Assuming that the epilayer is much thinner than the substrate (in the ideal case the substrate is considered semi-infinite, in the real case substrates are wafer typically 300 μm thick), the film can remain totally elastically strained (Figure 3.1(c) and (d)) and the substrate remains virtually unstrained because of his large thickness. The *misfit* (or

lattice mismatch) f is usually expressed by:

$$f = \frac{a_L - a_S}{a_S} \tag{3.1}$$

where a_L and a_S are the layer and substrate lattice parameters, respectively. The strain, ε, in a layer is the in-plane strain by which it is deformed from its natural lattice constant a_L. The strain will normally lie between 0 and f. Note that even in a pseudomorphic layer ε is not quite equal to f, for [1]

$$\varepsilon = \frac{a_L - a_S}{a_L} = \left(\frac{a_S}{a_L}\right) f \tag{3.2}$$

The misfit is linearly related to the elastic strain ε and the plastic strain ε_p. For compressive strain, it is

$$\varepsilon_p = f - \varepsilon \tag{3.3}$$

ε_p is an alternative way of quantifying plastic relaxation. The plastic relaxation corresponds to a reduction in ε by the introduction of suitable dislocations in the substrate-layer interface. Many authors use this concept in the form[1]

$$R = \frac{a - a_s}{a_L - a_s} \times 100\% \tag{3.4}$$

where a is the measured in-plane lattice parameter of the layer under strain.

In more general terms, the elastic strain is accommodated by tetragonal distortion of the crystal lattice and the plastic strain is associated with line-defects formation known as misfit dislocations (MDs) (shown in Figure 3.1(b)).

Back to the pseudomorphic case, in the tetragonal distortion the diagonals components of the strain of the strain tensor $\varepsilon_\perp$ and $\varepsilon_\parallel$ can be defined as:

$$\varepsilon_\parallel = \frac{a_\parallel - a_0}{a_0} \qquad \varepsilon_\perp = \frac{a_\perp - a_0}{a_0} \tag{3.5}$$

where $a_\parallel$ and $a_\perp$ are the parallel and perpendicular lattice parameters of the strained layer respectively, and a_0 is the unstrained lattice constant of the film. In a biaxial strain field with small distortions the two values are connected to each other and with the tetragonal distortion by the simple equations:

$$\varepsilon_\perp = -\frac{2C_{12}}{C_{11}}\varepsilon_\parallel = -\frac{2\nu}{1-\nu}\varepsilon_\parallel \tag{3.6}$$

where C_{12} and C_{11} are the elastic stiffness constants, and ν is Poisson's ratio (for cubic materials and stress along an axis of the unit cell, the ratio is

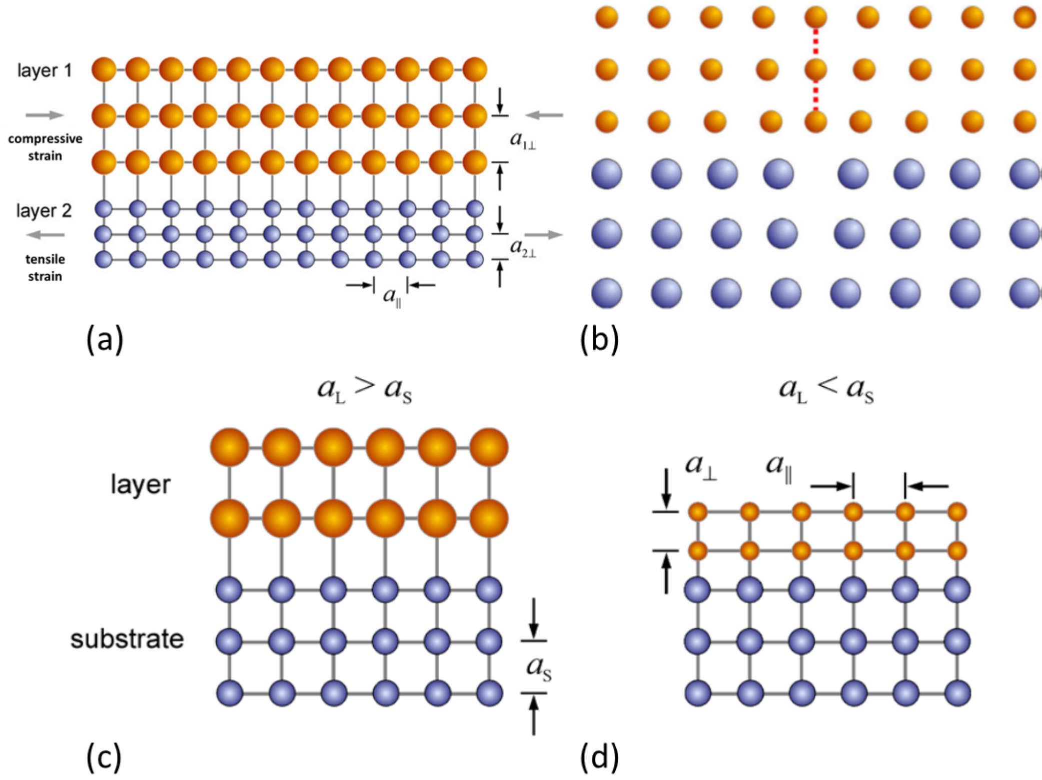

Figure 3.1: Pseudomorphic heterostructures sketches. (a) Schematic of a heterostructure consisting of two layers with a common interface. $a_{\parallel}$ is the common lateral lattice constant, $a_{1\perp}$ and $a_{2\perp}$ denote the vertical lattice constants of the strained layers 1 and 2. (b) Scheme of a misfit dislocation introduced into a layer, that plastically relaxes the strain. The inserted extra plane is shown in cross section and represented by the dashed red line. (c) and (d) Biaxially strained layers (yellow atoms) on substrates (blue atoms) with another lattice constant a_S. In (c) the unstrained lattice constant of the layer a_L is larger than a_S, and the layer is compressively strained in lateral direction; in (d) the layer is tensely strained. [2].

$\nu = C_{12}/(C_{11} + C_{12})$).

In strained epitaxy there is a critical thickness beyond which the formation of the misfit dislocation becomes energetically favourable. The concept of critical thickness (h_c) is schematically shown in Figure 3.2. The elastic strain is smaller than the energy of dislocation formations when epilayer thickness is less than h_c and it becomes larger when epilayer thickness is greater than h_c.

Historically, h_c was first defined by Frank, van der Merwe and co-authors (1949) [3–5]. In 1967, Jesser and Matthews gave the first analytic solution for this model, using a force balance approach [6], and later modified by Fitzgerald [7], were the h_c is approximately given by:

$$h_c \cong \frac{a_S}{2\,|f|} \tag{3.7}$$

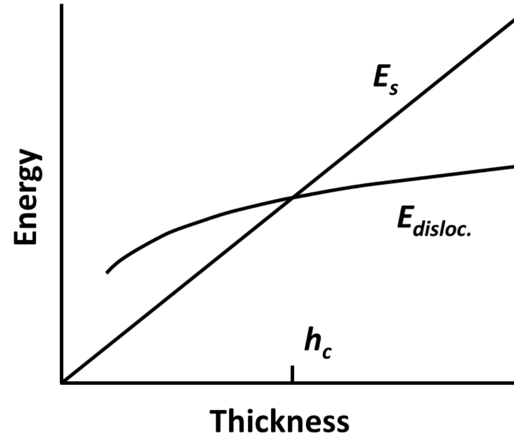

Figure 3.2: The elastic strain energy E_s increases in proportion to the strained layer thickness h, but the energy of a misfit dislocation E_{disloc} rises more slowly. The equilibrium critical thickness h_c is thus defined by the crossing of these two lines. Below h_c the pseudomorphic strained layer is thermodynamically stable; above h_c it relaxes or is metastable [1].

Many other different models have been established to predict the critical thickness for strained layers [8, 9]. The in-depth analysis of the critical thickness lies outside of this thesis work, however a good review covering the standard elasticity theory and methods of measuring the strain can be found for example in reference [1].

Here we will emphasize that the limits in pseudomorphic growth leads to the third class of the epitaxial growth: the metamorphic approach. Indeed, one problem with the pseudomorphic growth is that the limited choice of substrates greatly restricts device design, e.g. relatively thick $In_xGa_{1-x}As$ layers on GaAs substrates may not employ greater than 20% indium composition if coherency is to be maintained [10]. The other problem is the lack of a lattice-matched substrate variety, and an important example is the III-Nitride blue light-emitting diode (LED), usually fabricated on sapphire substrates.

Metamorphic growth involves forming a buffer layer with a different lattice constant from that of the substrate by employing strain relaxation. The idea underlying the metamorphic approach is to reduce the dislocation density introducing a buffer between the epitaxial structure and the substrate. The key is to design a buffer capable of confining the misfit dislocation in a region below the active part and suppressing the dislocation lines, i.e. *threading dislocations* (refer to Appendix A for a clarifying brief dissertation on dislocations).

Threading dislocation density (TDD) is generally determined by the kinetics of dislocation nucleation and glide, as threading dislocation segments

contribute relatively little to strain relaxation; threading dislocations are often nearly vertical, and the amount of strain relieved by a dislocation is proportional to its length projected onto the interface plane. Since they act as non radiative recombination centres, contribute to carrier scattering, and create spatial inhomogeneities that can lead to early device failure, one of the most important metrics for metamorphic epitaxial materials is a low TDD. Accordingly, relaxing strain through misfit dislocations while maintaining low TDD in the device region is the defining challenge of metamorphic growth.

3.2 $In_xGa_{1-x}As$ metamorphic substrate

The metamorphic strategy needs to meet certain requirements, not only for dislocation density, but also to allow cost-effective growth; that is, the thickness should be kept to a minimum. Therefore, while optimizing the designs in general, one needs to have in mind the highest possible lattice parameter change in minimal thickness, while preserving high surface quality (i.e., minimum appearing surface dislocation density, which often corresponds to minimum roughness). In the literature several types of different composition profiles have been tested. Compositional grading [11], is the most commonly used strategy. Step-graded buffers with just a few highly mismatched steps usually do not bring the best possible structural results, as the rapid relaxation leads to high defect density [12]. Gradually graded buffers, either continuous or dense multistep ones, usually allow for higher control over defect distribution [13]. The preferable epilayer relaxation is then obtained by creation of misfit dislocations, whose density corresponds to the compositional grading rate (lattice mismatch per thickness unit) and should be kept below a (specific) critical value, having a detrimental effect on the surface topography. Ideally, in a proper design, individual dislocations are given the possibility to glide for relatively long distances, providing the most efficient degree of strain relaxation [14].

In this work we refer to the design of the $In_xGa_{1-x}As$ graded buffer grown on GaAs(001) wafers, proposed by Muller et al [15]. In that work, the misfit dislocation (MD) depth distribution profile $n(t)$ and the residual parallel strain $\epsilon_{\parallel}(t)$ were estimated from the original model of Tersoff [16], where the equilibrium distribution of dislocations and residual strain along the growth direction

were calculated by minimizing the sum of strain energy and dislocation energy.

$$\left.\begin{aligned} n(t) &= \frac{1}{b_{eff}}\frac{df(t)}{dt} \\ \epsilon_{\|} &= 0 \end{aligned}\right\} \quad \text{for} \quad 0 < t < t_0 \\ \left.\begin{aligned} n(t) &= 0 \\ \epsilon_{\|} &= -[f(t) - f(t_0)] \end{aligned}\right\} \quad \text{for} \quad t > t_0 \tag{3.8}$$

where t is the distance from the substrate/buffer interface, t_0 is the thickness below which the layer is strain free and were MDs are confined, $f(t)$ the misfit profile, and b_{eff} the misfit component of the Burgers vector. During growth t_0 increases with the total layer thickness. With the assumption that the stain energy remains constant after the critical thickness is exceeded, the computation of the thickness t_0 is based on use of the empirical relaxation rate found for the homogeneous-composition layer [17]. Provided that the growth proceeds two-dimensionally, it has been found that the residual parallel strain can follow the general expression:

$$\varepsilon_{\|}^2 T = K = (0.0037 \pm 0.0007)\, nm \tag{3.9}$$

where T is the total thickness of the layer and K is the empirical constant, i.e the fitting parameter. If the Young's modulus Y is introduced in the equation we have the elastic energy per unit surface:

$$Y\varepsilon_{\|}^2 T = YK \tag{3.10}$$

In this way from the Eq.(3.9) it is considered that the MDs are nucleated when a critical elastic strain energy per unit surface is exceeded. This is valid for an homogeneous-composition layer, where the equilibrium energy density, i.e. the elastic energy of the free-standing structure, is zero. In graded-composition layers the equilibrium energy density is not zero and can be written as:

$$E_{eq} = Y \int_{t_0}^{T} \left[f(t) - \overline{f} \mid_{[t_0 - T]} \right]^2 dt \tag{3.11}$$

$$\overline{f} \mid_{[t_0 - T]} = 1/(T - t_0) \int_{t_0}^{T} f(t) dt \tag{3.12}$$

Here, $\overline{f} \mid_{[t_0 - T]}$ denotes the average misfit between t_0 and T parabolic. The critical energy for MD nucleation E_{exc} should thus be the difference between

the total energy density E_{tot} and the equilibrium energy density: $E_{exc} = E_{tot} - E_{eq} = YK$. This allows computation of the thickness t_0 by solving the equation

$$E_{exc}/Y = (T - t_0)(\overline{f}\mid_{[t_0 - T]} - f(t_0))^2 = K = 0.0037\,nm \tag{3.13}$$

According the Tersoff model a linear graded composition profile would lead to a uniform MD concentration up to t_0 [16], while a superlinear composition profile with negative curvature would lead to a MD concentration decreasing towards the surface, higher values of T/t_0 , and more uniform residual strain profile for $t > t_0$.

In particular the concentration parabolic profile turned out promising compared to different grading profiles studied [18], because of its simplicity, relatively flat behaviour in the near-surface region, making it less sensitive than other profiles to variations in composition and layer thickness; and its expected property of confining MDs away from the surface while minimizing dislocation interactions[19]:

$$x(t) = x_0\left[1 - \left(1 - \frac{t}{T}\right)^2\right] \tag{3.14}$$

were x_0 is the desired value of In concentration, T is the total thickness of the $In_xGa_{1-x}As$ layer and t is the distance from the GaAs substrate. The corresponding residual strain at the film surface in the direction parallel to the interface $\varepsilon_{\parallel}$ can be calculated from Eqs.3.8 and 3.13 as:

$$\varepsilon_{\parallel}^{5} = \left(\frac{9K}{4}\right)^2 \frac{x_0}{T^2}\left[\frac{a_0(InAs)}{a_0(GaAs)} - 1\right] \tag{3.15}$$

where a_0(InAs) and a_0(GaAs) are the equilibrium (unstrained) lattice parameters for the binary parent compounds.

In a more recent study [20] our group tested the goodness of the parabolic grading profile in MOVPE system adding significant insights to the investigation of strain, relaxation, and defect distribution in metamorphic buffer design. We reported a selection of stack designs for MOVPE grown $In_xGa_{1-x}As$ metamorphic buffer layers following various convex-down compositional continuous gradients of the In content, showing that defect generation and strain can be managed in a variety of ways. Observing that it is possible to grow surprisingly thick tensile strained layers on metamorphic substrates, without significant relaxation and defect generation. For example, in Figure 3.3 is shown a representative characterization of an $In_xGa_{1-x}As$ MBL ($\sim 0 < x < 0.33$), 1 μm thick, grown following the previously reported design of single parabolic exchange curve.

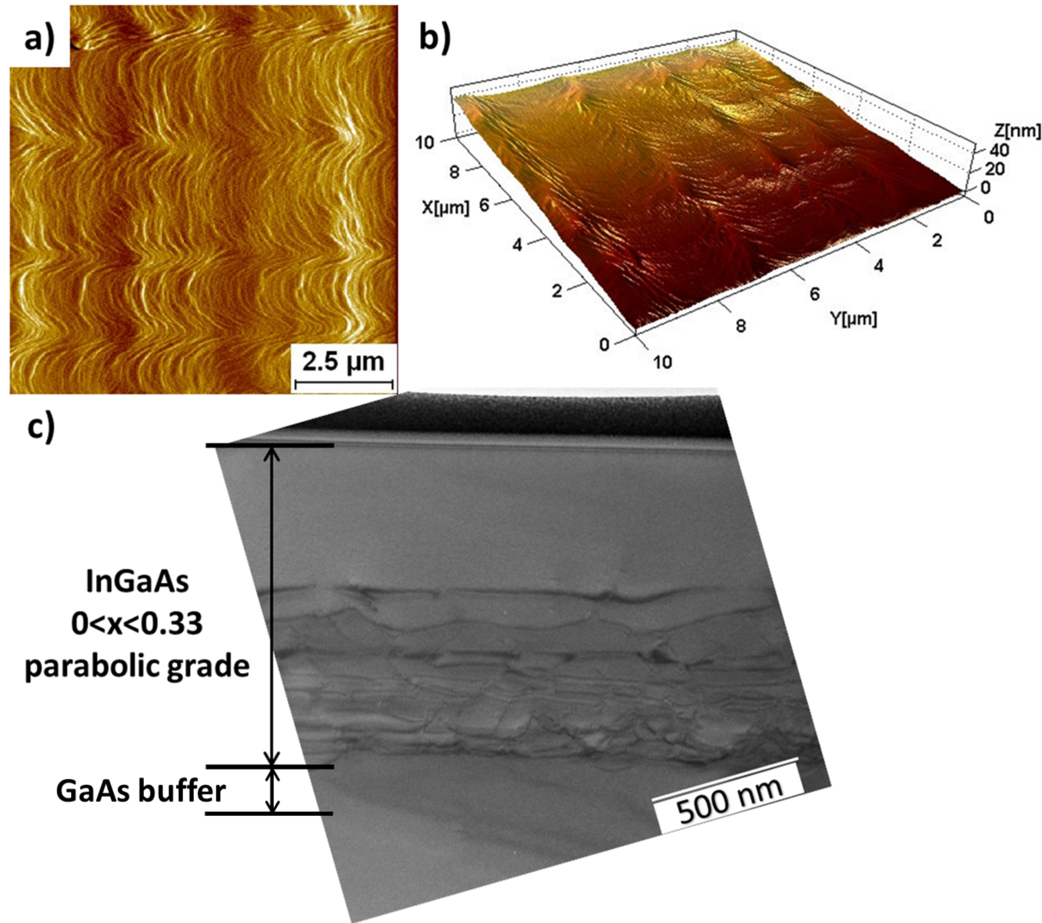

Figure 3.3: Surface morphology and defect distribution in an InGaAs MBL following a single parabolic exchange curve: AFM images (a) signal amplitude, (b) reconstructed 3D height image, and (c) cross-sectional TEM in [110] orientation. Sample grown on GaAs (100) ±0.02° perfectly oriented substrate.

It showed a "flat" (∼3 nm RMS), step-bunched surface and relatively low defect density (estimated $< 5 \times 10^5 cm^{-2}$) toward the end of the layer. The defects in the final growth layer were estimated by a combination of cross-sectional TEM and top-view AFM, as discussed in ref. [21]. Most of the threading dislocation network was buried down close to the GaAs substrate, as it is clear from TEM in Figure 3.3c). The in-plane lattice parameter in this growth was equivalent to a fully relaxed $In_{0.27}Ga_{0.73}As$, as estimated by HRXRD measurements; the residual parallel strain was -0.0044%. The TEM image is actually in agreement with that; the thickness corresponding to the end of the defected region (∼550 nm from the bottom of the growth) can be translated into approximately the same indium composition value (∼0.27), i.e. the growth proceeded from there on pseudomorphically. These results as such were not unexpected in view of the existing literature (see e.g. [15] and [22]).

3.3 Characterization of the MBL for the 1.3 μm QWs laser

The virtual substrate used in the full laser structure, the object of this research work, shares the superlinear parabolic grading profile just discussed. All epitaxial samples discussed here were grown in our high purity MOVPE commercial horizontal reactor (AIX 200) at low pressure (80 mbar) with purified N_2 as the carrier gas. The precursors were trimethylindium (TMIn), trimethylgallium (TMGa), arsine (AsH_3) and phosphine (PH_3). Samples were grown on (100) GaAs 0.2°, 4° and 6° misoriented substrates towards [111]A (on some occasion, in this thesis manuscript they will be indicated in the simplified manner 0.2°A, 4°A and 6°A). The graded buffers started from GaAs and were initiated with minimal controllable In flow, therefore the real initial composition can be estimated to be between 0.00 and 0.01 In. All samples had a homoepitaxial GaAs 100 nm thick buffer grown prior to the graded $In_xGa_{1-x}As$. Growth conditions were: V/III ratio 130, growth rate 1 $\mu m/h$, growth temperature 740°C. Figures 3.4, 3.5 and 3.6 show the surface morphology of one representative MBL sample grown on three different GaAs substrates miscuts.

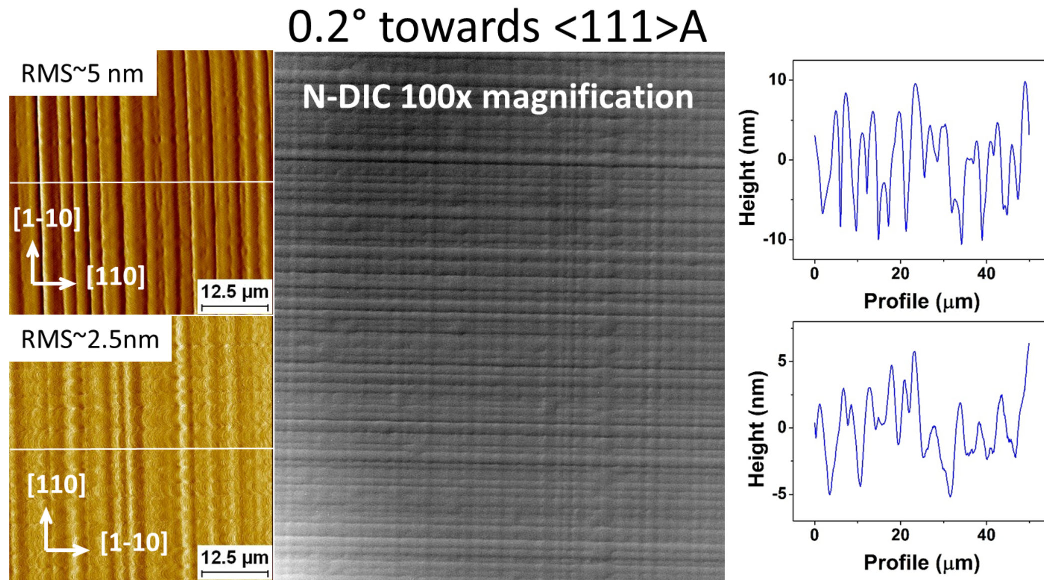

Figure 3.4: Surface morphology of the $In_xGa_{1-x}As$ MBL following a superlinear parabolic exchange curve. Left side: AFM image (signal amplitude) for the two <110> directions. Centre: N-DIC micrograph image, 100x magnification. Right side: AFM images(cross-sectional profile). Sample grown on GaAs (100) 0.2°A misoriented substrate.

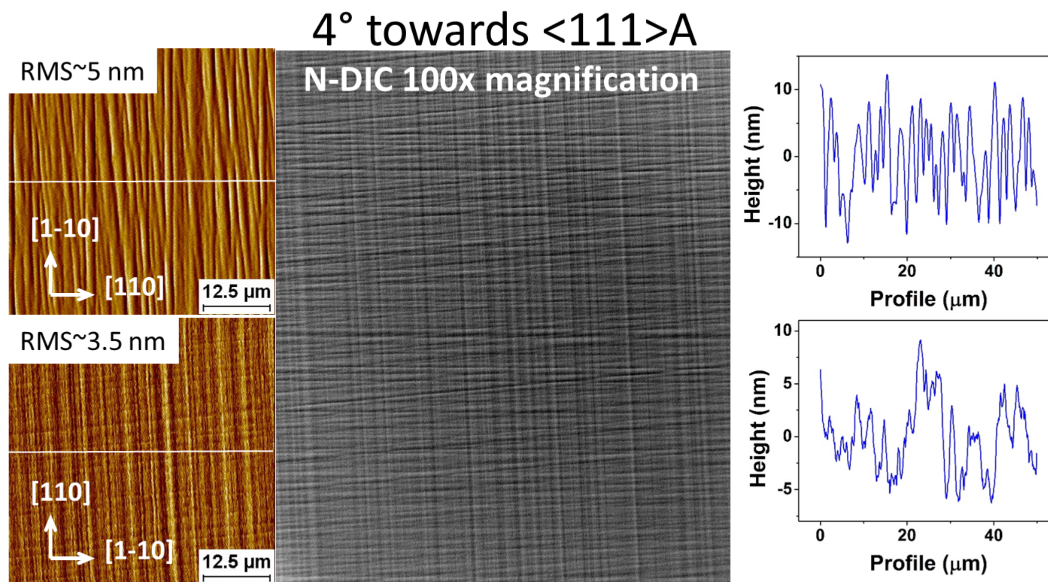

Figure 3.5: Surface morphology of the $In_xGa_{1-x}As$ MBL following a superlinear parabolic exchange curve. Left side: AFM image (signal amplitude) for the two <110> directions. Centre: N-DIC micrograph image, 100x magnification. Right side: AFM images(cross-sectional profile). Sample grown on GaAs (100) 4°A misoriented substrate.

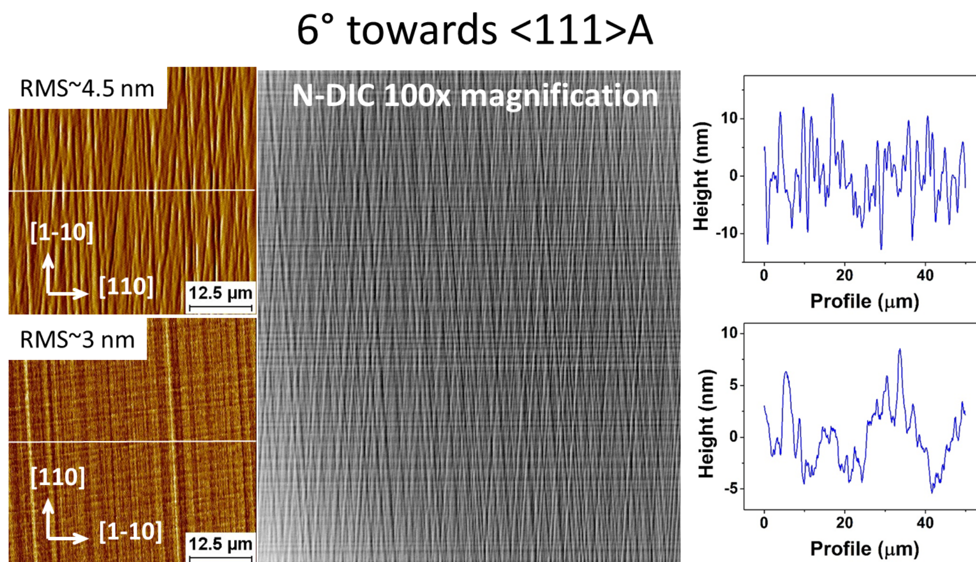

Figure 3.6: Surface morphology of the $In_xGa_{1-x}As$ MBL following a superlinear parabolic exchange curve. Left side: AFM image (signal amplitude) for the two <110> directions. Centre: N-DIC micrograph image, 100x magnification. Right side: AFM images(cross-sectional profile). Sample grown on GaAs (100) 6°A misoriented substrate.

The RMS value evaluated from an AFM scan size area of $50 \times 50 \quad \mu m^2$ reveals a successful smooth surfaces with cross-hatch (CH) pattern clearly

visible when inspected with an optical microscope in N-DIC. CH is a grid-like pattern consisting of ridges aligned along [110] and $[1\bar{1}0]$ directions, which leads to the asymmetry of the roughness in the two <110> directions. It is noticed that the [110] direction experiences a higher RMS than the $[1\bar{1}0]$ direction.

In our MBL we observed the roughness RMS value along the [110] direction of ∼5 nm and ∼3 nm along the $[1\bar{1}0]$ direction, for all three substrate misorientations studied. Similar surface organization and roughness behaviour is preserved in the subsequent layers deposited onto the MBL; the phenomenology and the study of surface organization with particular attention to the roughness evolution is carefully presented in chapter 4, where a special section is dedicated at the inversion and change of roughness along the two <110> directions (never observed or discussed before, to the best of our knowledge).

The CH pattern is not just unique for the growth of MBLs, it is a common characteristic occurring in low mismatched (less than 2%) heteroepitaxy [23]. The formation of the CH pattern depends on many factors such as growth temperature, misfit strain, and the thickness of the epitaxial layer. Despite the frequent observation of cross-hatch, its origin remains still unresolved in its full details. There are essentially two models described in the literature. One model suggests surface undulation forms during growth with elastic strain relaxation during pseudomorphic growth that leads to stress concentrations and subsequent formation of dislocations at troughs [24, 25]. The second one suggests that the lattice mismatch induced strain initially relaxes by forming misfit dislocations followed by enhanced growth rates on the relaxed surface areas above the dislocations, which then produces the surface undulations [23, 26]. This second model suggests that dislocations should exist for each line in the CH pattern. It should be noted that these models somehow account for the undulations produced during the relaxation process, but do not actually discuss in detail the evolution the subsequent pseudomorphic growth.

The assessment of composition and the strain in the layers was made according to measurements of Reciprocal Space Map (RSM) obtained by high resolution X-ray diffraction measurements (where the Bartel monochromator was replaced by a hybrid mirror guaranteeing higher throughput). Because symmetrical diffraction is only sensitive to the lattice spacing perpendicular to the sample surface, at least one asymmetrical diffraction pattern is needed for information about in-plane lattice spacing. Accordingly, measurements were done in a symmetric (004) and two asymmetric (224 and -2-24) reflections with sample positioned at 0°, 90°, 180° and 270° with respect to its main crystallographic axes (the calculations followed Vegard's law, which is a standard

method for calculating alloy composition and strain in partially relaxed III-V materials, see e.g., refs [27–30]). Details regarding one batch of MBL samples are summarized in Table 3.1 (similar results were found for all samples, but are not shown here).

Table 3.1: RMS values for the $[1\bar{1}0]$ direction, calculated from $50 \times 50 \quad \mu m^2$ AFM images after standardized flattening, and values corresponding to final grown layer, estimated by XRD measurements.

Substrate Misorientation	RMS nm	Composition In(%)	in-plane lattice Parameter [Å]	Equivalent Relaxed Composition In(%)	Residual Parallel Strain $\epsilon_\parallel$
0.2° tw <111>A	2.5	17.52	5.70703	13.27	-0.0030
6° tw <111>A	3	18.15	5.71076	14.19	-0.0028

The single parabolic MBL, grown onto GaAs (001) 0.2°A (6°A) miscut, showed a final indium composition $y_{real} = 17.52\%$ (18.15%), in-plane residual strain $\epsilon_\parallel = -0.0030$ (-0.0028), in-plane lattice parameter $a_\parallel = 5.707\,03$ Å (5.7176 Å) corresponding to relaxed indium composition $y_{in-plane} = 13.27\%$ (14.19%).

The in-plane lattice parameter at the end of the graded buffer is comprised between InP, $a_{InP} = 5.8687$ Å and the GaAs, $a_{GaAs} = 5.6532$ Å unstrained lattice constants, i.e presenting the right value to accommodate the full laser structure.

The laser structure will be essentially based on *p*-*i*-*n* design.

The desired emission wavelength (1.3 μm in our case) is achieved by tuning the alloy composition of different epilayers of the separate confinement heterostructure (SCH). The active or i (intrinsic) region consist of strained multi quantum wells. The changes regarding thickness, composition and order deposition of the layers will be described and justified in the dedicated chapter.

In the following chapters will be analysed and presented in morphological terms the experimental results of the claddings, lower and upper, barriers and QWS, with a final chapter regarding the complete laser epitaxial structure and the electro-optical results of the device associated.

Bibliography

[1] DJ Dunstan. “Strain and strain relaxation in semiconductors”. In: *Journal of Materials Science: Materials in Electronics* 8.6 (1997), pp. 337–375.

[2] Udo W Pohl. *Epitaxy of Semiconductors: Introduction to Physical Principles.* Springer Science & Business Media, 2013.

[3] FC Frank and Jan H van der Merwe. “One-dimensional dislocations. I. Static theory”. In: *Proceedings of the Royal Society of London. Series A. Mathematical and Physical Sciences* 198.1053 (1949), pp. 205–216.

[4] Frederick Charles Frank and JH Van der Merwe. “One-dimensional dislocations. II. Misfitting monolayers and oriented overgrowth”. In: *Proceedings of the Royal Society of London. Series A. Mathematical and Physical Sciences* 198.1053 (1949), pp. 216–225.

[5] FC Frank and JH Van der Merwe. “One-dimensional dislocations-III. Influence of the second harmonic term in the potential representation, on the properties of the model”. In: *Proceedings of the Royal Society of London. Series A. Mathematical and Physical Sciences* 200.1060 (1949), pp. 125–134.

[6] WA Jesser and J Wo Matthews. “Evidence for pseudomorphic growth of iron on copper”. In: *Philosophical Magazine* 15.138 (1967), pp. 1097–1106.

[7] EA Fitzgerald. “Dislocations in strained-layer epitaxy: theory, experiment, and applications”. In: *Materials science reports* 7.3 (1991), pp. 87–142.

[8] R People and JC Bean. “Erratum: Calculation of critical layer thickness versus lattice mismatch for Ge x Si1- x/Si strained-layer heterostructures [Appl. Phys. Lett. 4 7, 322 (1985)]”. In: *Applied Physics Letters* 49.4 (1986), pp. 229–229.

[9] FY Huang. “Effect of strain transfer on critical thickness for epitaxial layers grown on compliant substrate”. In: *Applied Physics Letters* 76.21 (2000), pp. 3046–3048.

[10] WE Hoke et al. “Properties of metamorphic materials and device structures on GaAs substrates”. In: *Journal of crystal growth* 251.1-4 (2003), pp. 804–810.

[11] MS Abrahams et al. “Dislocation morphology in graded heterojunctions: GaAs 1- x P x”. In: *Journal of Materials Science* 4.3 (1969), pp. 223–235.

[12] S. P. Ahrenkiel et al. “Characterization survey of GaxIn1-xAs/InAsyP1-y double heterostructures and InAsyP1-y multilayers grown on InP”. In: *Journal of Electronic Materials* 33.3 (Mar. 2004), pp. 185–193.

[13] Kenneth E. Lee and Eugene A. Fitzgerald. “High-quality metamorphic compositionally graded InGaAs buffers”. In: *Journal of Crystal Growth* 312.2 (2010), pp. 250–257. ISSN: 0022-0248.

[14] L.B. Freund. “Dislocation Mechanisms of Relaxation in Strained Epitaxial Films”. In: *MRS Bulletin* 17.7 (1992), pp. 52–60.

[15] BH Müller et al. “Zn 0.85 Cd 0.15 Se active layers on graded-composition In x Ga 1- x As buffer layers”. In: *Journal of applied physics* 85.12 (1999), pp. 8160–8169.

[16] J Tersoff. “Dislocations and strain relief in compositionally graded layers”. In: *Applied physics letters* 62.7 (1993), pp. 693–695.

[17] AV Drigo et al. “On the mechanisms of strain release in molecular-beam-epitaxy-grown In x Ga1- x As/GaAs single heterostructures”. In: *Journal of Applied Physics* 66.5 (1989), pp. 1975–1983.

[18] A Bosacchi et al. “Continuously graded buffers for InGaAsGaAs structures grown on GaAs”. In: *Journal of crystal growth* 175 (1997), pp. 1009–1015.

[19] B Müller et al. “Native extended defects in Zn 1- y Cd y Se/In x Ga 1- x As heterostructures”. In: *Journal of Vacuum Science & Technology B: Microelectronics and Nanometer Structures Processing, Measurement, and Phenomena* 16.4 (1998), pp. 2334–2341.

[20] Agnieszka M Gocalinska, Marina Manganaro, and Emanuele Pelucchi. “Unexpected aspects of strain relaxation and compensation in InGaAs metamorphic structures grown by MOVPE”. In: *Crystal Growth & Design* 16.4 (2016), pp. 2363–2370.

[21] Agnieszka Gocalinska et al. “Evaluation of defect density by top-view large scale AFM on metamorphic structures grown by MOVPE”. In: *Applied Surface Science* 349 (2015), pp. 849–854.

[22] H Choi et al. "Effectiveness of non-linear graded buffers for In (Ga, Al) As metamorphic layers grown on GaAs (0 0 1)". In: *Journal of Crystal Growth* 311.4 (2009), pp. 1091–1095.

[23] Kevin H Chang et al. "Crosshatched surface morphology in strained III-V semiconductor films". In: *Journal of applied physics* 67.9 (1990), pp. 4093–4098.

[24] AG Cullis. "Strain-induced modulations in the surface morphology of heteroepitaxial layers". In: *Mrs Bulletin* 21.4 (1996), pp. 21–26.

[25] AJ Pidduck et al. "Evolution of surface morphology and strain during SiGe epitaxy". In: *Thin Solid Films* 222.1-2 (1992), pp. 78–84.

[26] AM Andrews et al. "Modeling cross-hatch surface morphology in growing mismatched layers". In: *Journal of applied physics* 91.4 (2002), pp. 1933–1943.

[27] J Sass et al. "Determination of In concentration in InGaAs/GaAs 0 0 1 epilayers in the early stage of anisotropic stress relaxation". In: *Journal of alloys and compounds* 401.1-2 (2005), pp. 249–253.

[28] C Ferrari et al. "Lattice parameter dependence versus composition in semiconductor alloys: the InGaAs case". In: *MRS Online Proceedings Library Archive* 677 (2001).

[29] A Benediktovitch et al. "Concentration and relaxation depth profiles of In x Ga 1- x As/GaAs and GaAs 1- x P x/GaAs graded epitaxial films studied by x-ray diffraction". In: *Physical Review B* 84.3 (2011), p. 035302.

[30] D Lee et al. "Characterization of metamorphic In x Al 1- x As/ Ga As buffer layers using reciprocal space mapping". In: *Journal of applied physics* 101.6 (2007), p. 063523.

Chapter 4

Cladding: Superlattice approach

This chapter focus is on upper and lower cladding layers of a metamorphic laser structure: they are studied in terms of morphology and roughness control. First of all two different alloys, InGaP and AlInGaAs, are considered as possible cladding layer, then studied in terms of surface morphology by AFM. A high RMS value connected with the defects lines on the surface reveals the existence of correlation between epilayer thickness and defect generation. Then a study is presented, related to the surface organization change/inversion in terms of roughness (RMS value) and morphology (as a function of surface orientations) discovered during the deposition of InGaP and AlInGaAs on the MBL. In the last section a possible combination of the two alloys to be used in our laser structure is then discussed.

4.1 The choice of the cladding layer

AlInGaAs and InGaP represent two suitable alloys for the cladding selection in order to maintain efficient optical field confinement and waveguiding, while a peak at 1.3 μm emission in a SCH-multiQWs configuration for lasing.

As already discussed in chapter 3 the use of the InGaAs virtual substrate with a lattice constant between those of GaAs and InP allows the engineering of the cladding barrier and leads towards a large conduction band offset for the 1.3-µm-range emission increasing optical confinement. Referring to Figure 4.1 AlInGaAs and (Al)InGaP can be engineered to any lattice parameter of interest, keeping a relatively high bandgap . We will show later in this chapter the rationale for the specific combined choice we made, which is linked to specific surface morphology evolutions, and not only by specific material properties.

Indeed in the quaternary AlInGaAs layer the Al composition can be varied over a wide range keeping lattice matching to the $In_xGa_{1-x}As$ MBL. Moreover, the AlInGaAs material system provides simplicity to a metamorphic laser design, as it allows by simply varying the Aluminum content both strong QW

confinement when used for barriers, and also allows the engineering of a separate confinement heterostructure (SCH) to enhance the optical confinement and hence reduce the material gain at threshold as recently discussed [1].

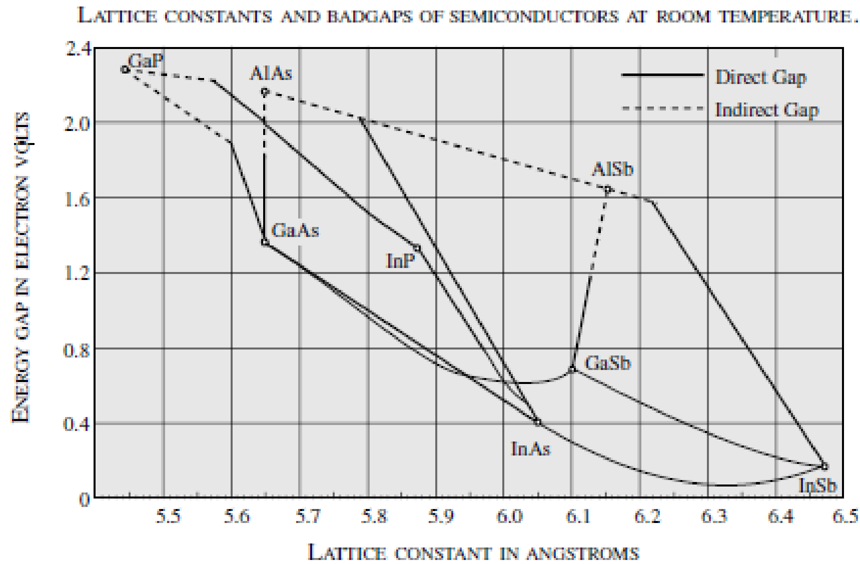

Figure 4.1: The range of bandgaps achievable by alloy formation in some III-V compound semiconductors.

Obviously the optimization of the cladding must be done considering the implications of defects formation and propagation during the epitaxial deposition and other variables as will become clear. The study and observation of this phenomenology is the subject of this chapter.

4.1.1 Structure and growth condition of the cladding layer

All epitaxial samples discussed here were grown in our high purity MOVPE commercial horizontal reactor (AIX 200) at low pressure (80 mbar) with purified N_2 as carrier gas. The precursors were trimethylindium (TMIn), trimethylgallium (TMGa), trimethylaluminum (TMAl), arsine (AsH_3), phosphine (PH_3) and trimethylantimony (TMSb) used as a surfactant during cladding layer growth. All epitaxial growths resulted in general in smooth surfaces (see comments on samples non-uniformities in the dedicated paragraph later in the text) with a cross-hatch pattern clearly visible when inspected with an optical microscope in (Nomarski) Differential Interference Contrast (N-DIC) or in dark field mode. Subsequent detailed morphological studies were performed by AFM in tapping/non contact mode at room temperature and in air. The assessments of composition and strain in the layers were made according to measurements

of RSMs obtained by High resolution X-ray diffraction (HRXRD) measurements. Measurements were done in a symmetric (004) and two asymmetric (224) and (-2-24) reflections with sample positioned at 0°, 90°, 180° and 270° with respect to its main crystallographic axes.

Different GaAs (001) substrates with miscuts of 0.2° and 6° towards (111)A were used in the majority of the samples grown. In some case we used also GaAs (001) perfectly oriented, and GaAs (001) with the miscuts of 0.05° and 4° towards (111)A. We also observe that sometimes in view of the effectively broad phenomenology explored over a relatively long period of time, the substrate choices have also been dictated by contingent availability. As it will be clear from our discussion, this has not affected out conclusions.

4.2 AlInGaAs

The determination of the lattice parameter of a quaternary alloy follows the same procedure used for the ternary alloy explained in the previous chapter. However, to acquire the composition, being the generic quaternary alloy $A_xB_{1-x}C_yD_{1-y}$ specified by two variables, Vegard's law was combined with the energy gap obtained by photoluminescence measurements.

4.2.1 Effect of trimethylantimony

The direct deposition of AlInGaAs onto a MBL immediately showed the appearance of a significant surface roughening if compared to InGaAs alloys. It is likely that this is due to the presence of Al in the alloy. In the 2D surface reconstruction (Figure 4.2 (a) and (b)) obtained by AFM amplitude images, scan size 10x10 μm, is clear a transition from a surface with elongated features aligned to one plane direction (as concerns the MBL) to a surface where islands spread across with an irregular shape leaving spaces in-between appearing as holes.

The addition of the TMSb (Figure 4.2 (c)) as a surfactant during the AlInGaAs layer deposition smoothed the surface, somehow elongating the islands towards the "original" order. While it is not completely understood how the TMSb interacts during the deposition, it should be said that in our group the use of trimethylantimony (or its decomposition products) as a surfactant has been previously observed to strongly modify surface organization, for example it was found to crucially enable the control over defect formation during the relaxation process in a metamorphic buffer growth in InAs/InGaAs/InP

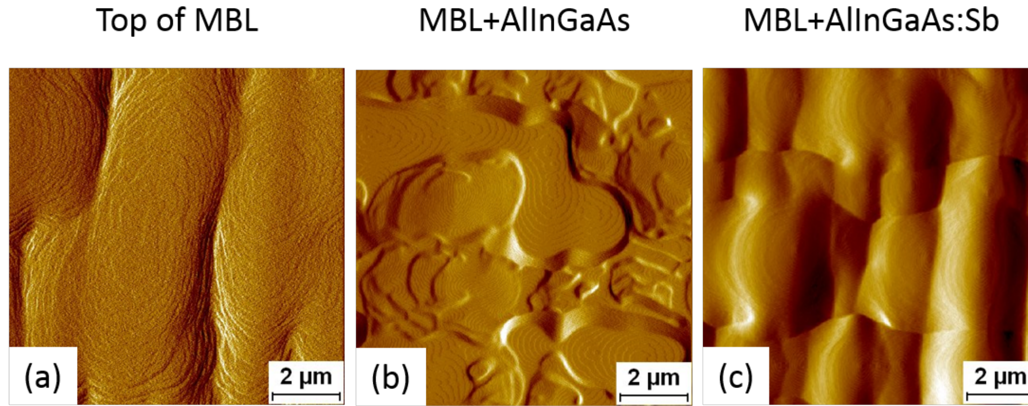

Figure 4.2: AFM images (amplitude signal 10x10 μm scan size). Morphology comparison between (a) MBL, (b) "nude" $Al_{0.30}In_{0.18}Ga_{0.52}As$ and (c) $Al_{0.30}In_{0.18}Ga_{0.52}As$ with TMSb as a surfactant both deposited lattice matched on MBL. The MBL was grown on GaAs (001) perfectly oriented. In (b), (c) the AlInGaAs layer thickness was 300 nm. The RMS value for the three images are $\sim$ 4 nm, $\sim$ 6 nm and $\sim$ 5.5 nm respectively.

structures [2]. In another study the surfactant effect of antimony was reported to be useful in controlling the epitaxial growth mode, preventing 3-D growth in compressively strained InGaAs layers, mostly with applications to quantum wells (QWs) [3].

Both samples shown in Figure 4.2 (b) and (c) are grown with 300 nm of $Al_{0.30}In_{0.18}Ga_{0.52}As$ lattice matched to the in plane lattice parameter of the metamorphic buffer layer. The RMS extracted from AFM 10x10 μm scans was $\sim$ 4 nm for the MBL, $\sim$ 6 nm and $\sim$ 5.5 nm for the sample without and with TMSb respectively.

The "planarization" process and the consequent decrease of the RMS obtained with the antimony become less vivid when increasing the thickness of the AlInGaAs layer. The sample in Figure 4.3 (a) was grown with 1000 nm of AlInGaAs and TMSb, and presents a RMS value of $\sim$ 8 nm. The higher RMS value can be accredited to the increased of peak to valley range (from $\sim$24 nm for AlInGaAs 300 nm sample to $\sim$50 nm for the 1000 nm sample, by comparing the height profile of the two samples in Figure 4.3(b)), while no other substantial morphological differences can be found.

Unfortunately while 8 nm RMS can be an acceptable value for a micron thick layer, we found problems related to the growth of other similar or thicker AlInGaAs layers. For example we observed a RMS value of 16.26 nm (evaluated by an AFM scan size $10 \times 10 \mu m^2$) for the A1633 sample, which was grown with $Al_{0.13}In_{0.17}Ga_{0.7}As$ 1000 nm plus 50 nm of $Al_{0.40}In_{0.17}Ga_{43}As$ lattice

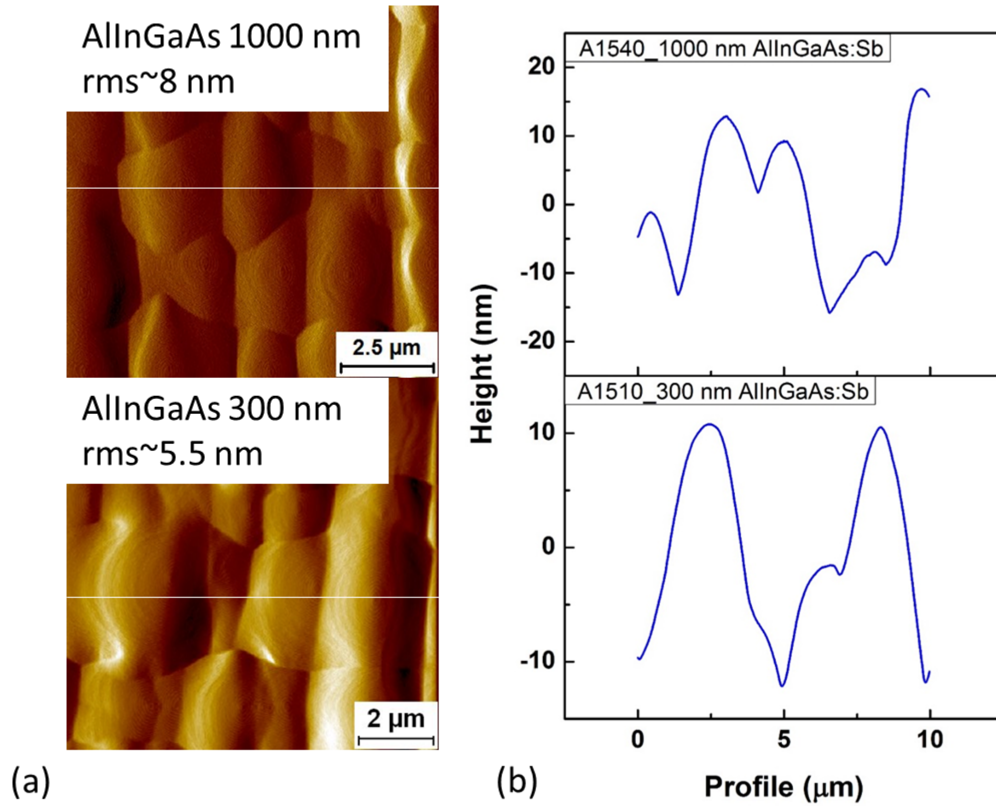

Figure 4.3: Comparison between (a) AFM amplitude signal and (b) AFM cross-sectional profile of AlInGaAs:Sb thick 300 nm and 1000 nm grown lattice matched on MBL. GaAs (001) perfectly oriented was used as substrate.

matched onto the MBL. Moreover in one of our first attempts to grow the whole laser structure, with both lower and upper *AlInGaAs* claddings plus *AlInGaAs* barriers, we recorded an even bigger total RMS value of 26 nm with evident defect lines on the surface in the sample grown on 0.2° towards [111]A (Figure 4.4) and a peak to valley range exceeding 120 nm (Figure 4.4 perfectly oriented sample). More details about the full laser structure will be provided in chapter 6. Here we want to underline and report that the increase of the layer thickness corresponded to the increase of the roughness with strong detrimental effects on device performance, effectively resulting in inoperable devices. Hence the motivation and necessity to explore new growth solutions and different cladding materials in order to obtain efficient devices.

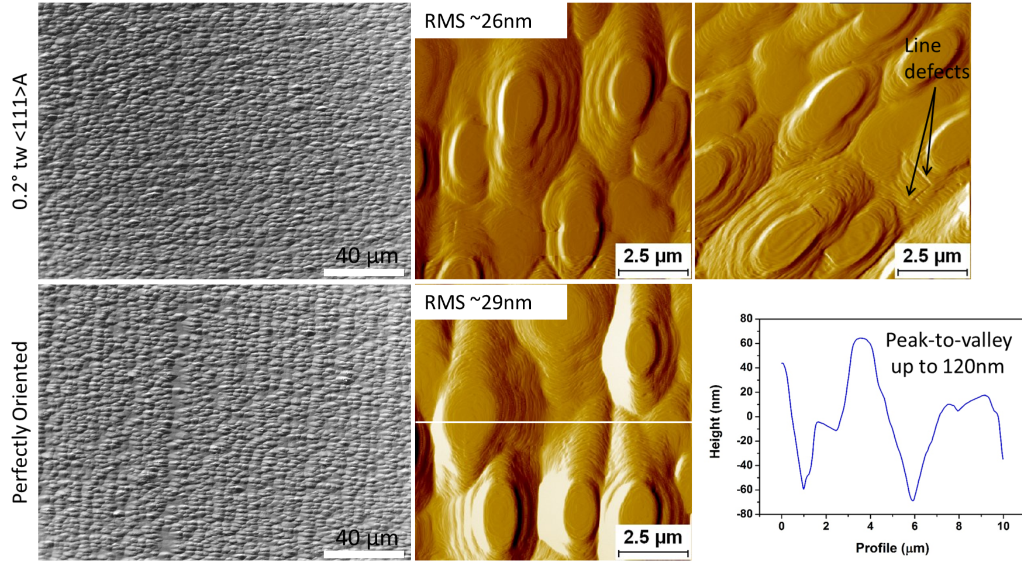

Figure 4.4: N-DIC and AFM images (amplitude signal and cross-sectional profile) of full laser structure first attempt growth. The laser design comprised of AlInGaAs lower and upper claddings 1400 nm each, and AlInGaAs lower and upper barrier guide 100 nm each. Substrate GaAs (001) perfectly oriented.

4.2.2 Effect of Strain Balancing Layer

In order to try and suppress the RMS increase with grown layer thickness, we first reverted to introducing a Strain Balancing Layer (SBL), initially estimated on the simplifying assumption that the pseudomorphic part of the MBL if fully strained and the defected part fully relaxed. Recently our group observed that very thick tensile strained layers can be grown on top of an metamorphic substrates without significant relaxation and defect generation (for a fully understanding of the process refer to [4]). In the mentioned work A. Gocalinska *et al* followed a simple theoretical model for the composition and thickness of the tensile strained region where the accumulated elastic energy E can be calculated from the following formula:

$$E_{MBL} = \int_{h_3}^{h_2} \epsilon_p^2(h) Y(y)\, dh \tag{4.1}$$

where: h – *thickness*, Y – *Young's modulus*, y - *indium concentration*, ϵ_p - *in-plane strain* (points 2 and 3 determine beginning and end of the strained region, variables indicated on graph on Figure 4.5 for clarification). Since in the case of a continuous parabolic grading, the composition y relates to

thickness h by the following [5]:

$$y(h) = (y_3 - y_0)\left[1 - \left(1 - \frac{h}{h_3}\right)^2\right] + y_0 \tag{4.2}$$

To balance the accumulated elastic energy fully, a tensile SBL needs to have $E_{SBL} = -E_{MBL}$, where

$$E_{SBL} = \epsilon_p^2 Y(y) h \tag{4.3}$$

for a constant composition layer, and the minus has been added to show the opposite strain contribution. An SBL needs to fulfill additional criteria: the lattice parameter offset between the end of the previous layer and the SBL cannot exceed the critical value leading to creation of dislocations (or of Stranski-Krastanow dot like structures), but it needs to be large enough to provide good interfacial stress for (eventual) dislocation glide. Also small thicknesses would be preferable, in general, with the scope of maintaining the overall thickness the minimum possible.

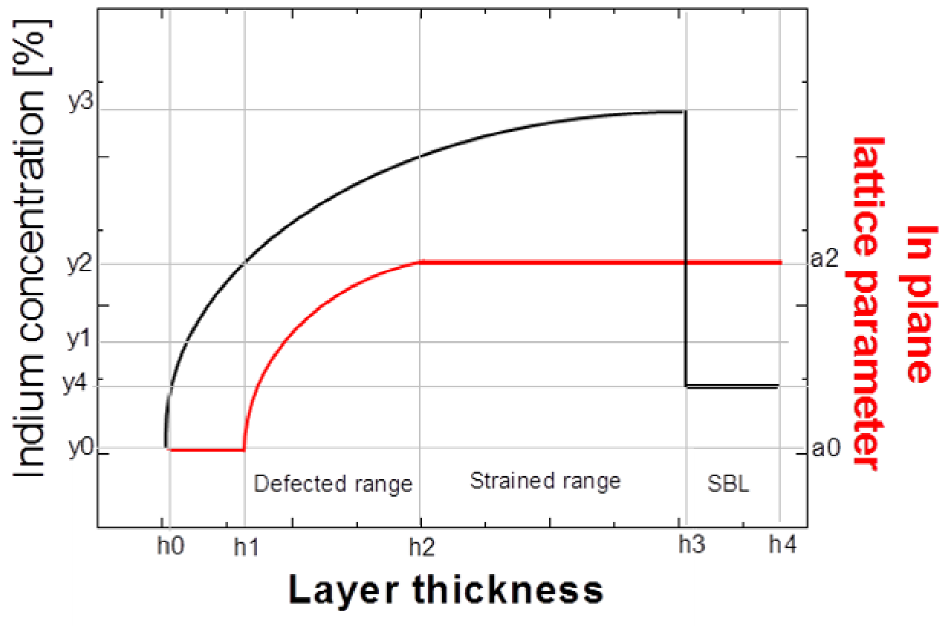

Figure 4.5: Simplified design sketch of single parabolic grading with SBL (black curve: alloy composition regarding indium concentration, red curve: in-plane lattice parameter change in the structure – before the relaxation threshold the substrate lattice parameter is preserved, then increases during the defected part and finally settles at a value preserved for the rest of the structure in the pseudomorphic fraction of the MBL and in the SBL).

The intent in this contest is insert a SBL before the AlInGaAs cladding

deposition to control and improve the overall stress and hopefully morphology, comparing the result with the direct deposition of AlInGaAs.

For this purpose three different SBL were overgrown on the MBL (Figure 4.6). In this case we abandoned the use of the GaAs (100) perfectly oriented substrate, choosing instead a slightly misoriented substrate, i.e. 0.2° towards [111]A. From approximate estimates and calculations concerning the A2173

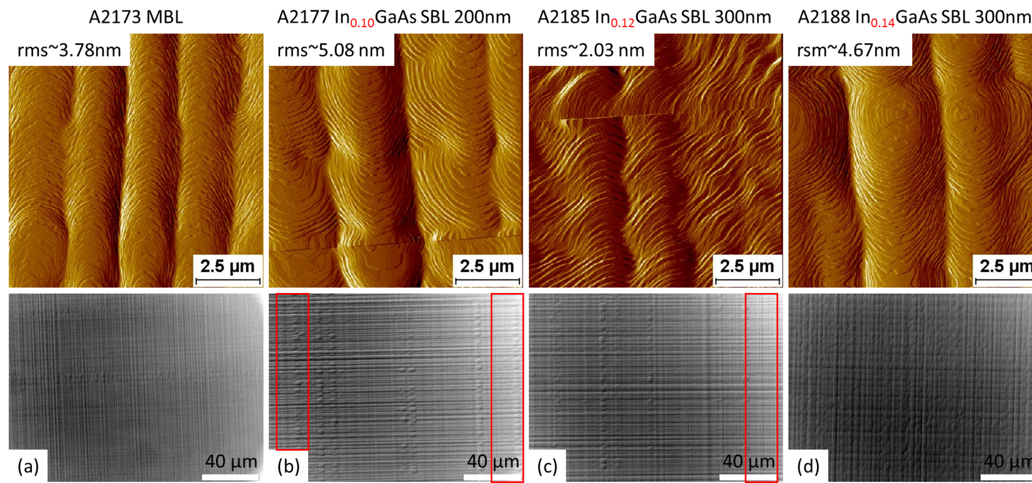

Figure 4.6: AFM (amplitude signal) and N-DIC images of (a) metamorphic buffer layer on 0.2° towards [111]A misoriented substrate, and overgrowth of: (b) $In_{0.10}$GaAs SBL 200 nm thick, (c) $In_{0.12}$GaAs SBL 300 nm thick, and (d) $In_{0.14}$GaAs SBL 300 nm thick.

sample, an $In_{0.10}$GaAs SBL thick 200 nm, was grown on top of the MBL (Figure 4.6 (a) and (b)). The capping with an SBL of such strain and thickness resulted in a worsening of the RMS roughness (from ∼4 nm to ∼5 nm) associated with threading dislocations clearly visible even when inspected with the optical microscope (underlined by the red rectangles in Figure 4.6). When we added strain and increased the thickness in the SBL (Fig.4.6 (c)) there was a notable reduction of the RMS roughness (from ∼4 nm to ∼2 nm) indicating the potential feasibility of such an approach. Nevertheless, we still ascertained the presence of sharp, perpendicular lines, reported in Figure 4.7 for a more accurate examination of the same sample, which we identify as possible dislocations threading to the surface plane, in analogy to what was proven in Ref [6]. We observe that the surface roughness is not the only factor which needs to be considered with laser optimisation, as step bunching, or long range step organisation, might not have necessarily a severe detrimental effect on a device performance, despite their contribution to a higher RMS. Nevertheless, here a different parameter presented issues. Threading dislocations are obviously, of

major relevance as well, as they are affecting the subsequent overgrowth, and their presence does not necessarily correlate with surface step organization [7].

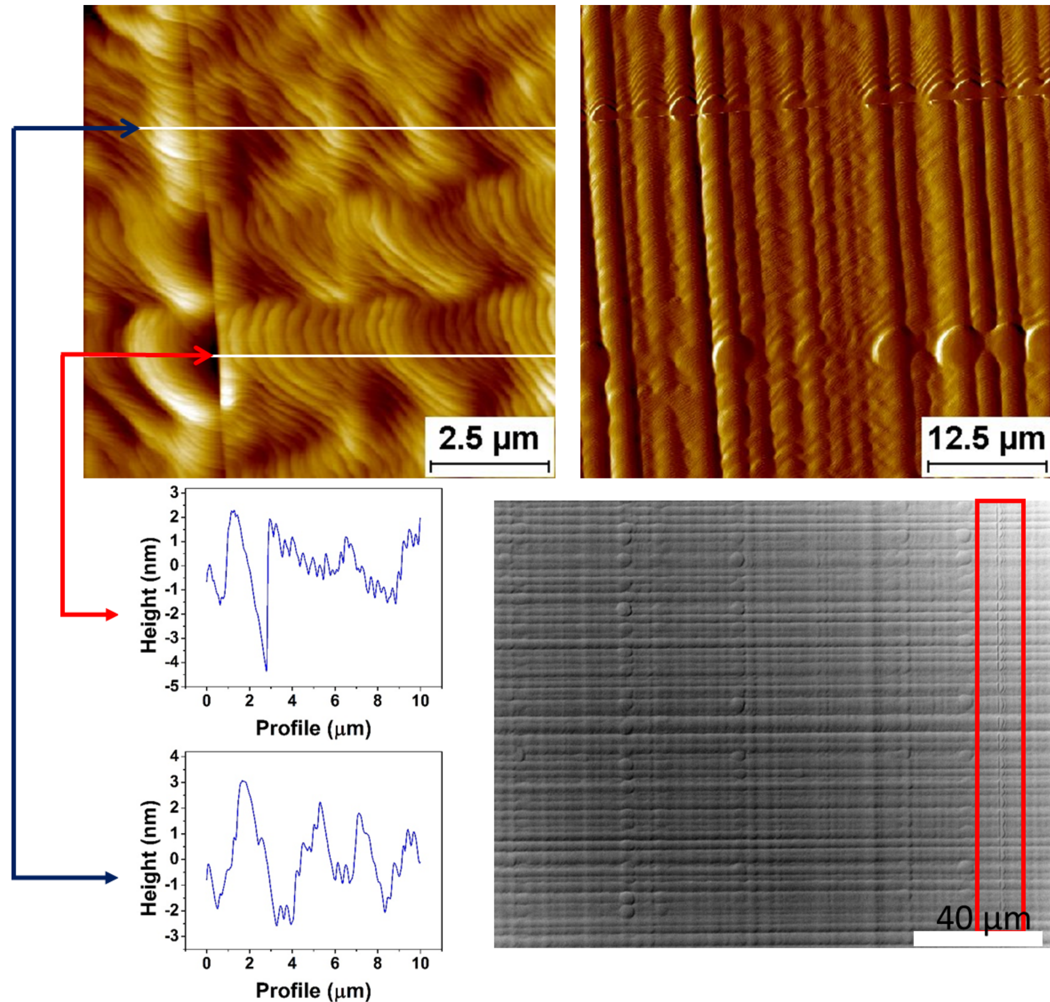

Figure 4.7: AFM (height, amplitude signal, and cross-sectional profile) and N-DIC images of $In_{0.12}GaAs$ SBL 300 nm thick grown on top of MBL.

Adding more Indium in the InGaAs SBL layer, 2% more, and keeping the thickness of 300 nm (sample Figure 4.6(d)) obtained a visibly improved morphology surface, where no defect lines were detected, although the RMS roughness turned out (mildly) higher than the MBL.

Based on those results from our SBL study, we opted for a test with the following composition of $In_{0.13}GaAs$ and 300 nm of thickness of SBL to grow the full subsequent AlInGaAs cladding layer. The results is shown in Figure 4.8. As observed in the case of direct deposition of AlInGaAs on the MBL, the SBL thickness increase results in an increase of the RMS roughness, significantly higher than the starting value (from ~4 nm to ~13.5 nm). In Figure 4.8(b),

we can evaluate from the cross-sectional profile of a larger sample area a peak to valley range exceeding 120 nm. In the following sections the RMS will be evaluated from $50\mu m \times 50\mu m$ area sample to minimize the error in the statistical analysis.

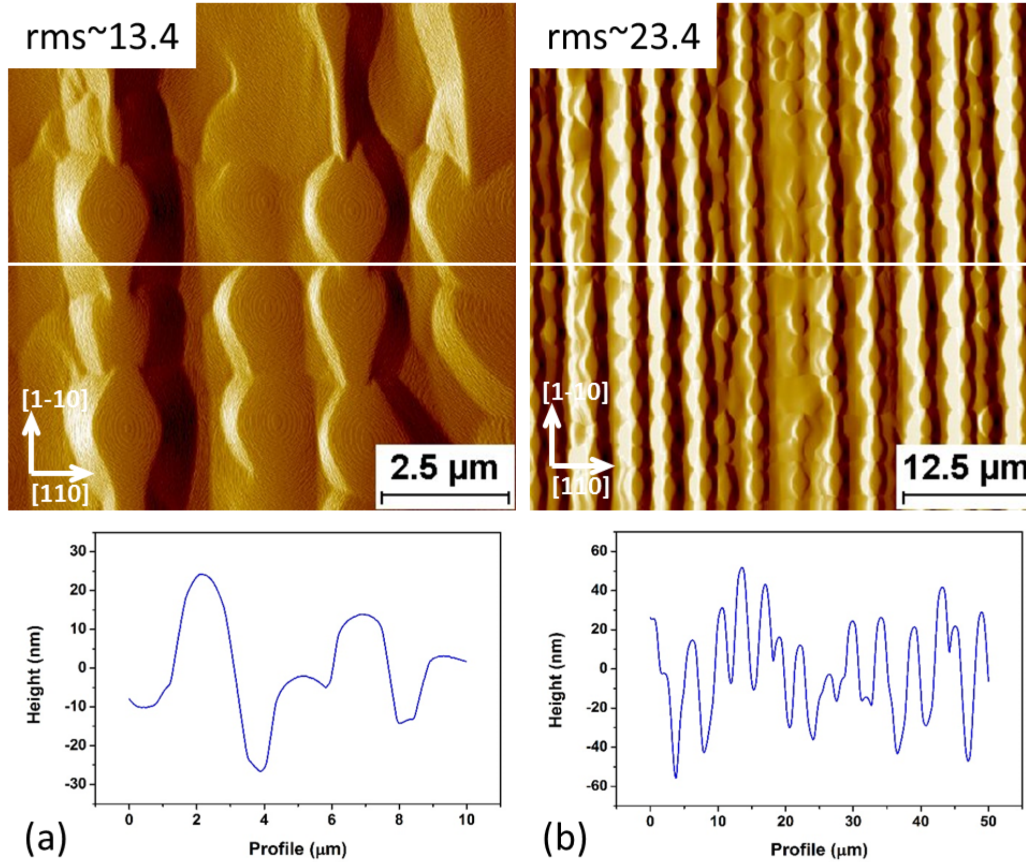

Figure 4.8: AFM images (amplitude signal and cross-sectional profile) of 1400 nm of AlInGaAs lattice matched to MBL with $In_{0.13}GaAs$ SBL 300 nm thick. (a) AFM scan size 10×10 μm^2 and (b) 50×50 μm^2.

The possible presence of potential threading dislocations and the persisting alloy roughness suggested the SBL strategy alone was not providing us with a solution to the high RMS values, and we decided to explore an alternative material alloy, i.e the ternary InGaP (which has also a similar index of refraction).

4.3 InGaP

The lattice matched condition, confirmed by HRXRD and matlab calculations, between the end of the buffer grading and the InGaP layer is reached

with $\sim In66\%$ and we could obtain good in plane lattice matching conditions (see for example table 4.1).

Table 4.1: Calibration, from HRXRD and matlab calculations, of the InGaP cladding deposited on three different substrate misorientation, 0.05°, 6° and 4° towards [111]A respectively.

Parameters	0.05°***A***	4°**A**	6°**A**
In%	0.6588	0.6569	0.6697
a_l(Å)	5.7260	5.7252	5.7306
ϵ_p	-8.1053×10^{-4}	-1.4916×10^{-4}	-3.6171×10^{-5}
ϵ_o	8.3118×10^{-4}	1.5288×10^{-4}	3.7196×10^{-5}
$a_{l-inplane}$ (Å)	5.7214	5.7244	5.7304

All InGaP samples were grown with the use of TMSb as a surfactant, not only for coherence with the analysis of the AlInGaAs alloy given in the previous section, but also because preceding experience with similar alloys (admittedly not systematic in nature) suggested that TMSb is able to smooth and improve the surface roughening.

4.3.1 InGaP on MBL

We observed in chapter 3 that, overall, at the end of MBL the RMS value, evaluated from an AFM image scan size of 50x50 μm^2, is $\sim 5nm$ for a [011] direction scan. After 300 nm of InGaP layer deposition, lattice matched to the MBL, the RMS value ([011] direction) grows substantially and results in 12.5, 11.8 and 7.03 nm for 0.05°A 4°A and 6°A substrate miscuts respectively (Fig.4.9).

The degradation of the surface is linked with the depth of the trenches that are present on the surface and, as it happened for the AlInGaAs layer, strictly proportional to the layer thickness. In chapter 3 we discussed the alternation of the peaks and valley on the surface, typical of the CH pattern of the MBLs. In that case the depth of the valley, was around 15 nm for the [011] direction and 5 nm for the [0$\bar{1}$1] direction for the slightly misoriented samples, and around 10 nm for both directions <011> in samples with the 4° and 6° miscut. The general qualitative trend is similar also for the InGaP alloy. In Figure 4.9 we observe in the AFM cross-sectional profiles some individual trenches deep ∼40 nm for the slightly and 4° misoriented samples, while less deep trenches ∼25 nm are observed for the 6°A sample.

The trench depths increase with the thickness of the InGaP layer; indeed when 1400 nm of InGaP are deposited directly on the metamorphic substrate

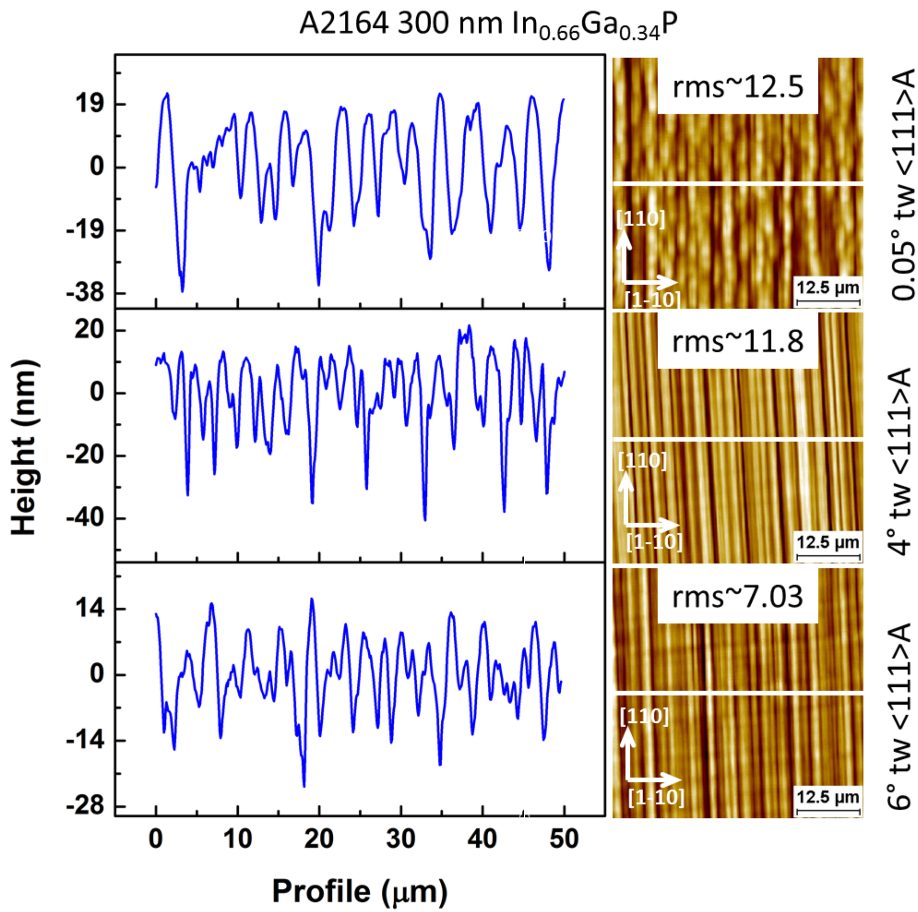

Figure 4.9: AFM images (height and cross-sectional profile) of $In_{0.66}Ga_{0.34}P$ 300 nm thick grown lattice matched on top of MBL. Comparison between samples grown on 0.05°A 4°A and 6°A substrate miscuts.

grooves appear with depth reaching more than 150 nm for the sample grown on 0.2° towards [111]A and the RMS value exceeds 30 nm (Figure 4.10).

As the misorientation of the substrate is increased, more pronounced degradation of the surface occurs (Table 4.2).

Table 4.2: RMS value for the A2168 4°A and 6°A samples, 1400 nm of InGaP LM to MBL.

misorientation	"good area" RMS value (nm)	"defected area" RMS value (nm)
0.2° **tw [111]A**	n/a	34.2
4° **tw [111]A**	16.5	41.9
6° **tw [111]A**	13.1	53.6

The 4°A and 6°A samples differ from the 0.2°A, although they are grown

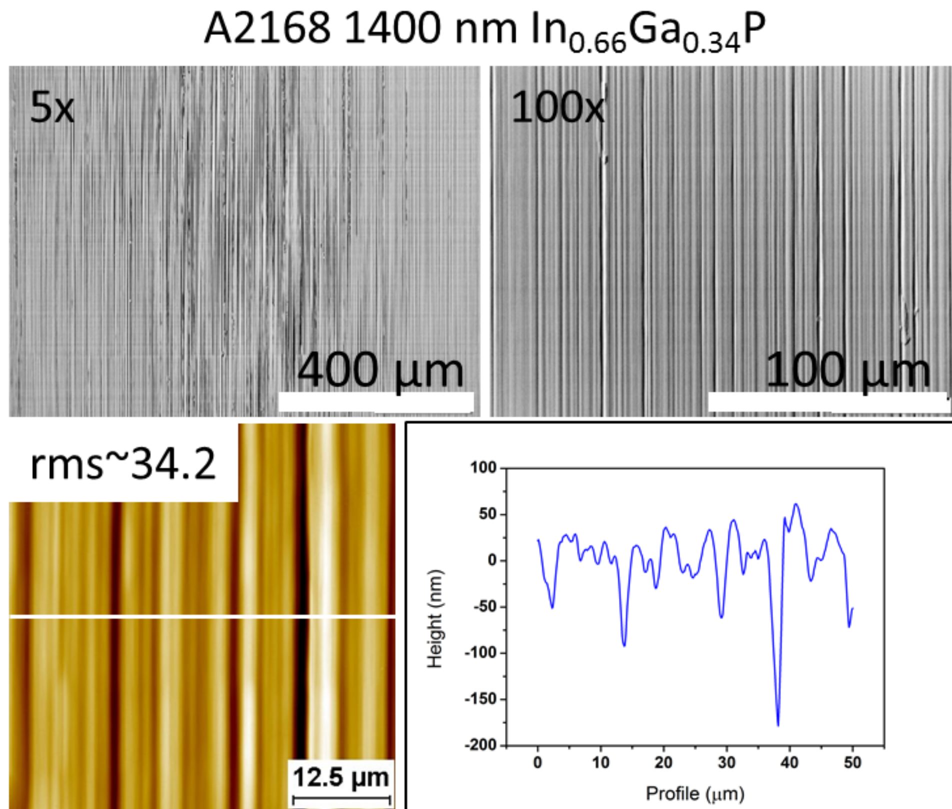

Figure 4.10: AFM (height and cross-sectional profile) and N-DIC images of 1400 nm $In_{0.66}Ga_{0.34}P$ in-plane lattice matched to MBL. Sample grown on 0.05°A substrate miscuts.

under the same conditions and in the same batch, because after the deposition of 1400 nm InGaP they present a non-homogeneous surface with an area more defected than the rest (the sample sizes were half wafer of 2" diameter). The effect is clearly visible when inspected with an optical microscope in (Nomarski) differential interference contrast (Figures 4.11). As regards the roughness we can observe a transition from 16.5 nm to 41.9 nm in the 4°A and from 13.1 nm to 53.6 nm for the 6°A sample. The groove depths exceed 160 nm in both 4°A and 6°A samples (parameters evaluated from AFM scan size ($50 \times 50\ \mu m^2$, images not shown).

To have a direct comparison with the AlInGaAs cladding study, a sample with the addition of the SBL was grown. Having shown, until here, how much the thickness of the layer is the greatest contributor to surface degradation, it was chosen to growth directly 1400 nm InGaP (lattice matched to the substrate) onto the $In_{0.13}GaAs$ SBL (300 nm thick). The sample observed with the optical microscope in N-DIC moode showed (Figure 4.12) a completely defected surface, and when scanned with AFM revealed the RMS value over

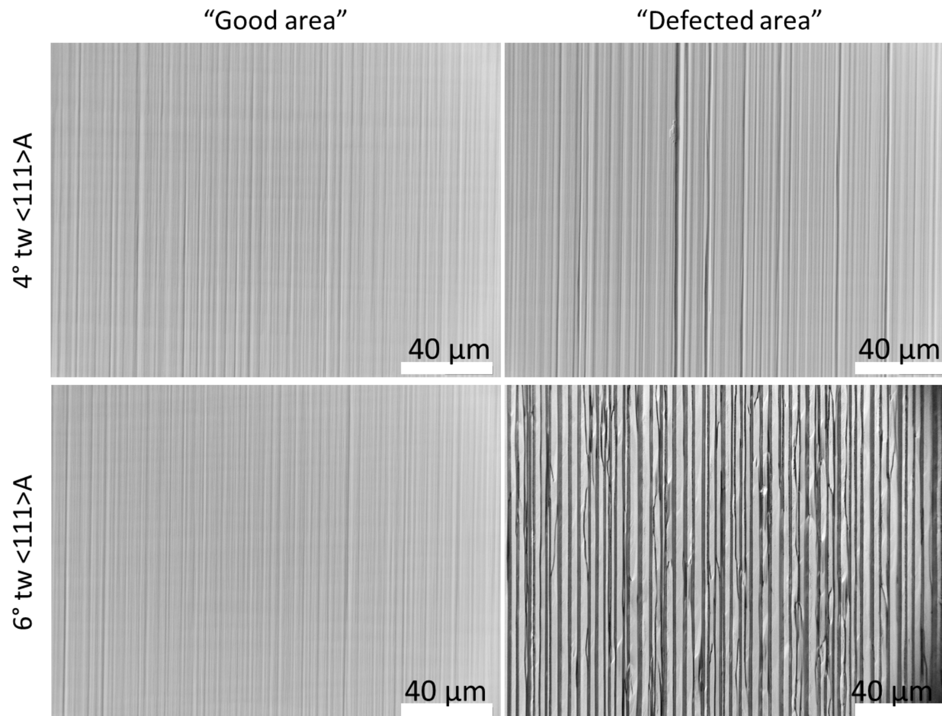

Figure 4.11: N-DIC images of 1400 nm $In_{0.66}Ga_{0.34}P$ in-plane lattice matched to MBL grown on 4°A and 6°A substrate miscuts. Comparison between two areas detected in the samples surface; (a) "Good area" and (b) "Defected area".

65 nm reaching a peak to valley excursion more than 300 nm (AFM images not shown here.)

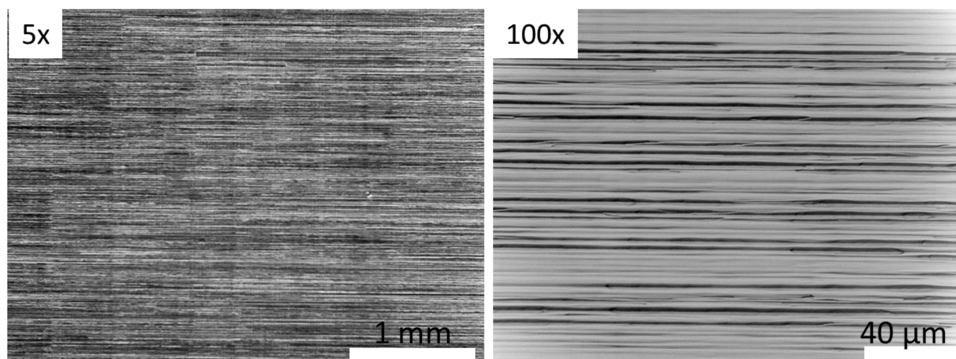

Figure 4.12: N-DIC (two magnification scans) images of 1400 nm $In_{0.66}Ga_{0.34}P$ in-plane lattice matched to MBL with the intermediate $In_{0.13}GaAs$ SBL 300 nm thick. Sample grown on 0.2°A substrate miscuts.

Obviously the tensile strained InGaAs layer (SBL) inserted between the MBL and the cladding was not improving the surface roughness, probably not balancing the MBL residual strain, neither for the AlInGaAs nor the InGaP cladding. Nevertheless moving the tensile strain directly into the InGaP layer

itself seems to slow down a bit the process of deep grooves formation achieving a smoother surface and a reduced RMS value. In Figure 4.13 is shown the diffraction profiles of samples grown with $In_{0.66}GaP$ lattice matched onto the MBL and $In_{0.62}GaP$ tensile strained.

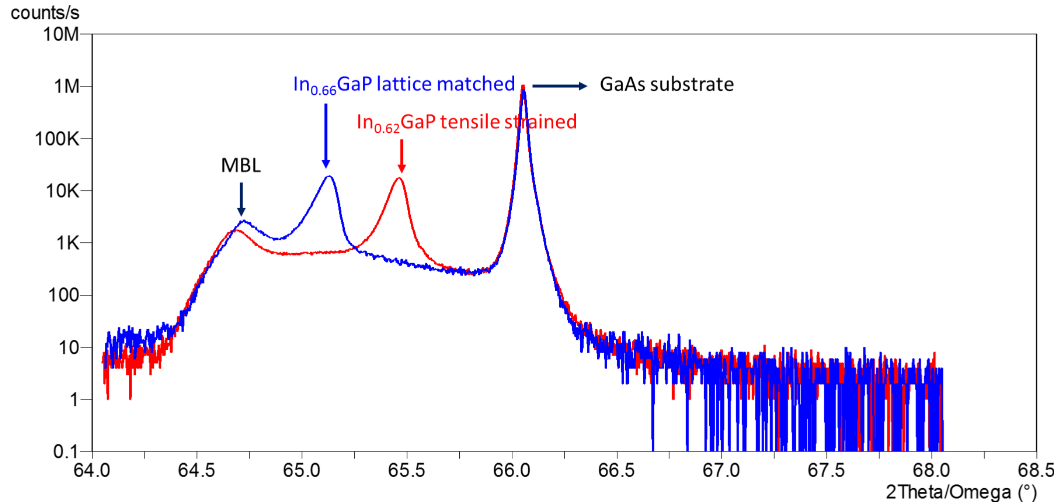

Figure 4.13: Rocking curve (004 reflection) of 1400 nm $In_{0.66}GaP$ lattice matched onto MBL and $In_{0.62}GaP$ tensile strained. GaAs (100) 0.2° towards [111]A was used as a substrate.

In Figure 4.14 are presented AFM images of samples grown with 100 nm, 250 nm and 300 nm thickness of $In_{0.62}Ga_{0.38}P$ tensile layer onto the MBL, using a 0.2°A GaAs substrate. There is an increment in the RMS value of approximately one nm per 100 nm of material deposited, with an RMS value of $\sim$ 6 nm for the sample with 300 nm of InGaP. The profile nevertheless starts to present significantly differences at a 300 nm growth thickness where the excursion peak to valley reaches $\sim$30 nm. Anyway the RMS value obtained for 300 nm of InGaP tensile strained is half the one obtained with the deposition of InGaP lattice matched (see Figure 4.9 for comparison, where the RMS value is 12.5 nm for the slightly misoriented sample and the range peak to valley is $\sim$ 60 nm).

Similar behaviour is observed for the sample grown on 6°A substrate: no dramatic changes until 300 nm of InGaP tensile strained is deposited on the surface (Figure 4.15).

Nevertheless even if the slightly tensile layer smooths the surface, we can identify 300 nm as limiting thickness beyond which the surface features start to increase. The evolution of the RMS value as a function of the $In_{0.62}Ga_{0.34}P$ thickness is summarized in the table 4.3. When $In_{0.62}Ga_{0.34}P$ reaches 500 nm the RMS almost doubles for the 0.2°A cutoff sample and triples for 6°A cutoff

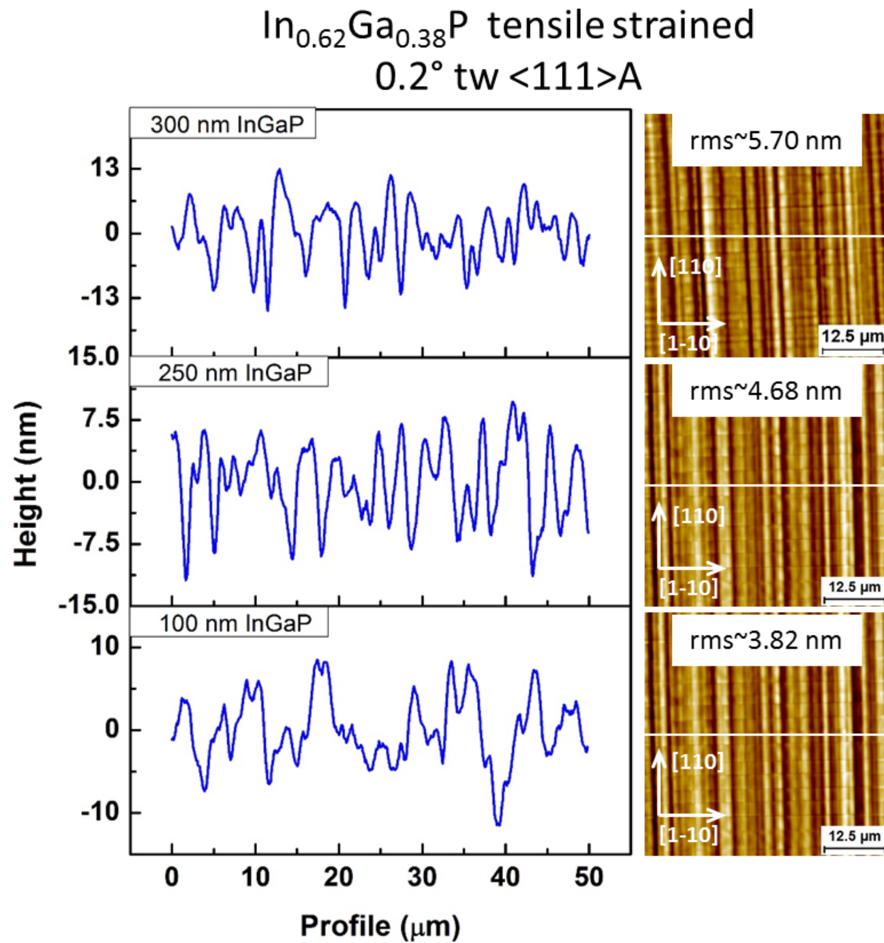

Figure 4.14: AFM images (heigh and cross-sectional profile) of $In_{0.62}Ga_{0.34}P$ tensile cladding layer with 100 nm, 250 nm and 300 nm thickness deposited directly onto MBL. The three samples are grown on 0.2°A GaAs substrate miscut.

sample, comparing with 100 nm of deposition. Concerning samples grown on a 4°A substrate miscut we can't supply the comparison values for the 100 nm, 250 nm and 300 nm.

Table 4.3: The evolution of the RMS value (evaluated from AFM images of 50×50 μm^2 scan size) as a function of the $In_{0.62}Ga_{0.34}P$ thickness.

Thickness (nm)	0.2° **tw [111]A RMS value (nm)**	4° **tw [111]A RMS value (nm)**	6° **tw [111]A RMS value (nm)**
100	3.82	n/a	4.92
250	4.68	n/a	4.65
300	5.7	n/a	5.62
500	6.4	9.24	12.1
1400	33.2	40.6	32.4

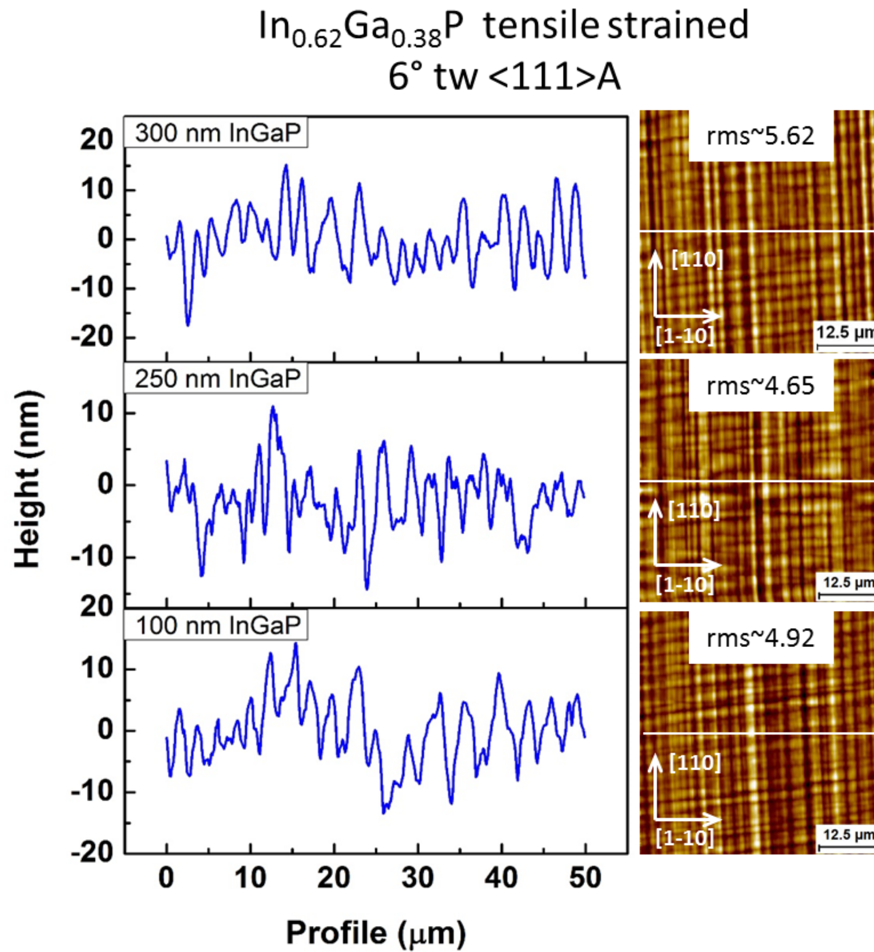

Figure 4.15: AFM images (heigh and cross-sectional profile) of $In_{0.62}Ga_{0.34}P$ tensile cladding layer with 100 nm, 250 nm and 300 nm thickness deposited directly onto MBL. The three samples are grown on 6°A GaAs substrate miscut.

The fact remains that after 300 nm of InGaP deposition the roughness starts to degrade in an irreversible manner. Indeed at 1400 nm, the roughness reaches high level of RMS value around 30-40 nm (Figure 4.16), with a strong presence of defects-like grooves.

Before continuing with the strategy for RMS containment, it is worth pausing a while and discussing the role of surface orientation when AFM scans are taken. Till now we showed AFM scans along the $[0\bar{1}1]$ plane direction, as representative of the surface roughness. Nevertheless some caution is necessary ([7]). Indeed AFM 2D images, are only a collection of line scans reassembled together by the AFM software, which averages out the lines' alignment with appropriate algorithms. In that sense, they cannot deliver the true surface average, but only line scan averages. In the literature this is rarely addressed,

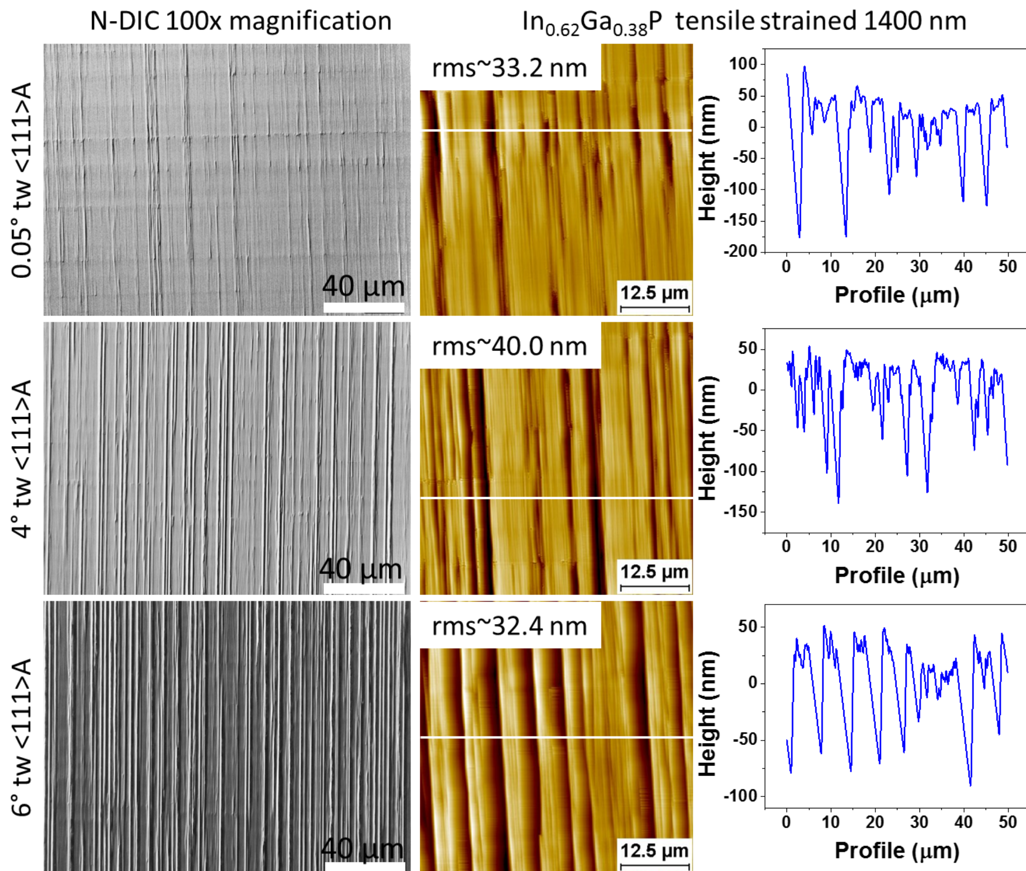

Figure 4.16: N-DIC images on the left side, and AFM (signal amplitude and cross-sectional profile) on the centre and right side, of 1400 nm $In_{0.62}Ga_{0.34}P$ tensile layer deposited directly onto MBL. The comparison in terms of surface topography and RMS is done between samples grown on 0.2°A, 4°A and 6°A misoriented GaAs substrates.

and often ignored. Nevertheless if proper RMS comparisons are due, it is vital to measure AFM scans along both the $[0\bar{1}1]$ and [011] directions, to understand the full surface behaviour.

In the following section we show how different surface roughness can be measured, and that not only $[0\bar{1}1]$ and [011] scans present different apparent roughnesses, but also that there is no dominating direction (i.e. one with stronger RMS than the other) and that the two surface directions can exchange roles when RMS values are considered, showing and observing a change (inversion) of rough surface organization in terms of roughness (RMS value) and morphology.

4.4 Roughness "inversion" study

The cross hatch pattern typical for graded epitaxial structures, like our MBL, which brings anisotropic characteristic in the two <110> directions was introduced in the second chapter (3). In the MBL case we observed, according to the literature, a lower RMS value for the $[1\bar{1}0]$ direction compared to the [110]. Here we are presenting a divergent behaviour depending on the alloy deposited onto the MBL.

We anticipate that with the AlInGaAs is preserved the anisotropy in the topography inherited from the MBL substrate and miscuts chosen, whereas with the InGaP we observed a change and inversion in terms of roughness (RMS value) and morphology. It should also be said that the data here presented are to be interpreted as indicative only, as no broad statistics (e.g. tens of surface scans) was taken, in view of the effort required. Nevertheless we consider these observations useful , and report them here.

InGaP

This anisotropy between the two surface direction roughness changes, inverts (disappears) when the InGaP layer is deposited on top of the MBL. In table 4.4 we can observe the behaviour for the InGaP layer 100 nm, 250 nm and 300 nm thick.

Table 4.4: RMS overall values of the InGaP layer directly deposited on the MBL evaluated from AFM images of 50x50 μm^2 scan size. For the ease of the reader the highest RMS value between the two plan directions is indicated in bold.

No sample	0.2° **tw [111]A RMS (nm)**		6° **tw [111]A RMS (nm)**	
	[011]	$[0\bar{1}1]$	[011]	$[0\bar{1}1]$
(A2561) 100 nm InGaP	**4.94**	3.82	4.66	**4.92**
(A2562) 250 nm InGaP	4.15	**4.68**	**6.06**	4.65
(A2677) 300 nm InGaP	6.39	**6.83**	4.65	**6.00**

Observing the data collected from these samples, it seems that by increasing the thickness of the InGaP layer the possibility to have a lower RMS for the [011] instead of the $[0\bar{1}1]$ is increasing as well. In particular for the 250 nm InGaP sample for the 0.2°A substrate the RMS values for the two <011> directions are very close, 4.15 nm for the [011] direction and slightly higher, 4.68 nm, for the $[0\bar{1}1]$. Instead the sample with same 250 nm InGaP thickness

grown on 6°A doesn't seem to divert from the usual anisotropy. The inversion is appreciable when 300nm InGaP are deposited on MBL, referring to the 6°A sample. In this case the roughness stated by RMS value is 1.5 nm higher for the [0$\bar{1}$1] direction. The same happens for the sample grown on the 0.2°A but in a less evident manner.

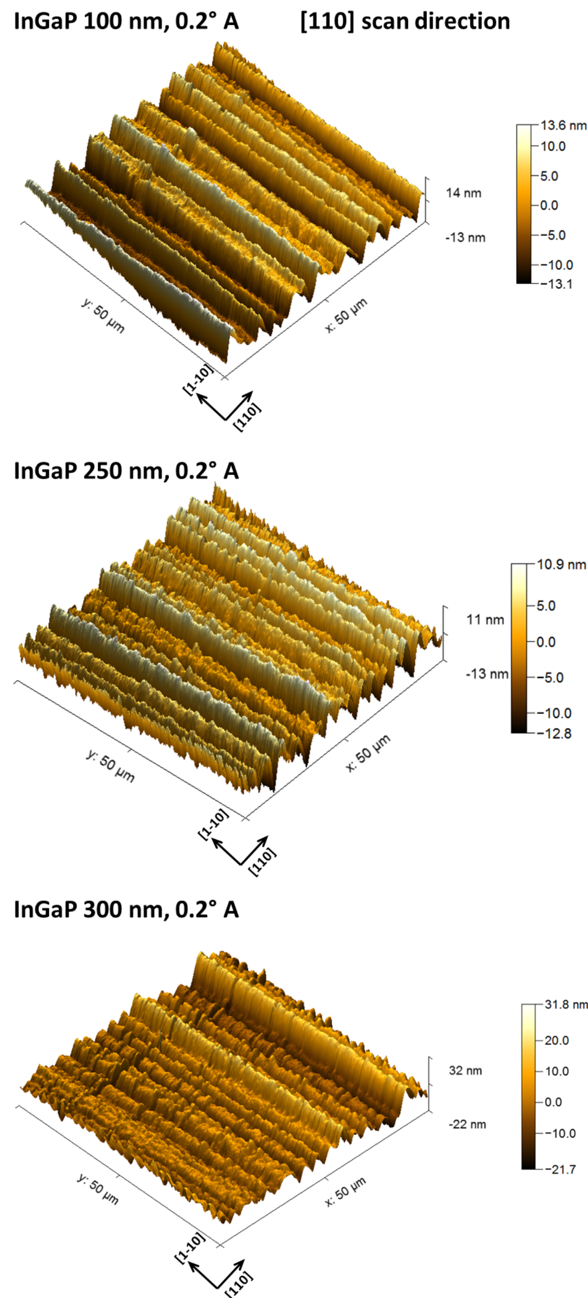

Figure 4.17: AFM images (3D-height reconstruction), along [110] direction, of 100 nm, 250 nm and 300 nm of $In_{0.62}GaP$ tensile strained deposited on MBL. Substrate misorientation of 0.2° towards [111]A.

In Figures 4.17, 4.18, 4.19 and 4.20 an overview of 3D-height reconstruction

along [110] and [$1\bar{1}0$] directions, of 100 nm, 250 nm and 300 nm of $In_{0.62}GaP$ tensile strained deposited on MBL are presented, substrate misorientation of 0.2° and 6° towards [111]A respectively.

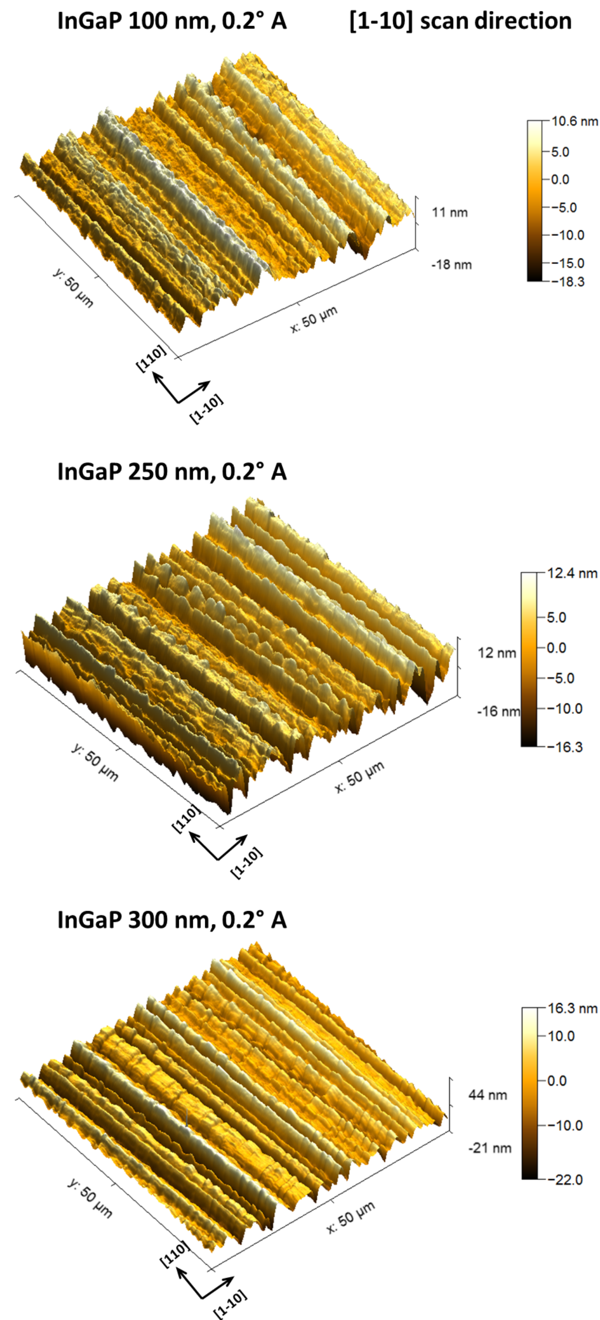

Figure 4.18: AFM images (3D-height reconstruction), along [$1\bar{1}0$] direction, of 100 nm, 250 nm and 300 nm of $In_{0.62}GaP$ tensile strained deposited on MBL. Substrate misorientation of 0.2° towards [111]A.

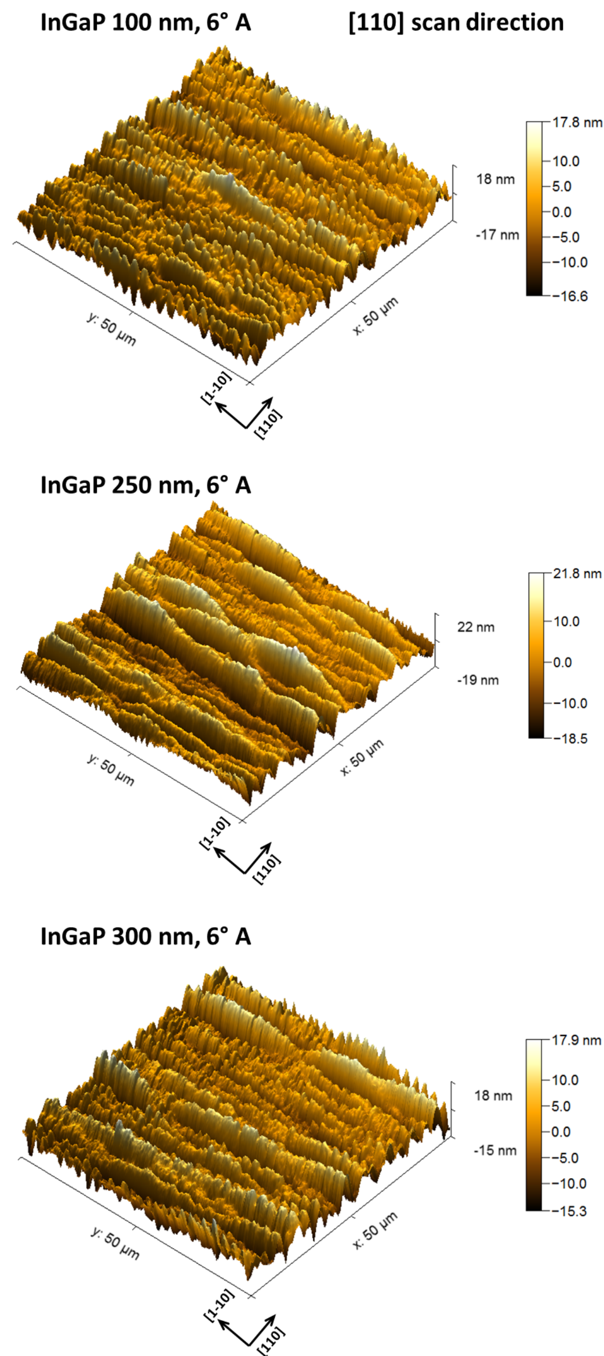

Figure 4.19: AFM images (3D-height reconstruction), along [110] direction, of 100 nm, 250 nm and 300 nm of $In_{0.62}GaP$ tensile strained deposited on MBL. Substrate misorientation of 6° towards [111]A.

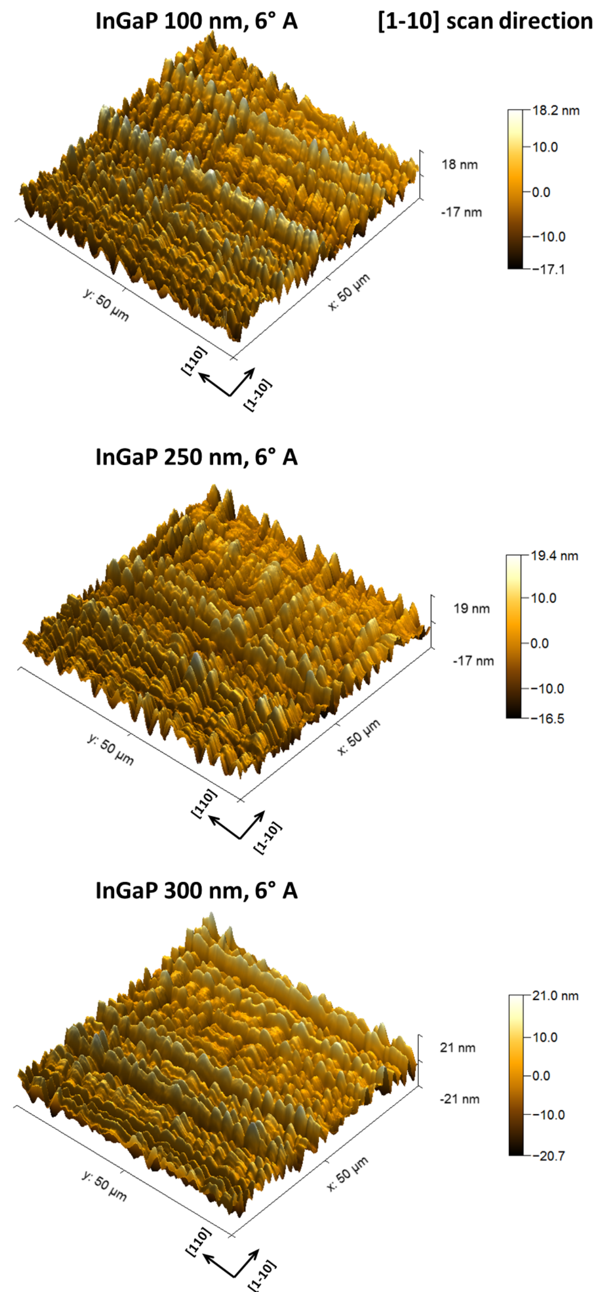

Figure 4.20: AFM images (3D-height reconstruction), along $[1\bar{1}0]$ direction, of 100 nm, 250 nm and 300 nm of $In_{0.62}GaP$ tensile strained deposited on MBL. Substrate misorientation of 6° towards [111]A.

AlInGaAs

To give an example (Figure 4.21), in a sample grown with 250 nm of $Al_{0.30}In_{0.15}GaAs$ onto a MBL (substrate 0.2° A) it is still clear that the morphology has dissimilar formatting in the two perpendicular <110> directions, as already observed for the metamorphic grading substrate (see chapter 3): the RMS roughness is lower for the $[1\bar{1}0]$ than the [110] direction showing a value of 4.5 nm and 6.5 nm respectively in this sample.

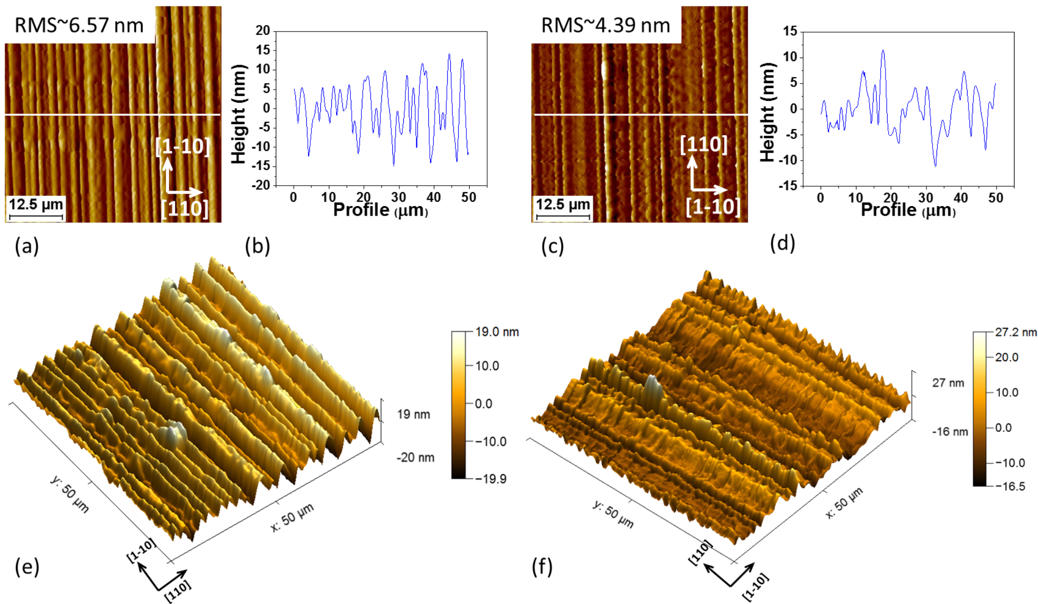

Figure 4.21: AFM images (signal amplitude, cross-sectional profile and 3D-height reconstruction), along [110] and $[1\bar{1}0]$ directions, of 250 nm $Al_{0.30}In_{0.15}GaAs$ in-plane lattice matched to MBL. Substrate misorientation of 0.2° towards [111]A.

From the highlighted line scan in the cross sectional profiles (Figure 4.21 (b) and (d)) it is possible to extract the peak to valley range, which is 38.90 nm for [110] and 43.68 nm for the $[1\bar{1}0]$. These values result pretty close and the main difference comes from the frequency and periodicity of this alternation peak-to-valley.

The same behaviour is found for the sample grown on 6°A substrates, with the $[1\bar{1}0]$ direction characterized by lower RMS value than [110] direction. In the sample shown in Figure 4.22 the RMS is $\sim 7nm$ for the [110] direction and $\sim 6nm$ for the $[1\bar{1}0]$, in addition as before the peak to valley range is $\sim 45nm$ for both direction and again the periodicity of the peaks is greater for the [110].

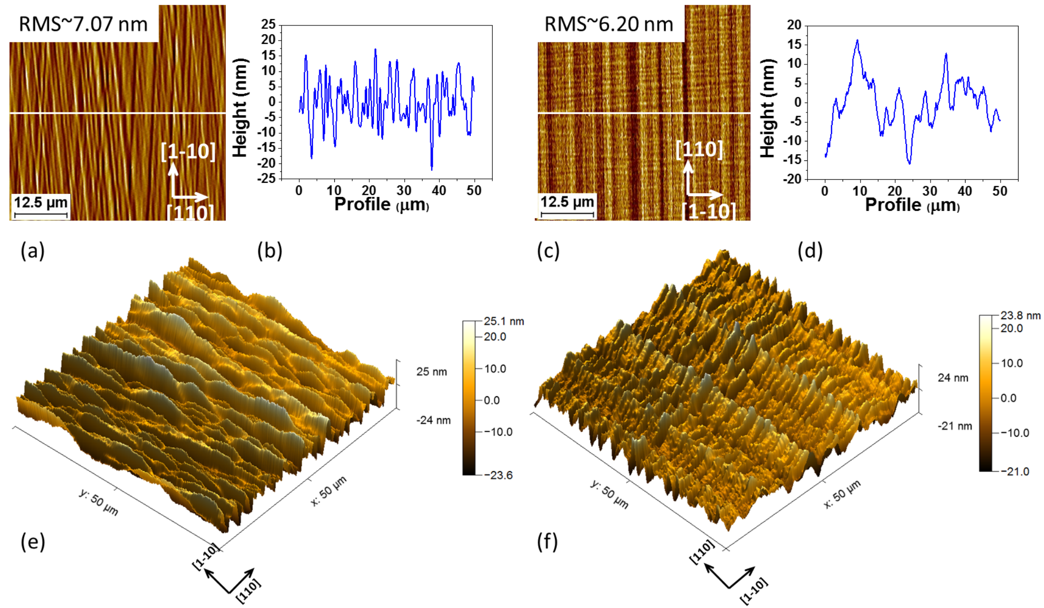

Figure 4.22: AFM images (signal amplitude, cross-sectional profile and 3D-height reconstruction), along [110] and [$1\bar{1}0$] directions, of 250 nm $Al_{0.30}In_{0.15}GaAs$ in-plane lattice matched to MBL. Substrate misorientation of 6° towards [111]A.

4.5 Superlattice approach

In view of all results reported in this chapter we decided to exploit a new strategy, combining together both of the alloys AlInGaAs and InGaP in only one cladding. To make more clear the next step in the cladding study, in table 4.5 are summarized the results for each approach presented until now in term of alloy chosen, thickness and RMS value.

Table 4.5: Summary table of the cladding study in terms of alloy choice, layer thickness and substrate misorientation.

Structure	Thickness (nm)	Offcut	RMS value (nm)
AlInGaAs:Sb(LM)	1050	p.o.	18.8
SBL+AlInGaAs:Sb(LM)	1400	p.o.	23.4
InGaP:Sb(LM)	1400	0.2°A	34.2
		4°A	41.9
		6°A	53.6
SBL+InGaP:Sb	1400	0.2°A	>65
InGaP:Sb strained	1400	0.2°A	33.2
		4°A	40.6
		6°A	32.4

Observing the values in the table, as already pointed out on numerous

occasions in this chapter, the increase of the thickness layer entails also the increase of the roughness. Although the AlInGaAs cladding might seem the most promising choice, presenting the RMS value of ∼ 19 nm for a layer thick 1050 nm, it should be recalled that the full laser structure grown employing AlInGaAs as cladding revealed a total RMS value of 26 nm with evident defect lines on the surface. That final morphology and surface organization prevented us from getting an emitting laser. On the other hand for thicknesses lower than 300 nm both AlInGaAs and the InGaP alloys exhibited RMS value of the same order of magnitude or close enough as those shown by the MBL. Also we observed that the different alloys seem to develop different roughness evolution along the in-plane directions. Hence the choice to try to combine the two alloy in the lower cladding barrier, alternating them and keeping the thickness for each interface below 300 nm. For simplicity this combined cladding structure will be called superlattice (SL).

Some of the preliminary results in terms of roughness from different order layer deposition and thicknesses are summarised in table 4.6.

Table 4.6: RMS overall values of the SL structure AlInGaAs/InGaP evaluated from AFM images of $(50x50)\mu m^2$ scan size. The comparison is done between structure grown with $In_{0.66}GaP$ in-plane LM layer and $In_{0.62}GaP$ TS both deposited on MBL. The samples are grown on 0.2°A substrates.

SL Structure Thickness(nm)	$In_{0.66}GaP$ **LM RMS (nm)**		$In_{0.62}GaP$ **TS RMS (nm)**	
	[011]	[0$\bar{1}$1]	[011]	[0$\bar{1}$1]
IGP 50 + (AIGA 250 + IGP 50)×5	15.50	na	10.9	13.9
(AIGA 250 + IGP 50)×5	9.89	16	8.69	6.15
(AIGA 275 + IGP 75)×4	7.53	9.22	na	na

The samples have been grown by three different strategies employing AlInGaAs in-plane lattice matched and InGaP both lattice matched and tensile strained.

Here we present data on a small misoriented MBLs, as the study review was obtained there. Similar results were also obtained on other misorientations.

The choice to alternate the AlInGaAs and InGaP layers in the lower cladding structure is revealed to be immediately promising. Indeed with every strategy evaluated, for the total thickness >1400 nm, the RMS value is kept around 15 nm. The best results are obtained from the samples grown employing $In_{0.62}GaP$ tensile strained, where we recorded ∼8.5 nm for the [011] direction

and ~6 nm for the [0$\bar{1}$1]. The worst result came from the structure with InGaP deposited directly on the MBL and before the AlInGaAs layer. For the sample grown with 275 nm of AlInGaAs and 75 nm of InGaP there is not the comparison between the InGaP LM and TS, nevertheless we are presenting the RMS results to confirm and highlight the changing in the anisotropy of the two <011> directions, as somehow already discussed in the previous section.

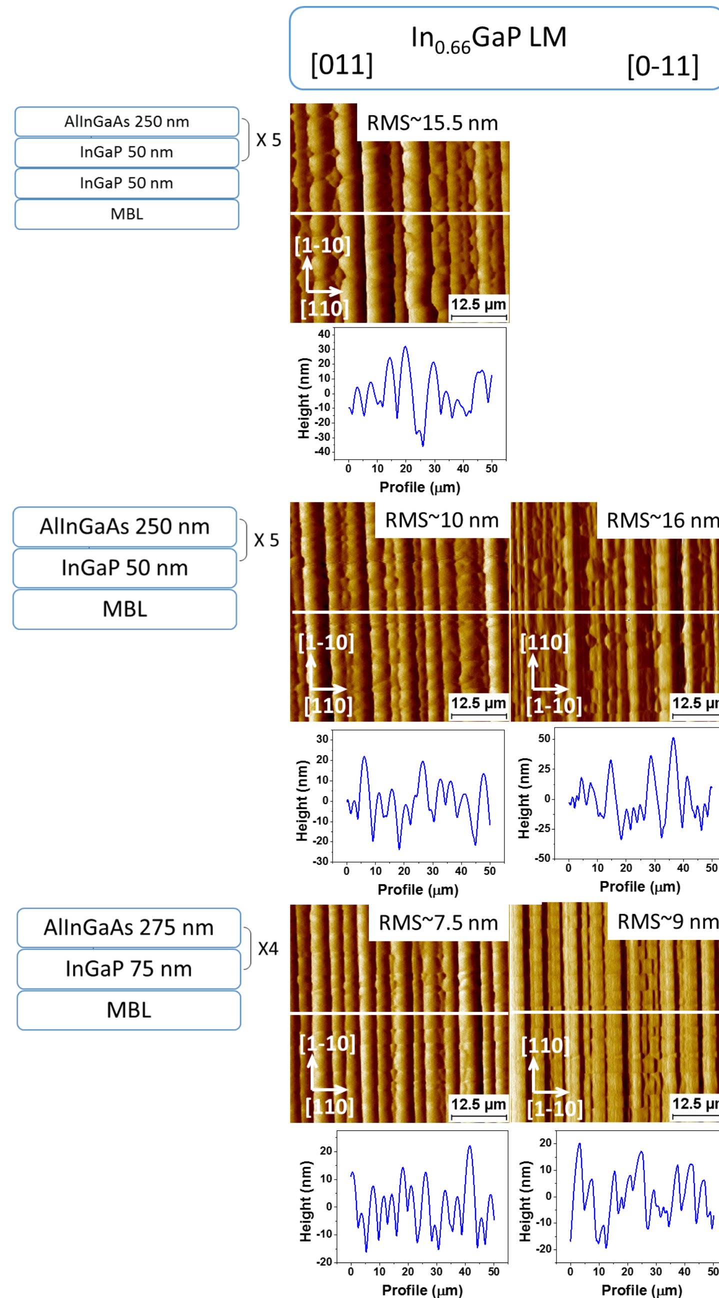

Figure 4.23: AFM images (signal amplitude, cross-sectional profile), along [110] and [1$\bar{1}$0] directions, of SL structures . Substrate misorientation of 0.2° towards [111]A.

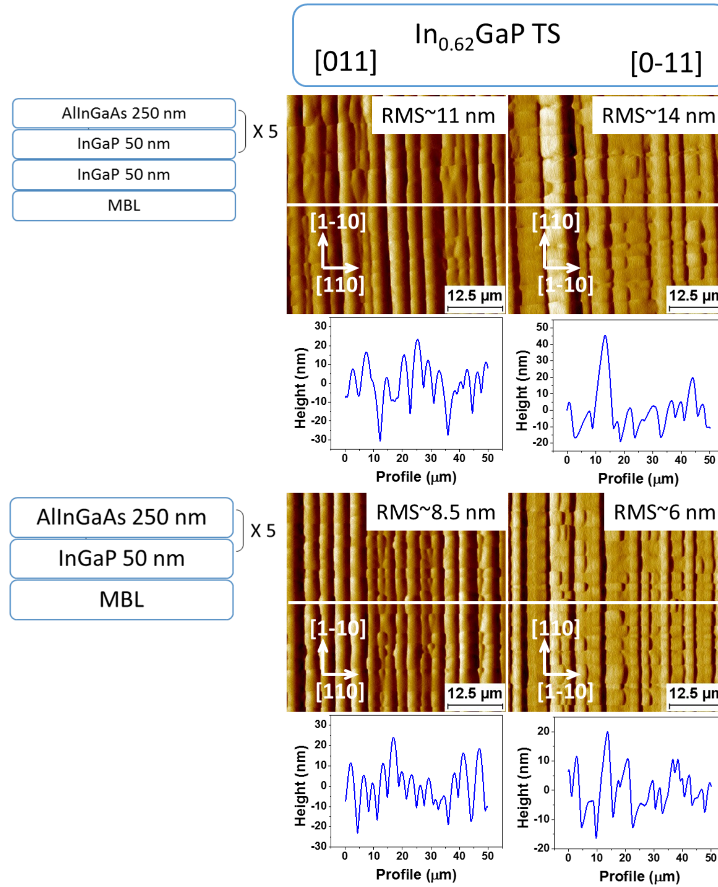

Figure 4.24: AFM images (signal amplitude, cross-sectional profile), along [110] and [$1\bar{1}0$] directions, of SL structures . Substrate misorientation of 0.2° towards [111]A.

In Figure 4.23 and in Figure 4.24 are presented the AFM images overview of all those combined SL structures grown with $In_{0.66}GaP$ LM and $In_{0.62}GaP$ TS, respectively.

We decided to use the structure with 250 nm of AlInGaAs LM and 50 nm of $In_{0.62}GaP$ tensile strained for a lower cladding total thickness of 1500 nm.

With this combination we obtained very good results also on samples grown on 6°A misoriented substrates (Figure 4.25) and we anticipate that this idea to space out two alloys in the cladding barrier will be successful for the laser operation.

In this way we can keep under control the increase of the ridge depth maintaining the peak to valley range around 40 nm and avoiding the main problem ascertained in the cladding evolution: i.e increase of the thickness equals increase of the roughness. In Figure 4.26 are reported the cross sectional profile of the all cladding structure studied and they are compared to the surface profile of the SL structure.

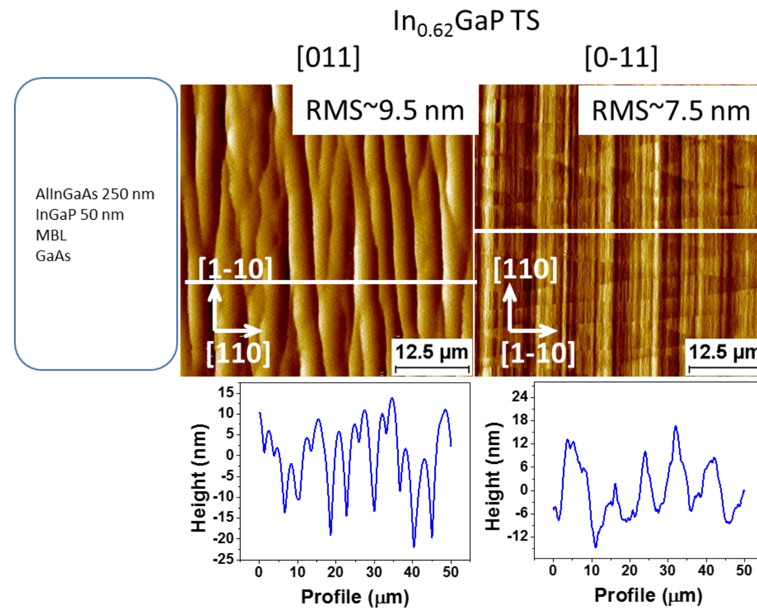

Figure 4.25: AFM images (signal amplitude, cross-sectional profile), along [110] and [1$\bar{1}$0] directions, of SL structure composed by (250 nm AlInGaAs LM + 50 nm InGaP TS)×5 . Substrate misorientation of 6° towards <111>A.

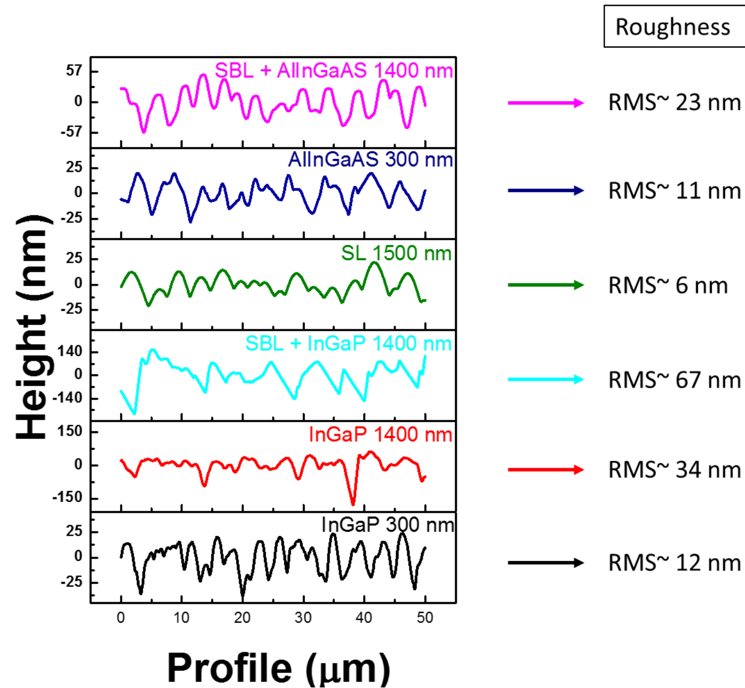

Figure 4.26: Comparison between all cladding structures studied until now and the combined superlattice structure in terms of RMS value and AFM cross-sectional profiles. All samples presented here are grown on perfectly oriented GaAs substrate or misoriented of 0.2° towards [111]A.

The same SL structure was applied in the upper cladding of the laser structure once implemented. Leaving out some aspects related to the growth temperature that will be discussed in the following chapter, we will focus only on the morphological analysis of the roughness in terms of RMS value and on the important observation that not only the increase in thickness contributes to the degradation of the surface but also the order of the layer deposition. In figures 4.27 and 4.28 are clearly visible defects lines that take shape on the surface after 600 nm of SL deposition. This might not be an unexpected result because, as already underlined, the deterioration of the surface is linked to the increase of the layer thickness. In this case 250 nm of $Al_{0.30}In_{0.15}Ga_{0.55}As$ is deposited onto 100 nm of $Al_{0.12}In_{0.15}Ga_{0.73}As$ (last layer of the SCH barrier) both lattice matched. On the sample grown on the 0.2°A substrate the threading dislocation appeared as a stripe elongated towards the $[0\bar{1}0]$ plane direction exceeding 100 nm in height, and fractures on the other plane direction. The RMS values associated (evaluated from AFM scan size 50x50 μm^2) are $\sim$ 36 nm and $\sim$ 15 nm for the [011] and $[0\bar{1}0]$ directions respectively.

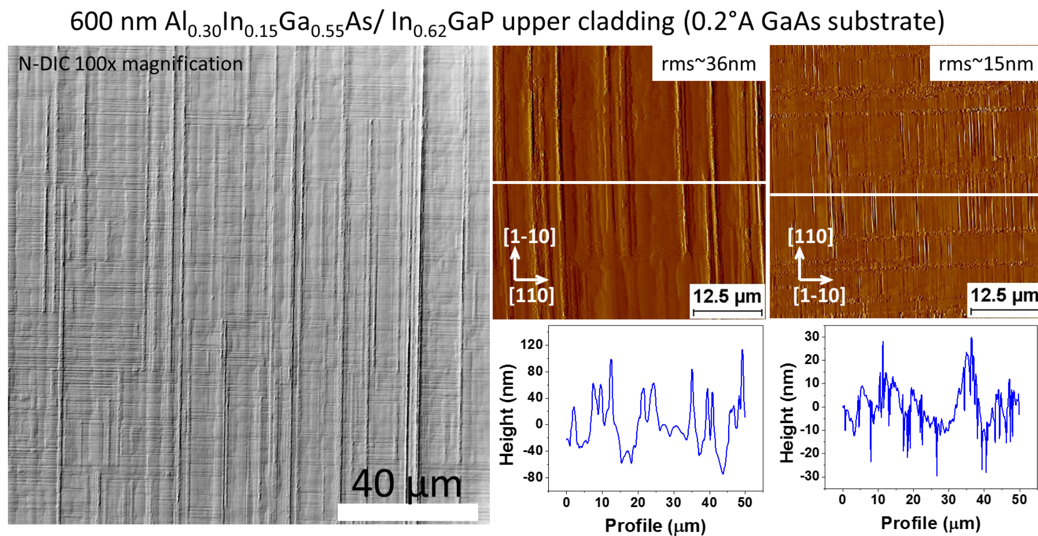

Figure 4.27: N-DIC and AFM (signal amplitude and cross-sectional profile) images of SL structure 600 nm thick, grown with the following order deposition layer: $Al_{0.30}In_{0.15}Ga_{0.55}As/In_{0.62}GaP$. GaAs misoriented substrate 0.2° towards [111]A.

However, the fractures are present on the sample grown on 6°A, detected long the $[0\bar{1}0]$ direction.

The simple switch of the growth order between InGaP and AlInGaAs in the layer deposition of the upper cladding brings back a surface free from threading dislocations (Figure 4.29). The topography of the samples grown onto GaAs 6°A seem to have the usual superficial organization, whereas as far as concerns

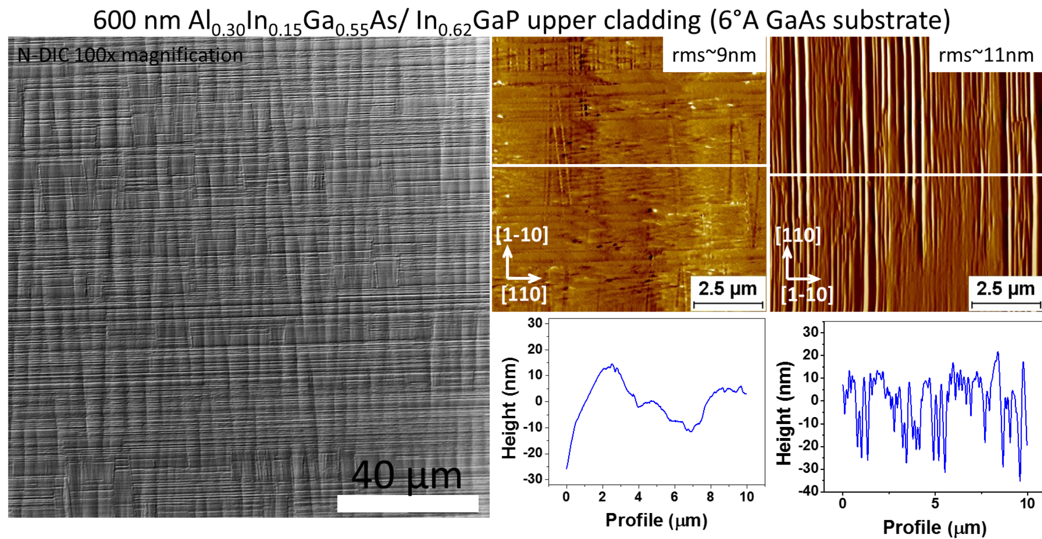

Figure 4.28: N-DIC and AFM (signal amplitude and cross-sectional profile) images of SL structure 600 nm thick, grown with the following order deposition layer: $Al_{0.30}In_{0.15}Ga_{0.55}As/In_{0.62}GaP$. GaAs misoriented substrate 6° towards [111]A.

the sample grown onto GaAs 0.2°A the topography appears different, with the presence of emphasised islands, although the peak to valley range is the same. We can observe also the roughness degraded for the 0.2A with an RMS value of $\sim$ 15 nm for the two <011> directions. To be noticed, always concerning the 0.2°A, that it is impossible, morphologically speaking, to discern the plane direction.

This cladding structure will be used for manufacturing the first lasers to test, while both lower and upper cladding, will be modified in subsequent structures, adding some graded layers, but keeping the SL structure. We will discuss about the modified cladding structure in chapter 6, as it is related to the electro-optical characterization of the device.

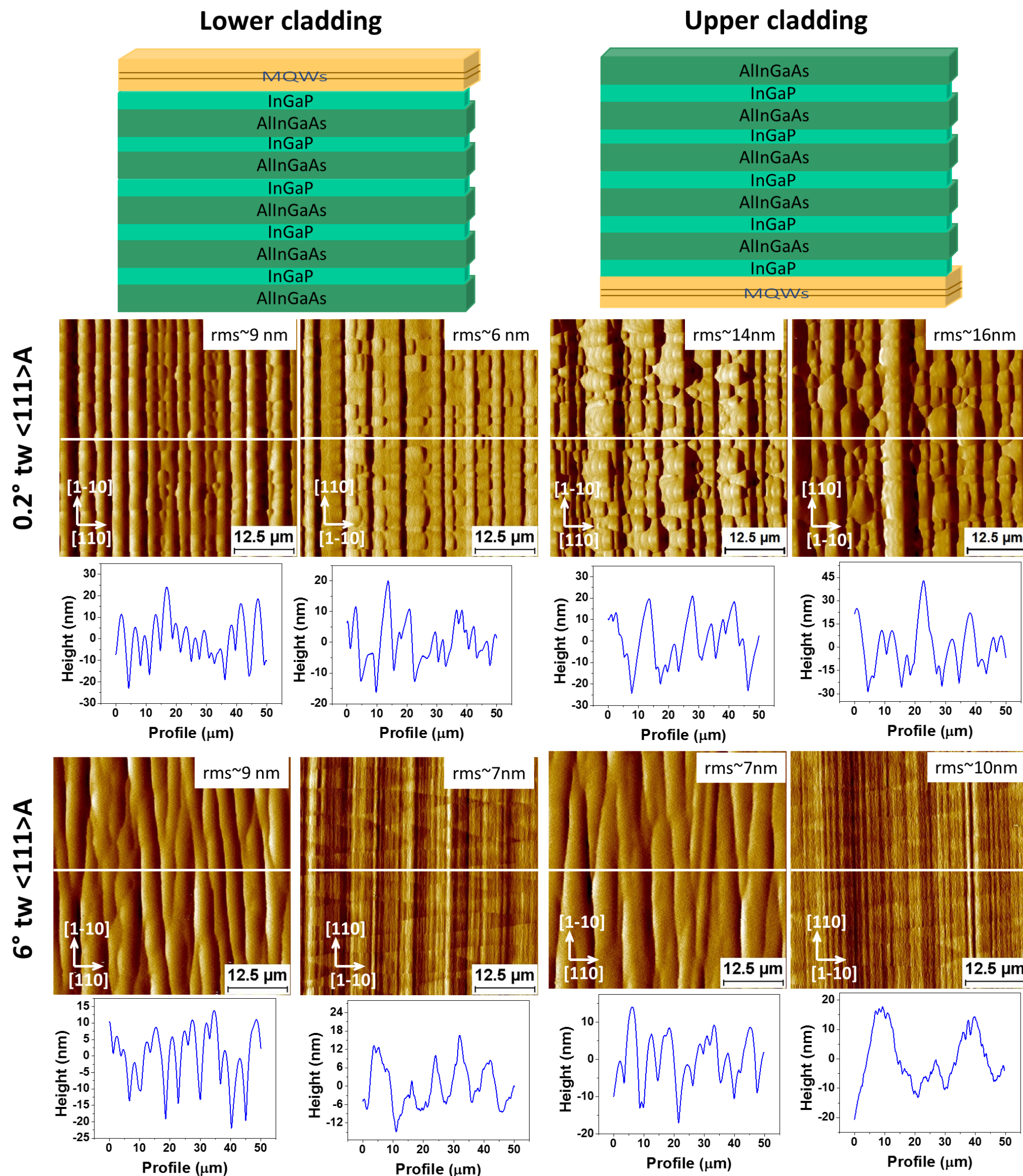

Figure 4.29: Morphology comparison in term of RMS values and surface organisation between lower and upper cladding SL deposition. For both lower and upper SL cladding are shown the structure scheme and related AFM images (amplitude signal and cross-section profile) along [110] and [$1\bar{1}0$] directions. Both lower and upper cladding are composed by AlInGaAs and InGaP in the SL structure for a total thickness of 1500 nm each. Samples are grown on GaAs misoriented substrate of 0.2° towards [111]A and 6° towards [111]A.

Bibliography

[1] Silviu Bogusevschi, Christopher A Broderick, and Eoin P O'Reilly. "Theory and Optimization of 1.3 μm Metamorphic Quantum Well Lasers". In: *IEEE Journal of Quantum Electronics* 52.3 (2016), pp. 1–11.

[2] A Gocalinska, Marina Manganaro, and Emanuele Pelucchi. "Suppression of threading defects formation during Sb-assisted metamorphic buffer growth in InAs/InGaAs/InP structure". In: *Applied Physics Letters* 100.15 (2012), p. 152112.

[3] Tomonari Sato et al. "Sb surfactant effect on defect evolution in compressively strained In0. 80Ga0. 20As quantum well on InP grown by metalorganic vapor phase epitaxy". In: *Applied physics express* 1.11 (2008), p. 111202.

[4] Agnieszka M Gocalinska, Marina Manganaro, and Emanuele Pelucchi. "Unexpected aspects of strain relaxation and compensation in InGaAs metamorphic structures grown by MOVPE". In: *Crystal Growth & Design* 16.4 (2016), pp. 2363–2370.

[5] BH Müller et al. "Zn 0.85 Cd 0.15 Se active layers on graded-composition In x Ga 1- x As buffer layers". In: *Journal of applied physics* 85.12 (1999), pp. 8160–8169.

[6] Kamil Gradkowski et al. "Crystal defect topography of Stranski–Krastanow quantum dots by atomic force microscopy". In: *Applied Physics Letters* 97.19 (2010), p. 191106.

[7] Agnieszka Gocalinska et al. "Evaluation of defect density by top-view large scale AFM on metamorphic structures grown by MOVPE". In: *Applied Surface Science* 349 (2015), pp. 849–854.

Chapter 5

Laser: active part (barriers and QWs)

In this chapter the dissertation covers the growth related issues encountered in the metamorphic laser design, specifically we address the active part of the SCH structure, which , as discussed before follows a simple and conventional design. I.e., the laser design bears no attempt here as before to optimize performance, but only that of solving the numerous issues related to metamorphic epitaxy. In particular we investigate the effect of the growth temperature with increasing thickness during the QW deposition, propose a temperatures range where the resulting surface is 3D-nanostructures and defects free. We investigate also the use of a thin 5 nm GaAs layer as a strain balancing layer, grown before the QW deposition. In the last section a summary of the best growth parameter ranges, which will be used in the final full laser structure, is presented.

5.1 Structure and growth condition of SCH structure

Most layers were grown on a metamorphic structure which comprised the InGaAs graded layers, and the lower cladding superlattice (refer to previous chapter 4). The structure was then cleaved in smaller pieces for utilization in the active layer growth studies. The intention being to mimic during the growth tests the effects of previous layers in the final laser structure, without an excessive burden. Deoxidation issues were circumvented as the layer grown upon was terminated by the InGaP layer of the cladding.

As done in previous chapters, the analysis of the samples studied will be debated for samples grown on GaAs 0.2°A and 6°A substrates.

5.2 Barriers

The deposition of the lower cladding resulted in morphology reflecting the metamorphic buffer surface appearance.

Table 5.1: Summary table of the RMS values related to the barriers layers, evaluated from AFM scan size of 50 × 50 μm^2.

Layer	Composition	0.2° tw [111]A RMS (nm)		6° tw [111]A RMS (nm)	
		[011]	[0$\bar{1}$1]	[011]	[0$\bar{1}$1]
Cladding (SL)	$Al_{0.30}In_{0.15}G_{0.55}aAs/In_{0.62}GaP$	9	6	9	7
Lower guide	$Al_{0.12}In_{0.15}Ga_{73}As$	14	8	10	8
Outer barrier	$In_{0.13}Ga_{0.87}As$	11	8	11	8

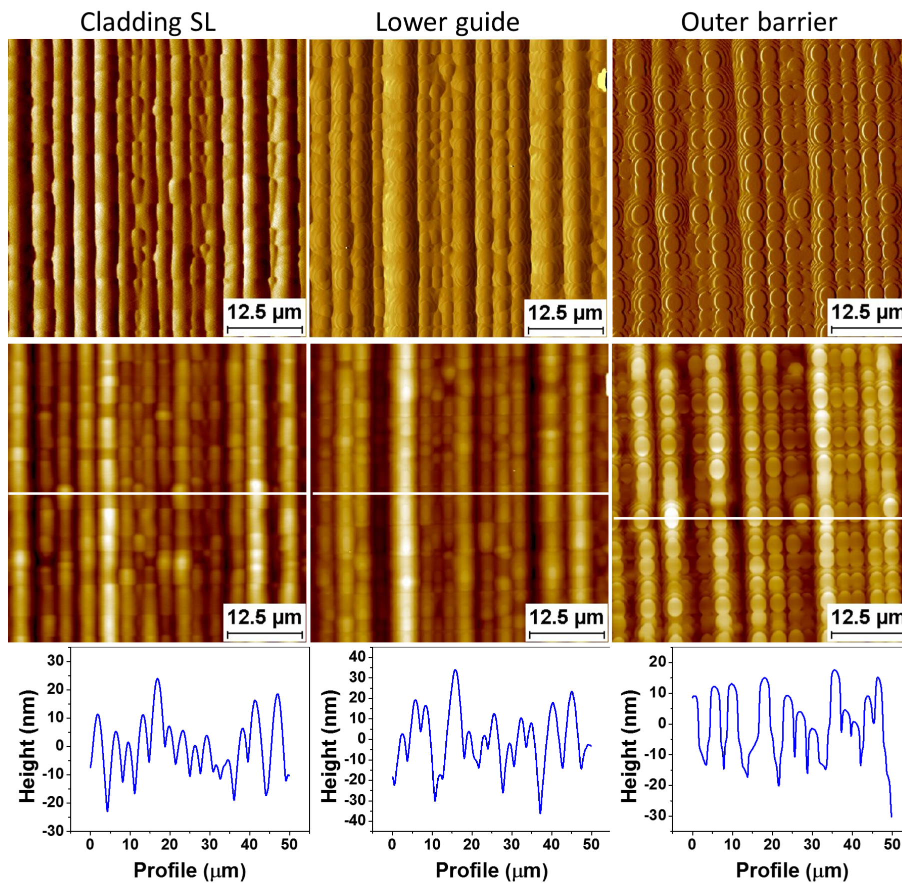

Figure 5.1: AFM (height, amplitude signal and cross-sectional profile) images of cladding SL and barriers, lower guide ($Al_{0.12}In_{0.15}Ga_{73}As$) and outer barrier ($In_{0.13}Ga_{0.87}As$) measured along the [011] direction. GaAs misoriented substrate 0.2° towards [111]A.

As from the structure design the barriers comprise of one $Al_{0.12}In_{0.16}Ga_{0.72}As$ layer lattice matched to the in-plane lattice parameter at the end of the grading, 100 nm thick, and one $In_{0.13}Ga_{0.87}As$ layer of 80 nm, slightly strained to compensate the strain arising from the following QWs, which will be separated from each other by 20 nm of the same $In_{0.13}Ga_{0.87}As$ barrier.

The RMS value for cladding and barriers are reported in table 5.1.

Overall the roughness remained in the same range, where lower values are associated with the $[0\bar{1}1]$ direction in both 0.2° A and 6° A substrates.

It is worth nothing that a change in the morphology/surface organization occurred after the deposition of the InGaAs layer for samples grown using the 0.2° cutoff GaAs substrate (Figure 5.1). The deposition of the InGaAs layer seems to round the top of the ridges and at the same time flatten the surface, reducing the peak to valley range. No significant differences were detected on the samples grown on the 6°A GaAs substrates.

5.3 Strained QWs

However, after the QWs deposition the morphology got a little more complex and substantial work was needed to optimize morphology. For example, after growing a 7 nm $In_{0.47}Ga_{0.43}As$ strained quantum well (Figure 5.2 and 5.3) 3D features appeared on the surface for samples grown on both the 0.2°A and the 6°A substrates.

These features present irregular shapes and are surprisingly tall, exceeding 120 nm. On the 0.2°A substrates the features gather together "methodically" around the circular plateaus, formed after the deposition of the InGaAs outer barrier. In the samples grown using a 6°A substrate the features didn't seem to follow a pattern, as they appear randomly on the surface, however with higher density than for the 0.2°A samples, $8 \times 10^7 cm^{-2}$ for the 6°A versus $1.7 \times 10^7 cm^{-2}$ for the 0.2°A. Here, the QW epitaxy was carried out with Sb as surfactant (consistently with what was done with the cladding layers, where the Sb had a positive planarizing effect), and with a 10 second growth interruption (GI) between the InGaAs barrier and the QW, to allow the change of gas flows.

Removing the Sb or reducing slightly the growth temperature, from 740 °C to 700 °C, did not remove the tall nanostructure from the surface. They appeared with the same frequency just described. A summary comprising growth condition, density and dimension of the features is presented in table 5.2. Before entering the discussion, we also point out that the given features' densities

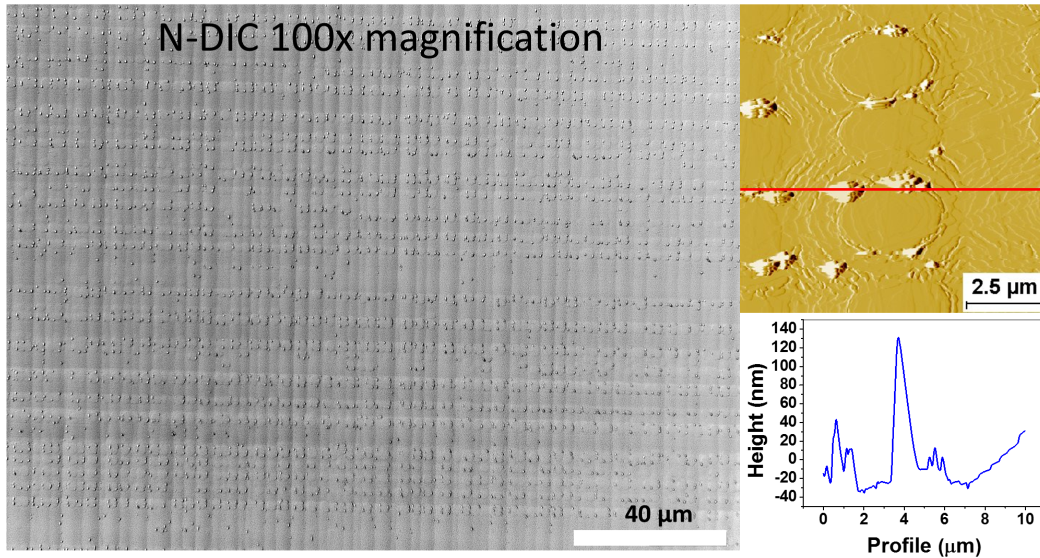

Figure 5.2: N-DIC and AFM (amplitude signal and cross-sectional profile) images of 7 nm $In_{0.47}Ga_{0.43}S$ QW directly deposited onto the InGaAs outer barrier. The QW is grown with 47% of In and Sb as surfactant. GaAs misoriented substrate 0.2° towards [111]A.

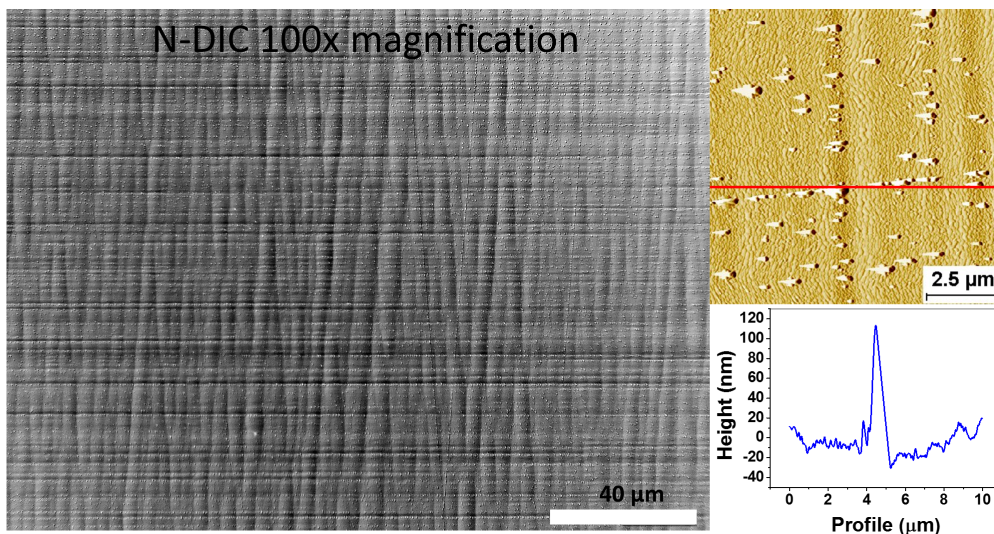

Figure 5.3: N-DIC and AFM (amplitude signal and cross-sectional profile) images of 7 nm $In_{0.47}Ga_{0.43}S$ QW directly deposited onto the InGaAs outer barrier. The QW is grown with 47% of In and Sb as surfactant. GaAs misoriented substrate 6° towards [111]A.

were evaluated by AFM inspecting a few images only, and should be treated as an observational estimate only.

We suspect that the origin of these nanostructures aggregation is the residual strain from the metamorphic buffer layer, somehow amplified by the lattice mismatched quantum wells. Moreover, the substantial step-bunched features

Table 5.2: Summary table of different growth condition for the QWs.

QW Structure	Growth T (°C)	0.2° tw [111]A		6° tw [111]A	
		Density cm^{-2}	Height nm	Density cm^{-2}	Height nm
$In_{0.47}Ga_{0.43}As$:Sb	740	1.7×10^7	140	8×10^7	140
$In_{0.47}Ga_{0.43}As$:Sb **no GI**	**700**	1.4×10^7	100	8×10^7	160
$In_{0.47}Ga_{0.43}As$: **No Sb**	740	6.5×10^7	140	1×10^8	100

inherited by the cladding layers, is likely to have a promoting effect, even if it is not totally clear how they influence the size and shape of the nucleated features.

For a clean data representation, the discussion of the phenomena in the subsequent text is subdivided into individual parts describing how the growth parameters are affecting the nanostructures formation and evolution.

5.4 Changes in the outer barrier

The first factor considered was the outer barrier composition. To investigate and rule-out a possible incompatibility between the AlInGaAs lower barrier and the InGaAs outer barrier, the $In_{0.13}Ga_{0.87}As$ layer was substituted with an $Al_{0.04}In_{0.17}Ga_{0.79}As$ quaternary alloy keeping the same lattice parameter. The changes in the layers' design are summarised in table 5.3.

Table 5.3: Summary table of various structural designs for the outer barrier.

Sample	Structure	0.2° tw [111]A		6° tw [111]A	
		Density cm^{-2}	Height nm	Density cm^{-2}	Height nm
A2294	$Al_{0.04}In_{0.17}Ga_{0.79}As$ + 1QW:Sb	1.7×10^7	140	8×10^7	140
A2295	$Al_{0.04}In_{0.17}Ga_{0.79}As$**:Sb** + 1QW:Sb	1.4×10^7	100	8×10^7	160
A2296	$Al_{0.04}In_{0.17}Ga_{0.79}As$:Sb +1QW:Sb +$Al_{0.04}In_{0.17}Ga_{0.79}As$:Sb	8×10^6	200	1.7×10^7	>200
A2297	$Al_{0.04}In_{0.17}Ga_{0.79}As$:Sb +1QW:Sb +$Al_{0.12}In_{0.15}Ga_{0.73}As$:Sb	6×10^6	150	4.9×10^7	>120

Figure 5.4 shows microscope images of the features to give an idea of the morphological phenomena.

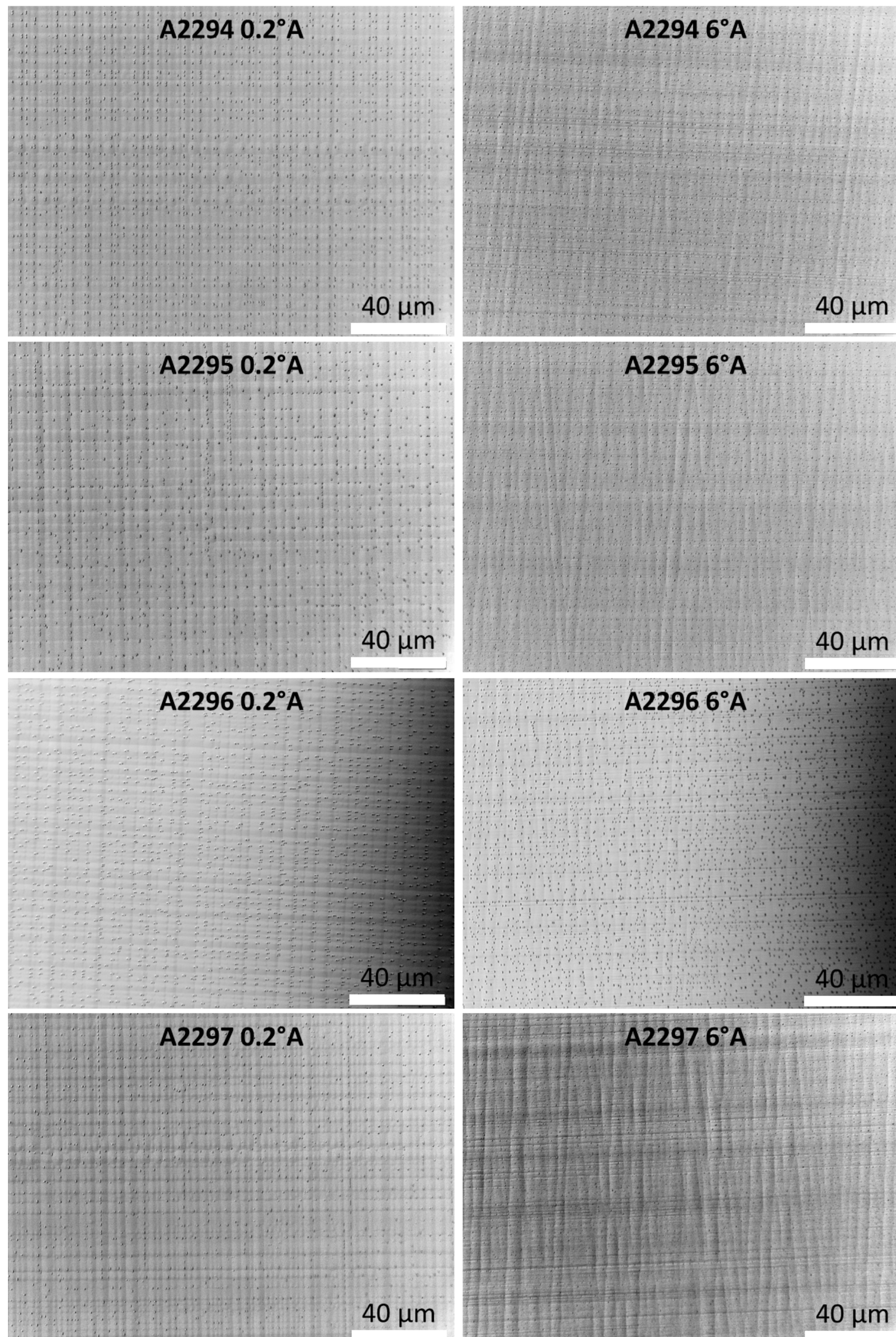

Figure 5.4: N-DIC images of the samples reported in the table 5.3. GaAs misoriented substrate 0.2° and 6° towards [111]A.

The exchange of the outer barrier alloy didn't stop the nanostructures formation. Moreover, with additional 20 nm of a barrier cap, the effect is a reduction in terms of density and a correspondent increase in the size (vertical or lateral) of the features; the cap material deposited covered the smallest features and increased the highest ones (samples A2296 and A2297).

5.5 QWs layer thickness

Figures 5.5 and 5.6 analyse how the strain (as a function of layer's thickness) between QW and barriers initiates the nanotructures's process formation.

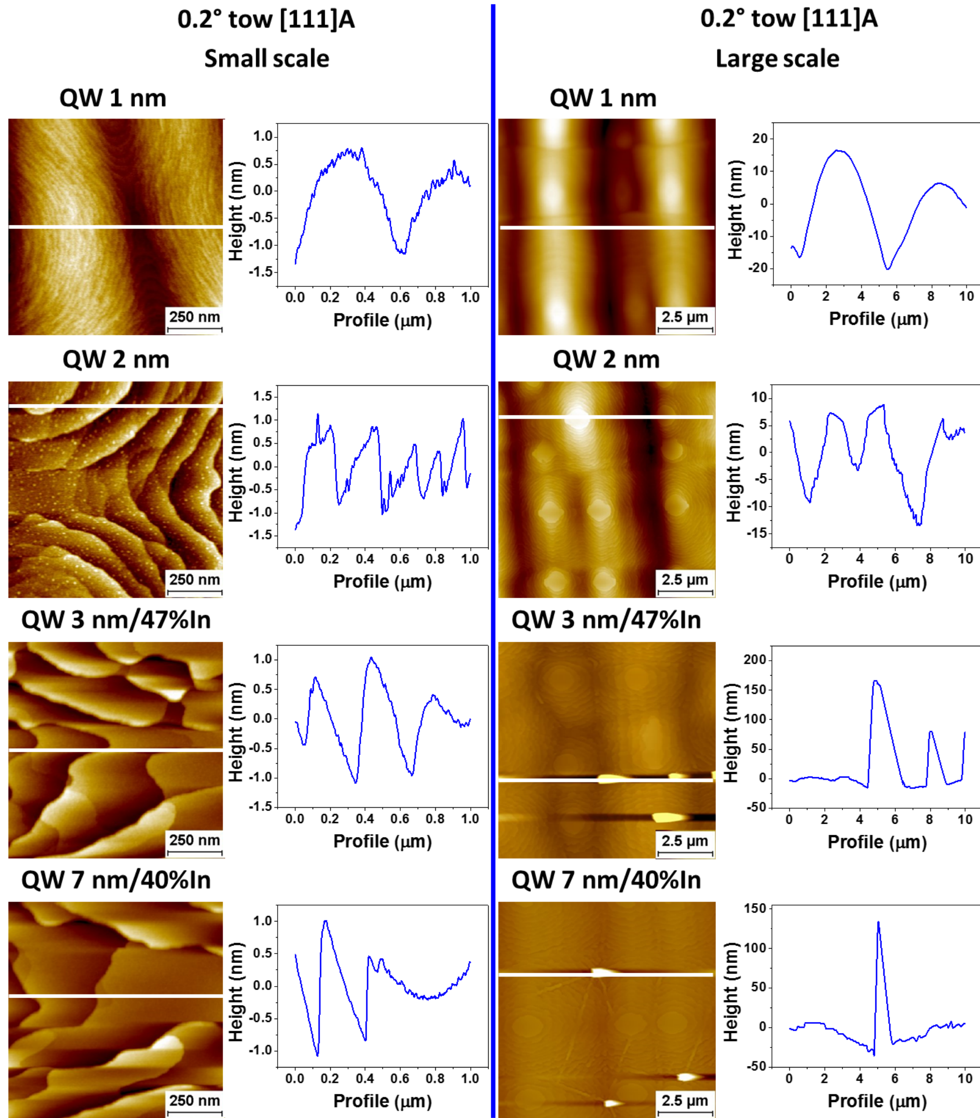

Figure 5.5: Surface morphologies (AFM height and cross-section profile) of samples grown with different $In_{0.40}Ga_{0.60}As$ QW thicknesses. For each sample are shown two X-Y AFM scales ($1 \times 1\ \mu m^2$ left side and $10 \times 10\ \mu m^2$ right side of the image). All samples were grown on GaAs misoriented substrate 0.2° towards [111]A. The samples were grown at $T_{gr} = 740$°C.

Observing the samples grown on the 0.2°A GaAs substrate (Figure 5.5), for 1 nm nominal of $In_{0.40}Ga_{0.60}As$ layer deposited, the surface shows the usual up and down ridges, with no evidence of defects and 3D features formation. After 2 nm of $In_{0.40}Ga_{0.60}As$ deposited in the same conditions, the material starts to aggregate in small dots up to $\sim$ 0.5 nm. The phenomenon is evident

only in the AFM image small scale, $1 \times 1\ \mu m^2$. The transition between the small dots and the huge features takes place abruptly, when 3 nm of InGaAs is deposited; it must be pointed out that the QW in this case was grown with 47% of In. We found again the same type of surface organization when 7 nm of $In_{0.40}Ga_{0.60}As$ are deposited, spotting the same step bunching (refer to AFM small scale) and large features formed ($>$ 150 nm in height).

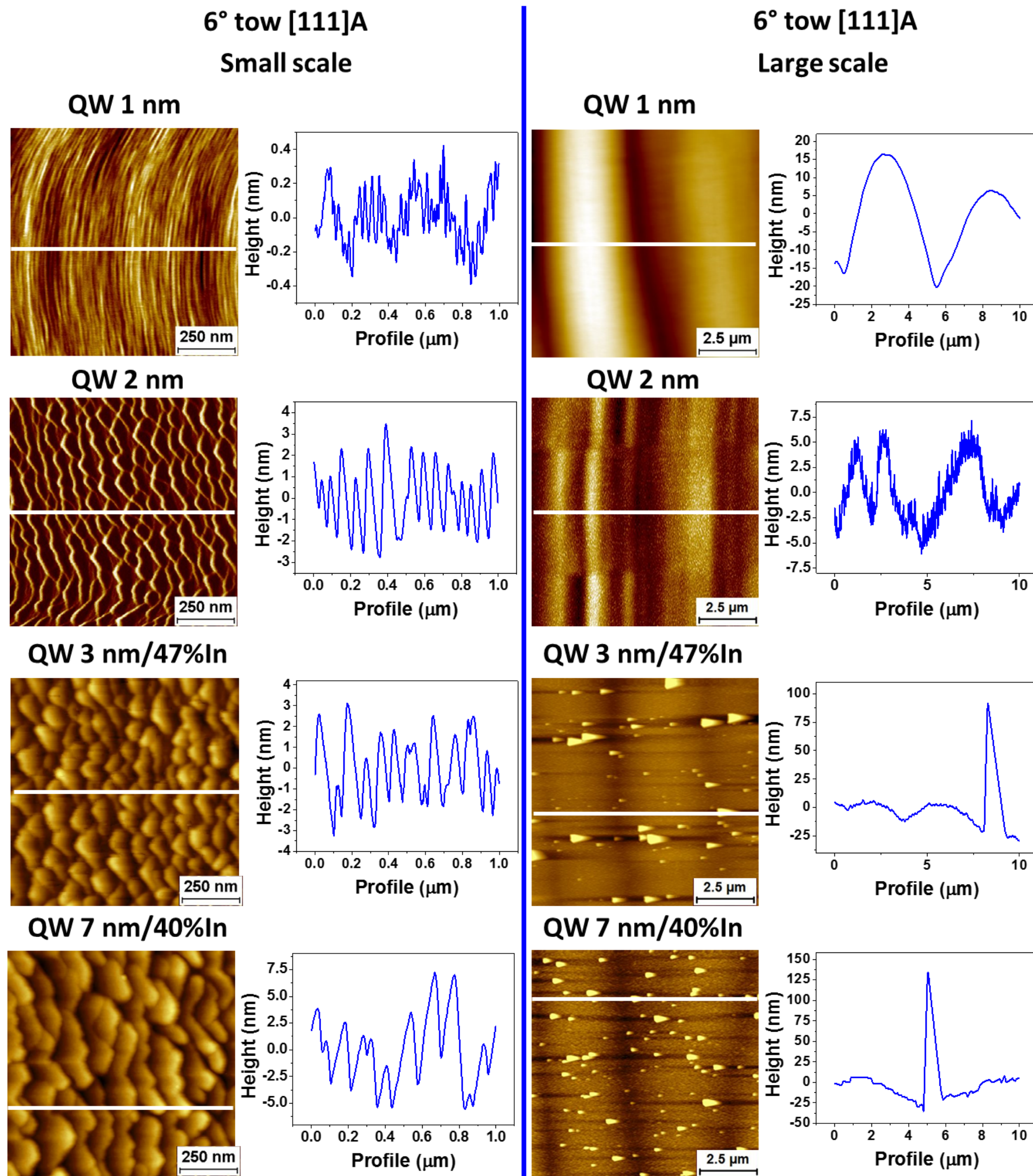

Figure 5.6: Surface morphologies (AFM height and cross-section profile) of samples grown with different $In_{0.40}Ga_{0.60}As$ QW thicknesses. For each sample are shown two X-Y AFM scales ($1 \times 1\ \mu m^2$ left side and $10 \times 10\ \mu m^2$ right side of the image). All samples were grown on GaAs misoriented substrate 6° towards [111]A. The samples were grown at $T_{gr} = 740$°C.

The nanostructures' process formation, on the samples grown on 6°A substrates, seems to be a bit delayed, or at least less evident at the beginning. Indeed step bunching occurs in the sample grown with 2 nm of $In_{0.40}Ga_{0.60}As$ cap (visible in the small scale of the Figure 5.6). In the samples with 3 nm of $In_{0.47}Ga_{0.53}As$ cap and with 7 nm ($In_{0.40}Ga_{0.60}As$ this time) the features are completely formed, covering the whole surface.

5.6 Strain compensation: GaAs effect

In an attempt to solve this issue, we studied the affect of a GaAs layer (sometime indicated as CIL, acronym of interface controlling layer) inserted between the barrier and the QWs. The QWs are heavily compressively strained and there is already a significant residual compressive strain in the metamorphic buffer layer, therefore a tensile compensation could be introduced into the structure. Despite the high lattice parameter mismatch, we could successfully grow 5 nm of GaAs without any Stransky-Krastanov dot or other nanostructures and defects formation and without perturbing the overall system morphology (Figure 5.7 " GaAs-no cap"), keeping the roughness value around 7.5 nm, similar in value to the one observed after the outer barrier deposition (compare Table 5.1).

The most evident and significant strain control effect of the GaAs layer is the delay in the nanostructures formation, especially for the samples grown on the 0.2°A substrates. Compared to the samples grown without the GaAs layer, we could deposit up to 2 nm of InGaAs without defects detection. When 4 nm of InGaAs are deposited, the surface start presenting irregularities around the plateau edges and after 7 nm of InGaAs deposition the features are completely formed (Figure 5.8).

A sightly different behavior was observed on samples grown on the 6°A substrate. They kept the same morphology for up to 2 nm of InGaAs cap then with 4 nm of cap the features covered the surface (Figure 5.9).

Some consideration can and must be done regards the GaAs layer thickness. In this section it is just reported that 5 nm of GaAs inserted between the barrier and the QW are able to delay the material aggregation in nanostrustructures, even though a thin layer as this one is not sufficient to balance the overall system strain.

To complete the picture we increased the GaAs layer, up to 8 nm, 50 nm and 100 nm. Onto the sample with 8 nm of GaAs we deposited 4 nm of InGaAs to have a comparison with previous investigated samples . Increasing the GaAs

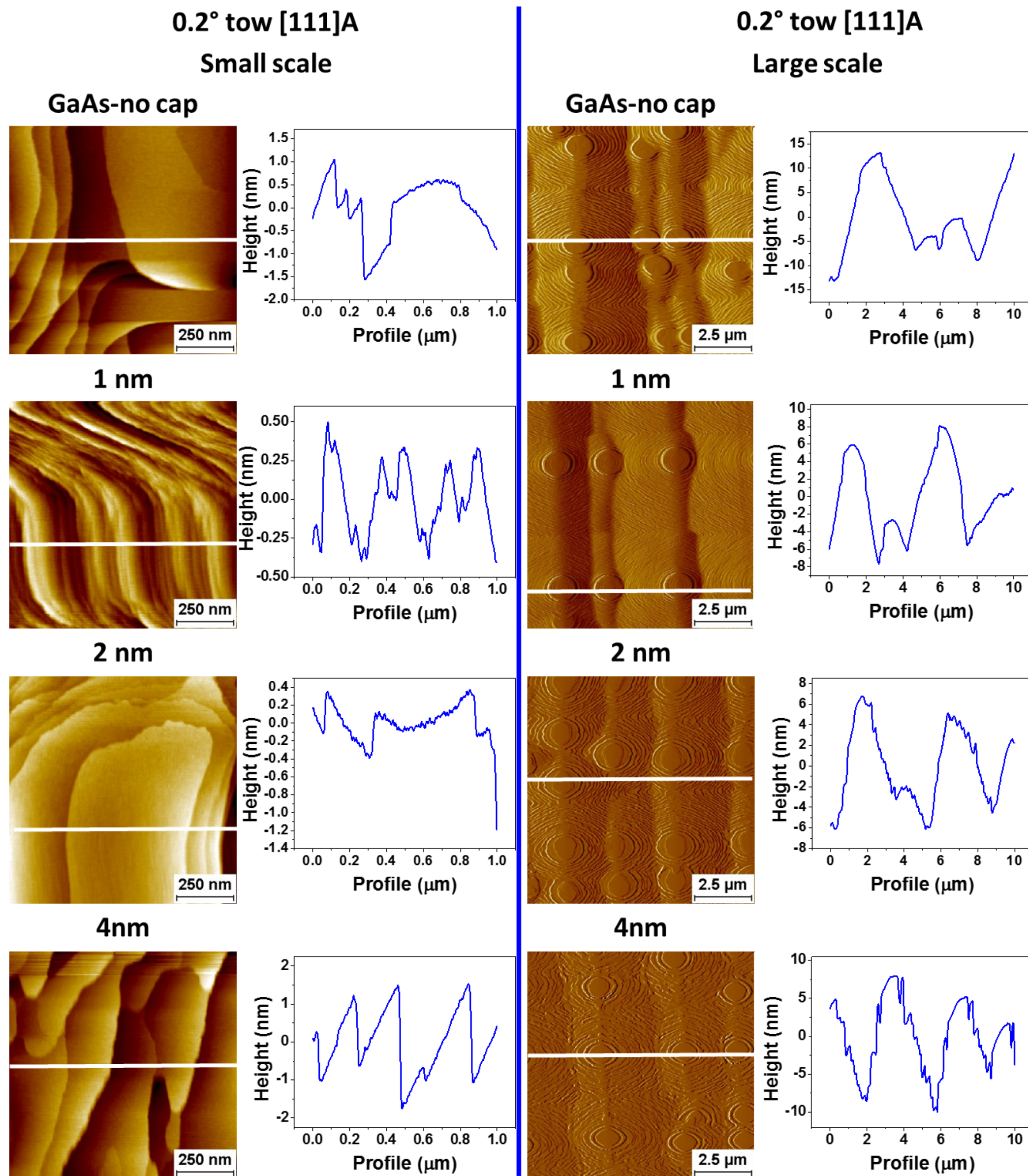

Figure 5.7: Surface morphologies (AFM height (small scale), signal amplitude (large scale) and cross-section profile) of samples grown with 5 nm of GaAs before the $In_{0.40}Ga_{0.60}As$ QW, and different $In_{0.40}Ga_{0.60}As$ cap layer thickness. For each sample are shown two X-Y AFM scales (1×1 μm^2 left side and 10×10 μm^2 right side of the image). All sample were grown in the GaAs 0.2°A substrate. The samples were grown at $T_{gr} = 740$°C.

layer by few nm resulted in lateral growth of the 3D features (Figure 5.10 and Figure 5.11 for samples grown on 0.2°A and 6°A respectively) as observed with 5 nm of GaAs. No big changes in the 3D features' density can be observed.

Increasing the thickness of the GaAs layer up to 50 nm didn't stop the 3D growth and the resulting morphology is even worse in terms of density of the features (Figure 5.12).

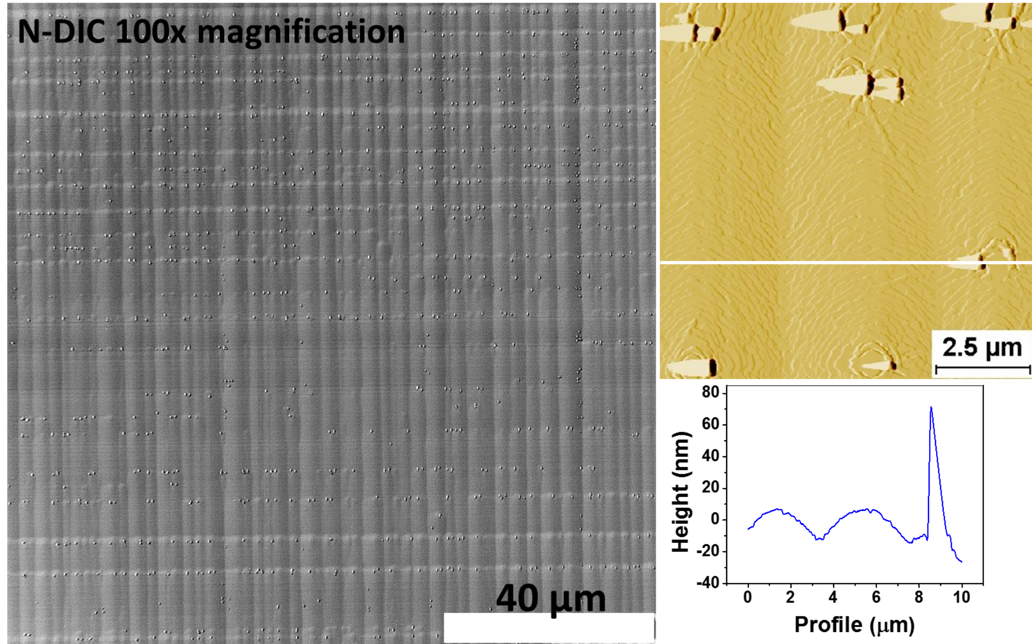

Figure 5.8: N-DIC and AFM (amplitude signal and cross-sectional profile) images of 7 nm $In_{0.40}Ga_{0.60}As$ QW preceded by a 5 nm of GaAs layer. GaAs misoriented substrate 0.2° towards [111]A.

When the GaAs layer thickness was increased to 100 nm we observed line defects on the surface of the 0.2°A samples and holes on the 6°A samples (Figure 5.12), an indication that major extra structural defects formed.

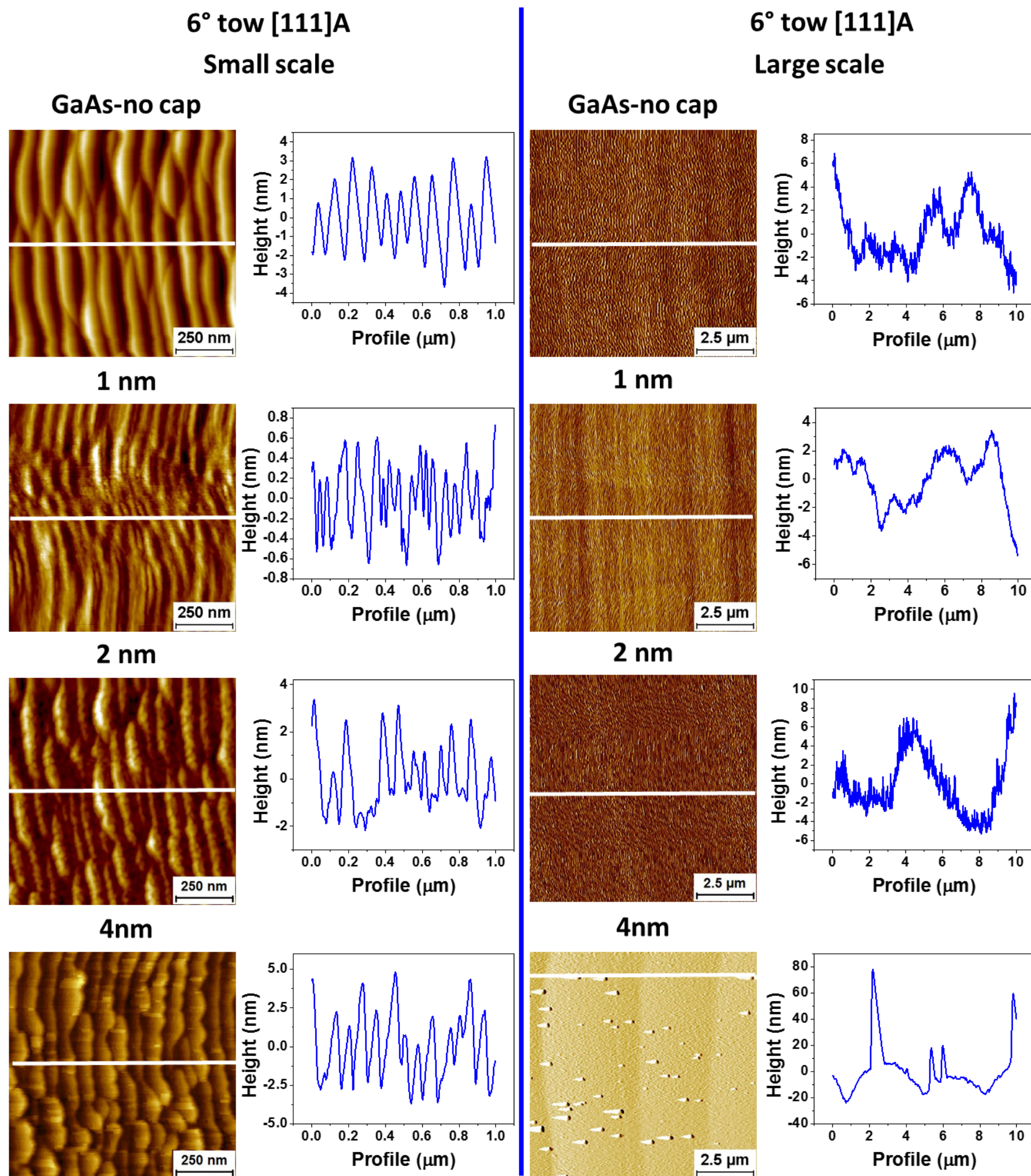

Figure 5.9: Surface morphologies (AFM height (small scale), signal amplitude (large scale) and cross-section profile) of samples grown with 5 nm of GaAs before the $In_{0.40}Ga_{0.60}As$ QW, and different $In_{0.40}Ga_{0.60}As$ cap layer thickness. For each sample are shown two X-Y AFM scales (1×1 μm^2 left side and 10×10 μm^2 right side of the image). All sample were grown in the GaAs 6°A substrate.The samples were grown at $T_{gr} = 740$°C.

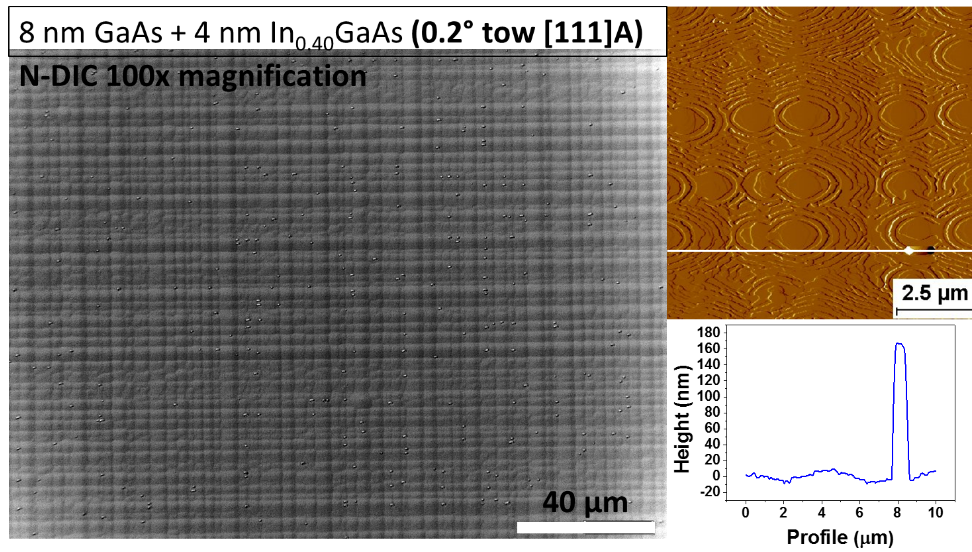

Figure 5.10: N-DIC and AFM (amplitude signal and cross-sectional profile) images of 4 nm $In_{0.40}Ga_{0.60}As$ QW preceded by a 8 nm of GaAs layer. GaAs misoriented substrate 0.2° towards [111]A.

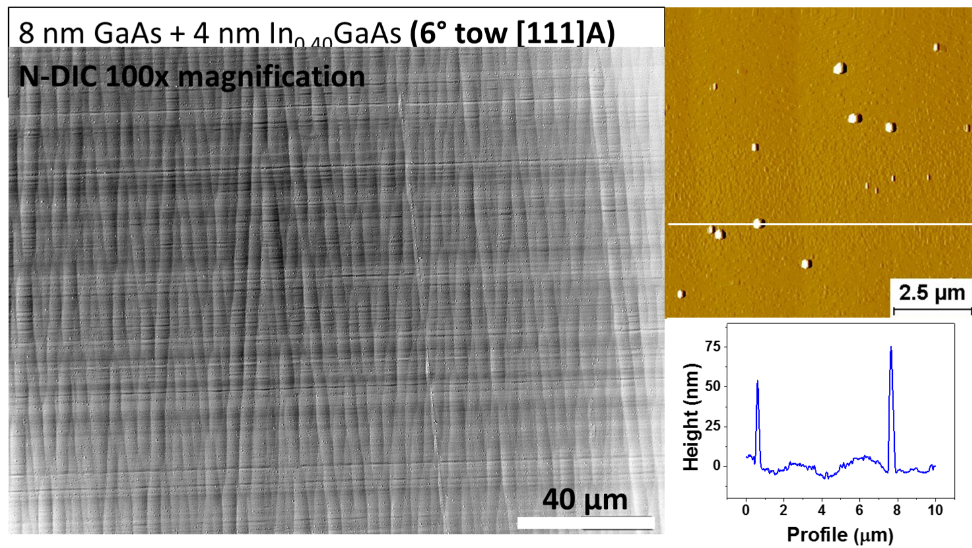

Figure 5.11: N-DIC and AFM images (amplitude signal and cross-sectional profile) of 4 nm $In_{0.40}Ga_{0.60}As$ QW preceded by a 8 nm of GaAs layer. GaAs misoriented substrate 6° towards [111]A.

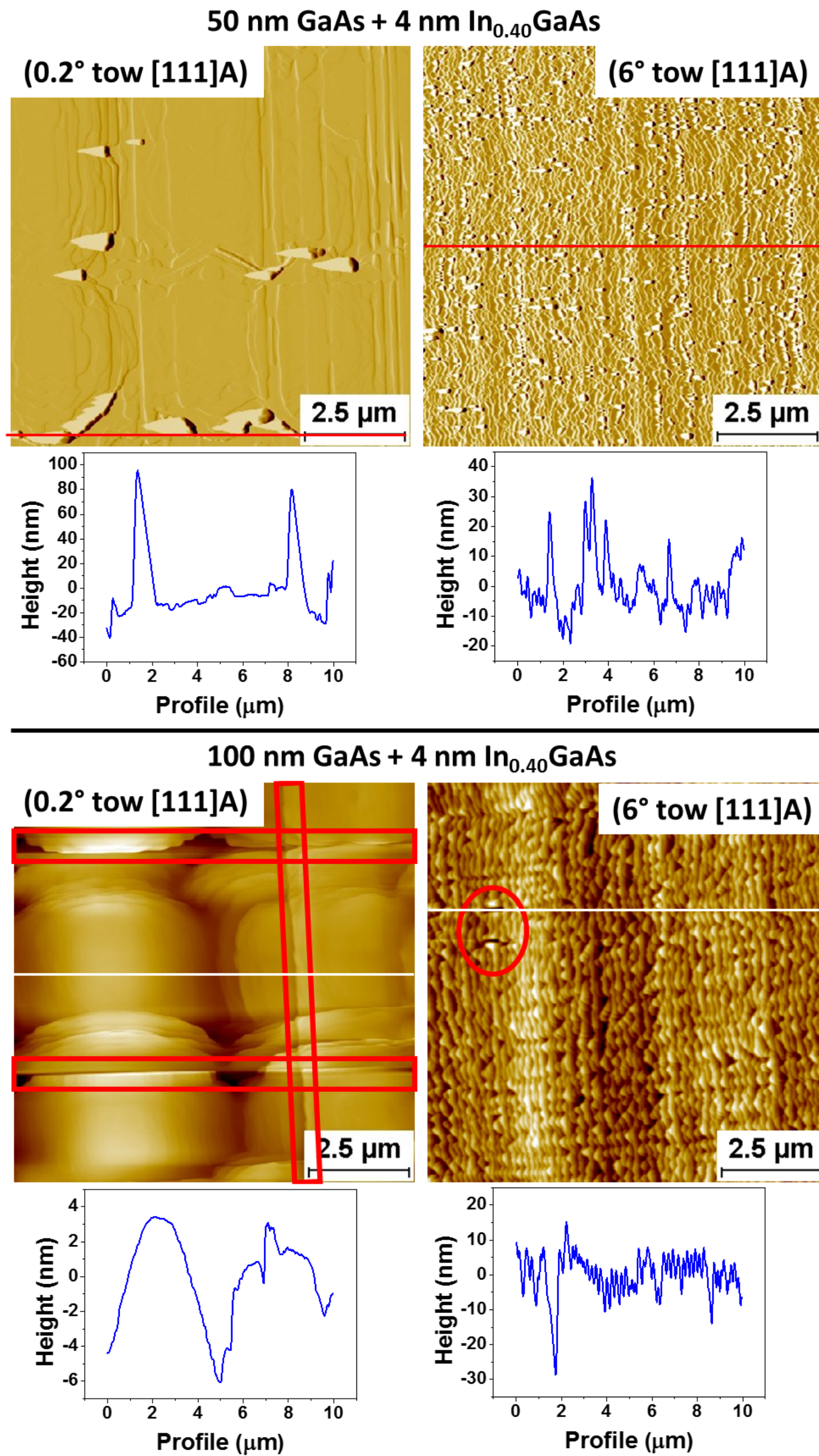

Figure 5.12: AFM images comparison (amplitude signal and cross-sectional profile) of 4 nm $In_{0.40}Ga_{0.60}As$ QW precede by a 50 nm and 100 nm of GaAs layer, respectively. GaAs misoriented substrate 0.2° and 6° towards [111]A.

5.6.1 The digital alloy

Exploiting the fact that the GaAs layer could slow down the the features formation (within limited thickness discussed above), we also explored the introduction of a "superlattice/digital alloy" to grow the 7 nm InGaAs QW. On Figure 5.13 a summary, refered to 0.2°A samples, shows the results of this approach.

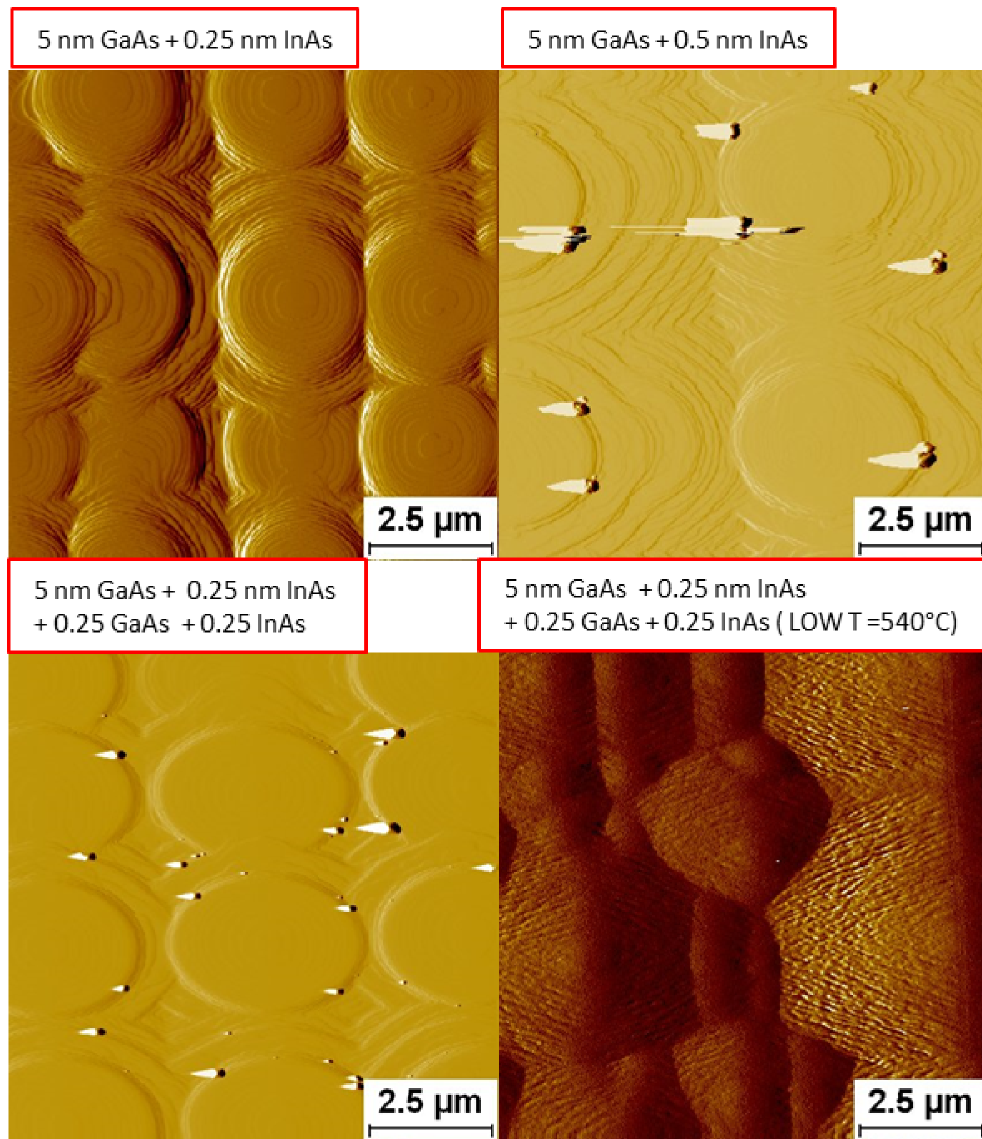

Figure 5.13: AFM images (amplitude signal) of the summary study related to the "digital alloy" approach. GaAs misoriented substrate 0.2° towards [111]A. The samples were grown at $T_{gr} = 740$°C.

5 nm of GaAs followed by 0.25 nm of InAs (i.e. ∼1 monolayer (ML)) leaves the surface covered with concentric islands, bigger than those observed with just GaAs, and no features were detected. A doubled InAs layer, 0.5 nm,

brings back the features. Using 0.25 nm of InAs and increasing the number of overlapped layers once again resulted in the the nanostructures formation; the concentric islands appeared flattened. Growing the digital alloy with lower growth temperature, 540°C instead of 740°C, removes the features almost completely. However it must be highlighted that the sample morphology was not macroscopically uniform, presenting some rough areas, especially on the wafer edges.

Also for the 6°A samples we found that with the increase of the number of the overlapped layers the density of 3D features increased, but the overall morphology was much smoother. The temperature had a strong impact on the formation of the features, which disappeared almost completely at 540°C as can be seen in the zoomed area in Figure 5.14 (d).

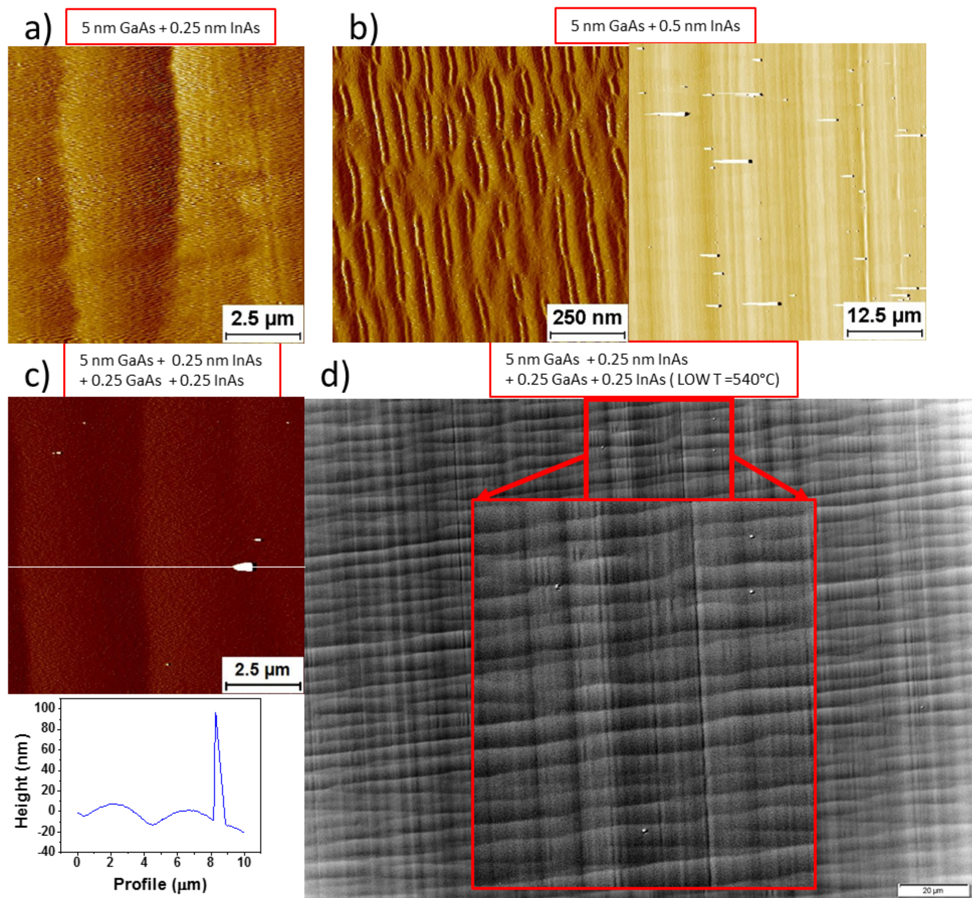

Figure 5.14: (a),(b), (c) AFM (amplitude signal) and (d) N-DIC images of the summary study related to the "digital alloy". GaAs misoriented substrate 6° towards [111]A.

The "digital alloy" didn't solve the problem with the 3D features formation, however the GaAs layer was able to delay the material aggregation. For this

reason in the development process we maintained from here on the GaAs pre-layer, and including what is presented in the next sections, unless otherwise stated. As a result the layer will be present in subsequent full laser structures, including the most success ones.

5.7 QWs vs Temperature

In this section, continuing the discussion about the QW growth optimization, a characterization of the QWs as a function of the growth temperature (T_{gr}) is presented. We have just discussed that somehow high T_{gr} favour the formation of unwelcome 3D structures. On the other hand, and as already found for the digital alloy, we anticipate that even in this particular case it will be observed that low T_{gr} disadvantages the material aggregation into 3D nanostructures but to some extent to the detriment of surface quality. Nevertheless it will be shown that a range of temperatures can be identified, in conjunction with tailored In% in the QWs layer, where nanostrustuctures and defects can be controlled and managed.

It should be also mentioned for clarity that the T_{gr} cited in this chapter is always the one derived by the thermocouple reading. We also estimate that in our Aixtron 200 reactor, the relation between thermocouple reading and real sample temperature follows the rule: $0.66025 \times thermoucouple + 159.22951$. This on the other hand ceases to be reliable close or below 500 degrees, where we estimate the thermocouple and sample temperature largely overlap.

5.7.1 Growth temperature 540°C

We started the study with low growth temperature of 540°C.

In table 5.4 the structures of relevant samples grown at 540°C are reported.

Table 5.4: Structures of the samples grown at the growth temperature of 540°C

No Sample	Structure
A2369	5 nm GaAs + 4 nm QW(40% In)
A2379	5 nm GaAs + **7 nm** QW(40% In)
A2385	5 nm GaAs + **7 nm** QW(40% In) + barrier + **7 nm** QW(40% In) + cap
A2392	+ 5 nm GaAs + 7 nm **QW(33% In)** + barrier + 7 nm **QW(33% In)** + cap

Combining the insertion of a GaAs layer and low growth temperature almost completely eliminates the problem of large 3D features, especially for

the samples grown on the 6°A substrates. Indeed after the deposition of the full 7 nm $In_{0.40}Ga_{0.60}As$ QW not a single feature was detected on the sample surface. The surface presented a roughness in the range of the cladding superlattice structure (refer to previous chapter to compare the values), with a RMS value of $\sim$ 10.5 nm evaluated from an AFM area scan of 50 $\times$ 50 μm^2 (Figure 5.15).

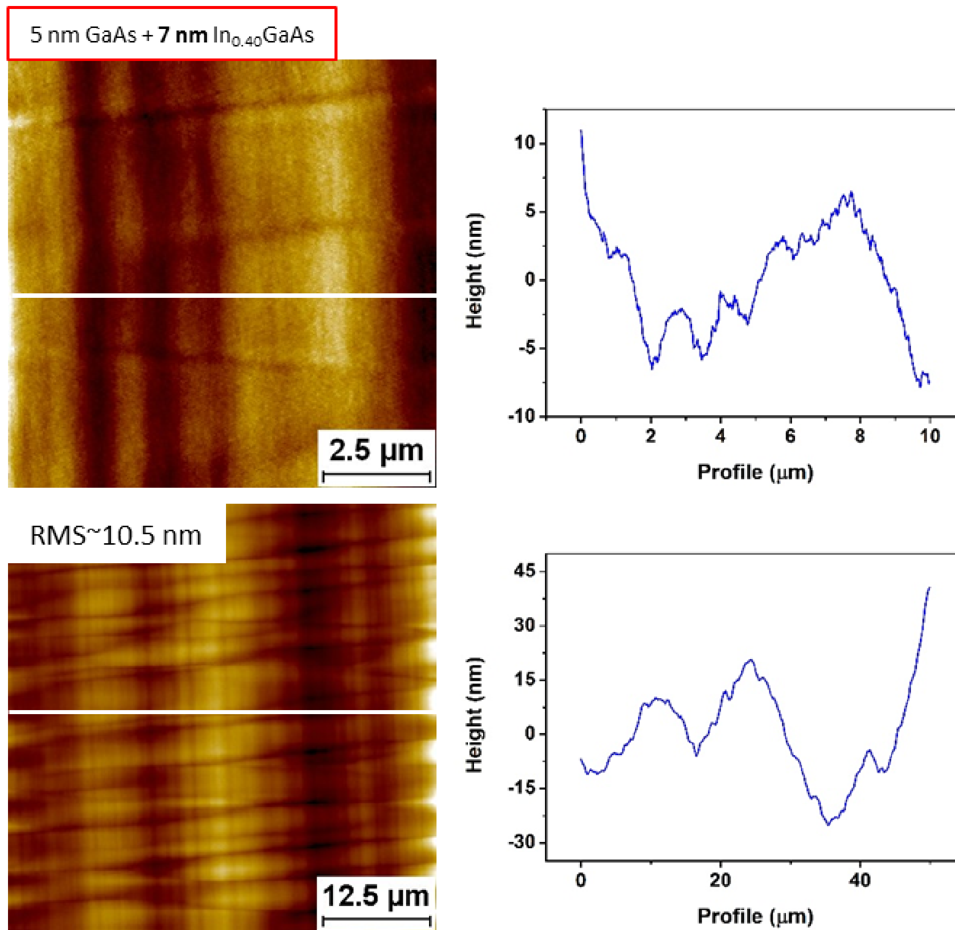

Figure 5.15: AFM images (height and cross-section profile) of 7nm $In_{0.40}Ga_{0.60}As$ QW grown at 540°C. GaAs misoriented substrate 6° towards [111]A.

Regarding the samples grown on the 0.2°A substrates (Figure 5.16) some residual defect-like dots of 10 nm were detected, but only after 7 nm of $In_{0.40}Ga_{0.60}As$ deposition and in limited spots on the sample. In the sample with thinner $In_{0.40}Ga_{0.60}As$ (4 nm) there were still some mildly jagged areas which clearly link to the features seen after 7 nm of $In_{0.40}Ga_{0.60}As$ (features which anyway are limited in size when compared to the tall nanostructures observed at high T_{gr}).

Nevertheless, under these growth conditions, when capped with the appropriate barriers, the QWs exhibited a wavelength exceeding 1400 nm of

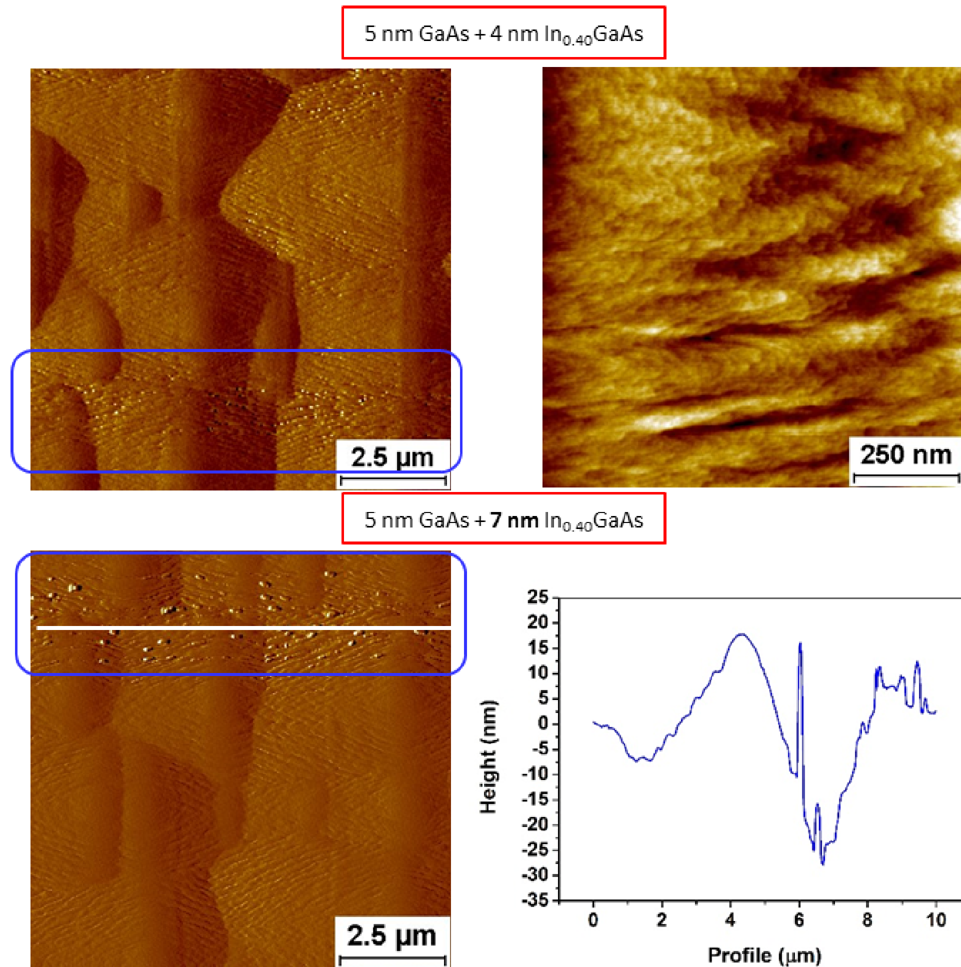

Figure 5.16: AFM images (height and cross-section profile) of 4 nm and 7nm $In_{0.40}Ga_{0.60}As$ QW grown at 540°C. GaAs misoriented substrate 0.2° towards <111>A.

emission. A slight blueshift was observed between the samples grown on the 0.2°A and 6°A substrates (Figure 5.17(a)).

It can be observed that a substantial difference is present when comparing between the emission obtained from a low T_{gr} nominal InGaAs 40% indium and a InGaAs 47% indium (Figure 5.17)(b) grown at higher $T_{gr} = 740$, i.e. with "older" growth conditions. It should be underlined that the sample with the longer wavelength (A2385), differed from the other (A2277) not only by the growth temperature, but also by the absence of Sb in the InGaAs QW, and the presence of the GaAs layer before the first QW. Indeed, the sample with $In_{0.47}Ga_{0.53}As$ was grown before the optimization to remove the large features from the surface.

The shifted emission, over 1400 nm, much longer than the one desired, gave the option of reducing the indium content in the QW, with added benefit of

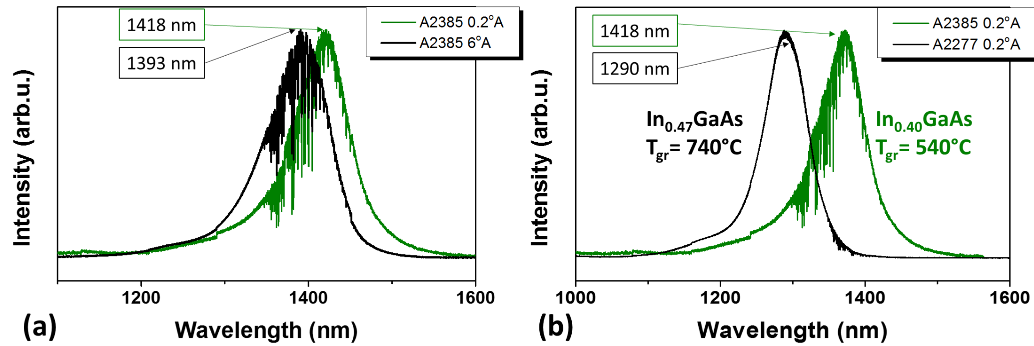

Figure 5.17: (a)Comparison between normalized room temperature PL spectra of active part comprising 2 $In_{0.40}Ga_{0.60}As$ QWs of samples grown on 0.2°A and 6°A substrates. Growth temperature of 540°C. (b)Comparison between normalized room temperature PL spectra of samples grown at low and high temperature and with different InGaAs QW composition, 540°C and $In_{0.40}Ga_{0.60}As$ QWs (sample A2385), 740°C and $In_{0.47}Ga_{0.53}As$ QWs (sample A2277). Samples grown on 0.2°A substrates.

decreasing the overall strain in the full structure. In Figure 5.18 the (room temperature) photoluminescence spectra of two $In_{0.33}Ga_{67}As$ QWs, 33% indium is shown.

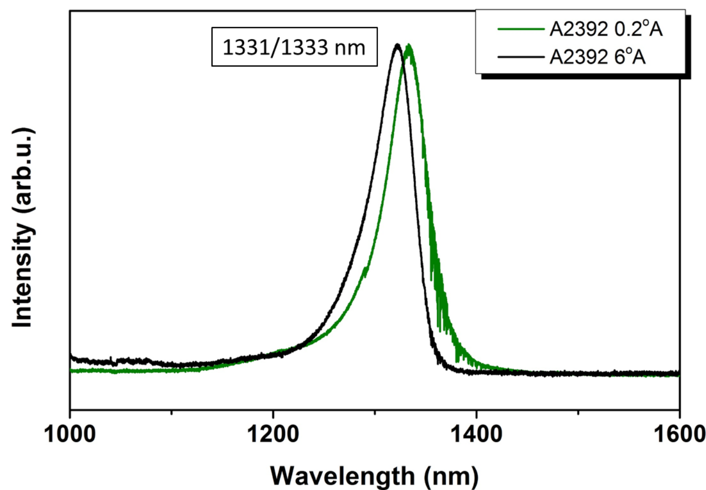

Figure 5.18: Comparison between normalized room temperature PL spectra of active part comprising of 2 $In_{0.33}Ga_{0.67}As$ QWs of samples grown on 0.2°A and 6°A substrates. Growth temperature of 540°C.

The morphology of the full active -2 QWs- samples grown at the same low temperature of 540°C but with different indium content, 33% and 40% respectively, showed similar "small" 3D structures, with the surface slightly improved in the sample with lower indium content (Figure 5.19). However, clear defect lines appeared on the surface of both samples. In the related AFM

cross sectional profile the ridges appeared more indented in the $In_{0.40}Ga_{0.60}As$ than in the $In_{0.33}Ga_{0.67}As$. An additional piece of information came from the RMS value, lower in the structure with 33% Indium.

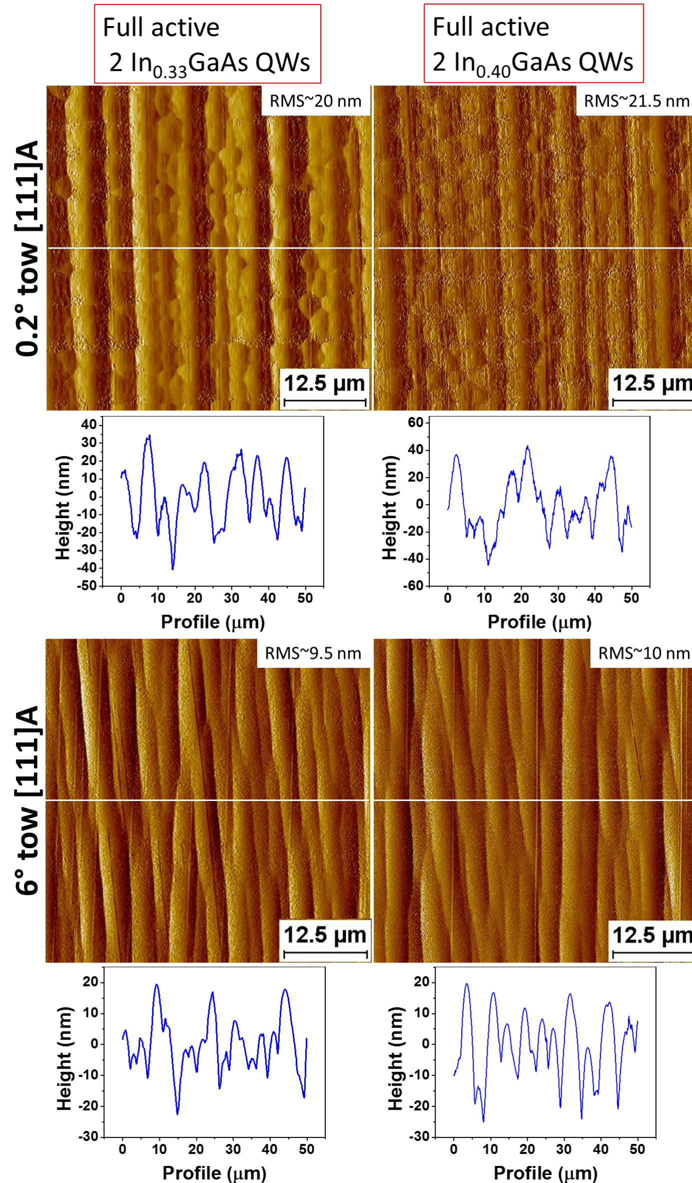

Figure 5.19: AFM images (signal amplitudes and cross section profile) of the top surface of samples grown with $In_{0.40}Ga_{0.60}As$ and $In_{0.33}Ga_{0.67}As$ QWs at the same Tg = 540°C. GaAs 0.2°A and 6°A substrates.

Defects lines and rough surfaces were detected also in the samples grown on the 6°a substrates, although the RMS value was lower of 10 nm respect to the 0.2°A substrate (Figure5.19).

5.7.2 Growth temperature 600°C

Table 5.5: Structures of the samples grown at the growth temperature of 600°C

No Sample	Structure $T_{gr} = 600°C$
A2394	5nm GaAs + 7nm QW(33% In)
A2464	5nm GaAs + 7nm QW(**40% In**)
A2463	5nm GaAs + 7nm QW(**43% In**)
A2469	5nm GaAs + 7nm QW(40% In) + barrier + 5nm GaAs + 7nm QW (40% In) + cap

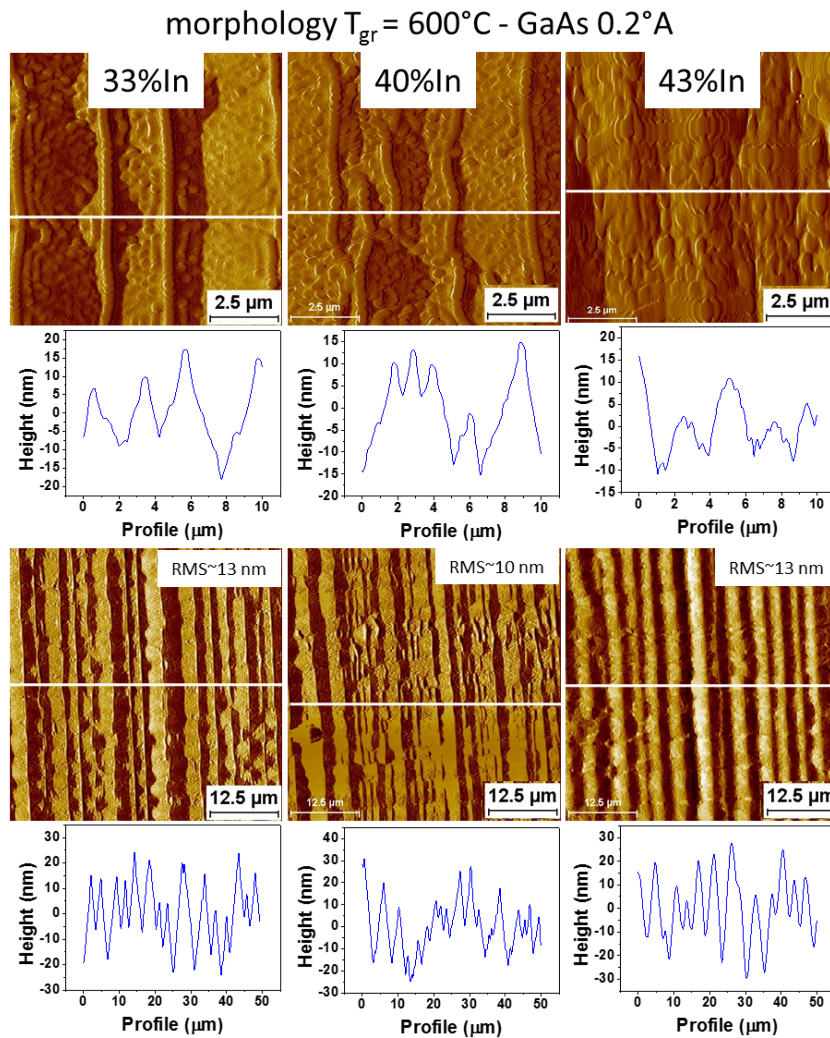

Figure 5.20: Surface morphologies (AFM signal amplitudes and cross sectional profile) of representative samples grown at 600°C with three different InGaAs QW composition. For each sample two X-Y scales ($10 \times 10\ \mu m^2$ and $50 \times 50\ \mu m^2$) are shown. GaAs 0.2°A substrate.

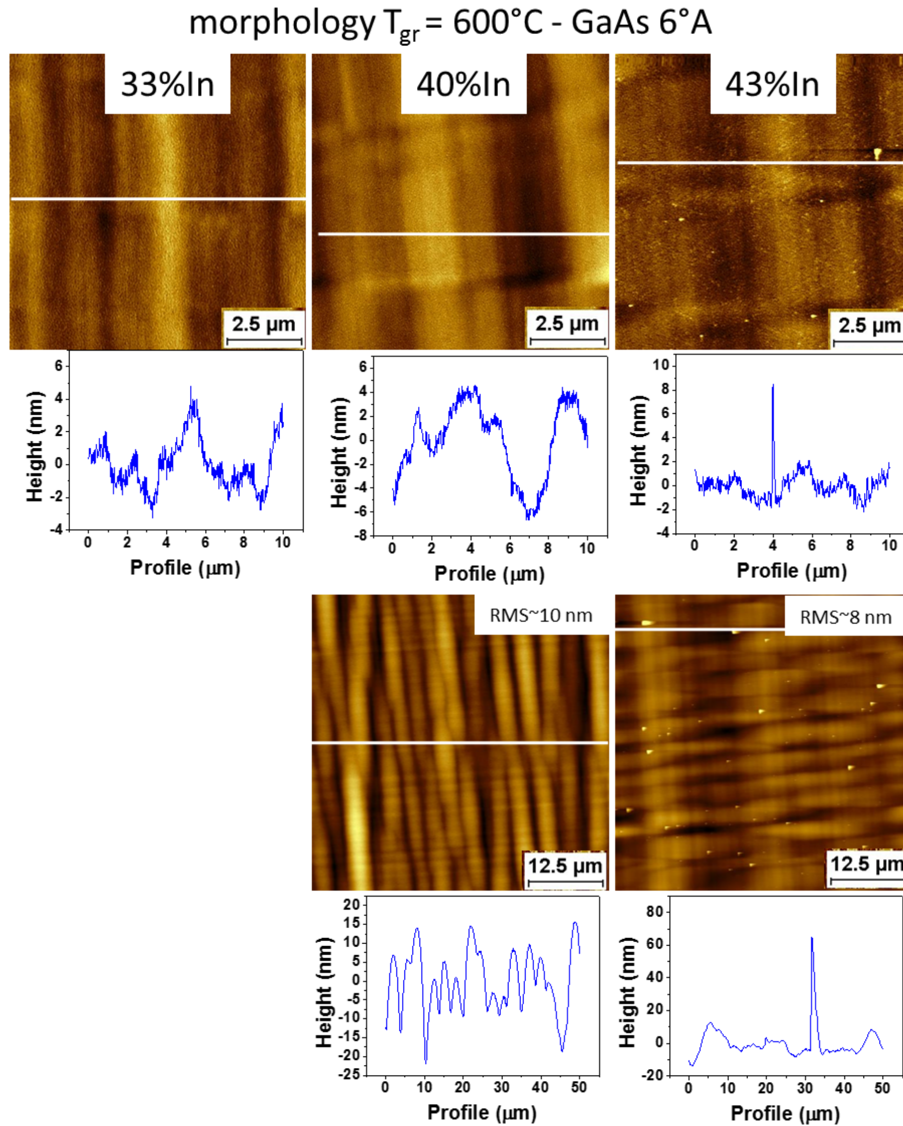

Figure 5.21: Surface morphologies (AFM signal amplitudes and cross sectional profile) of representative samples grown at 600°C with three different InGaAs QW composition. For each sample two X-Y scales ($10 \times 10\ \mu m^2$ and $50 \times 50\ \mu m^2$) are shown. GaAs 6°A substrate.

We noted that at 540°C the formation of the features was eliminated or delayed, but the surface deteriorated and defect lines were formed, both with lower 33% and higher 40% indium content. Increasing the T_{gr} of the active part up to 600°C (somehow surprisingly) changed completely the surface organization (Figure 5.20): on the 0.2°A samples little circles took shape along the ridges but importantly no defects were detected. No significant differences could be detected between the samples grown with 33% and 40% Indium content in the well, if not a greater order in the surface organization occurred in the sample with $In_{0.33}Ga_{0.67}As$. With 43% of indium for the 0.2°A the RMS

value started to increase, but still no evidence of nanostructures formation.

Different behaviour was observed for the 6°A samples, where the higher percentage of indium in the QW ($In_{0.43}Ga_{0.57}As$) promoted the formation of the 3D nanostructures, reaching about 60 nm in height (Figure 5.21). Therefore we concluded that up to 40% indium at 600°C the defect and nanostructure formation can be managed.

The increase nominal in the T_{gr}, on equal terms of indium in the QWs, resulted in a redshift in the emission. Indeed, 2 $In_{0.40}Ga_{0.53}As$ QWs capped for photoluminescence measurements showed the emission peaked at ∼1360 nm. The photoluminescence spectrum is shown in Figure 5.22, were it is compared with the spectrum obtained from 2 QWs grown in the same conditions directly onto the InGaAs barrier, i.e without the GaAs layer. This test showed that the GaAs layer can be inserted before the QWs without perturbing significantly the emission of the active part. By virtue of this consequently, having tested this improved planarizing effect on the surface, we used the GaAs layer in each full laser grown at a later stage.

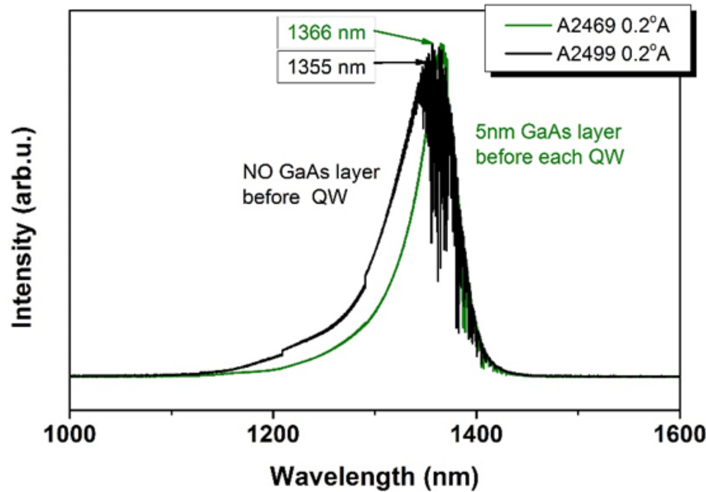

Figure 5.22: Comparison between 2 $In_{0.40}Ga_{0.60}As$ QWs with 5 GaAs layer before each QW and without grown at the same Tg = 650°C. Top and central row: AFM images (amplitude signal and cross sectional profile). Bottom row: room temperature photoluminescence spectra of both samples.

5.7.3 Growth temperature 625 − 650°C

Switching from T_{gr} = 600°C to T_{gr} = 625°C didn't affect the morphology for structures grown with 33% indium concentration in the QWs, while at T_{gr}

Table 5.6: Structures of the samples grown at the growth temperature of 625−650°C

No Sample	Structure	T_{gr}(°C)
A2407	GaAs 5nm + 1 QW(33%In) 7nm	625
A2461	GaAs 5nm + 1 QW(43%In) 7nm	625
A2396	GaAs 5nm + 1 QW(33%In) 7nm	650
A2401	full active (2 GaAs 5nm + 2 QWs(33%In) 7nm)	650
A2417	full active (2 GaAs 5nm + 2 QWs(35%In) 7nm) + 1500nm cladding	650

= 650°C we noted a modified surface organization, with smoothed and less sharpened ridges (Figure 5.23).

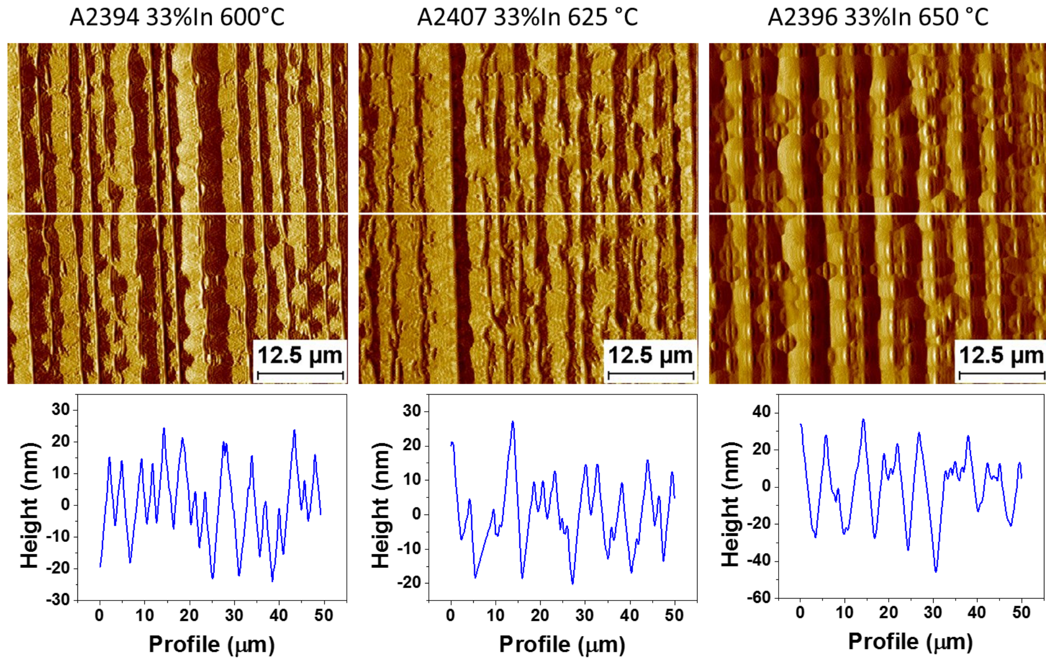

Figure 5.23: Comparison of surface morphology (AFM images, amplitude signal and cross sectional profile) between $In_{0.33}Ga_{0.67}As$ QWs grown at three different growth temperature, T_{gr} = 600°C, T_{gr} = 625°C and T_{gr} = 650°C respectively. GaAs 0.2°A substrate.

Importantly with the 33%In the 3D feature formation has never been observed in the range of T_{gr} between 600 and 650 °C . Nevertheless, as expected, with 43% of indium in the QW at T_{gr} = 625°C the 3D features started to grow also on the 0.2°A substrate, and not only on the 6°A (Figure 5.24), as was the case for samples grown at lower temperature (T_{gr} = 540°C).

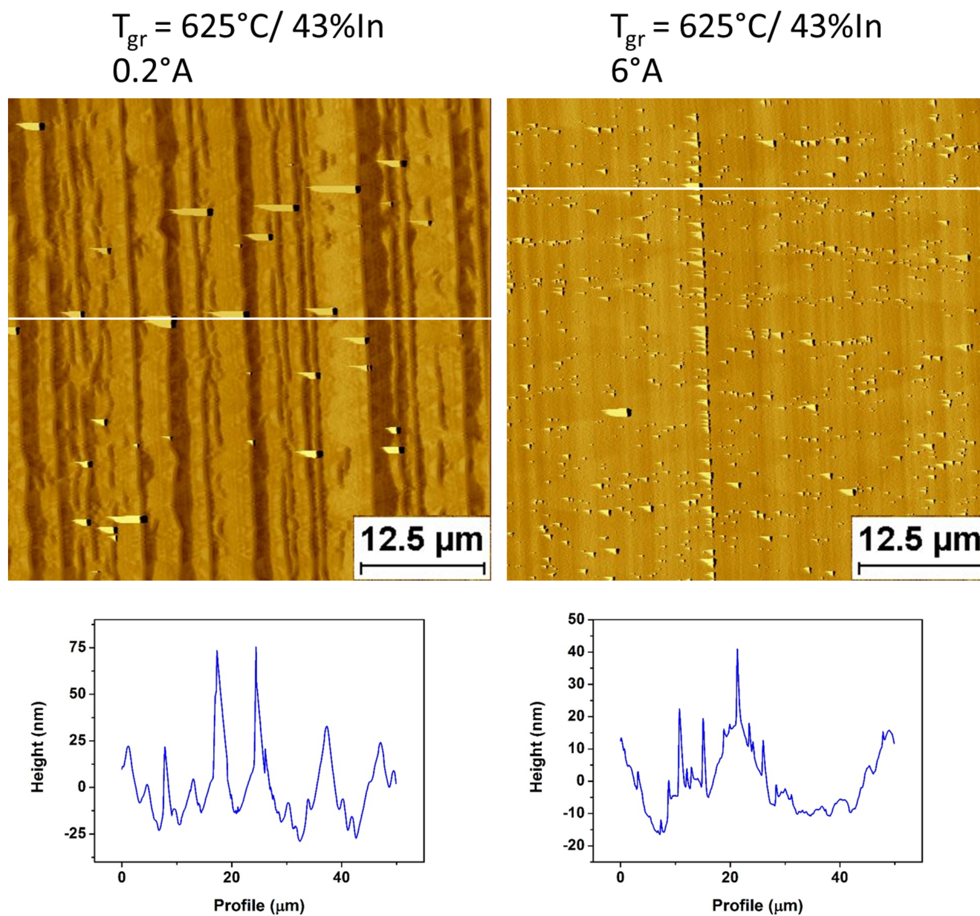

Figure 5.24: Surface morphologies (AFM signal amplitudes and cross sectional profile) of sample A2461. The structure comprised 1 $In_{0.33}Ga_{0.67}As$ QW preceded by 5 nm of GaAs layer grown at 625°C. GaAs 0.2°A and 6°A substrates.

The emission of two QWs with 33% of indium grown at 650°C peaked at ∼1225 nm, below the wavelength of interest, but increasing the indium percentage up to 35% ensured the right wavelength without morphology degeneration or 3D features formation, even after the upper cladding deposition. In Figure 5.25 is shown the surface morphology of a full laser structure comprising MBL, lower SL cladding, SCH- 2 $In_{0.35}Ga_{0.65}As$ QWs grown at T_{gr} = 650°C and upper SL cladding. Best results were obtained with the 6°A substrate, presenting a smoother surface than 0.2°A. The RMS values for the 6° was 7 nm and 10 nm for the [1$\bar{1}$0] and [110] respectively, whereas for the 0.2° was ∼ 15 nm for both <100> directions.

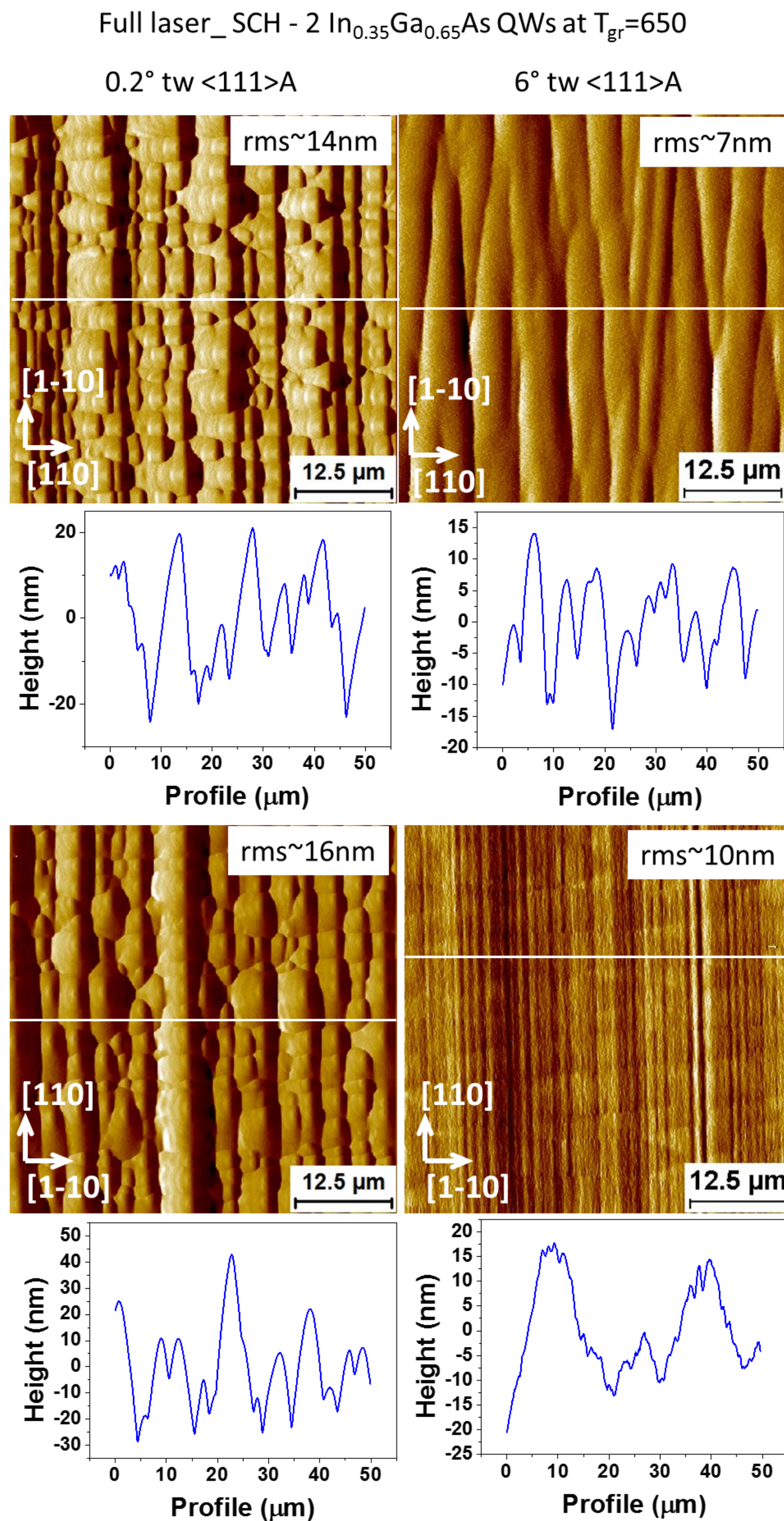

Figure 5.25: AFM images (amplitude signal and cross-section profile) of the full laser structure comprising MBL, lower SL cladding, SCH- 2 $In_{0.35}Ga_{0.65}As$ QWs grown at T_{gr} = 650°C and upper SL cladding. The full structure was grown at the T_{gr} of 740°C, and just the SCH part at 650°C. Samples were grown on GaAs misoriented substrate of 0.2° towards [111]A and 6° towards [111]A.

In Figure 5.26 a comparison between the photoluminescence spectra from SCH-2 InGaAs QWs capped with barrier and the upper cladding superlattice structure of 600 nm for the QWs at 33% and 1500 nm for the QWs at 35% indium content respectively, is shown.

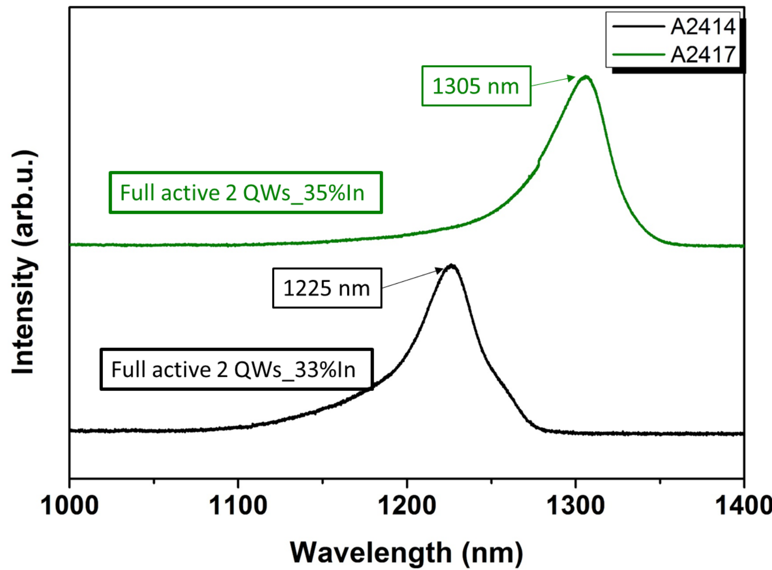

Figure 5.26: Comparison between normalized room temperature PL spectra of sample grown with different indium concentration of the QWs, 33% and 35%, and same growth temperature of 650°C. The QWs were capped with InGaAs barrier and upper cladding superlattice structure of 600 nm and 1500 nm respectively. Samples grown on 0.2°A substrates.

5.8 Three strained QWs

In this chapter, the structure of the samples, analysed up to now, comprised a SCH active part composed by two QWs. However to improve the electro-optical performance of the laser (refer to chapter 6), we finally grew a full laser structure, the one that will then bring the best results, with 3 InGaAs QWs, with 40% indium at T_{gr} = 580°C.

We selected these growth condition because 3D feature formation was observed for 3 InGaAs QWs with 40% indium and T_{gr} = 600°C, probably due to the increased strain (Figure 5.27).

When grown at T_{gr} = 580°C the three QWs structure didn't show 3D nanostructures (Figure 5.28), but some evidence of jagged ridges for the 6°A samples, probably pointing out the limits for a 3D nanostructures and defects

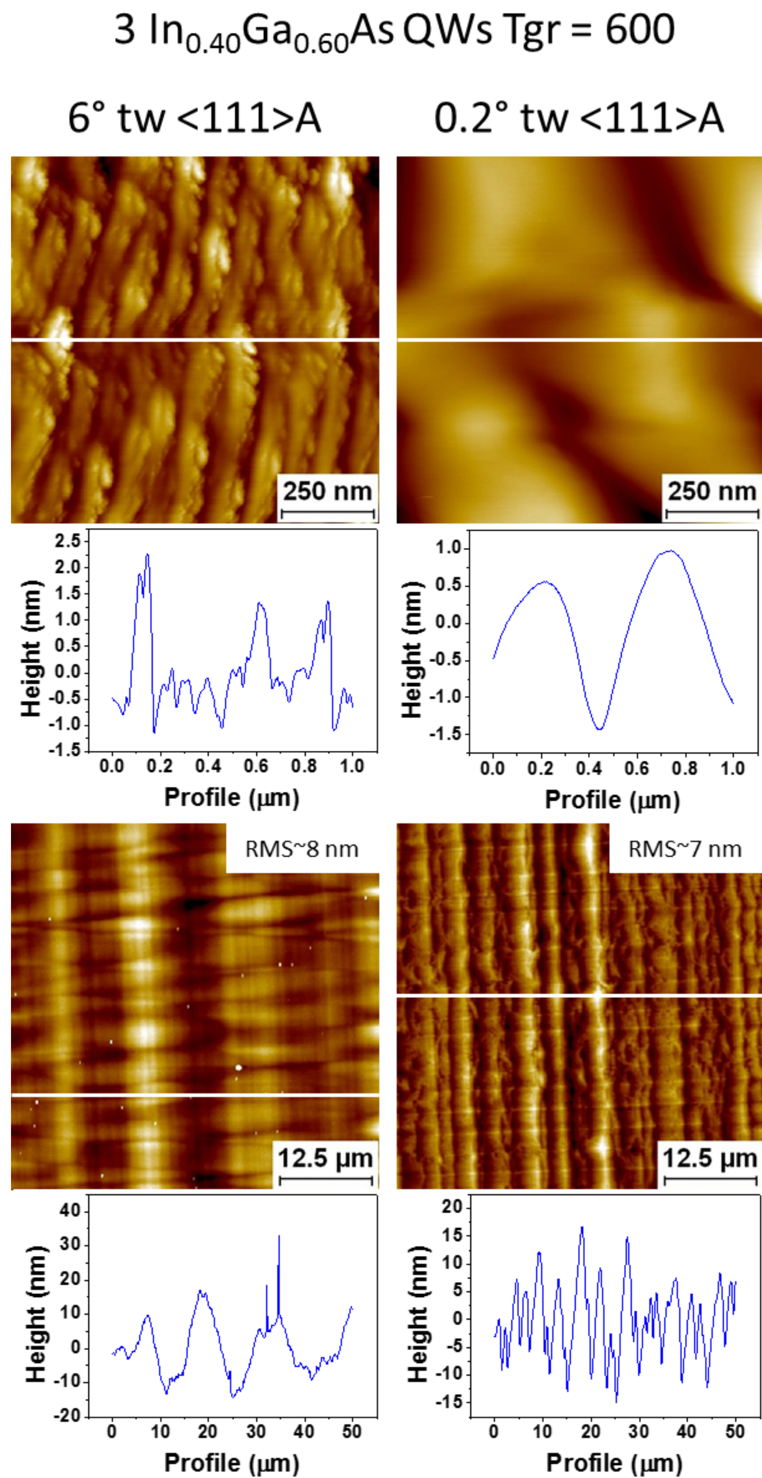

Figure 5.27: AFM images (height and cross-section profile) of three $In_{0.40}Ga_{0.60}As$ QWs grown at T_{gr} = 600°C. Samples grown on GaAs misoriented substrate of 0.2° towards [111]A and 6° towards [111]A.

free surface. Nevertheless we anticipate no significant effect on the final laser structure, as will be discussed in chapter 6.

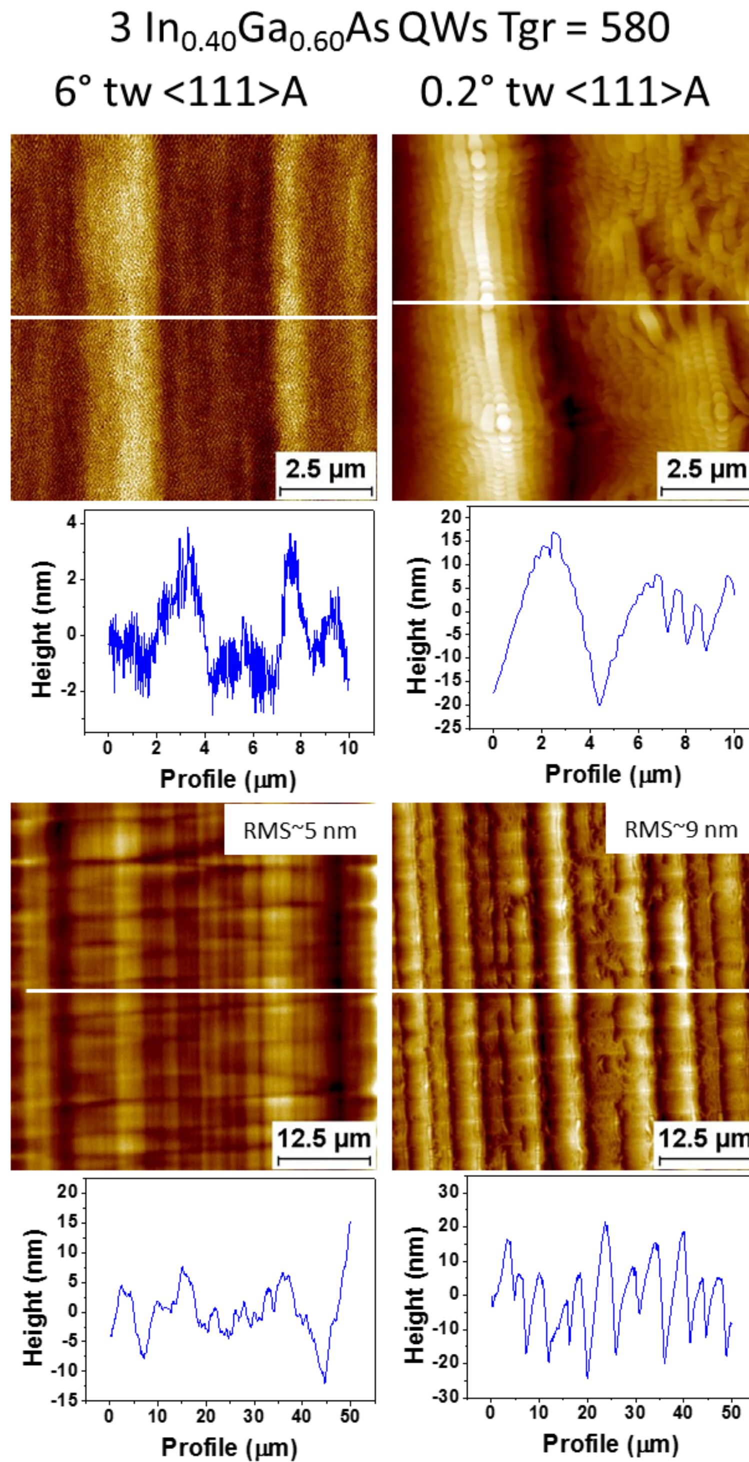

Figure 5.28: AFM images (height and cross-section profile) of three $In_{0.40}Ga_{0.60}As$ QWs grown at T_{gr} = 580°C. Samples grown on GaAs misoriented substrate of 0.2° towards <111>A and 6° towards <111>A.

In Figure 5.29 are showed the room temperature PL spectra of three $In_{0.40}Ga_{0.60}As$ QWs grown at T_{gr} = 580°C with the emission peaked at ~1360 nm, same wavelength detected with two QWs.

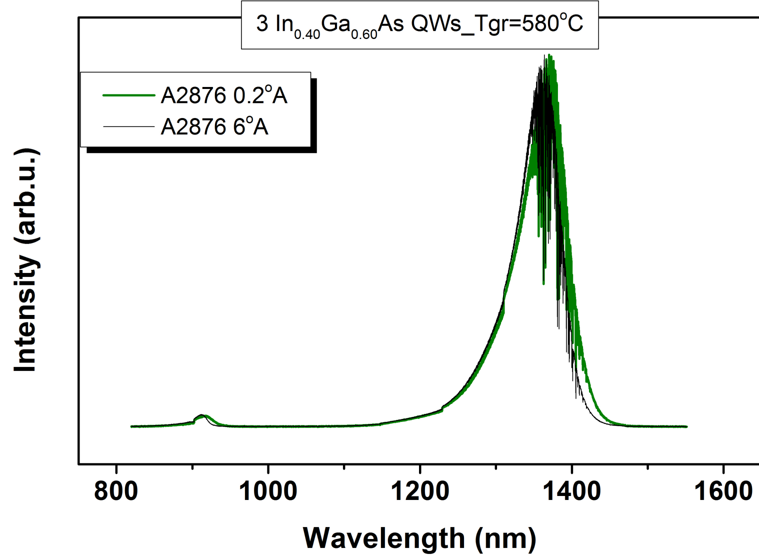

Figure 5.29: Room temperature PL spectra of three $In_{0.40}Ga_{0.60}As$ QWs grown at T_{gr} = 580°C. Samples grown on GaAs misoriented substrate of 0.2° towards [111]A and 6° towards [111]A.

5.9 Summary

The heavily compressive strain in QWs and in the metamorphic buffer layer (in combination with the surface step bunched ordering) promote 3D feature formation under certain growth temperatures and for a certain percentage of indium in the QWs.

To avoid and control the 3D nanostructuring we proposed as a possible solution the insertion of a GaAs layer deposited before the QW. We attested that 5 nm of GaAs was sufficient to delay the nanostructures formation process, without perturbing the optical emission from the active SCH part.

Moreover, we studied a range of growth temperature and indium content in the QWs 3D-nanostructures and defects free, verifying the emission of interest.

Between 540°C and 650°C the 3D nanostructures don't appear on the surface; in this range of growth temperatures we can grow 2 InGaAs QWs with up to 40% of indium, the limit in temperature is shifted at 580°C for 3 InGaAs QWs with same 40% of indium.

The optical emission is obviously affected by the composition of the QWs: i.e. high value of indium in the QW means long wavelength. However the emission can be redshifted or blueshifted by decreasing or increasing the growth temperature respectively (by probably affecting incorporation), choosing in this manner the desired emission in the free defects and 3D-nanostructures

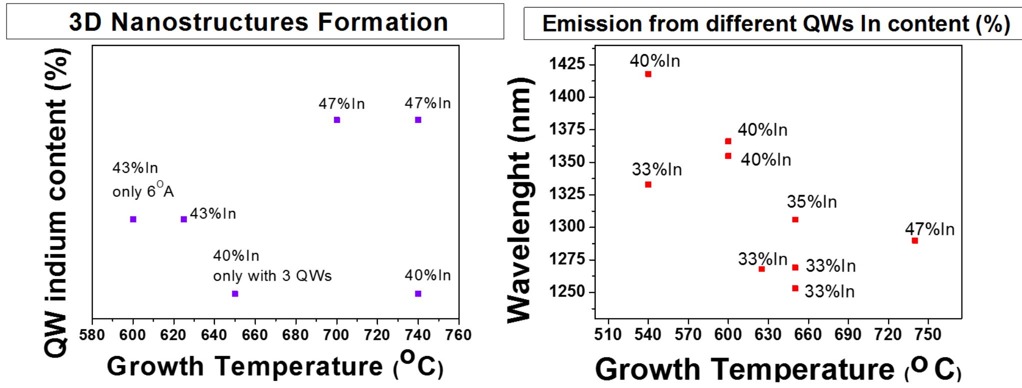

Figure 5.30: Left side: 3D nanostructures formation depending on QWs indium content(%) and growth temperature of the SCH part. Right side: Emission wavelength from different composition of the QWs depending on the growth temperature of the SCH part.

range (Figure 5.30). Following the observations just discussed we developed (at different moments of the development process) different full epitaxial laser structure with the following growth parameters:

- full laser- 5 nm of GaAs before each QW, SCH-2 $In_{0.35}Ga_{0.65}As$ QWs at $T_{gr} = 650°C$;
- full laser- 5 nm of GaAs before each QW, SCH-2 $In_{0.40}Ga_{0.60}As$ QWs at $T_{gr} = 600°C$;
- full laser- 5 nm of GaAs before each QW, SCH-3 $In_{0.40}Ga_{0.60}As$ QWs at $T_{gr} = 580°C$.

We refer to chapter 6 for a complete analysis of the full laser structures as a function of the opto-electrical proprieties, including the motivations (morphological and optical) which determined the evolution from one to the other.

Chapter 6

Electro-optical characterization of the metamorphic laser

The performance of the metamorphic epitaxial laser structures are discussed here. The final laser structures are the result of all morphological results, strain consideration and epitaxial studies faced in the thesis work. Three different full laser structures were grown. In each addressed section the changes in the epitaxial structure will be discussed . For each epitaxial structure stripe waveguide lasers were fabricated, then characterized electro-optically. In the first part of this chapter an overview is provided, in general terms, of the laser characterization technique.

The device fabrication and the opto-electrical measurements were performed by Brian Corbett's group (III-V photonics group based in Tyndall). The TEM images are provided by the Belfast group of Dr. Miryam Arredondo-Arechavala (School of Mathematics and Physics, Centre for Nanostructured Media (CNM), Queen's University Belfast).

6.1 Laser characterization

The material overal quality characterization and the laser diodes performance can be extracted from the light-current (L-I) and the voltage-current (V-I) characteristics [1, 2]. The L-I characteristics plot the light output in lasing mode as a function of the injected current, allowing the determination of the threshold condition. When the laser diode is forward biased, electrons and holes are injected into the active region of the laser, which, when recombining, emit photons. As the injected current is increased, the laser structure first demonstrates spontaneous emission which then increases very gradually until it begins to emit stimulated radiation (Figure 6.1). The threshold condition is reached when the cavity gain overcomes the cavity loss for any photon energy. The first parameter of interest is the exact current value at which this

phenomenon takes place. This is typically referred to as the threshold current and is denoted by the symbol I_{th}. However, because the threshold current (I_{th}) depends upon the size and the area of the laser devices, to compare threshold conditions it is common use to refer to the density threshold current (J_{th}), obtained by dividing the experimental I_{th} by the area of the laser.

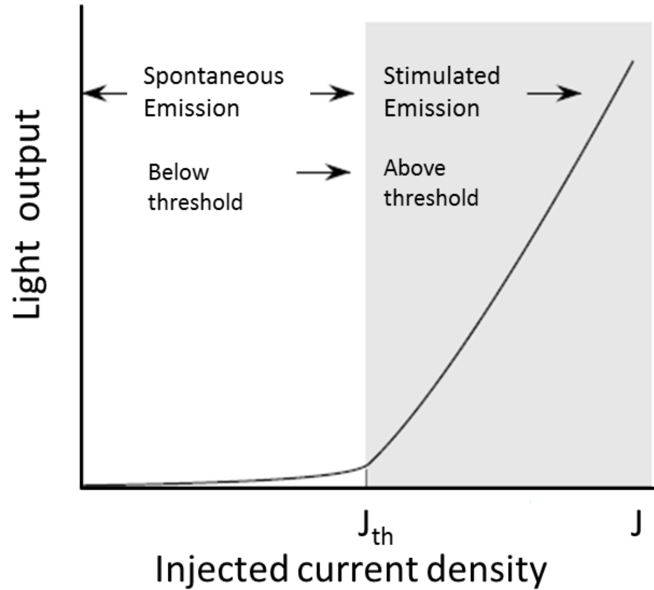

Figure 6.1: The light output in the lasing modes as a function of current injection in a semiconductor laser. Above threshold, the presence of a high photon density causes stimulated emission to dominate [3].

The laser diode quality in terms of conversion rate is related to the slope of the L-I curve above the threshold current, denoted as $\Delta P/\Delta I$, indicating how many Watts of power the laser outputs for every 1 Amp increase in its input current. Directly from the slope efficiency it is possible to compute the external differential quantum efficiency η_d, i.e. efficiency in converting electron-holes pairs in emitted photons, and the internal quantum efficiency η_i, i.e. the overall efficiency of a laser in converting electron-hole pairs (injected current) into the photons (light) within the laser diode structure. The external differencial quantum efficiency (η_d) value is based on the comparison between the behaviour of an ideal perfect laser and the real laser under test. In an ideal laser diode, the recombination of each electron-hole pair results in the emission of one photon. In a real laser diode, however, the recombination of some electron-hole pairs result in the generation of other, undesirable, forms of energy, such as heat. Moreover, not all the photons generated inside the cavity are emitted from the laser diode. Some of them are reabsorbed within

the waveguide structure. Thus, on increasing current I by an amount ΔI, i.e., by injecting $\Delta I/q$ numbers of charge carriers in time Δt, where q is the fundamental electronic charge, if the optical power increases by an amount ΔP, then we get $\Delta P/(hc/\lambda)$ number of photons emitted out, where h is the Planck's constant and (hc/λ) is the energy of single photon with wavelength λ. Thus, according to the definition of external differential quantum efficiency,

$$\eta_d = \frac{\Delta P/(hc/\lambda)}{\Delta I/q} = 2\frac{\Delta P}{\Delta I}\left[\frac{q\lambda}{hc}\right] \tag{6.1}$$

where the number 2 should be taken into account when the laser emits light from both its front and back mirror facets; h is the Planck's constant, c is the velocity of light in vacuum and $\Delta P/\Delta I$ is the slop efficiency of the laser diode. Whereas, the $\boldsymbol{\eta}_{\mathrm{i}}$ is extracted by plotting the curve of inverse external differential quantum efficiency versus the cavity length. Not all of the photons that are generated find their way out of the device; some of them are reabsorbed due to various internal loss mechanisms. According to Biard et al. [4], the $\boldsymbol{\eta}_{\mathrm{d}}$ and $\boldsymbol{\eta}_{\mathrm{i}}$ are related by :

$$\frac{1}{\eta_d} = \frac{1}{\eta_i}\left[1 + \frac{\alpha_i}{\ln(1/R)}L\right] \tag{6.2}$$

where α_i is the internal loss, R is the reflectivity of the mirror facets of the laser, and L is the cavity length.

The turning voltage (V_0), i.e. the minimum required externally applied voltage to have the lasing from the device, together with the series resistance can be extract from the V-Is characteristics.

6.2 First full laser: cladding SL

In table 6.1 is reported the detailed layers sequence of the first full metamorphic laser structure. The structure is based on the epitaxial layer analysis in terms of morphology, strain and defect formation control explained in the relative previous chapters. For ease of reading the structure will be indicated in the chapter with the sequence number of sample growth, A2426.

All the layers were grown with MOVPE on n-GaAs (100) with a specific misorientation towards (111)A substrate . After a 100 nm thick GaAs buffer, a 1000 nm $\mathrm{In}_x\mathrm{Ga}_{1-x}\mathrm{As}$ parabolic graded MBL was grown. Then, a metamorphic MQW structure containing cladding, active, and contact layers was grown. The claddings were grown with the relevant and signature superlattice structure built as a combination of AlInGaAs and InGaP alloys. The lower

and upper cladding layers were Si-doped and Zn-doped, with concentration of $\sim 1 \times 10^{18} cm^{-3}$ and $\sim 8 \times 10^{17} cm^{-3}$ respectively. The active region consisted of two compressively strained $In_{0.35}Ga_{0.65}As$ quantum wells sandwiched between $In_{0.13}Ga_{0.87}As$ and $Al_{0.12}In_{0.14}Ga_{0.74}As$ barrier layers, and preceded by 5 nm of GaAs interface controlling layer (CIL) layer. Finally, a 100 nm thick InGaAs top p-contact layer with Zn doping of $1 \times 10^{19} cm^{-3}$ was grown. The growth temperature was kept at 740°C for all the laser structure except in the active region, were it was decreased down to 650°C to avoid the 3D nanostructure formation as discussed in chapter 5.

Table 6.1: Layer structure sequence of the first metamorphic layer tested: sample A2426

Layer	**Composition**	**Thickness** (nm)	**Doping** (cm^{-3})
contact	$In_{0.18}GaAs$	100	1×10^{19} (Zn)
p-cladding	$In_{0.15}Al_{0.31}Ga_{0.54}As$:Sb $In_{0.62}Ga_{0.38}P$:Sb	250×5 50× 5	8 -10 × 10^{17} (Zn)
upper guide	$In_{0.14}Al_{0.12}Ga_{0.74}As$:Sb	100	
barrier	$In_{0.13}Ga_{0.87}As$	80	
QW	$In_{0.35}Ga_{0.65}As$	7	
CIL	GaAs	5	
barrier	$In_{0.13}Ga_{0.83}As$	20	
QW	$In_{0.35}Ga_{0.65}As$	7	
CIL	GaAs	5	
barrier	$In_{0.13}Ga_{0.83}As$	80	
lower guide	$In_{0.14}Al_{0.12}Ga_{0.74}As$:Sb	100	
n-cladding	$In_{0.62}Ga_{0.38}P$:Sb $In_{0.15}Al_{0.31}Ga_{0.54}As$:Sb	50× 5 250×5	1×10^{18} (Si)
MBL	InGaAs	1000	
buffer	GaAs	100	
n-Substrate	GaAs	100	1-2 × 10^{18} (Si)

The opto-electrical characterization was performed on a stripe waveguide with 80 µm wide stripe contacts and variable cavity length (CL). The L-Is curves were achieved in pulsed mode at room temperature with 0.1% of duty cycle, which indicates the percentage of how long the laser is in the "on" state and defined as the ratio between pulse width and period.

From a preliminary analysis, the devices showed a promising lower threshold current (in pulse mode). For cavity lengths in the range 0.4-1.36 mm the

J_{th} per QW span between 147 A/cm^2 and 217 A/cm^2. Some parameters related to these devices and extracted from the L-Is characteristics are reported in table 6.2.

Table 6.2: Parameters extracted from L-Is relatives to A2426 metamorphic laser sample grown on GaAs (100) 0.2° and 6°A towards <111>A substrates.

	CL (μm)	I_{th} (mA)	J_{th} per QW (A/cm^2)	η_d (%)
0.2°A	400	130	204	18.87
	720	184	160	15.15
	1000	231	147	10.91
6°A	700	243	217	7.03
	1000	257	161	8.34
	1360	327	150	9.64

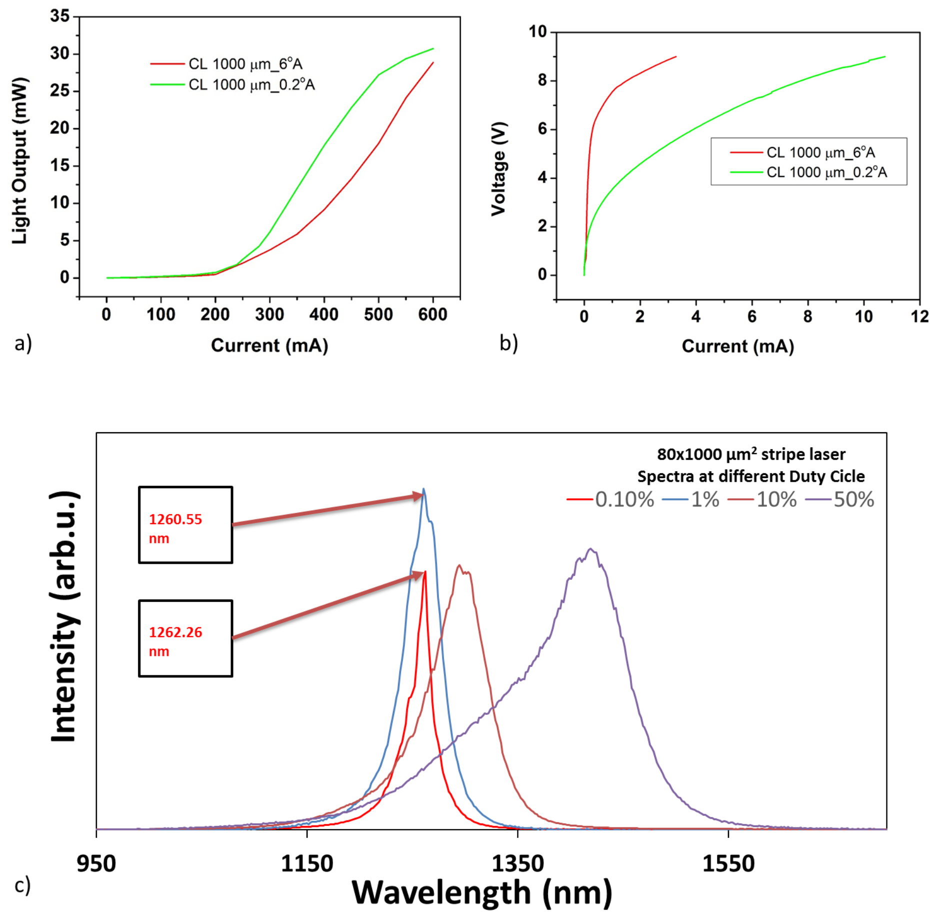

Figure 6.2: a) L-I characteristic for a stripe laser from metamorphic laser samples grown on GaAs (100) 6° towards <111>A substrates. c) Spectrum of the same device as a function of different duty cycles .

However, the slope efficiency and consequently the external differential quantum efficiency resulted extremely low, evidently underling a limited conversion rate of electric power into light power. Also we observed a fast power saturation, especially for the laser structure grown on GaAs (100) 0.2° towards [111]A (Figure 6.2 (a)). However, the main issue was originated from the high turning voltage, e.g. exceeding 7 Volts for ridge laser grown on GaAs (100) 6° towards [111]A as shown in Figure 6.2(b), and the extremely high series resistance close to 50Ω, entailing the electrical power dissipation, limiting the output optical power, the temperature range for CW operation, and the overall power efficiency.

The emission spectrum for the stripe $80 \times 1000 \mu m^2$ laser at different duty cycles, is reported in Figure 6.2(c). The wavelength emission centred at ∼1260 nm was achieved with two InGaAs QWs with 35% indium content. The composition of the QWs was successively, in the second laser structure, increased up to 40% indium content, to reach 1300 nm emission at low duty cycle.

No lasing was observed in CW mode operation.

6.3 Second full laser: upper cladding SL ramp

The detailed epitaxial structure of the second full metamorphic laser, sample A2642, is reported in table 6.3, where the main changes are highlighted in different colour to facilitate the reading.

The p-cladding SL layer sequence was modified following the aim to improve the carrier transport. Also the number of the interfaces was reduced at 4, increasing the InGaP layer thickness up to 100 nm.

At the interface InGaP/AlInGaAs the percentage of gallium was linearly graded from ∼ 0% to 54% and the aluminium from 85% to 31%, keeping the indium content constant, over a distance of 26 nm. In this manner the holes transport toward the active part is supposed to be facilitated, and the band structure can be sketched like in Figure 6.3.

Using a linear grading in the cladding part is not an original way to improve the electrical characteristic, especially because it can be readily achieved by MOVPE. For example in reference [5], distributed Bragg reflectors, inserted in a VCSEL structure, were linearly graded to successfully reduce the series resistance and operating voltage.

The strategy revealed promising also in our case. Indeed the V-I characteristics show a turning voltage considerably reduced. In Figure 6.4 is shown

Table 6.3: Layer structure sequence of A2642 laser sample

Layer	Composition	Thickness (nm)	Doping (cm^{-3})
contact	$In_{0.18}GaAs$	100	1×10^{19} (Zn)
p-cladding	$In_{0.15}Al_{0.31}Ga_{0.54}As{:}Sb$	224×4	8 -10 $\times 10^{17}$ (Zn)
	$Al_{0.85}In_{0.15}As \rightarrow In_{0.15}Al_{0.31}Ga_{0.54}As$	26×4	
	$In_{0.62}Ga_{0.38}P{:}Sb$	100× 4	
upper guide	$In_{0.14}Al_{0.12}Ga_{0.74}As{:}Sb$	100	
barrier	$In_{0.13}Ga_{0.87}As$	80	
QW	$In_{0.40}Ga_{0.60}As$	7	
CIL	GaAs	5	
barrier	$In_{0.13}Ga_{0.87}As$	20	
QW	$In_{0.40}Ga_{0.60}As$	7	
CIL	GaAs	5	
barrier	$In_{0.13}Ga_{0.87}As$	80	
lower guide	$In_{0.14}Al_{0.12}Ga_{0.74}As{:}Sb$	100	
n-cladding	$In_{0.62}Ga_{0.38}P{:}Sb$	50× 5	1×10^{18} (Si)
	$In_{0.15}Al_{0.31}Ga_{0.54}As{:}Sb$	250×5	
MBL	InGaAs	1000	
buffer	GaAs	100	
n-Substrate	GaAs	100	1-2 $\times 10^{18}$ (Si)

the Light-current-voltage (L-I-V) characteristic and the corresponding emission spectrum of the best device examined, $80 \times 400\mu m^2$ stripe contacts. For this specific device we registered a J_{th} of $\sim 420A/cm^{-2}$ ($210A/cm^{-2}$ per QW), a slope efficiency of $\sim 0.2WA^{-1}$ and a very low $V_0 \sim 0.76V$. Nevertheless, the series resistance (R_s) remained high, $R_s \sim 32\Omega$.

The increased strain in the QWs compared to the first laser tested, red-shifted the wavelength up to the desired range $\sim 1320nm$. The emission was tested just in pulsed mode at room temperature.

In addition, a more accurate characterization of different cavity length stripes exhibited high variability between devices on the same bar, i.e for adjacent devices. In particular, the plot of the cavity length dependence of the inverse external differential quantum efficiency highlighted major fluctuations on the devices built on the epitaxial structure which shared the GaAs 6°A off-cut substrate (Figure 6.5). We could still individuate a linear fit for the stripe laser built on the 0.2°A GaAs substrate, and from the Equation 6.2 extrapolate the internal loss. Assuming the linear fit indicated in Figure 6.5(a) the α_i was $\sim 15cm^{-1}$, and η_i was $\sim 22.5\%$. Whereas competitive values from the pseudomorphic literature are around 10% for the internal loss and 90% for the efficiency. However, it was not clear how to rank the different epi-structures.

An extra epitaxial laser structure was grown with the only variation of a double grading/ramp in the upper cladding, as sketched in Figure 6.6.

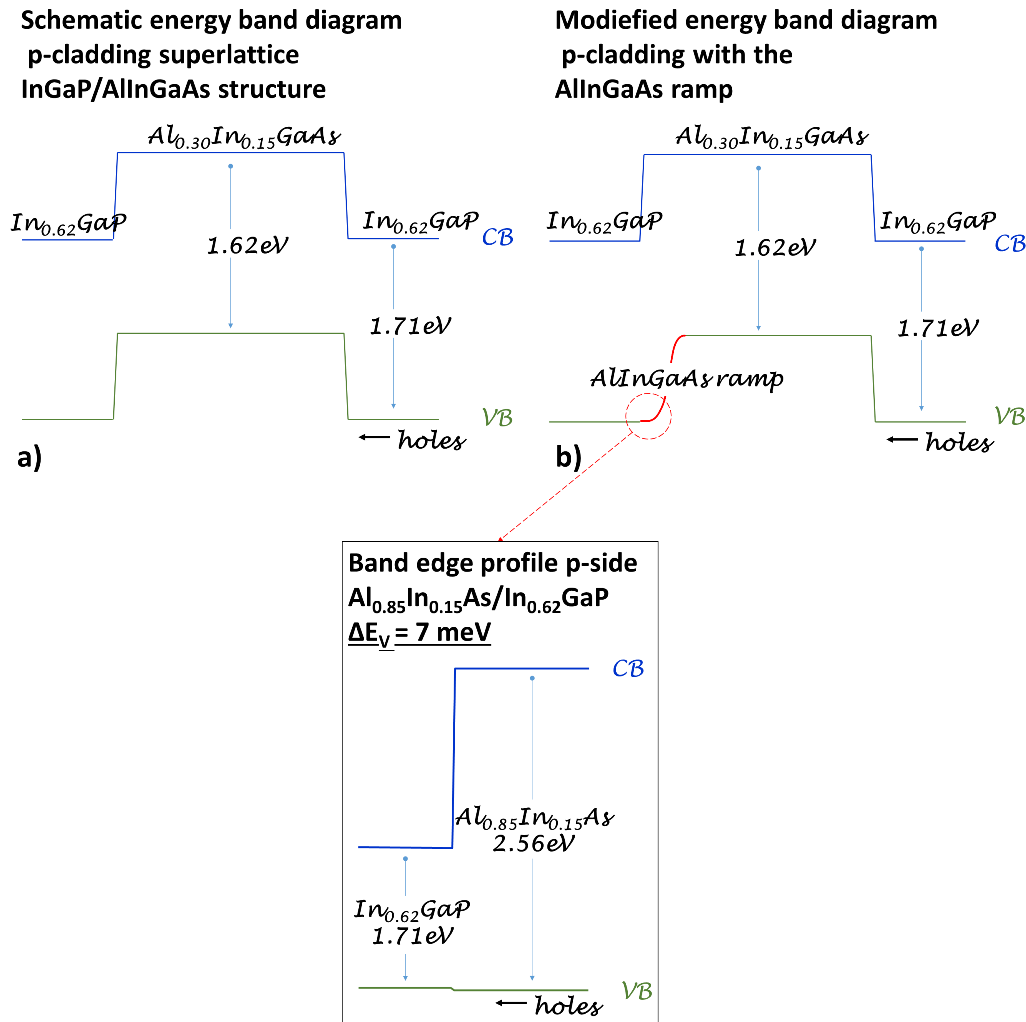

Figure 6.3: Schematic energy band diagram of the p-cladding InGaP/AlInGaAs superlattice structure: a) for InGaP/AlInGaAs SL p-cladding layer, used in the first laser design; and b) for the modified p-cladding with the AlInAs/AlInGaAs grading at the interfaces InGaP/AlInGaAs, used in the second laser structure. Theoretical calculation of the band gap alignment were performed by Silviu Bogusevschi (Photonics Theory group based in Tyndall).

The stripe laser built on this structure showed opto-electrical results similar to those obtained with the one ramp upper cladding structure (not shown here). In particular, we observed the same high variability between devices on same bar. On the other hand both structure designs shared similar low threshold current and low turning voltage, showing best results in term of threshold efficiency for short devices. The dependency of short cavity length versus efficiency is not a novelty but several times observed in strained QWs lasers, e.g [6, 7].

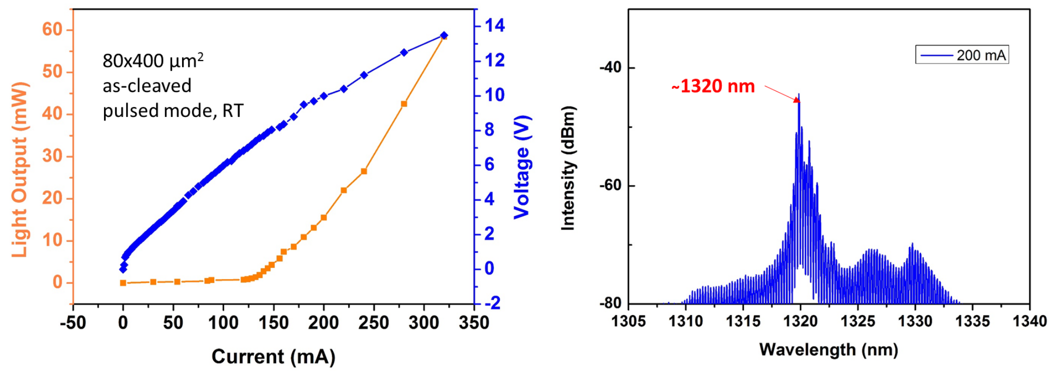

Figure 6.4: L-I-V characteristic of a stripe laser waveguide with a cavity length of 400 μm and corresponding spectrum laser at high resolution, peaked at 1320 nm.

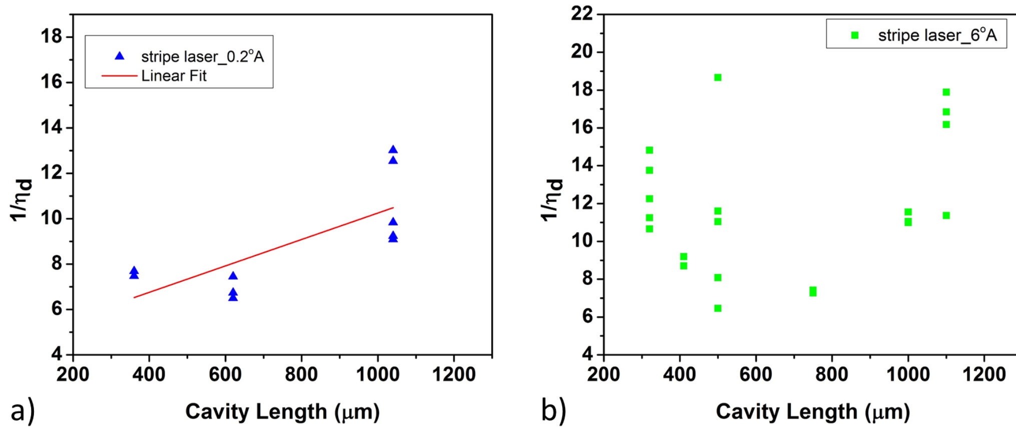

Figure 6.5: The cavity length dependence of the inverse external differential quantum efficiency for stripe devices fabricated with two different misoriented epitaxial structures: GaAs a) 0.2°A and b) 6°A offcut.

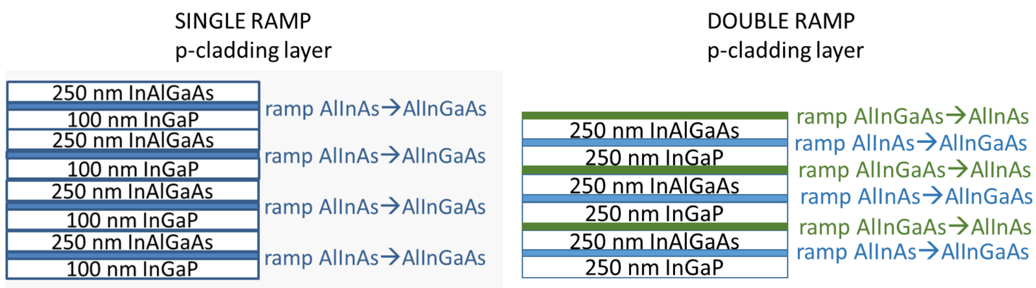

Figure 6.6: Sketch of the layer sequence in the upper cladding layer: a) single grading/ramp at the interface InGaP/AlInGaAs and b) double grading/ramp at the interface InGaP/AlInGaAs and AlInGaAs/InGaP.

6.4 Third full laser: MBL substrate doping

Table 6.4: Layer structure sequence of A2938 laser sample

Layer	Composition	Thickness (nm)	Doping (cm^{-3})
contact	$In_{0.18}GaAs$	100	1×10^{19} (Zn)
p-cladding	$In_{0.15}Al_{0.31}Ga_{0.54}As{:}Sb$ $Al_{0.85}In_{0.15}As{:}Sb \rightarrow In_{0.15}Al_{0.31}Ga_{0.54}As{:}Sb$ $In_{0.62}Ga_{0.38}P{:}Sb$	1400	$8/10 \times 10^{17}$ (Zn)
upper guide	$In_{0.14}Al_{0.12}Ga_{0.74}As{:}Sb$	100	
barrier	$In_{0.13}Ga_{0.87}As$	80	
3rd QW	$In_{0.40}Ga_{0.60}As$	7	
CIL	GaAs	5	
barrier	$In_{0.13}Ga_{0.87}As$	20	
2nd QW	$In_{0.40}Ga_{0.60}As$	7	
CIL	GaAs	5	
barrier	$In_{0.13}Ga_{0.87}As$	20	
1st QW	$In_{0.40}Ga_{0.60}As$	7	
CIL	GaAs	5	
barrier	$In_{0.13}Ga_{0.87}As$	80	
lower guide	$In_{0.14}Al_{0.12}Ga_{0.74}As{:}Sb$	100	
n-cladding	$In_{0.62}Ga_{0.38}P{:}Sb$ $In_{0.15}Al_{0.31}Ga_{0.54}As{:}Sb$	1200	1×10^{18} (Si)
MBL	InGaAs	1000	$1/3 \times 10^{18}$ (Si)
buffer	GaAs	100	1×10^{18} (Si)
n-Substrate	GaAs	100	$1/2 \times 10^{18}$ (Si)

The main changes implemented in the third laser structure concerned:

- addition of the third $In_{0.40}Ga_{0.60}As$ QW;
- lower cladding grown with AlInGaAs layer ramped from $Al_{0.07}In_{0.15}Ga_{0.78}As$ to $Al_{0.31}In_{0.15}Ga_{0.54}As$ at the InGaP/AlInGaAs interface;
- doping of the MBL.

The full epitaxial laser structure is summarized in table 6.4.

Three QWs

The morphology and the surface organization related to the deposition of three QWs has already been presented in chapter 5. It should be reminded that the introduction of a third QW in the active part entailed the reduction of the growth temperature to T_{gr}= 580°C, to keep the surface smooth and to avoid the formation of 3D nanostructures. In addition to the AFM images, shown in the previous chapter, high angle annular dark field (HAADF) images recorded with a scanning transmission electron microscope (STEM), confirmed

the absence of defects and 3D features in the active part (Figure 6.7). An average evaluation of the layers thickness by the HAADF images confirmed also the nominal thickness of the deposited layers.

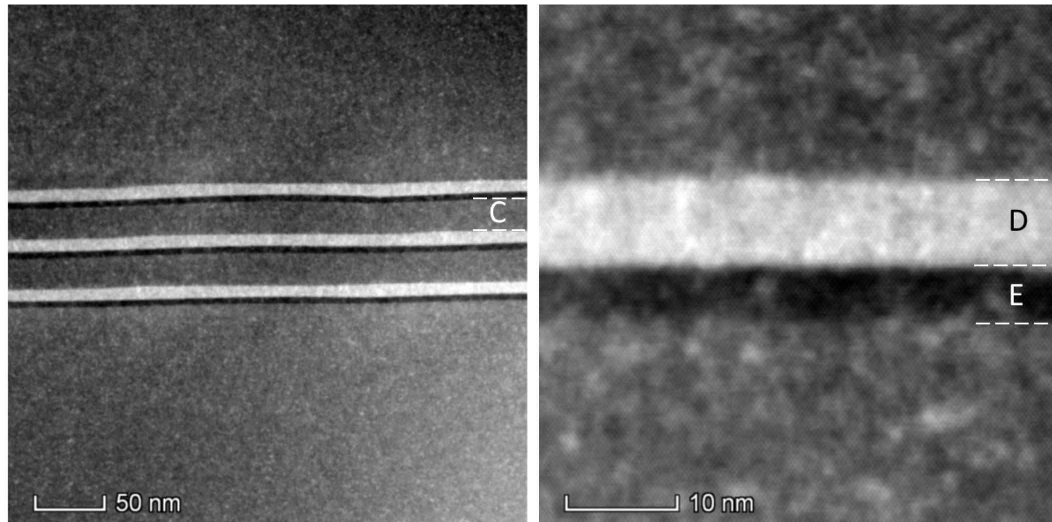

C 22.59 nm
D: 9.26 nm
E: 5.05 nm

Figure 6.7: HAADF TEM image zoomed-in the laser active part, composed by three $In_{0.40}Ga_{0.60}As$ QWs (labelled as D), preceded by GaAs CIL layer(labelled as E) and separated by $In_{0.13}Ga_{0.83}As$ barrier (labelled as C).

Lower cladding ramp

The lower cladding was upgraded reducing the number of interfaces and the total thickness to 1200 nm instead of 1500 nm as in the previous laser structure.

In addition the lower SL cladding was implemented with an AlInGaAs layer ramped from $Al_{0.07}In_{0.15}Ga_{0.78}As$ to $Al_{0.31}In_{0.15}Ga_{0.54}As$ at the InGaP/AlInGaAs interface. This modified the band alignment gap between AlInGaAs and InGaP in the conduction band, easing the electron motion towards the active part. In Figure 6.8 is presented a sketch of the assumed band alignment at the InGaP/AlInGaAs interface.

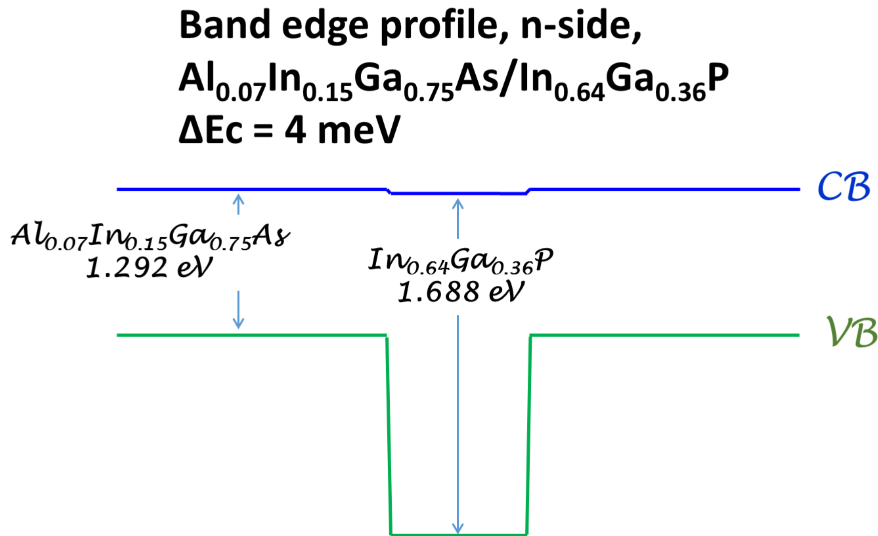

Figure 6.8: Schematic energy band diagram of the n-cladding at the interface AlInGaAs/InGaP of the superlattice structure implemented with AlInGaAs layer ramped from $Al_{0.07}In_{0.15}Ga_{0.78}As$ to $Al_{0.31}In_{0.15}Ga_{0.54}As$ at the InGaP/AlInGaAs interface. Theoretical calculation of the band gap alignment were performed by Silviu Bogusevschi (Photonics Theory group based in Tyndall)

MBL doping

The doping of the grading buffer is a delicate question, because it is not completely understood. In the literature, some groups investigated the beryllium and silicon doping effect on the surface roughness on $In_xGa_{1-x}As$ metamorphic buffers on GaAs [8, 9], grown by MBE technology. They found that doping can have a strong influence on the strain relaxation of InGaAs buffer layers with a linear source temperature grading, observing that the Be reduced the threading dislocations density and the surface roughness while the Si doping increased both, with respect to the undoped reference. At a later stage they showed that the negative doping effect was reduced using a linearly graded profile in the InGaAs buffer, affirming that a moderate In grading slope is preferable for the strain relaxation and the minimization of the negative effect of Si doping. The explanation proposed is that Be doping, in part acting as a surfactant, suppresses In segregation and Si doping enhances the effect. When the amount of In on the surface is reduced, strain induced In surface diffusion is also reduced correspondingly.

On the other hand, and differently from what observed by MBE, the sample A2938, grown using the superlinear parabolic grading profile (please, refer to chapter 3 for MBL design details), didn't present any degradation of the surface due to the Si doping, as confirmed by AFM, TEM and HRXRD examination.

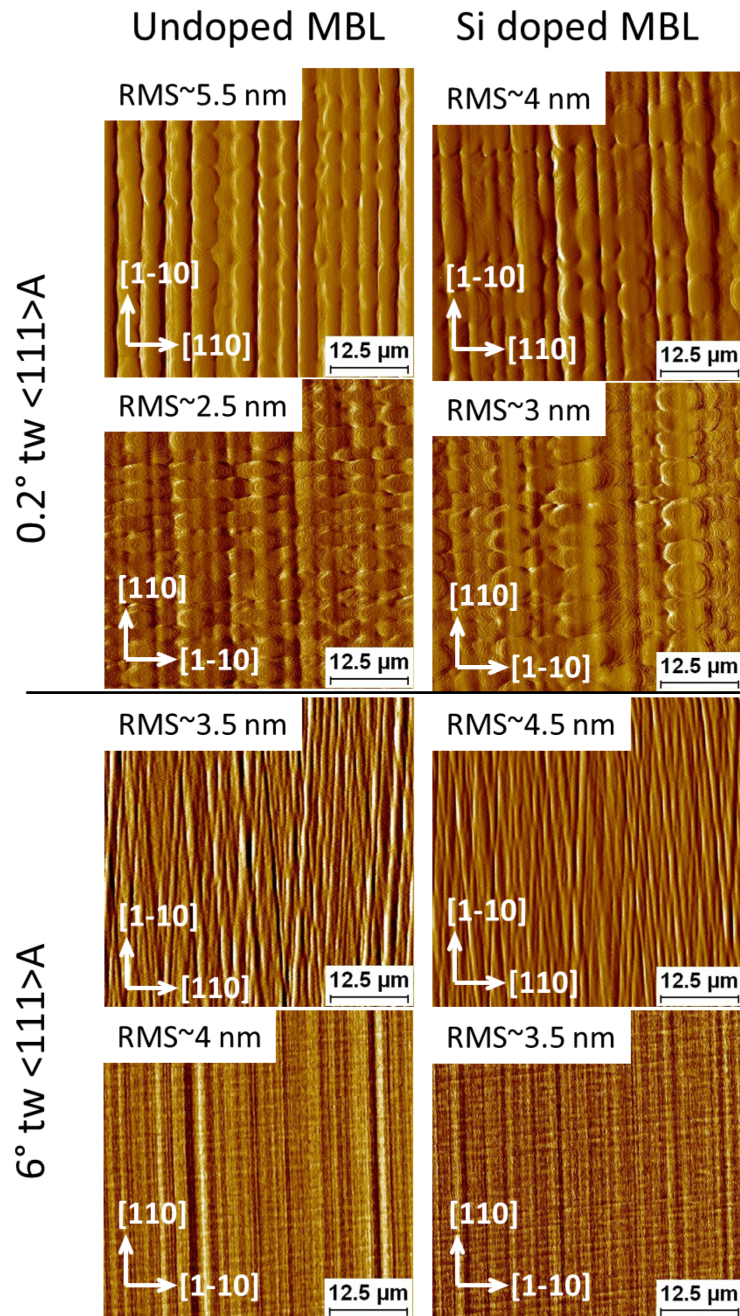

Figure 6.9: Surface morphology of the $In_xGa_{1-x}As$ MBL following a superlinear parabolic exchange curve. AFM images (signal amplitude) for the two <110> directions for undoped, on the left side, and Si doped, on the right side, samples, grown on GaAs (100) 0:2°A, 4°A and 6°A misoriented substrate.

In Figure 6.9 is presented the comparison, in terms of surface morphology, between one undoped and one Si doped MBL samples. The AFM images highlight same surface morphology and same order of magnitude for the RMS value for both samples.

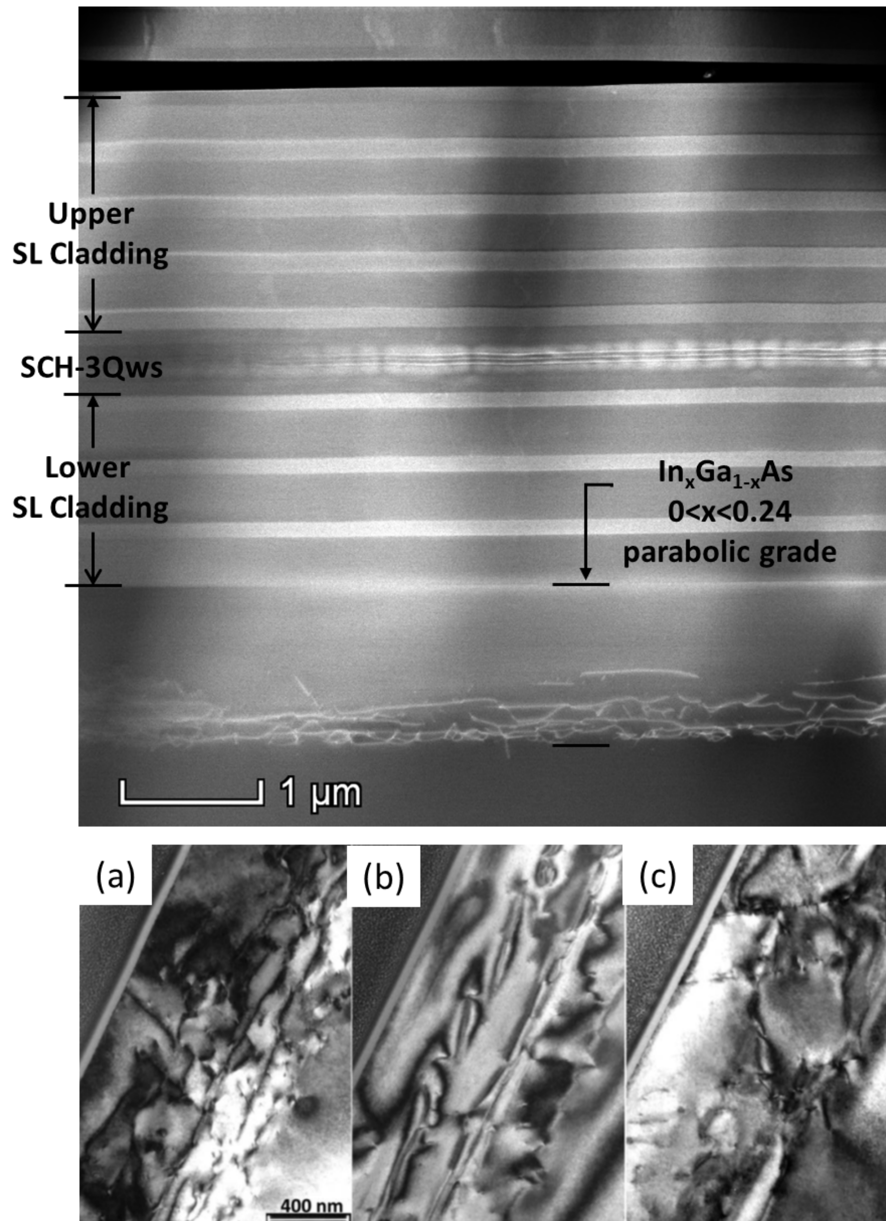

Figure 6.10: Cross-sectional TEM of Si doping effect: (top row) sample of our parabolic grading buffer profile, grown with MOVPE technology, and (bottom row) linear grading buffer profile for three samples with different In grading slope and composition, grown with MBE technology [9].Sample with a) In 63%, b) In 42% and c) In 21%.

In addition the TEM micrograph of the full laser epitaxial structure confirmed that the Si doping doesn't affect the surface morphology of the buffers

when a parabolic grading buffer profile is used. The threading dislocation didn't propagate, but remained confined in the first part of the grading close to the GaAs substrate. For the sake of clarity in Figure 6.10 is reported the comparison between the TEM image of our MBL Si doped, top side, and the TEM images extracted from the paper aforementioned [9].

The HRXRD evaluation confirmed the absence of extra peak between the GaAs substrate and the metamorphic buffer, and no obvious evidence of In segregation is revealed (Figure 6.11).

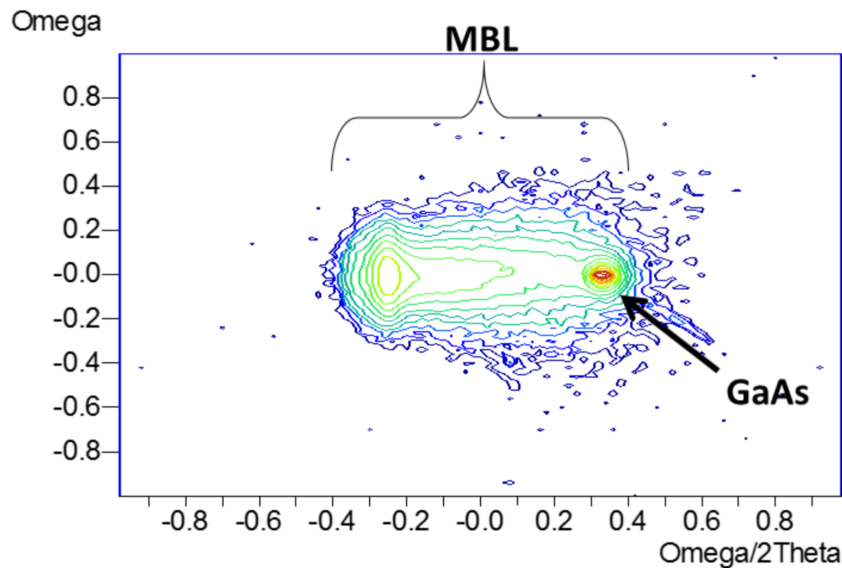

Figure 6.11: 2-axis X-ray diffractogram in 004 reflection of the Si doped sample.

6.4.1 Third laser characterization

The modified epitaxial laser structure showed improved electric and optical characteristics, no more fluctuation in the results between adjacent devices and no substantial differences were noted between the samples grown on GaAs 0.2 A and 6 A miscut.

It should be said that further characterization and processing is ongoing while this thesis is writing, and the reported results should be considered representative, but still in their preliminary phase.

A 500 μm long and 2.5 μm wide stripe waveguide was fabricated to be immediately comparable with previous devices of the same size. This specific stripe exhibited a threshold current I_{th} of $\sim$ 152 mA, corresponding to a J_{th} of $\sim$ 127 mA per QWs , operating at room temperature in pulse mode. The turning voltage was $\sim$ 0.8 V, and the resistance series resulted reduced to 4.5

Ω. The emission wavelength was peaked at ∼ 1.34 μm, registered in pulse mode at low duty cycle (Figure 6.12).

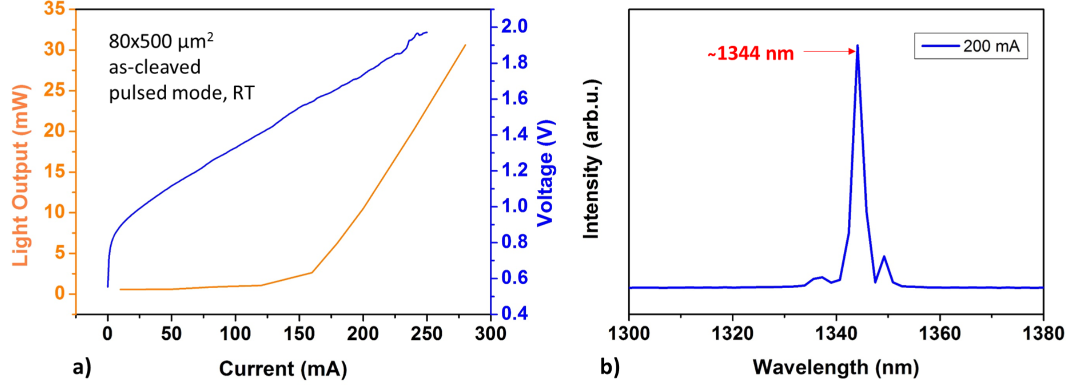

Figure 6.12: LIV characteristic of a stripe laser waveguide with a cavity length of 500 μm and the corresponding spectrum laser at low resolution, peaked at 1340 nm.

Moreover, shorter stripes laser, 10 μm and 20 μm wide, with different cavity lengths were fabricated to have a lower threshold current and to perform the characteristic temperature study. The analysis of the threshold current at different temperatures permits the extraction of the characteristic temperature, T_0 according to

$$I_{th} = I_0 e^{(T/T_0)}$$
$$T_0 = \frac{\Delta T}{\Delta ln(I_{th})} \tag{6.3}$$

Where, I_{th} is the threshold current, I_0 is a fitting parameter, T is the temperature of the stage and T_0 is the characteristic temperature. High values of T_0 imply that the threshold current density of the device increases less rapidly with increasing temperatures. The measurements were performed in pulsed mode with pulse width of 1 μs to ensure limited additional heating. The threshold current varied from 130 mA to 170 mA in the operating temperature range of 30 °C-80 °C (Figure 6.13a)). The T_0 was 95 K. This T_0 value is below the remarkable value of 187 K achieved in the R. Nakao et al work for an InGaAs multi quantum wells metamorphic laser diode [10], but remain a significant achievement if it is compared with T_0 values for multi wells laser grown on InP substrates, for which is typically around 60-80 K [11, 12]. From this preliminary measurement improvements in terms of efficiency of the laser in converting injected current (electron-hole pairs) into light(photons) within

the laser diode structure were observed. For devices 10 and 20 μm wide the α_i and the η_i extrapolated were $\sim 30cm^{-1}$ and $\sim 57\%$ respectively (Figure 6.13(b)).

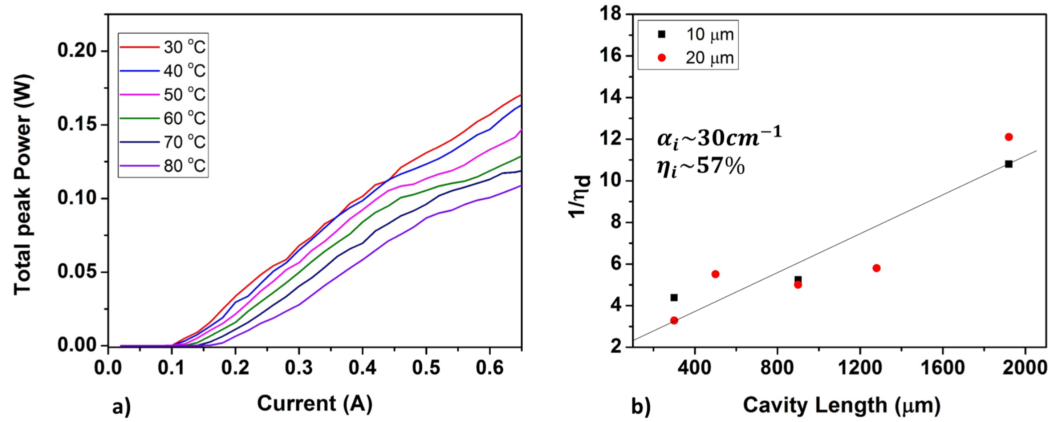

Figure 6.13: (a)L-I characteristics of a stripe laser $20 \times 300\mu m^2$ operating in pulse mode, pulse width $1\mu s$, at temperatures in the range 30 °C-80 °C. (b) The Cavity length dependence of the inverse external differential quantum efficiency for stripes laser, 10 μm and 20 μm wide.

An other significant achievement reached with this epitaxial structure was the lasing in CW mode at $\lambda > 1.3\mu m$. In Figure 6.14 is reported the lasing spectra of a stripe laser, size $10 \times 300\mu m^2$, at 15 °C in function of various injection current, and the corresponding L-Is characteristic measured at 15 °C and 20 °C.

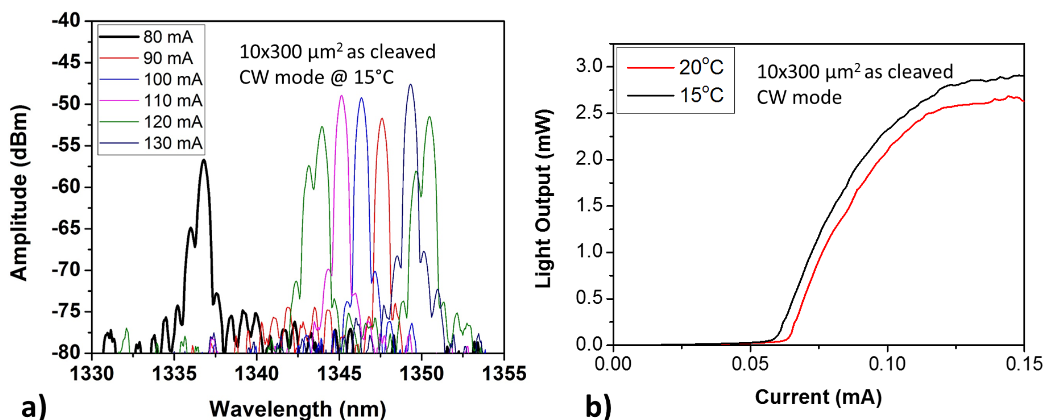

Figure 6.14: (a) Lasing spectra in CW operation mode, of a stripe laser, size 10×300 μm^2, at 15 °C in function of various injection current; and (b) corresponding L-Is characteristic measured at 15 °C and 20 °C.

Those results prove that the epitaxial structures developed in this thesis work allow the fabrication of an InGaAs metamorphic, GaAs based, QW lasers, operating CW at $> 1.3\mu m$ using the MOVPE technology. Specifically the second one after that one reported by the NTT group in Japan [10]. It is important to highlight again that those are preliminary results; the complete material and device characterization is still on going. The device fabricated to date was a simple stripe contact laser. One extra remark is due on the temperature stability of the up to now characterized structures. Our collaborators tell us that they have strong evidence that the superlattice cladding structure has reduced thermal conductivity, complicating CW laser performances. More work is needed to clarify this point which is obviously very relevant, and points to future changes of the cladding structure to improve laser performances.

A final remark is to say that one of the motivations for the outstanding characterization work is linked to the realization that the metamorphic buffer can have detrimental effects on the facets of cleaved devices. For this reason work is ongoing to develop a processing to facet etch. We expect that once such processing will be developed, even stronger performances are to be expected.

Bibliography

[1] KS Mobarhan. "Application note: Test and Characterization of Laser Diodes: Determination of Principal Parameters". In: *Newport Corp., Irvine* (1999).

[2] T Hertsens. "Application note: An Overview of Laser Diode Characteristics". In: *Newport Corp., Irvine* (2005).

[3] Jasprit Singh. *Electronic and optoelectronic properties of semiconductor structures*. Cambridge University Press, 2003.

[4] JR Biard, WN Carr, and BS Reed. "ANALYSIS OF GAAS LASER". In: *Transactions of the metallurgical society of AIME* 230.2 (1964), p. 286.

[5] Ping Zhou et al. "Low series resistance high-efficiency GaAs/AlGaAs vertical-cavity surface-emitting lasers with continuously graded mirrors grown by MOCVD". In: *IEEE Photonics technology letters* 3.7 (1991), pp. 591–593.

[6] JZ Wilcox et al. "Dependence of external differential efficiency on laser length and reflectivities in multiple quantum well lasers". In: *Applied Physics Letters* 55.9 (1989), pp. 825–827.

[7] DP Bour and A Rosen. "Optimum cavity length for high conversion efficiency quantum well diode lasers". In: *Journal of applied physics* 66.7 (1989), pp. 2813–2818.

[8] Ivar Tångring et al. "Manipulation of strain relaxation in metamorphic heterostructures". In: *Applied physics letters* 90.7 (2007), p. 071904.

[9] Yuxin Song et al. "Effects of doping and grading slope on surface and structure of metamorphic InGaAs buffers on GaAs substrates". In: *Journal of Applied Physics* 106.12 (2009), p. 123531.

[10] Ryo Nakao et al. "1.3-μm InGaAs MQW Metamorphic Laser Diode Fabricated With Lattice Relaxation Control Based onIn SituCurvature Measurement". In: *IEEE Journal of Selected Topics in Quantum Electronics* 21.6 (2015), pp. 201–207.

[11] Sandra R Selmic et al. "Design and characterization of 1.3-/spl mu/m AlGaInAs-InP multiple-quantum-well lasers". In: *IEEE Journal of selected topics in Quantum Electronics* 7.2 (2001), pp. 340–349.

[12] T Tsuchiya et al. "Low-threshold and high-temperature characteristics of 1.3-/spl mu/m InGaAlAs MQW lasers grown by metalorganic vapor-phase epitaxy". In: *Conference Proceedings. 2000 International Conference on Indium Phosphide and Related Materials (Cat. No. 00CH37107)*. IEEE. 2000, pp. 266–269.

Chapter 7

InP(As) self-assembled nanostructures: an alternative method for achieving telecom wavelengths

This chapter is based on the published journal letter **Appl. Phys. Lett. 110, 113101 (2017)** [1]. In this chapter, we report on the possibility of transforming novel self-assembled InP nanostructures grown by metalorganic vapour phase epitaxy (MOVPE) on lattice-matched InP substrates into variously shaped InP(As) emitters in the telecom windows. This work represents and interesting alternative for the active material. This ideally follows our proposal for an alternative substrate presented in previous chapters.

The first part of the chapter is devoted to give a brief introduction on the physical principles related to the achievement of quantum confinement. Then the most employed QD fabrication methods will be briefly compared.

In the second part a large phenomenology of morphologies induced by growth condition choices and the post-growth layer exposure to hydrides is critically discussed. The main focus here is to show how the combination of arsenization and cooldown protocols affects the final nanostructures' shape, changing the original dots into rings or domes (and others), conveying a rich variety of nanostructures in a controlled manner.

The chapter concludes with the presentation of the optical results from the engineered nanostructures, with specific configurations delivering clear signatures of single dot emission at both 1.3 and 1.55 microns.

7.1 Quantum size effect

One of the most direct effects of reducing the size of materials to the nanometer range is the appearance of quantization effects due to the confinement of the charge carriers. The confinement of the carriers produces a modification of the electronic density-of-states (DOS), and these changes result in strong variations in the optical and electrical properties with size. In a quantum confined structure the motion of the carriers (electrons and holes) is confined in one or more directions by potential barriers [2]. Four possible confinements are depicted in the Figure 7.1. In the bulk material there is no confinement and the DOS presents a square-root dependence for the energy. In quantum wells, the mobility of the charge carriers (electrons and holes) is confined in the xy plane and the charge carriers are free to move in two-dimensions. The two-dimensional DOS results in a staircase-like function (constant function of the energy). Adding a further confining leads to the one-dimensional semiconductor. In the quantum wires the charge carriers are free to move only along the “x” axis. The energies along the y and z axes are quantized. As one more dimension is confined, more discrete energy levels can be found. In the zero-dimensional case, quantum dots structures, the mobility is restricted in all three spatial dimensions. The energy is quantized in all directions and the DOS is a sum of delta (δ) functions, like an atom.

The quantum-size effect gets observable when the number of dimension in which the carriers can freely move becomes comparable with the de Broglie wavelength λ_{DB}. In semiconductors, the λ_{DB} is related to the effective mass m^* and temperature T, where $\lambda_{DB} = h/\sqrt{3m^* k_B T}$, where h is the Planck's constant and k_B is Boltzmann's constant. For typical semiconductors, the effective electron and hole masses are smaller than the free electron mass m_0. For instance, $m^*_{e,GaAs} = 0.067m_0$ and $m^*_{h,GaAs} = 0.5m_0$. This leads to a de Broglie wavelength on the order of 10-100 nm at low temperatures. In semiconductors often are taken into account the effects of excitons, i.e., correlated electron-hole pairs. Instead of considering λ_{DB} for electrons and holes separately, the relevant quantity of the two-particle states is the exciton Bohr-radius, given by

$$a_X = \frac{h^2 \epsilon_r}{\pi \mu e_0^2} \tag{7.1}$$

where ϵ_r is the permittivity of the dielectric material, μ is the reduced effective mass ($1/\mu = 1/m^*_e + 1/m^*_{hh}$) and e_0 is the electron charge. Due to the large value of ϵ_r and the small value of m^* in typical semiconductors, the exciton Bohr radius is generally much larger than that of a hydrogen atom ($0.53 \times$

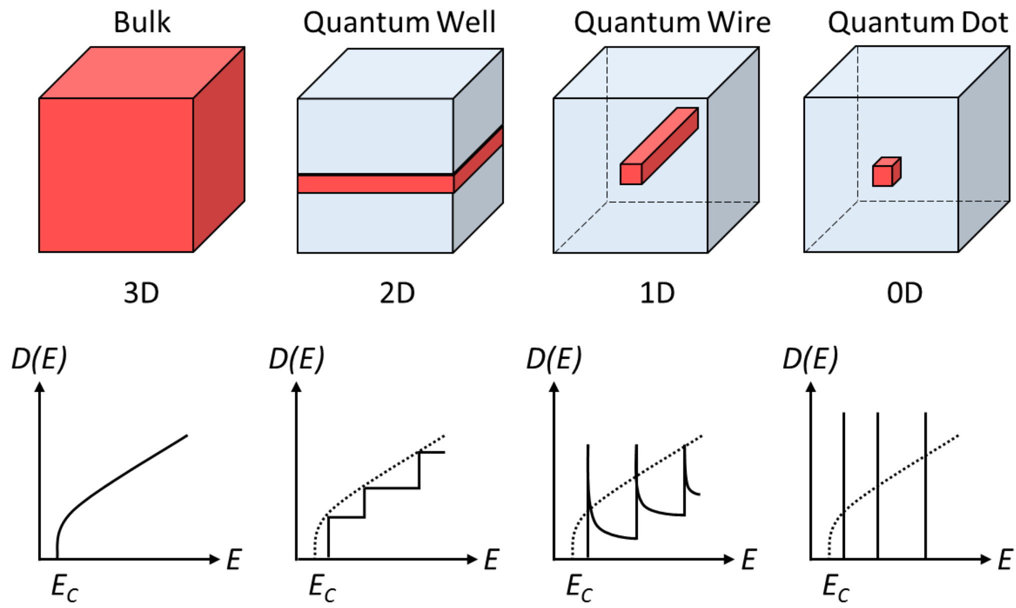

Figure 7.1: Electronic density of states D(E) in isotropic semiconductors (red) with different dimensionalities: 3D bulk semiconductor, 2D quantum well, 1D quantum wire, and 0D quantum dot. The environment drawn in blue provide potential barriers for the charge carriers. E_C denotes the conduction-band edge in the semiconductor [3].

$10^{-10}m$) and of the lattice constant of material.

7.1.1 Self-organized standard growth of QDs

Traditionally, three possible growth modes for heteroepitaxy have been identified as Frank-van der Merwe (FM, 1949), Volmer-Weber (VW, 1926) and Stranski-Krastanow (SK, 1937). The different growth mode is depending on the interaction energies of substrate atoms and film atoms. In general terms these are described as (Figure 7.2):

- **layer-by-layer FM mode**, the interaction between substrate and film atoms is greater than between adjacent film atoms;
- **island growth VW mode**, separate three-dimensional islands form on the substrate, where the interaction between film atoms is greater than between adjacent film and substrate atoms;
- **layer-by-layer plus island SK growth mode**, one or two monolayers form first, followed by individual islands.

Growth modes can be systematically classified in terms of surface energies with Young's equation taken into account (Figure 7.3). The island growth

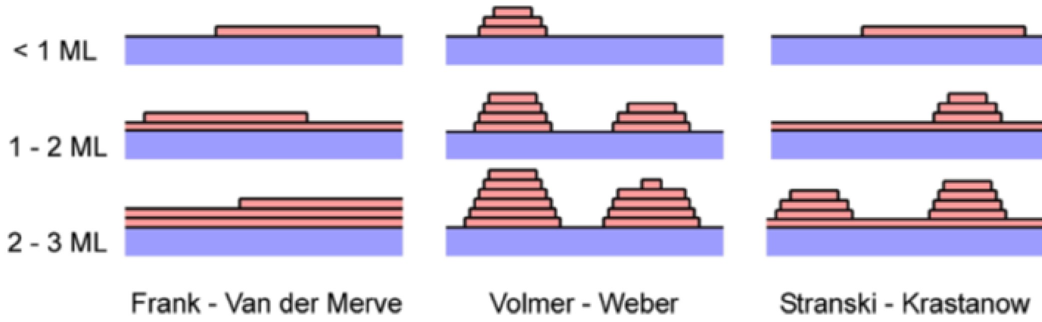

Figure 7.2: Schematic of the three growth modes, illustrated as a function of approximately equal coverage given in units of monolayers (ML) [3].

($\phi > 0$) requires that $\gamma_B < \gamma^* + \gamma_A$, whereas the layer growth ($\phi = 0$) requires that $\gamma_B > \gamma^* + \gamma_A$. The layer-plus-island growth occurs because the interface energy increases with film thickness; typically the layer on top of the substrate is strained to fit the substrate.

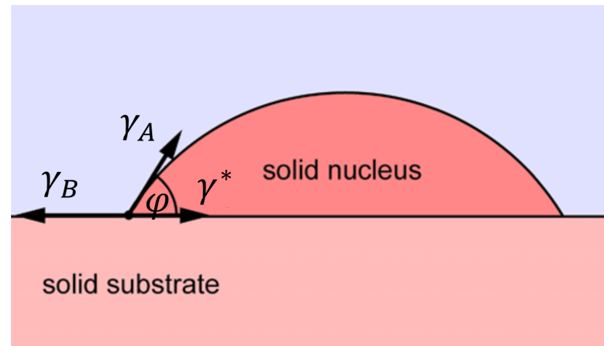

Figure 7.3: Wetting angle of a liquid nucleus on a substrate is described by Young's equation: $\gamma_B = \gamma^* + \gamma_A \cos(\phi)$, where γ_B is the surface energy of the substrate, γ_A is the surface energy of the film material, and γ^* is the interface energy film-substrate. Adapted from [4].

7.2 Influence of the hydrides exposure

The full study of hydrides influence here presented is based on nanostructures widely studied in a previous work by the EPN group (Ref.[5]), with a more comprehensive analysis that will be presented elsewhere. The mentioned studies have shown unforeseen evidence that the presence of $Al_{0.48}In_{0.52}As$, together with specific surface organization (and possible associated phase separation), has profound effects on the nucleation of InP (mono)layers. Indeed,

InP deposited directly on lattice-matched AlInAs forms a variety of nanostructures, despite the nominally strain free environment. These results are far from the epitaxial step-flow expected for perfect lattice matching.

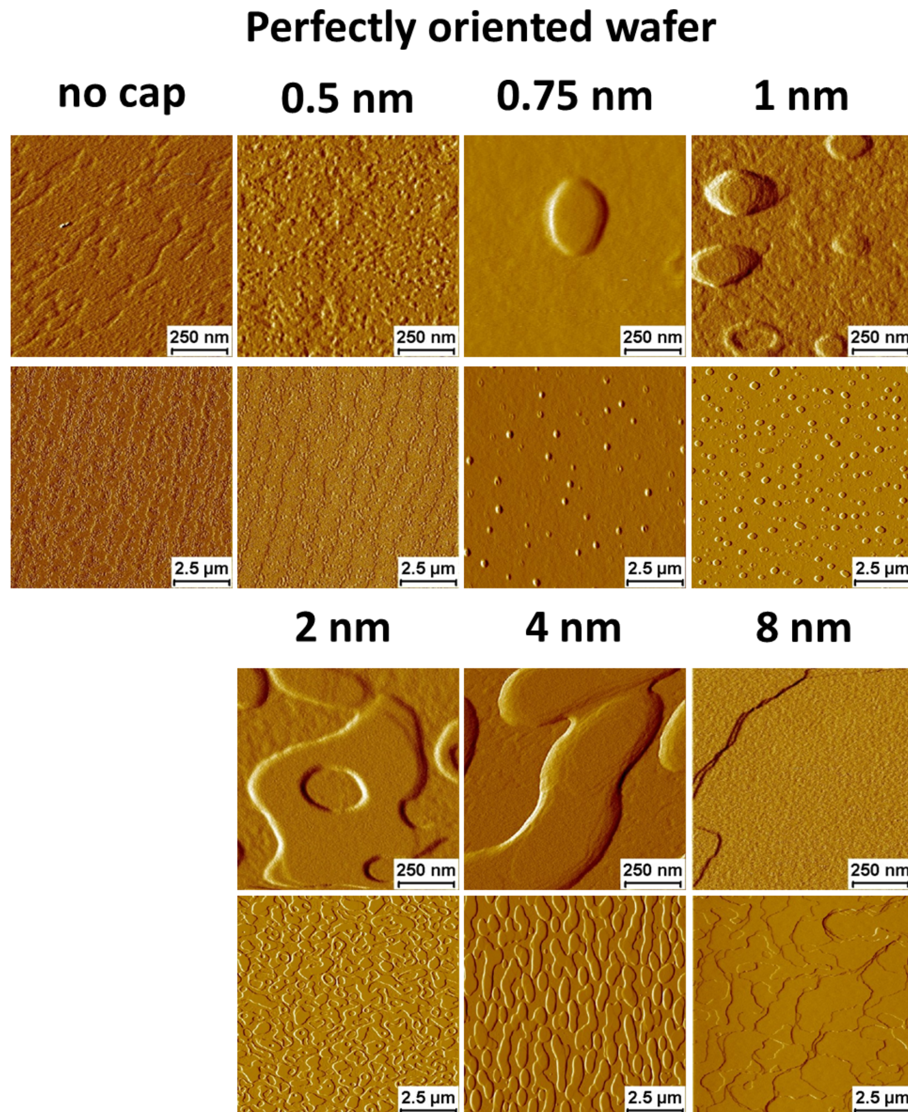

Figure 7.4: Surface morphologies (AFM signal amplitudes) of representative samples grown at 630°C, $G = 0.7\mu m/h$, $V/III = 180$, on a perfectly oriented $(100) \pm 0.05°$ wafer, for different InP cap layer thicknesses. For each sample is shown the AFM image in two X-Y scales (1x1 μm^2 and 10x10 μm^2). [6].

These structures, if capped, would generally result in a relatively broad type II emission around one micron, while preliminary transmission electronic microscopy (TEM) images show that the nanostructures evolve during capping, and are, partially, preserved after overgrowth (TEM not shown). To give the complexity of the phenomenology involved in Figures 7.4, 7.5 and 7.6 a representative AFM image from the systematic study [6] is shown.

The pictures in particular highlight how the nanostructure in term of formation and evolution are affected by the thickness of InP directly deposited on lattice matched AlInAs and by different substrates misorientations (nominally perfectly oriented (100) $\pm 0.05°$ wafers and slightly ($0.4° \pm 0.05°$) misoriented toward [111]A or [111]B planes, referred to as “p.o.”, “0.4°A” and “0.4°B”, respectively).

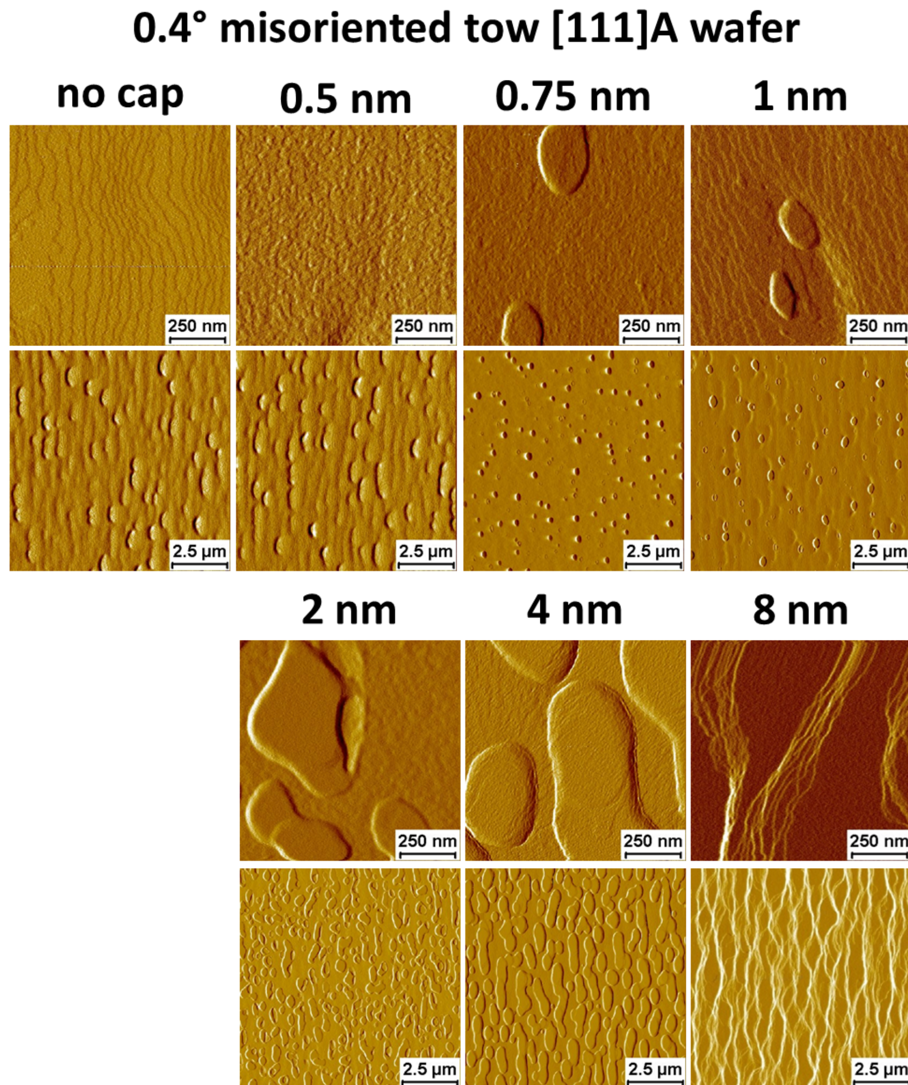

Figure 7.5: Surface morphologies (AFM signal amplitudes) of representative samples grown at 630°C, $G = 0.7\mu m/h$, $V/III = 180$, on a slightly ($0.4° \pm 0.05°$) misoriented toward [111]A wafer, for different InP cap layer thicknesses. For each sample is shown the AFM image in two X-Y scales (1x1 μm^2 and 10x10 μm^2). [6].

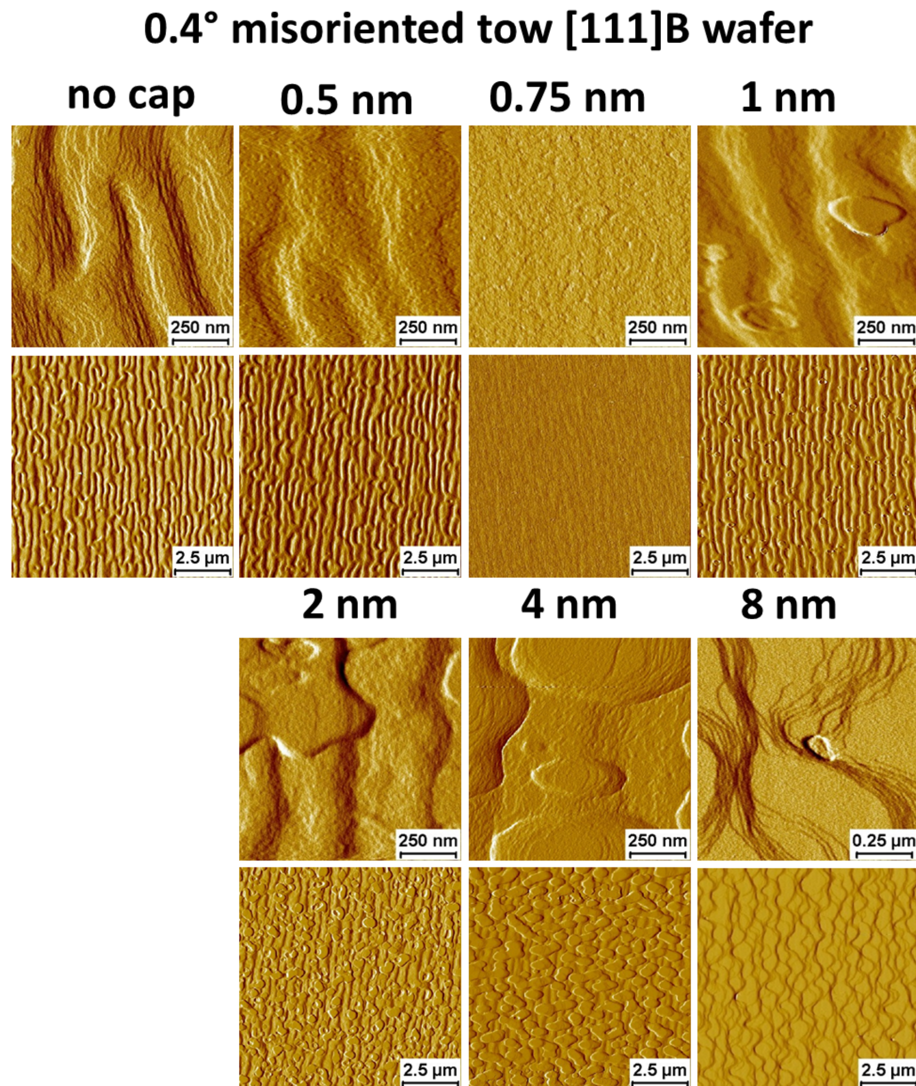

Figure 7.6: Surface morphologies (AFM signal amplitudes) of representative samples grown at 630°C, $G = 0.7\mu m/h$, $V/III = 180$, on a slightly $(0.4^{\circ} \pm 0.05^{\circ})$ misoriented toward [111]B wafer, for different InP cap layer thicknesses. For each sample is shown the AFM image in two X-Y scales (1x1 μm^2 and 10x10 μm^2). [6].

7.2.1 Samples structure and growth parameters

Sample growths were carried out in a commercial horizontal MOVPE reactor at low pressure (80 millibars) with purified N_2 as the carrier gas [7]. The precursors were trimethylindium (TMIn), trimethylaluminum (TMAl), trimethylgallium (TMGa), arsine (AsH_3), and phosphine (PH_3). Concerning morphological studies different sample designs were grown. Due to former laboratory practice, and to keep consistency with previous work, a first family of samples (which we will refer as "combined seed-heterostructure") comprised a 100 nm $Al_{0.48}In_{0.52}As$ layer (lattice matched to InP) grown on a 100 nm

homoepitaxial InP buffer on an <100> InP semi-insulating substrates, nominally perfectly oriented. Then a 20 nm layer of $In_{0.10}Ga_{0.90}P$ was deposited followed by 0.5 nm of $Al_{0.48}In_{0.52}As$. InP based nanostructures were then grown depositing a thin InP film (1 nm) on the previous 0.5 nm AlInAs layer. Following the InP film deposition, the nanostructures were then transformed by exposure to AsH_3 and PH_3 as required, and then the precursor was switched to PH_3 or AsH_3 for the cooldown protocol [5]. In the second set the structure was intentionally simplified removing the 20 nm of $In_{0.10}Ga_{0.90}P$ and 0.5 nm of $Al_{0.48}In_{0.52}As$ layers. In this "simple seed-structure" the InP based nanostructures were grown directly on the 100 nm of $Al_{0.48}In_{0.52}As$ layer [5] with the same protocol as in the "combined seed heterostructure", including exposure and cooldown. This work started on well characterized structures including the InGaP layers, and only subsequently evolved to a simplified seed structure on which we obtained our best optical results. The InGaP layer was historically broadly used in our InP nanostructure work to test the effects of thin AlInAs layers and possible group III adatom exchange. Both "combined seed-heterostructure" and "simple seed-structure" are sketch in Figure 7.7.

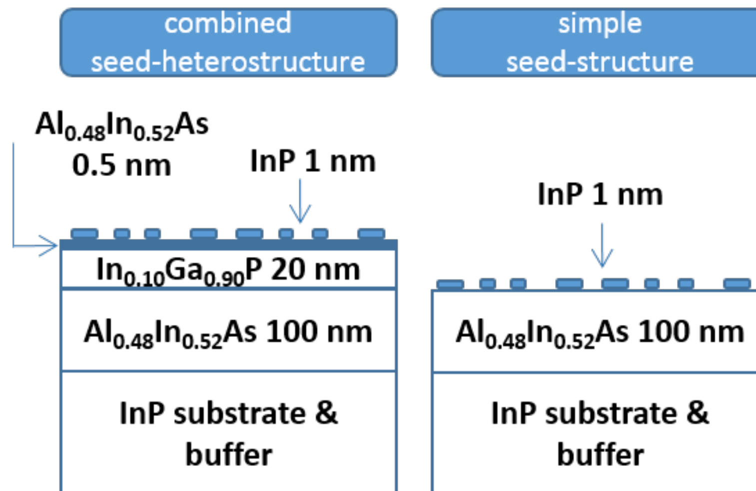

Figure 7.7: Schematic structure design of the "combined seed heterostructure" and "simple seed-structure".

For all samples the InP buffer growth conditions were as in Ref. [8].

Growth conditions for the others layer are summarized in the table 7.1. The self-organized InP nanostructures growth by MOVPE is described in more detail elsewhere [5].

Table 7.1: Growth parameters for the layers of both structures.

Parameters	InP	$Al_{0.48}In_{0.52}As$	$In_{0.10}Ga_{0.90}P$
GR ($\mu m/h$)	0.7	1	1
T (°C)	630	600	600
V/III	180	120	195

7.2.2 Zoology of the nanostructures

In Figure 7.8, 10x10 μm^2 AFM images of representative InP nanostructures are shown (all obtained on "combined seed heterostructure" like designs). To give a baseline Fig.7.8(a) shows InP QD nanostructures obtained as in Ref.[5] (i.e., by depositing InP directly on lattice matched AlInAs, and critically cooling them down under PH_3). Here, a mixture of islands and small rings emerges. The height of the QDs does not exceeded 8 nm with a base maximum diameter of $\sim 300nm$ and areal density of $\sim 1.9 \times 10^8 cm^{-2}$. Nanorings exhibit a base diameter of $\sim 300-200nm$ outer and $\sim 200-100nm$ inner. The overall height is comparable with the QDs whereas the areal density is slightly lower, about $\sim 1.2 \times 10^8 cm^{-2}$.

The morphology of one sample in which a previously deposited InP layer is subsequently exposed to an arsine flow (AsH_3 provided post-growth and during cooldown time, as described in the figure caption) is shown in Figure 7.8(b). Nanorings have disappeared, giving way to large dome-like structures [9]. The areal density, $\sim 2.7 \times 10^7 cm^{-2}$, is notably one order of magnitude lower when compared with the previous structure without the arsenisation process. The features are slightly elongated in the [011] direction with lateral dimension of $\sim$ 430 nm and $\sim$ 320 nm. The domes are unexpectedly tall, with height in excess of 150 nm.

It should also be said that in other samples where the constant growth temperature (T_{gr}) arsenisation was kept for longer (5 min instead of one), no significant morphological differences were detected by AFM (not shown). Altogether, the arsenisation time seems to not only substitute phosphorous atoms in the original structures, but also rearrange adatom distribution, enhancing their attachment to selected seeds, and presumably promote Ostwald ripening-like processes, hence the reduced density and larger overall dimensions [10, 11].

For the sample shown in Figure 7.8(c) the InP layer was exposed to the same arsine flow (one minute AsH_3) as for the sample shown in Figure7.8(b), but it was flushed with PH_3 during cooldown. It is evident that the sequence

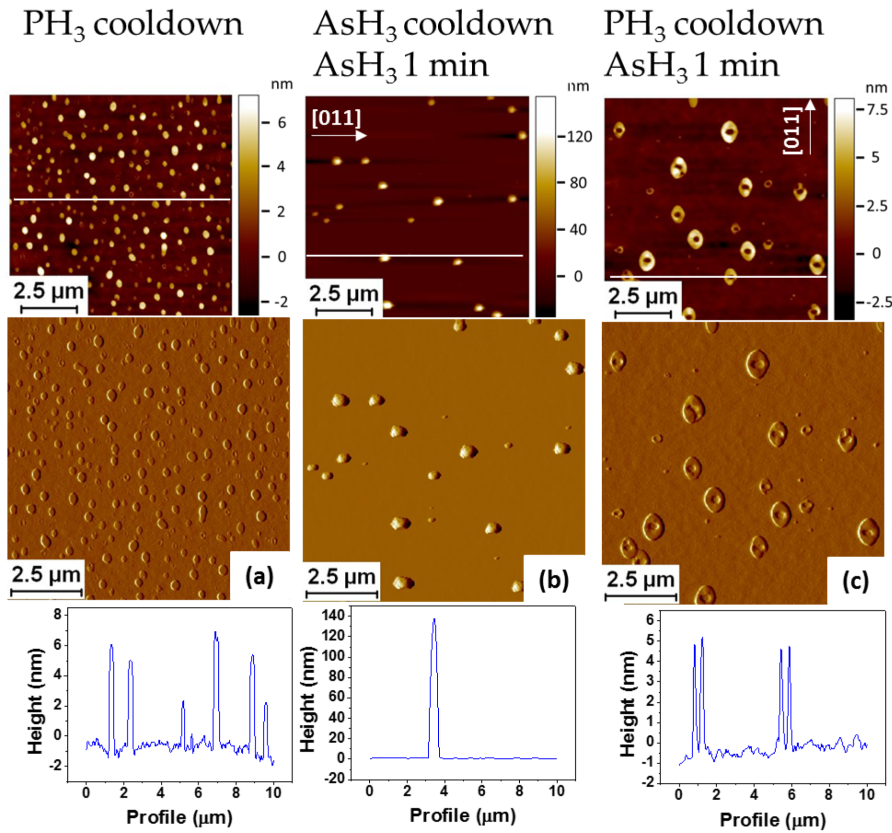

Figure 7.8: AFM images (height, amplitude signal and profile) of representative InP nanostructures, grown on a "combined seed heterostructure"(a) immediately cooled down under PH_3, (b) exposed to AsH_3 at growth temperature for 1 min at constant T (i.e. at the same T_{gr} used for the InP dots growth) and then flushed with AsH_3 during cooldown, and (c) exposed to AsH_3 at growth temperature for 1 min and then flushed with PH_3 during cooldown.

of hydride exposure transmuted the final nanostructures morphology, transforming the original domes into large rings. The rings exhibit inner and outer diameter of ~ 240 nm and ~ 640 nm, respectively, with areal density similar to the previous sample discussed, $\sim 4.0 \times 10^7 cm^{-2}$ in this image. Some rings acquire irregular shape, appearing elongated in the [011] direction. In Figure 7.9 are reported 3D reconstructed AFM images of every nanostructures just described: InP dot-like, InP(As) dome and InP(As) ring.

Similar trends are observed in other reported systems. The InAs/GaAs(001) system gives an example of the anisotropy in the redistribution of the material [12] ascribed to different diffusion rates of indium atoms along the crystallographic directions [13].

The rings as obtained in Fig. 7.8(c) actually evolve and change shape with arsine interaction time, i.e., the arsine (pre)exposure time is a relevant variable. After five minutes of arsenisation (instead of only one) the structures

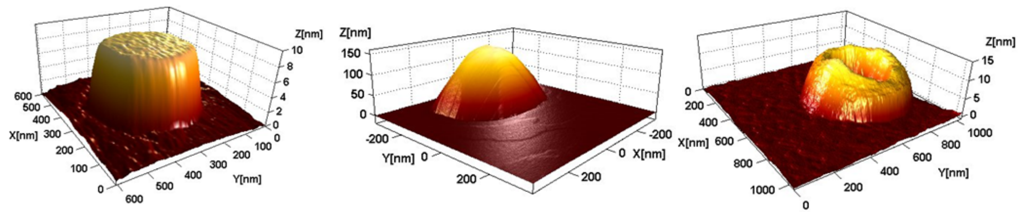

Figure 7.9: AFM images (3D reconstruction) of representative (a) InP dot-like nanostructure (b) InP(As) dome, and (c) InP(As) ring.

finally presented a definite and "ordered" round shape (see Fig. 7.10(a)). It is worth noting that we did not observe a significant excavation in the centre of the fully formed rings in the investigated samples, coming much closer to an "ideal" ring shape [14] than the typical craterlike InAs/GaAs [15] reported in the literature.

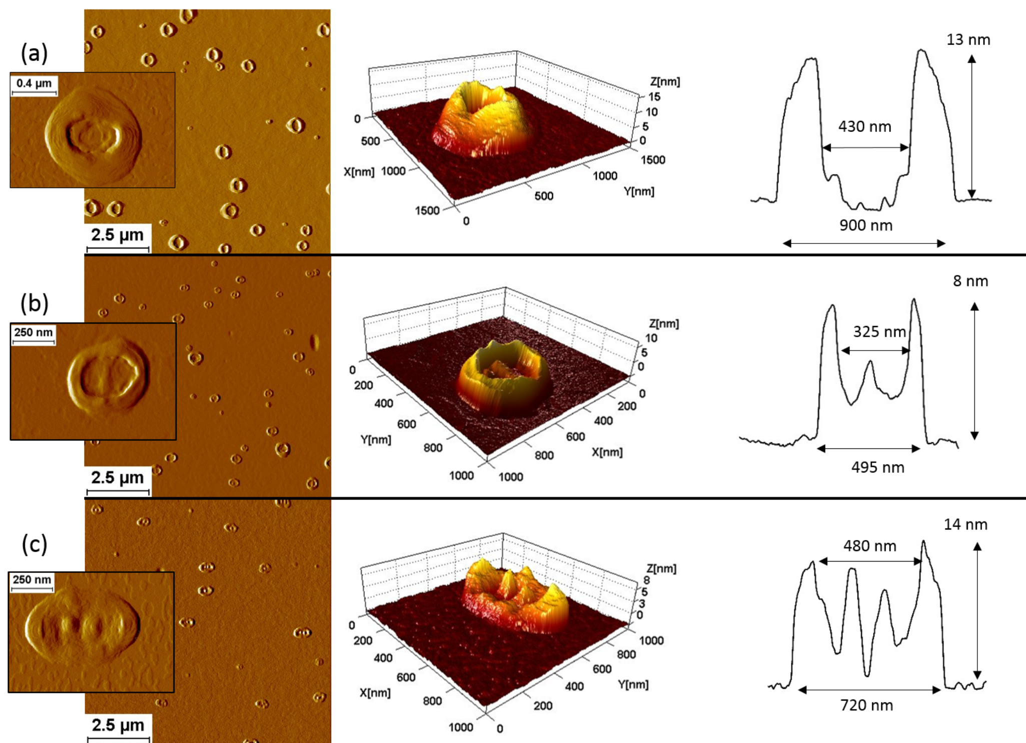

Figure 7.10: AFM images (amplitude signal, 3D reconstruction, and cross-sectional profile) of InP(As) nanostructures fabricated with same AsH_3 exposure time and same cooldown protocol under PH_3, but grown on: (a)"combined seed heterostructure"; (b) "simple seed-structure"; and (c) "simple seed structure" exposed to arsine and antimony at growth temperature.

Nevertheless, the rings' shape changed when we grew them on the "simple seed-structure" while keeping the same hydride exposure time of five minutes (Fig. 7.10(b)). The elimination of the InGaP layer between the AlInAs layer

and the InP QDs, and a thicker AlInAs nucleation layer (instead of only ~ 2 monolayers) seems to slow down the transformation process from dots to rings, highlighted by a central strip/band inside the ring, with the combined effect to generate what looks like a dot/wire in a ring structure. The heights (~ 10 nm) and inner diameters of the rings are comparable with those of the dots (those obtained right after InP deposition with no AsH_3 flux). We want also to stress that the morphology of the InP(As) nanostructures grown in our InP/AlInAs system is strongly sensitive to hydride exposure and to simple changes in the process parameters. The zoology of morphologies that we observed is indeed broader than what is reported here. Without digressing too much from the core of our contribution, in Fig. 7.10(c) we show one example: the AFM image of a "simple seed-structure" exposed to arsine for five minutes with the addition of antimony as surfactant. The Sb addition has a relevant effect: a different surface organization appears with one or two dots enclosed into elongated rings. The dots and the rings keep roughly the same overall height (~ 10 nm) and the same outer diameter, respectively, as observed in previous samples. It is worth observing that a similar kind of complexity of morphologies in the III–V system was observed till now only by droplet epitaxy [16, 17].

7.3 Rings growth mechanism

Post investigations of selective etching performed on the samples without the arsine exposition indicate that there was a possible difference in composition in the InP dots and the small rings (Figure 7.8(a)), with a suspicion of the presence of a compositional gradient in the islands (i.e., the rings and the outer parts of the dots seemed to be more P-alloy like, while the centers of the islands more As-alloy like, at least by the responsivity to the acids used during the etching experiments) [5]. This may suggest a transformation process, with the As rich regions in the domes, the ones originally formed during the InP dot nucleation and those obtained by P-As exchange by the successive arsenisation, redistributing during the last phosphorization stage, with the central atoms migrating to the external boundaries. While this process happens here in a rather striking manner, rings formation is not qualitatively a completely unexpected observation. For example, most studies on quantum rings (QRs) have been done with the typical approach to cover QDs with a complete or partial capping layer and post growth annealing processes[18, 19]. Instead, just few growths are reported without the use of any cap layer, for example, by annealing as-grown InAs QDs [20] or by direct deposition as in the case

of GaSb/GaAs where sometimes As/Sb soaking time is necessary to observe transition between nanostructures [21], or just by changing the amount of deposited GaSb [22]. The majority of these studies have been done by MBE and only a few by MOVPE [23–25]. Anyway in most of these studies strong material rearrangement is observed.

Two main different models have been proposed to explain the ring formation process. The first model is based on kinetic considerations, specifically on the different surface diffusion rate of group III atoms [18]. On the other hand a thermodynamic model [26] suggests that the presence of the capping layer creates variation in the balance of free energy and induces a force that pulls the QDs structures radially outward, leading to the QRs formation. This model explains the ring formation in the case of partial QD capping evolution to rings, for example. In this work, where QRs are fabricated uncapped, it is unclear which kind of model or combination of both effects takes place and brings to QRs formation. Notably in Refs. [22] and [20] where samples are fabricated with an MOVPE system, a method similar to ours, adatom rearrangement is reported; in one case the role of surface As-Sb exchange reactions was identified as one of the factors contributing to the formation of QRs, and in the other case the mechanism is discussed in terms of As/P exchange with a relevant role of strain in the QD-QR system.

7.4 Nanostructures emission properties

7.4.1 Capping studio and optical properties

The optical properties of the nanostructures presented in this chapter are investigated on the capped samples with different alloys. The complexity of the processes involved does not exclude some group III rearrangement as an extra process, not only regarding these specific nanostructures. Indeed the AFM evidence is only obtained after a full sample cooldown, and the nanostructure formation will be forcibly the result of the full process. When samples are capped, the morphological evolution is probably arrested/modified, and clearly different capping strategies affect this evolution and final results. In Figure 7.11 a preliminary investigation of AFM images of sample grown in the "simple seed structures", capped with different cap layer thickness, is presented. The rings still visible and well defined with 2 nm of InGaP cap change their appearance to volcano-like structures with just 5 nm of InGaP. The surface appears covered with "bubbles" after the deposition of 20 nm of InGaP, keeping the same bumps

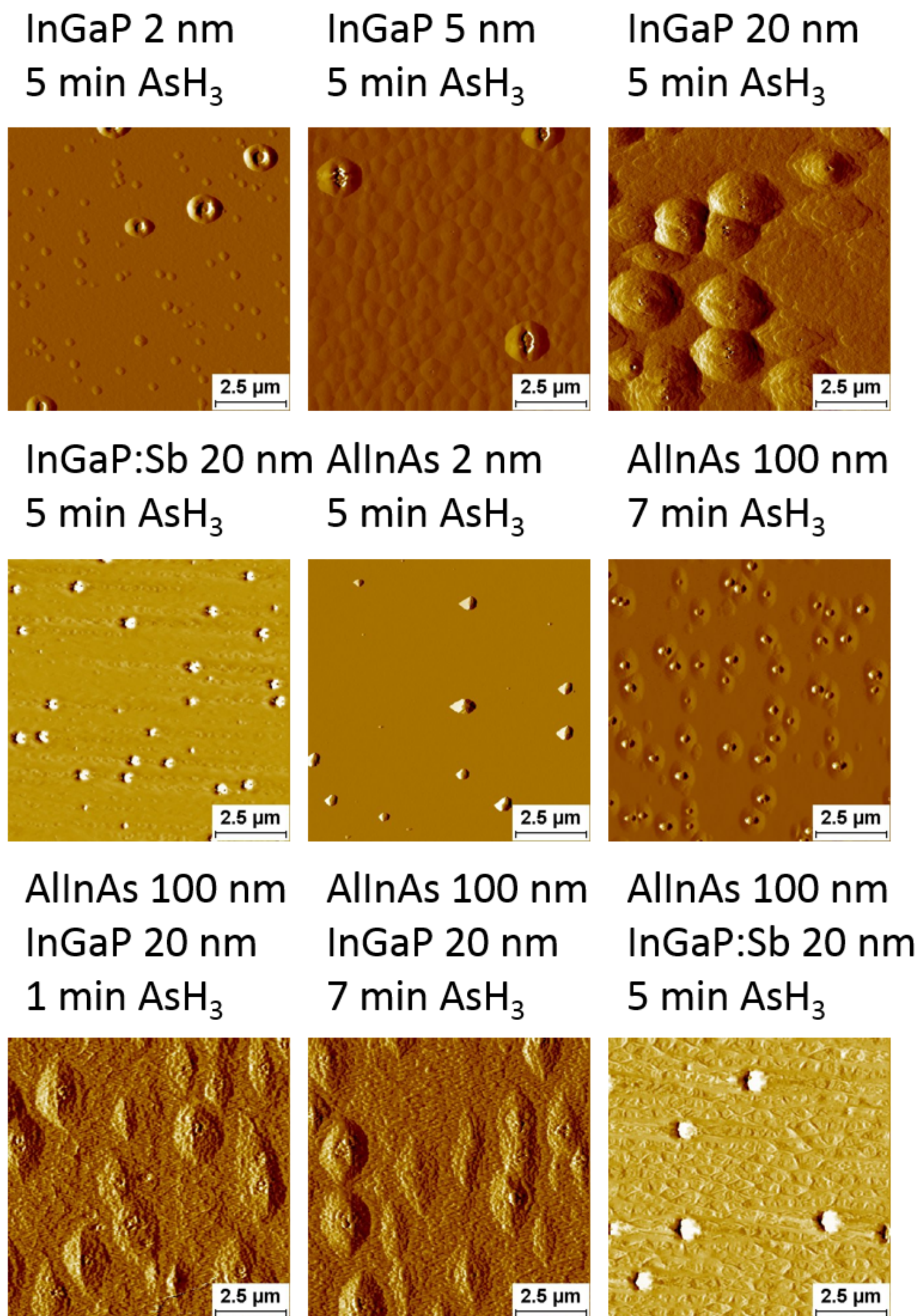

Figure 7.11: Flattened AFM amplitude images of samples grown in the "simple seed structure", exposed to arsine flow at growth temperature for and then capped with different cap layer thickness.

morphology when 100 nm of AlInAs are added as final layer. The capping InGaP layer was indeed inserted/intended to allow for keeping the ring-shape

(and preventing the transformation to domes) and the AlInAs to guarantee a sufficient quantum confinement. When AlInAs is the only cap layer, it seems that the domes are preserved and they are not completely covered also after 100 nm of AlInAs deposition. An extra sample grown with 20 nm of InGaP and antimony added as a surfactant, exhibits a rough surface covered with holes deep ∼40-50 nm.

In photoluminescence at low temperature we observed a typical type II band alignment structure emission peaked around 1 micron (Fig.7.12) for the InP/AlInAs system in the structures with "pure" InP/AlInAs nanostructures without the "arsenisation" step (Fig. 7.8(a)) when simply capped with the $Al_{0.48}In_{0.52}As$. As an example, the photoluminescence spectrum relative to a "combined seed heterostructure" exposed to the arsine flow for seven minutes (we chose here a longer arsenisation time than previously discussed so as to compare with the "optimized" result in Fig.7.13) and then capped with 100 nm of $Al_{0.48}In_{0.52}As$ (inset Fig. 7.12) shows similar features and additional few spread peaks around (1140–1170) nm, with relatively broad "single nanostructure like" emissions (probably linked to the dome structures Fig. 7.8(b), or better with their evolution with capping).

The spectral characteristics change completely when the "arsenised" nanostructures, grown here following the "simple seed structure", are capped with 20 nm $In_{0.10}Ga_{0.90}P$ and then 100 nm $Al_{0.48}In_{0.52}As$. In Figure 7.13 we present the low temperature PL spectrum from these capped nanostructures, showing individual transitions with very narrow linewidths (the best one found was 27 μeV in FWHM), and with power dependencies characteristic typical of single quantum dots [27]. They emit in a very attractive (and extraordinarily broad) spectral region, covering nearly the whole 1.1–1.6 micron range (not all shown in Fig. 4). Notably, this is very hard to achieve with traditional SK type dots, grown either on GaAs or InP, where emission is concentrated in relatively narrow bands specific to the growth protocol exploited. Indeed the emission from the dots assembly is spread across over more than 350 nm (240 meV) through the telecom window.

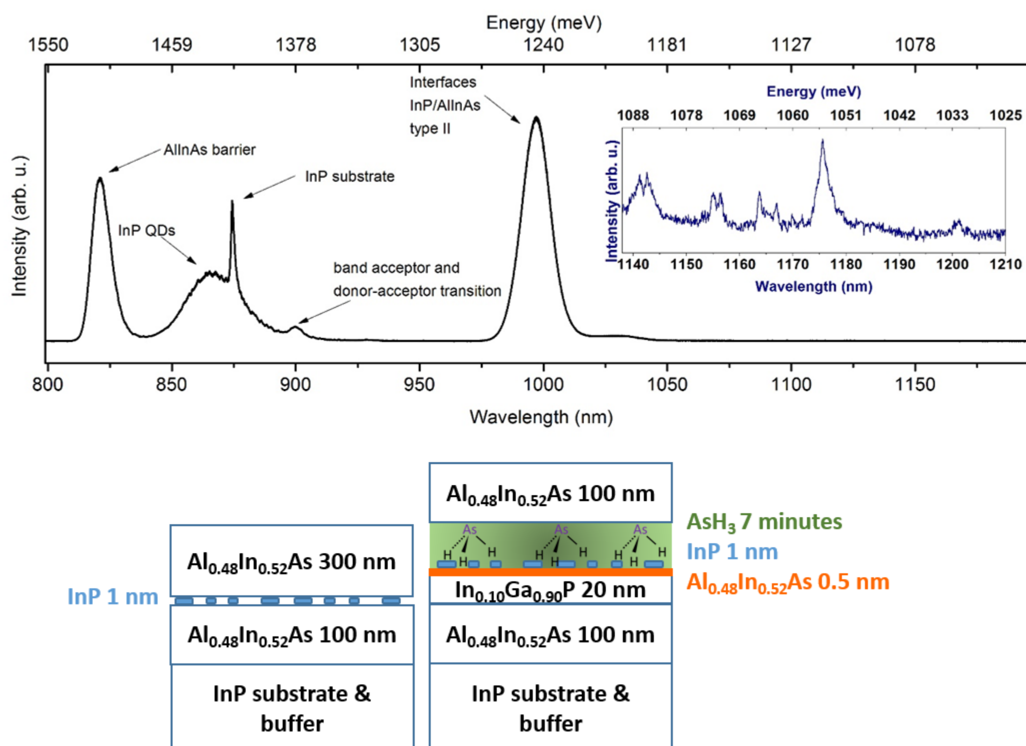

Figure 7.12: Top image: Low temperature photoluminescence spectrum of a "simple seed structure" directly capped with 300 nm of $Al_{0.48}In_{0.52}As$ and no special hydride treatment. The inset shows a part of photoluminescence spectrum of the "combined seed heterostructure" exposed to AsH_3 for seven minutes and then capped with 100 nm of $Al_{0.48}In_{0.52}As$. Bottom image: schematic structure design of the samples used for the photoluminescence in the top image.

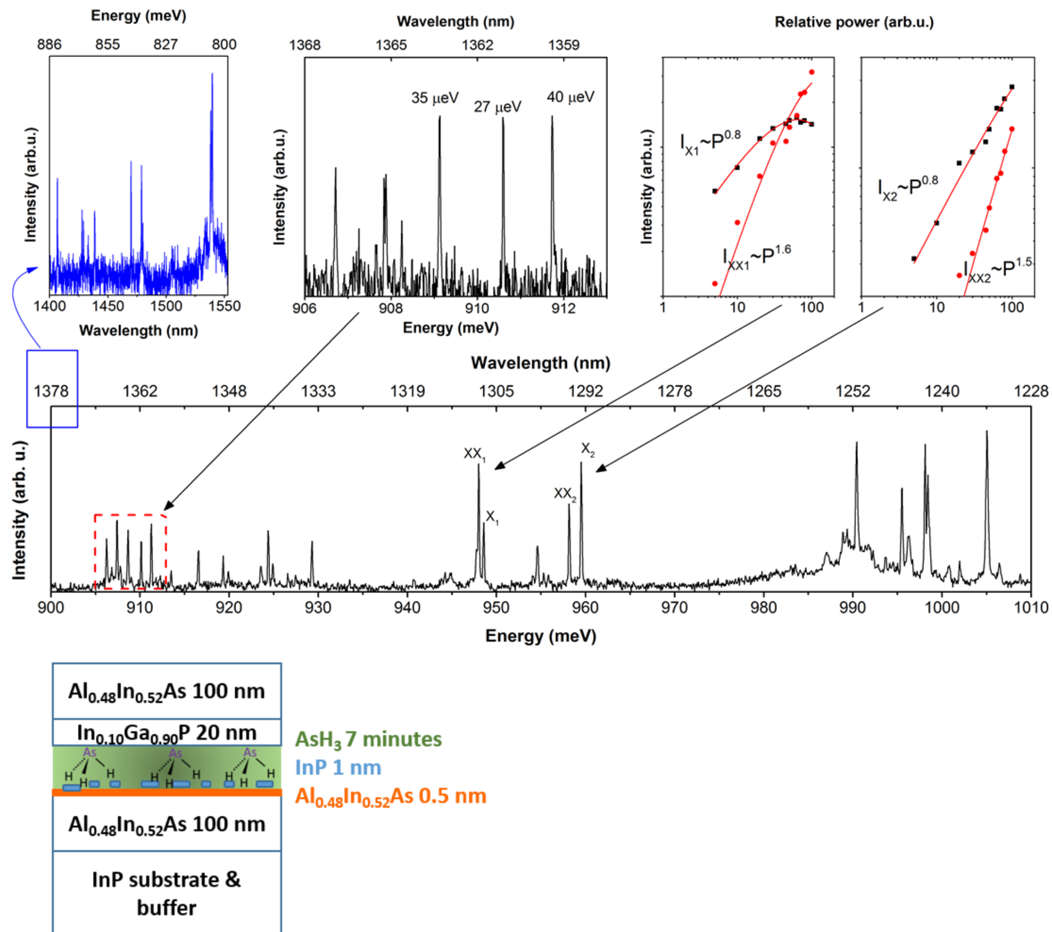

Figure 7.13: Part of the low temperature photoluminescence spectrum and relative structure design of "simple seed structure" exposed to AsH_3 for seven minutes and then capped with 20 nm of $In_{0.10}Ga_{0.90}P$ and 100 nm of $Al_{0.48}In_{0.52}As$. Left insert shows detail into a specific spectrum range. Top central insert shows zoom in to the spectrum range with FWHM of transitions stated for each line, and top right inserts show power dependence of the peak intensity, allowing for identification of the individual peaks as corresponding to exciton (X) and biexciton (XX) transitions.

7.5 Summary

In conclusion, the influence of hydrides on unusual selfassembled InP(As) nanostructures was investigated, showing unexpected morphological variability producing a different family of, possibly, pseudomorphic quantum structures. Notably, we have demonstrated that InP(As) ring-like structures can be spontaneously formed by MOVPE on lattice matched AlInAs. Ring formation is observed when unstrained InP nanostructures are exposed to AsH_3/PH_3. Moreover, preliminary microphotoluminescence data are indicating that the capped rings system is an interesting and promising candidate for single quantum emitters at telecom wavelengths, covering a very wide spectral range and delivering narrow emission lines, potentially becoming a possible alternative to InAs QDs for telecom and quantum technology applications.

Bibliography

[1] Enrica E Mura et al. "Tuning InP self-assembled quantum structures to telecom wavelength: A versatile original InP (As) nanostructure "workshop"". In: *Applied Physics Letters* 110.11 (2017), p. 113101.

[2] David AB Miller et al. "Band-edge electroabsorption in quantum well structures: The quantum-confined Stark effect". In: *Physical Review Letters* 53.22 (1984), p. 2173.

[3] Udo W Pohl. *Epitaxy of Semiconductors: Introduction to Physical Principles.* Springer Science & Business Media, 2013.

[4] Norbert Kaiser. "Review of the fundamentals of thin-film growth". In: *Applied optics* 41.16 (2002), pp. 3053–3060.

[5] A Gocalinska et al. "Unusual nanostructures of "lattice matched" InP on AlInAs". In: *Applied Physics Letters* 104.14 (2014), p. 141606.

[6] A Gocalinska et al. "Phenomenology of early stage epitaxy of (Volmer-Weber) aggregation InP nanostructures on AlInAs". In: (to be published).

[7] Valeria Dimastrodonato et al. "Relevance of the purity level in a MetalOrganic Vapour Phase Epitaxy reactor environment for the growth of high quality pyramidal site-controlled Quantum Dots". In: *Journal of Crystal Growth* 315.1 (2011), pp. 119–122.

[8] A Gocalinska et al. "Surface organization of homoepitaxial InP films grown by metalorganic vapor-phase epitaxy". In: *Physical Review B* 86.16 (2012), p. 165307.

[9] G Costantini et al. "Universal shapes of self-organized semiconductor quantum dots: Striking similarities between InAs/ GaAs (001) and Ge/ Si (001)". In: *Applied physics letters* 85.23 (2004), pp. 5673–5675.

[10] Peter W Voorhees. "The theory of Ostwald ripening". In: *Journal of Statistical Physics* 38.1-2 (1985), pp. 231–252.

[11] Byung Don Min et al. "Suppression of Ostwald ripening in In 0.5 Ga 0.5 As quantum dots on a vicinal (100) substrate". In: *Physical Review B* 57.19 (1998), p. 11879.

[12] Daniel Granados and Jorge M Garcia. “In (Ga) As self-assembled quantum ring formation by molecular beam epitaxy”. In: *Applied physics letters* 82.15 (2003), pp. 2401–2403.

[13] Axel Lorke et al. “Morphological transformation of InyGa1- yAs islands, fabricated by Stranski–Krastanov growth”. In: *Materials Science and Engineering: B* 88.2-3 (2002), pp. 225–229.

[14] R Timm et al. “Quantum ring formation and antimony segregation in Ga Sb/ Ga As nanostructures”. In: *Journal of Vacuum Science & Technology B: Microelectronics and Nanometer Structures Processing, Measurement, and Phenomena* 26.4 (2008), pp. 1492–1503.

[15] P Offermans et al. “Atomic-scale structure of self-assembled In (Ga) As quantum rings in GaAs”. In: *Applied Physics Letters* 87.13 (2005), p. 131902.

[16] JH Lee et al. “InGaAs quantum dot molecules around self-assembled GaAs nanomound templates”. In: *Applied physics letters* 89.20 (2006), p. 202101.

[17] Takaaki Mano et al. “Self-assembly of concentric quantum double rings”. In: *Nano letters* 5.3 (2005), pp. 425–428.

[18] JM Garcıa et al. “Intermixing and shape changes during the formation of InAs self-assembled quantum dots”. In: *Applied physics letters* 71.14 (1997), pp. 2014–2016.

[19] Axel Lorke et al. “Growth and electronic properties of self-organized quantum rings”. In: *Japanese Journal of Applied Physics* 40.3S (2001), p. 1857.

[20] Jaakko Sormunen et al. “Transformation of self-assembled InAs/InP quantum dots into quantum rings without capping”. In: *Nano letters* 5.8 (2005), pp. 1541–1543.

[21] Chi-Che Tseng et al. “Influence of As on the morphologies and optical characteristics of GaSb/GaAs quantum dots”. In: *IEEE Journal of Quantum Electronics* 47.3 (2011), pp. 335–339.

[22] Shigeki Kobayashi et al. “Self-assembled growth of GaSb type II quantum ring structures”. In: *Japanese journal of applied physics* 43.5B (2004), p. L662.

[23] Bing Chi Lee and Chien Ping Lee. “Formation of semiconductor quantum rings using GaAs/AlAs partially capped layers”. In: *Nanotechnology* 15.7 (2004), p. 848.

[24] A Aierken et al. "Transformation of InAs islands to quantum ring structures by metalorganic vapor phase epitaxy". In: *Nanotechnology* 19.24 (2008), p. 245304.

[25] Jeong-Sik Lee et al. "In 0.5 Ga 0.5 As quantum dot intermixing and evaporation in GaAs capping layer growth". In: *Journal of applied physics* 84.12 (1998), pp. 6686–6688.

[26] Ralf Blossey and Axel Lorke. "Wetting droplet instability and quantum ring formation". In: *Physical Review E* 65.2 (2002), p. 021603.

[27] E Dekel et al. "Cascade evolution and radiative recombination of quantum dot multiexcitons studied by time-resolved spectroscopy". In: *Physical Review B* 62.16 (2000), p. 11038.

Chapter 8

Conclusion and future work

$1.3\mu m$ metamorphic laser

A $>$ 1.3 μm-band laser grown by MOVPE on an engineered metamorphic graded InGaAs buffer has been demonstrated and presented. This thesis work has focused on a detailed and systematic study of the morphology and the surface organization of each layer (part) composing the full laser structure, bringing to a possible and reproducible "recipe" for a working laser device in the relevant emission telecom range.

The lattice constant gap between the two III-V semiconductors, InP and GaAs, was bridged with an $In_xGa_{1-x}As$ superlinear composition profile with negative curvature (somehow based on Tersoff's model and adapted to our MOVPE system), using and advancing the knowledge about metamorphic graded buffers previously start up in the group. The RMS value evaluated from an AFM scan size area of $50 \times 50\mu m^2$ reveals a successful smooth surfaces: ∼5 nm along the [110] direction and ∼3 nm along the $[1\bar{1}0]$ direction, for all three 0.2°A, 4°A and 6°A substrate misorientation studied.

We demonstrated that with the combination of two alloys InGaP and AlInGaAs in only one superlattice cladding layer structure is possible to control the defect formation in large part due to the residual strain from the MBL growth. Usually in laser structures built for long-wavelength emission devices the cladding layer is grown with one single alloy species, and usually a quaternary alloy of AlInGaAs is preferred as a lower cladding, as it has more degrees of freedom to engineer the lattice parameter. However, we observed the existence of correlation between epilayer thickness, surface roughness and defect generation. It was also observed that for thickness lower than 300 nm both AlInGaAs and the InGaP alloys exhibited RMS value of the same order of magnitude or close enough as those shown by the MBL. Hence the choice to combine the two alloys in the lower cladding barrier, alternating

them and keeping the thickness for each interface below 300 nm. One interesting phenomenon, never observed before, came from the cladding study: after the deposition of the AlInGaAs layer is preserved the anisotropy between the two surface direction inherited from the MBL substrate and miscuts chosen, whereas with the InGaP we observed a change or inversion in terms of roughness (RMS value) and morphology.

The heavily compressive strain in QWs and in the metamorphic buffer layer (in combination with the surface step bunched ordering) promoted 3D features formation under certain growth temperatures and for certain percentage of indium in the QWs. To avoid and control the 3D nanostructuring we proposed as a possible solution the insertion of a GaAs layer deposited before the QW. We attested that 5 nm of GaAs were sufficient to delay the nanostructures formation process, without perturbing the optical emission from the active SCH part. Moreover, we individuated a range of growth temperature and indium content in the QWs 3D-nanostructures and defects free, verifying the emission of interest. Between 540°C and 650°C the 3D nanostructures don't appear on the surface; in this range of growth temperatures we could grow 2 InGaAs QWs with up to 40% of indium, shifting at 580°C for 3 InGaAs QWs with same 40% of indium.

Building on these results, three different full laser structures were grown, and for each epitaxial structure stripe waveguide lasers were fabricated, then characterized electro-optically. The problems concerning high turning voltage and high series resistance were overcome with the third laser structure: a 1 μm thick n+ $In_{0.18}Ga_{0.82}As$ doped parabolic graded virtual substrate was grown by MOVPE preceded by a 100 nm thick GaAs buffer. A combination of both AlInGaAs and InGaP in a superlattice structure was employed as waveguide. The SCH region consisted of 3 $In_{0.4}Ga_{0.6}As$ QWs embedded in 100 nm $Al_{0.12}In_{0.14}Ga_{0.74}As$ and 80 nm $In_{0.13}Ga_{0.87}As$ barriers on each side. Significantly, it was discovered that the Si doping of the MBL didn't cause any degradation of the surface, differently from what observed in metamorphic structures grown by MBE. In the few existing papers concerning the n-doping of a graded substrate was indeed observed In segregation associated to the Si doping. However, it should be highlighted that the different graded profile was used in the InGaAs buffer growth, linear in the MBE case and parabolic in our case.

Lower and upper SL cladding structures were implemented adding graded composition layers at the interfaces following the aim to improve the carrier

transport. For the p-cladding: at the interface InGaP/AlInGaAs the percentage of gallium was linearly graded from $\sim$ 0% to 54% and the aluminium from 85% to 31%, keeping the indium content constant, over a distance of 26 nm. In this manner the hole transport toward the active part is supposed to be facilitated. For the n-cladding: the AlInGaAs layer was ramped from $Al_{0.07}In_{0.15}Ga_{0.78}As$ to $Al_{0.31}In_{0.15}Ga_{0.54}As$ at the InGaP/AlInGaAs interface. This modified the band alignment gap between AlInGaAs and InGaP in the conduction band, easing the electron motion towards the active part.

The modified epitaxial laser structure showed improved electric and optical characteristics (with $\sim$ no fluctuation in the results between adjacent devices), compared to the first two fabricated. A 500 μm long and 2.5 μm wide stripe waveguide was fabricated to be immediately comparable with previous devices of the same size. This specific stripe exhibited a threshold current I_{th} of $\sim$ 152 mA, corresponding to a J_{th} of $\sim$ 127 mA per QW, operating at room temperature in pulse mode. The improved turning voltage was $\sim$ 0.8 V ($\sim$ 10 times lower than first structure tested) and the resistance series resulted reduced to 4.5 Ω ($\sim$32 Ω was the value of the second laser structure). The emission wavelength was peaked at $\sim$ 1.34 μm, registered in pulse mode at low duty cycle. From shorter stripes laser, 10 μm and 20 μm wide, with different cavity lengths, T_0 was extracted. The threshold current varied from 130 mA to 170 mA in the operating temperature range of 30 °C-80 °C, and a T_0 of 95 K was calculated. From preliminary measurements, improvements in terms of efficiency of the laser were also observed. For devices 10 μm and 20 μm the $\boldsymbol{\alpha}_i$ and the $\boldsymbol{\eta}_i$ extrapolated were $\sim 30cm^{-1}$ and $\sim$ 57% respectively. An other significant achievement reached with this epitaxial structure was lasing in CW mode at $\lambda > 1.3$ μm.

Those results prove that the epitaxial structure developed in this thesis work allowed the fabrication of one the few (specifically the second one, referring to that proposed by a NTT Japanese group in 2015) InGaAs metamorphic QW laser GaAs based, operating at > 1.3 μm using the MOVPE technology.

Future development

It is important to highlight again that those are preliminary results; the complete material and device characterization is still on going, and still much work is required to transform the demonstrated 1.3 μm laser into a reliable technology.

As far as is concerned the growth dynamics:

- The cladding superlatice structure, improved with less interfaces replaced with graded composition layers, solved the issue of high turn on voltage. However, the effects that such graded layers will have on surface roughness will need to be assessed with a systematic and extensive study of surface roughness as a function of the solution adopted.
  - The effects of metamorphic substrate in-plane lattice parameter over the roughness process formation, i.e. how different metamorphic buffer designs (with in–plane lattice parameter ranging x = 0.10 - 0.20 $In_xGa_{1-x}As$ equivalent lattice parameter, obtained by varying both the final layer composition and the parabolic grading profile) affect the surface instabilities development dynamics. A specific metamorphic buffer design can be expected to deliver a slower roughness build-up in a single layer (e.g., increasing 20% in 1 μm to change the relaxation pattern and defect interaction), allowing to build less superlattice layers, each thicker in composition, reducing the interface effects.
  - Effects of doping (Zn) on surface roughness: it is known that Zn doping affects surface roughness in a number of MOVPE grown materials (e.g. reducing step bunching in InP based alloys, and increasing it in GaAs based alloys [1]). Could be interesting explore this avenue on metamorphic laser structures, and the specific Zn doping choice during growth should provide an effective way of reducing roughness and limiting the need for specific interfaces and eventually improve device performances. Also explore and eventually replace (in arsenide alloys) Zn doping with carbon doping, to reduced roughness and dopants diffusivity if needed.
- Effects of surfactants: the Epitaxy and Physics of Nanostructures (EPN) group has already shown that Sb can be effectively used as a surfactant in managing surface roughness [2]. The use of Sb could be extend to the MBL used in this thesis work, also varying the Sb content during growth for each layer, to analyse its role and effect on the novel planned designs.

As far as is concerned the laser engineering and optimisation:

- The devices fabricated and characterized to date were simple stripe contact lasers. Once solved the cleaving issues, ridge devices, differently sized, testing structures will be fabricated and electrical-optical characterisation performed.

- Being that the GaAs based metamorphic structures is perfectly compatible with current hybrid integration approaches (such as micro-transfer printing, a technology also developed in Tyndall), the laser structure as active layers could be transferred from the GaAs substrate to a silicon photonic platform.

InP(As) nanostructures

With the side work concerning the unusual self-assembled InP(As) nanostructures, we propose an alternative active material to the InGaAs MQWs for telecom wavelengths. We show how the hydrides effect is able to change shape and size of the 3D-nanostructures, producing a different family of, possibly, pseudomorphic quantum structures. InP(As) ring-like formation is observed when unstrained InP nanostructures are exposed to AsH_3/PH_3. Moreover, preliminary microphotoluminescence data are indicating that the capped rings system is an interesting and promising candidate for single quantum emitters at telecom wavelengths, covering nearly the whole 1.1–1.6 micron range, a very wide spectral range and delivering narrow emission lines; potentially becoming a possible alternative to InAs QDs for telecom and quantum technology applications.

Future development

Since the hydride exposure also influences the initial emission moving from a type-II band alignment into type-I and resulting in a photoluminescence spectrum (in the telecom range) with several sharp QD-like lines , a possible direction is to broad our study on the development of multilayer structures coupling the InP(As) features with InGaAs quantum wells. In this respect we recently started to find the way to convert the emission from that of a collection of single QDs to a broad optical spectrum. Some very good results are achieved (not shown in this thesis work), suggesting the idea of possible exploitation as tuneable broadband light emitters.

Appendix A

Dislocations

Dislocations are defect lines characterized by two vectors: the vector along the dislocation line, called *line vector* **l** and the Burgers vector **b**, which defines the magnitude and direction of the deformation, determined by a closed path around the dislocation core, the burgers circuit (Figure A.1). The symbol to represent a general dislocation is ⊥. Usually dislocations are individuated in edge and screw and mixed. The edge defect can be easily visualized as an extra half-plane of atoms in a lattice.

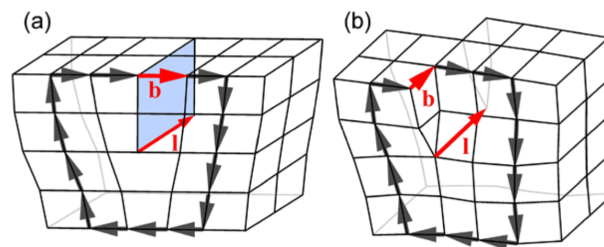

Figure A.1: (a) Edge dislocation and (b) screw dislocation. **b** and **l** denote the Burgers vector and the dislocation-line vector, respectively.[1]

In the edge dislocation **b** is perpendicular to **l**. In a screw dislocation **b** is parallel to **l**. This kind of dislocation is built by a shift of one part of the solid by an amount **b**. Most dislocations occurring in solids are of mixed character with an edge and a screw component. Understanding the movement of a dislocation is key to understanding why dislocations allow deformation to occur at much lower stress than in a perfect crystal. When a shear force is applied to a material, the dislocations move, gliding and climbing. During gliding the dislocation moves by turning crystal planes. The total number of atoms and lattice sites is conserved in such motions. In the process of slipping one plane at a time the dislocation propagates across the crystal (Figure A.2) For pure edge dislocations the process can only occur along slip planes which contain both the Burgers vector and the dislocation line.

Pure screw dislocations can glide along any plane, since **l** and **b** are parallel.

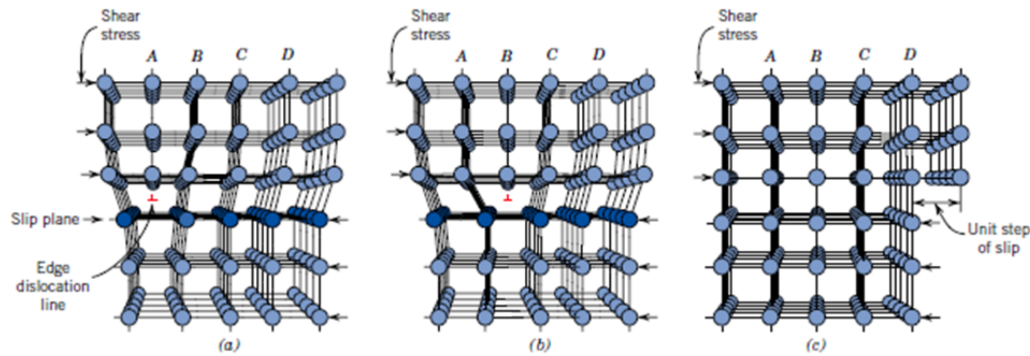

Figure A.2: Atomic rearrangements that accompany the motion of an edge dislocation as it moves in response to an applied shear stress. (a) The extra half-plane of atoms is labeled A. (b) The dislocation moves one atomic distance to the right as A links up to the lower portion of plane B; in the process, the upper portion of B becomes the extra half-plane. (c) A step forms on the surface of the crystal as the extra half-plane exits. (Adapted from A. G. Guy, Essentials of Materials Science, McGraw-Hill Book Company, New York, 1976, p. 153.)[2]

Climbing occurs within a plane, which contains the dislocation line but is perpendicular to the Burgers vector (Figure A.3). Climbing is accompanied by a material transport, i.e., emission or absorption of interstitials or vacancies (point defects).

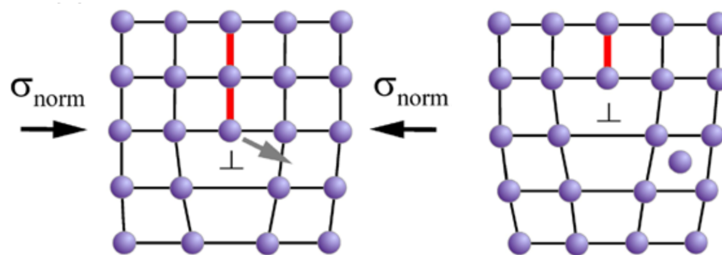

Figure A.3: Edge dislocation performing a climbing process. σ_{shear} and σ_{norm} indicate shear and normal stresses acting on the solid. [1]

Early studies in this area found that misfit dislocation that accommodate the lattice mismatch between the epilayer and the substrate often generate a Threading dislocations (TDs), i.e a dislocation penetrating the layer [3]. In the cited article the authors attested that since the dislocation line can neither begin nor end within a crystal, its ends must lie at the surface, proposing two mechanism of the process sketched in Figure A.4. Both mechanisms lead to the formation of a dislocation network at the interface between layer and substrate (Figure A.4(c)).

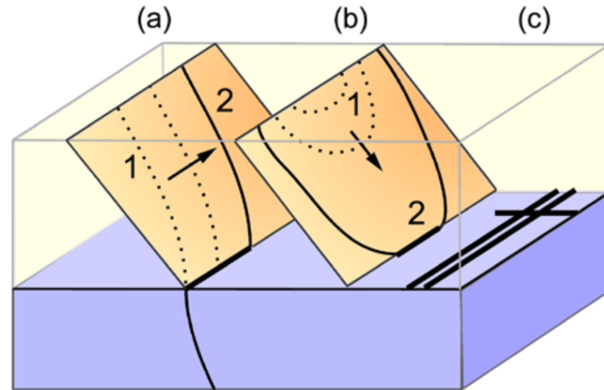

Figure A.4: Generation of a misfit dislocation network (c) at the interface between layer (upper part) and substrate (lower part, blue) from (a) a pre-existing threading dislocation of the substrate and (b) from the nucleation of a dislocation half loop. [1]

In the particular case of zincblende semiconductor structures with $\frac{1}{2} < 110 >$ Burgers vectors, three main type of perfect dislocation can be located: edge dislocations, screw dislocations and 60°-mixed dislocations. The 60°-mixed type is the most common, they can be further classified as α and β dislocations. In the semiconductor AB type, the α dislocations have all A atoms at the core, whereas β dislocations have all B atoms at their cores [4]. The orthogonal directions are not equivalent, which affects the uniformity of the strain relaxation and the dislocation density because of the significant differences in activation energies for α and β dislocation nucleation and glide. It α and β dislocations can be expected to behave differently due to their different core structures. Differences in mobility have been demonstrated for the two types of dislocations, e.g in undoped and n-type GaAs it has been found experimentally that α dislocations have a higher glide velocity than β dislocations GaAs [5, 6].

Bibliography

[1] Udo W Pohl. *Epitaxy of Semiconductors: Introduction to Physical Principles*. Springer Science & Business Media, 2013.

[2] William D Callister, David G Rethwisch, et al. *Materials science and engineering: an introduction*. Vol. 7. John Wiley & Sons New York, 2007.

[3] JW Matthews. "Defects associated with the accommodation of misfit between crystals". In: *Journal of Vacuum Science and Technology* 12.1 (1975), pp. 126–133.

[4] John E Ayers et al. *Heteroepitaxy of semiconductors: theory, growth, and characterization*. CRC press, 2016.

[5] H Steinhardt and P Haasen. "Creep and dislocation velocities in gallium arsenide". In: *physica status solidi (a)* 49.1 (1978), pp. 93–101.

[6] I Yonenaga and K Sumino. "Behaviour of dislocations in GaAs revealed by etch pit technique and X-ray topography". In: *Journal of crystal growth* 126.1 (1993), pp. 19–29.

Acknowledgements

Firstly, I would like to express my sincere gratitude to my supervisor *Dr. Emanuele Pelucchi* for the continuous support of my Ph.D study and related research, for his patience, motivation, and immense passion for physics and science, which is of exceptional inspiration for me and many. His guidance helped me in all the time of research and writing of this thesis.

Thanks to *Dr. Agnieszka Gocalinska* for teaching me most of what I learnt during these years, for the massive amount of time she dedicated to me and for his patience and support.

I would like to thank the rest of my thesis committee: my co-supervisor *Prof. Paul Townsend*, *Dr. Ian Povey*, and my enterprise mentor *Dr. Roger Nagle*, for their helpfull comments and encouragement.

I would like to thank all people in the EPN group: *Simone Varo*, *Dr. Gediminas Juska*, *Dr. Kevin Thomas*, *Iman Ranjbar*, *Ayse Atar*. I would like also to acknowledge all the help and good memories from colleagues who are not in Tyndall anymore: *Dr. Hanno Kroencke*, *Dr. Andrea Pescaglini*, *Dr. Tung-Hsun Chung (Mau)* and *Francesco Azzarello*. In particularly, I thank *Dr. Eleonora Secco* and *Dr. Stefano Moroni* for being not only valid and caring colleagues but also great friends.

I thank the people in the III-V group at Tyndall National Institute for providing device fabrication and electro-optical characterization. In particular, I thank *Mr. Brian Corbett*, *Dr. Ruggero Loi* and *Megan O'Brien*.

I thank all my colleagues and friends at Tyndall National Institute, and all my friends around the world.

Last but not least, a special "thanks" goes to my "big-loved" family and to my loving husband.

I would like to thank Irish Research Council under grant EPSPG/2014/35 for the financial support.